

DEVELOPMENT AND APPLICATIONS OF TWO AND THREE
COMPONENT PARTICLE IMAGE VELOCIMETRY TECHNIQUES FOR
SIMULTANEOUS MEASUREMENT IN MULTI-PHASE FLOWS AND
AUTOMOTIVE FUEL SPRAYS

Diego Alejandro Angarita Jaimes

Submitted in accordance with the requirements for the degree of
Doctor of Philosophy

The University of Leeds
School of Mechanical Engineering

September 2010

The candidate confirms that the work submitted is his own, except where work which has formed part of jointly-authored publications has been included. The contribution of the candidate and the other authors to this work has been explicitly indicated below. The candidate confirms that appropriate credit has been given within the thesis where reference has been made to the work of others

CHAPTER 4

CHENNAOUI, M., ANGARITA-JAIMES, D., ORMSBY, M. P., ANGARITA-JAIMES, N., MCGHEE, E., TOWERS, C. E., JONES, A. C. & TOWERS, D. P. Optimization and evaluation of fluorescent tracers for flare removal in gas-phase particle image velocimetry. *Measurement Science and Technology*, 19. (2008). This paper presents the development of fluorescent tracers and their experimental use under laser illumination. The development of the fluorescent tracers is a contribution of Mourad Chennaoui and Anita Jones, School of Chemistry, University of Edinburgh. All the experimental images under laser illumination, sizing of the tracers and vector fields are a contribution of Diego Angarita-Jaimes under the supervision of Prof David Towers and Dr Catherine Towers.

CHAPTER 5

M. P. ORMSBY, M. CHENNAOUI, D. A. ANGARITA-JAIMES, N. C. ANGARITA-JAIMES, C. E. TOWERS, A. C. JONES, D. P. TOWERS. Optically efficient fluorescent tracers for multi-constituent PIV and flare removal. 7th International Symposium on Particle Image Velocimetry University La Sapienza Via Eudossiana 18, Roma ITALY 11-14 September 2007. The fluorescent tracers used in this paper are a contribution of Mourad Chennaoui and Anita Jones, School of Chemistry, University of Edinburgh. Everything else presented in this publication is a contribution of Matthew Ormsby and Diego Angarita-Jaimes under the supervision of Prof David Towers and Dr Catherine Towers.

ANGARITA-JAIMES, D. A., ORMSBY, M. P., CHENNAOUI, M., ANGARITA-JAIMES, N. C., TOWERS, C. E., JONES, A. C. & TOWERS, D. P. (2008) Optically efficient fluorescent tracers for multi-constituent PIV. *Experiments in Fluids*, 45, 623-631.

The fluorescent tracers used in this paper are a contribution of Mourad Chennaoui and Anita Jones, School of Chemistry, University of Edinburgh. Everything else presented in this paper is a contribution of Diego Angarita-Jaimes under the supervision of Prof David Towers and Dr Catherine Towers.

CHAPTERS 6 AND 7

DIEGO ANGARITA-JAIMES, MOURAD CHENNAOUI, CATHERINE TOWERS, ANITA JONES, DAVID TOWERS. Multi-phase measurements on a GDI spray using optically efficient fluorescent tracers. 14th International Symposium on Applications of Laser Techniques to Fluid Mechanics Lisbon, Portugal, 07-10 July, 2008. The fluorescent tracers used in this paper are a contribution of Mourad Chennaoui and Anita Jones, School of Chemistry, University of Edinburgh. Everything else presented in this paper is a contribution of Diego Angarita-Jaimes under the supervision of Prof David Towers and Dr Catherine Towers.

DIEGO ANGARITA-JAIMES, CATHERINE TOWERS, DAVID TOWERS. 3-Component multi-phase velocimetry measurements on a GDI spray using optically efficient fluorescent tracers. 15th International Symposium on Applications of Laser Techniques to Fluid Mechanics Lisbon, Portugal, 05-08 July, 2010. The contents of this paper are a contribution of Diego Angarita-Jaimes under the supervision of Prof David Towers and Dr Catherine Towers.

This copy has been supplied on the understanding that it is copyright material and that no quotation from the thesis may be published without proper acknowledgement.

The right of Diego Alejandro Angarita Jaimes to be identified as Author of this work has been asserted by him in accordance with the Copyright, Designs and Patents Act 1988.

Acknowledgments

I would like to thank my supervisors Professor Dave Towers and Dr Cathy Towers for their invaluable support, guidance and encouragement during the course of this research work. Additional thanks go to Mourad Chennaoui, Anita Jones and Matthew Ormsby for their input in this project and Dave Hollis at LaVision.

I would like to thank everyone at the Roberto Rocca Education Program for their financial support for my PhD studies especially Daniel Krishock, Cecilia Pezzolano and Matías García.

I would like to thank all the technicians at the Mechanical Engineering department, without whom, this project would not have been possible. Special thanks go to Paul Banks for his continuous help with the experimental rig used in this project. Thanks are also given to my colleagues within our research group as well as Dr Nik Kapur and James Eves for their help during the writing up process.

My gratitude is extended to all my friends in and around Leeds and London especially Jule, Juan, Kosta, Sarah, Gen, Yadira, Sabine, Olga, Paula, Tatiana and Juan Carlos who have always helped, entertained and supported me (or put up with me) during my time in England.

I am especially indebted to my family especially my mother and my sister for all their love and support throughout my life.

Finally I would like to dedicate this work to the memory of my father who inspired me to be a Mechanical Engineer.

Abstract

The introduction of a new imaging approach for simultaneous multi-phase and multi-constituent velocity measurements is the main focus of this research. The proposed approach is based on the use of a single off-the-shelf colour camera which will enable simultaneous imaging of phases/constituents which are colour-tagged using fluorescent droplets and multi-wavelength illumination. Highly efficient fluorescent tracers used to seed the constituents are presented and their visibility in full field imaging experiments is evaluated. A commonly found problem in experimental systems using laser illumination, known as flare, is discussed and the application of the developed fluorescent tracers for its reduction is presented. A strong focus of the imaging approach proposed is its flexibility and simplicity allowing its extension to stereoscopic imaging to obtain simultaneous multi-phase/constituent 3-component measurements with the addition of a second imaging camera. Proof of principle experiments with spatially separated and well mixed flows are presented for which successful phase discrimination is obtained and the uncertainty of the measurements is estimated. The imaging system developed is applied for simultaneous air and fuel velocimetry measurements in a Gasoline Direct Injection spray for which a more detailed understanding of the interaction mechanisms is required to generate improved designs. The modified imaging system and experimental setup are presented and previously unavailable simultaneous air/fuel 2 and 3-component velocity fields are presented and analysed.

List of abbreviations

2C	2-component
2D	2-dimensional
3C	3-component
3D	3-dimensional
AGW-FD	Adaptive Gaussian Window - Finite Difference
AVG	Average
Bis-MSB	1,4-bis(2-methylstyryl)benzene
CCD	Charge-Coupled Device
CO ₂	Carbon dioxide
DCM	4-(Dicyanomethylene)-2-methyl-6-(4-dimethylaminostyryl)- 4H-pyran
DMSO	Dimethyl Sulfoxide
D _{v90}	90% Cumulative volume diameter
ELWD	Extra Long Working Distance
FFT	Fast Fourier Transform
FWHM	Full Width Half Maximum
GDI	Gasoline Direct Injection
GDV	Global Doppler Velocimetry
HC	Hydrocarbon
IPI	Interferometric Particle Imaging
IR	Infrared
LDA	Laser Doppler Anemometry
LDV	Laser Doppler Velocimetry
LED	Light-emitting Diode
LIF	Laser-Induced Fluorescence

LSV	Laser Speckle Velocimetry
M	Molar
MART	Multiplicative Algebraic Reconstruction Technique
N ₂	Nitrogen
ND	Neutral Density
Nd:YAG	Neodymium: Yttrium Aluminium Garnet
NO _x	Nitrogen Oxides
PFI	Port Fuel Injection
PIV	Particle Image Velocimetry
PLV	Pulsed-light Velocimetry
PTV	Particle Tracking Velocimetry
RGB	Red Green Blue
RMS	Root Mean Square
RPM	Revolutions per minute
SAE	Society of Automotive Engineers
SDV	Shadow Doppler Velocimetry
SMD	Sauter Mean Diameter
UV	Ultraviolet

Nomenclature

d_p	particle diameter
ρ	liquid density
μ	liquid dynamic viscosity
σ	liquid surface tension
U_p	particle velocity
λ	laser wavelength
x	particle size parameter
n	refractive index
m	ratio of refractive indices
h	Planck's constant
$\Delta\nu$	droplet shift of the light scattered by particles
ν_o	frequency of a light source,
c	speed of light
\vec{V}	particle velocity
V_x, V_y, V_z	Velocity components in the x, y and z directions
a	acceleration
C_D	drag coefficient
A	area of a particle
ν_f	fluid kinematic viscosity
f	focal length
d_o	distance between the object plane and the imaging lens
d_i	distance between the image plane and the lens

M	magnification of the system
$F_{\#}$	Lens f number
d_i	image diameter
d_{diff}	diameter of Airy function
K_{np}	Knudsen number
l	molecular free path
Δ	grid separation for vorticity calculation
$P1, P2$	Correlation peaks
u, v, w	velocity components for stereo calculation

Contents

ACKNOWLEDGMENTS	IV
ABSTRACT	V
LIST OF ABBREVIATIONS	VI
NOMENCLATURE	VIII
LIST OF FIGURES	XIV
LIST OF TABLES	XIX
CHAPTER 1	
INTRODUCTION	1
1.1. MOTIVATION	1
1.2. AIMS AND ORIGINAL CONTRIBUTIONS	2
1.3. THESIS FORMAT	4
CHAPTER 2	
MULTI-PHASE FLOWS AND GASOLINE DIRECT INJECTION ENGINES.....	8
2.1. MULTI-PHASE FLOWS.....	8
2.1.1. Applications of multi-phase flows.....	9
2.1.2. Measuring multi-phase flows	10
2.2. GASOLINE DIRECT INJECTION ENGINES	11
2.2.1. The need for direct injection technology	11
2.2.2. History of Direct Injection	13
2.2.3. Theoretical advantages over conventional port injection engines	14
2.2.4. Combustion process in GDI engines	15
2.2.4.1. Homogeneous.....	15
2.2.4.2. Stratified.....	16
2.2.5. Operating modes.....	17
2.2.6. Fuel Injectors for GDI Engines.....	19
2.2.6.1. Fuel atomisation.....	19
2.2.6.2. GDI spray requirements	22
2.2.6.3. Development of GDI sprays.....	22
2.2.7. Current and future GDI research	24
2.3. SUMMARY	25
CHAPTER 3	
OPTICAL DIAGNOSTICS TECHNIQUES	26
3.1. LIGHT SCATTERING FROM SMALL PARTICLES	26
3.1.1. Mie scattering.....	27
3.1.2. Fluorescence.....	29
3.2. SINGLE POINT MEASUREMENT TECHNIQUES	31

3.3. FULL FIELD MEASUREMENT TECHNIQUES	33
3.3.1. Global Doppler Velocimetry (Planar Doppler Velocimetry).....	34
3.3.2. Pulsed-light Velocimetry	36
3.4. PARTICLE IMAGE VELOCIMETRY	37
3.4.1. Light sources	39
3.4.2. Tracer particles for PIV	40
3.4.3. Particle Imaging	44
3.4.4. Image acquisition	46
3.4.5. Image Analysis.....	46
3.4.5.1. Cross-correlation.....	47
3.4.5.2. Particle displacement estimation	48
3.4.5.3. Validation of velocity vectors.....	49
3.4.6. Sources of error in PIV.....	51
3.4.6.1. Peak locking or bias error	51
3.4.6.2. Acceleration error.....	53
3.4.6.3. Tracking error.....	54
3.4.6.4. Gradient error.....	54
3.4.6.5. Perspective error.....	54
3.4.6.6. Errors due to out of plane motion.....	55
3.4.7. Stereoscopic PIV (Stereo PIV).....	55
3.4.7.1. Errors in Stereo PIV measurements	59
3.4.8. Other related PIV techniques.....	60
3.4.8.1. Particle tracking velocimetry (PTV).....	60
3.4.8.2. Microscopic scale PIV (Micro PIV).....	61
3.4.8.3. Holographic PIV	62
3.4.8.4. Tomographic PIV (Tomo PIV).....	63
3.4.9. Use of fluorescent tracers in PIV	63
3.5. PIV IN MULTI-PHASE FLOWS.....	64
3.5.1. Phase separation by image post processing	64
3.5.2. Phase separation by optical arrangement	68
3.6. OPTICAL DIAGNOSTICS IN GDI AIR/FUEL SYSTEMS.....	71
3.6.1. Use of Mie imaging for GDI injector characterisation	72
3.6.2. Use of PIV for flow analysis	74
3.7. FLARE	76
3.8. SUMMARY	79

CHAPTER 4

FLARE REMOVAL IN GAS-PHASE PARTICLE IMAGE VELOCIMETRY	82
4.1. FLUORESCENT DYE SELECTION.....	83
4.2. SIZING OF ATOMIZED TRACERS USING INTERFEROMETRIC PARTICLE IMAGING.....	84
4.3. IMAGING OF FLUORESCENT TRACERS FOR PIV	86
4.3.1. Seed imaging using 532nm illumination	87
4.3.2. Seed imaging using 355nm illumination	90
4.4. COLOUR IMAGING OF FLARE.....	93
4.5. SUMMARY	95

CHAPTER 5

OPTICALLY EFFICIENT FLUORESCENT TRACERS FOR MULTI-CONSTITUENT PIV	96
5.1. FLUORESCENT TRACERS SELECTION AND IMAGING SYSTEM.....	97
5.2. EXPERIMENTAL SETUP.....	99
5.3. DROPLET SIZING	102
5.4. DATA PROCESSING	105
5.4.1. Crosstalk correction	105
5.4.2. Chromatic and lens distortions.....	107
5.5. RESULTS	108
5.6. SUMMARY	112
CHAPTER 6	
TWO-PHASE MEASUREMENTS IN A GDI SPRAY – EXPERIMENTAL SETUP	115
6.1. FUEL SELECTION AND INJECTION SYSTEM	116
6.2. USE OF AN ABSORBER IN THE FUEL.....	118
6.2.1. Required characteristics for the absorber	119
6.3. SPRAY MORPHOLOGY AND VELOCITY MEASUREMENTS.....	122
6.3.1. Penetration rate and cone angle measurements	122
6.3.2. Velocity measurements.....	127
6.4. CHARACTERISTICS OF FUEL JETS	131
6.5. TWO PHASE AIR/FUEL EXPERIMENTS.....	134
6.5.1. Optical Setup.....	134
6.5.2. Pulse order and exposure on CCD channels	136
6.5.3. Seeding Particles	136
6.5.4. Image processing.....	140
6.6. STEREO PIV MEASUREMENTS	141
6.6.1. Stereoscopic optical setup	142
6.7. SUMMARY	143
CHAPTER 7	
TWO-PHASE MEASUREMENTS IN A GDI SPRAY - RESULTS	145
7.1. TWO-PHASE AIR/FUEL VECTOR FIELDS 2D	145
7.1.1. Two-phase RGB images.....	146
7.1.2. Vector field computation	148
7.1.2.1. Image Pre-processing:.....	148
7.1.2.2. Vector calculation parameters	149
7.1.2.3. Vector post-processing	149
7.1.2.4. Average vector fields calculation	149
7.1.3. Instantaneous and average vector fields	150
7.1.4. Average vector field statistics	163
7.1.5. Gas phase vectors within the spray	164
7.1.6. RMS vector fields	165
7.1.7. Turbulence intensity	167
7.1.8. Vorticity	169
7.2. STEREO PIV RESULTS.....	172
7.2.1. Stereo vector field calculation	174
7.2.2. Stereo PIV average vector fields	174

7.2.3. Stereo vector fields statistics	179
7.3. DISCUSSION OF RESULTS.....	180
7.3.1. Optical system.....	180
7.3.2. Spray measurements	181
7.3.3. Significance of measurements	184
7.4. SUMMARY	185
CHAPTER 8	
CONCLUSIONS AND FUTURE WORK	187
8.1. USE OF FLUORESCENT TRACERS FOR FLARE REMOVAL.....	187
8.2. IMAGING SYSTEM FOR MULTI-PHASE MEASUREMENTS.....	188
8.3. GDI MULTI-PHASE MEASUREMENTS.....	189
8.4. OUTLOOK	190
8.4.1. PIV System Improvements	191
8.4.2. Measurements on the two-phase fuel / air flow from an injector	191
APPENDIX A	
INTERFEROMETRIC PARTICLE IMAGING FOR DROPLET SIZING.....	193
REFERENCES	197

List of Figures

Figure 2-1 Comparison of PFI and GDI mixture preparation systems	14
Figure 2-2 Combustion concepts in GDI engines	17
Figure 2-3 GDI operating mode map	17
Figure 2-4 Liquid sheet breakup	20
Figure 2-5 Description of observed regions in a GDI fuel spray	21
Figure 2-6 Effect of chamber pressure on a GDI single-hole spray	23
Figure 3-1 Mie intensity vs. scattering angle for a 10 μ m olive oil droplet in air	28
Figure 3-2 Geometrical ray tracing	29
Figure 3-3 Energy levels of a molecule for absorption and fluorescence.....	30
Figure 3-4 Schematic representation of a commercial LDA system	32
Figure 3-5 Schematic representation of the optical arrangement for GDV and the frequency to intensity conversion of a molecular iodine filter	35
Figure 3-6 Three image density modes: a low (PTV), b medium (PIV), c high (LSV).....	37
Figure 3-7 Schematic representation of a conventional PIV setup	38
Figure 3-8 Olive oil particles response to a step change in air velocity of 5 m/s.....	44
Figure 3-9 Geometric image reconstruction	45
Figure 3-10. Cross-correlation process	47
Figure 3-11 Peak ratio calculation	50
Figure 3-12 Intensity distribution of 2 particles with a Gaussian curve fitting.....	51
Figure 3-13 Acceleration error	53
Figure 3-14 Perspective error	54
Figure 3-15 Camera arrangement for a Stereo PIV setup	56
Figure 3-16 Scheimpflug criterion.....	57
Figure 3-17 2C vector fields recorded from two cameras in a forward-forward Stereo PIV setup	58
Figure 3-18 3C velocity fields obtained after combining 2 2C vectors fields shown in Figure 3-17	59
Figure 3-19 Flare obtained when illuminating the flow around a car valve using 532nm illumination	77
Figure 4-1 Bis-MSB droplet size distribution under experimental conditions	85
Figure 4-2 Emission from micron sized Bis-MSB fluorescent tracers.	86
Figure 4-3 Schematic of the camera view and laser sheet orientation for a laboratory flare removal experiment	87
Figure 4-4 Schematic representation of experimental setup for 532nm illumination	88
Figure 4-5 Mie scatter of Bis-MSB tracers under 532nm illumination	89
Figure 4-6 Vector field of Bis-MBS tracers under 532nm illumination.....	89

Figure 4-7 Schematic representation of experimental setup for 355nm illumination	90
Figure 4-8 Fluorescence of Bis-MSB tracers with 355nm illumination	92
Figure 4-9 Vector field of Bis-MBS tracers under 355nm illumination	92
Figure 4-10 Colour image of Mie scatter of Bis-MSB tracers with 532nm illumination	94
Figure 4-11 Colour image of fluorescence of Bis-MSB tracers with 355nm illumination	94
Figure 5-1 Bis-MSB (left) and DCM (right) tracers excited by a 355 nm laser light sheet.....	98
Figure 5-2 Pulse order and CCD exposure on 3CCD colour camera	99
Figure 5-3 Schematic representation of experimental setup	100
Figure 5-4 Laser Light Sheet imaged on JAI CV-A50 and UV, green and combined horizontal intensity profile	101
Figure 5-5 Hitachi HV F22F spectral response characteristics	102
Figure 5-6 Drop size distribution under experimental conditions	103
Figure 5-7 Cumulative drop size distribution for DCM tracers highlighting the size range visible on the red channel of a Hitachi HV-F22F 3CCD colour camera	104
Figure 5-8 RGB image of spatially separate flow streams seeded with DCM doped tracers and Bis-MSB doped tracers)	107
Figure 5-9 PIV vectors found from cross correlation of the data in Figure 5-8	109
Figure 5-10 Second example of a multi-constituent flow	110
Figure 5-11 PIV vectors found from cross correlation of the data in Figure 5-10	110
Figure 5-12 Resultant velocity comparison for vector field in Figure 5-11 with DCM-doped (red) and Bis-MSB-doped (blue) tracers	111
Figure 6-1 Fuel injector and spray rig system	117
Figure 6-2 Calibration line for pressure transducer	118
Figure 6-3 Absorbance measurements for Sudan 673 dye in hexane	120
Figure 6-4 Heptane Mie scattering before (left) and after being mixed with the Sudan 673 absorber.....	121
Figure 6-5 Scattering of gas (left) and fuel phase (right) in the red channel	121
Figure 6-6 Scattering of gas (left) and fuel phase (right) in the green channel	122
Figure 6-7 Axial penetration for heptane and gasoline at 30 and 54 bar	127
Figure 6-8 Vector fields for absorber (A), gasoline (B) and difference A-B (C) at 30 bar full injection	129
Figure 6-9 Vector fields for absorber (A), gasoline (B) and difference A-B (C) at 54 bar full injection	130
Figure 6-10 Detailed view of multi-hole GDI injector	131

Figure 6-11 Fuel jets from multi-hole GDI injector and wetted footprint showing axis of symmetry	132
Figure 6-12 Gasoline jets 1 (left) and 5 (right) under 532nm illumination	133
Figure 6-13 Heptane + absorber jets 1 and 5 under 532 nm illumination	133
Figure 6-14 Emission spectrum from 532-pumped red dye laser	134
Figure 6-15 Schematic representation of experimental setup	135
Figure 6-16 Pulse order and CCD exposure on colour camera	136
Figure 6-17 Bis-MSB droplet size distribution under experimental conditions	137
Figure 6-18 Bis-MSB particles response to a 10m/s velocity change	140
Figure 6-19 Schematic representation of Stereo PIV setup	143
Figure 7-1 RGB multi-phase image for jet 1 – 30bar half injection.....	147
Figure 7-2 RGB multi-phase image for jet 5 – 30bar half injection.....	147
Figure 7-3 Red (a), green – blue (b) and blue (c) component images in greyscales for the multi-phase image shown in Figure 7-1	148
Figure 7-4 Instantaneous and average vector fields for fuel and air at 30bar, jet 1 – early injection	151
Figure 7-5 Instantaneous and average vector fields for fuel and air at 30bar, jet 1 – half injection	152
Figure 7-6 Instantaneous and average vector fields for fuel and air at 54bar, jet 1 – early injection	153
Figure 7-7 Instantaneous and average vector fields for fuel and air at 54bar, jet 1 – half injection	154
Figure 7-8 Instantaneous and average vector fields for fuel and air at 30bar, second injector – half injection	155
Figure 7-9 Instantaneous and average vector fields for fuel and air at 30bar, jet 5 – early injection	156
Figure 7-10 Instantaneous and average vector fields for fuel and air at 30bar, jet 5 – half injection	157
Figure 7-11 Instantaneous and average vector fields for fuel and air at 54bar, jet 5 – early injection	158
Figure 7-12 Instantaneous and average vector fields for fuel and air at 54bar, jet 5 – half injection	159
Figure 7-13 Averaged vector fields for fuel and air and an injection pressure of 30 bar, jet 1 early injection	160
Figure 7-14 Averaged vector fields for fuel and air and an injection pressure of 30 bar, jet 1 - half injection	161
Figure 7-15 Averaged vector fields for fuel and air and an injection pressure of 54 bar, jet 1 - early injection	161

Figure 7-16 Averaged vector fields for fuel and air and an injection pressure of 54 bar, jet 1 - half injection	161
Figure 7-17 Averaged vector fields for fuel and air and an injection pressure of 30 bar, second injector - half injection.....	162
Figure 7-18 Averaged vector fields for fuel and air and an injection pressure of 30 bar, jet 5 - early injection	162
Figure 7-19 Averaged vector fields for fuel and air and an injection pressure of 30 bar, jet 5 - half injection	162
Figure 7-20 Averaged vector fields for fuel and air and an injection pressure of 54 bar, jet 5 - early injection	163
Figure 7-21 Averaged vector fields for fuel and air and an injection pressure of 54 bar, jet 5 - half injection	163
Figure 7-22 Instantaneous gas phase vector fields showing velocity vectors obtain with the spray.	165
Figure 7-23 RMS for jet1 and jet5 for at 30 bar - early injection.....	166
Figure 7-24 RMS for jet1 and jet5 for at 30 bar - half injection.....	166
Figure 7-25 RMS for jet1 and jet5 for at 54 bar - early injection.....	166
Figure 7-26 RMS for jet1 and jet5 for at 54 bar - half injection.....	167
Figure 7-27 RMS for jet1 for two nominally identical injectors – half injection	167
Figure 7-28 Turbulence intensity for jet1 and jet5 for at 30 bar - early injection	168
Figure 7-29 Turbulence intensity for jet1 and jet5 for at 30 bar - half injection	168
Figure 7-30 Turbulence intensity for jet1 and jet5 for at 54 bar - early injection	168
Figure 7-31 Turbulence intensity for jet1 and jet5 for at 54 bar - half injection	169
Figure 7-32 Turbulence intensity for jet1 for two nominally identical injectors – half injection	169
Figure 7-33 Notation for vorticity calculation	170
Figure 7-34 Vorticity for jet1 and jet5 for at 30 bar - early injection.....	170
Figure 7-35 Vorticity for jet1 and jet5 for at 30 bar - half injection.....	171
Figure 7-36 Vorticity for jet1 and jet5 for at 54 bar - early injection.....	171
Figure 7-37 Vorticity for jet1 and jet5 for at 54 bar - half injection.....	171
Figure 7-38 Vorticity for jet1 for two nominally identical injectors – half injection.....	172
Figure 7-39 RGB stereo multi-phase image for jet 1 and camera 1 – 30bar early injection	173
Figure 7-40 RGB stereo multi-phase image for jet 1 and camera 2 – 30bar early injection	173
Figure 7-41 Stereo vectors of fuel phase at 30 bar – early injection; background and side colour bar show out of plane velocity	175
Figure 7-42 Stereo vectors of gas phase at 30 bar – early injection; background and side colour bar show out of plane velocity	175

Figure 7-43 Stereo vectors of fuel phase at 30 bar – half injection; background and side colour bar show out of plane velocity	176
Figure 7-44 Stereo vectors of gas phase at 30 bar – half injection; background and side colour bar show out of plane velocity	176
Figure 7-45 Stereo vectors of fuel phase at 54 bar – early injection; background and side colour bar show out of plane velocity	177
Figure 7-46 Stereo vectors of gas phase at 54 bar – early injection; background and side colour bar show out of plane velocity	177
Figure 7-47 Stereo vectors of fuel phase at 54 bar – half injection; background and side colour bar show out of plane velocity	178
Figure 7-48 Stereo vectors of gas phase at 54 bar – half injection; background and side colour bar show out of plane velocity	178
Figure 7-49 Vorticity (a), out of plane velocity (b), RMS (c) and turbulence intensity (d) for fuel phase at 30bar half injection	182
Figure A-0-1 Interference fringes from olive oil droplets and a 10x microscope objective	194

List of Tables

Table 2-1 Categories and examples of multi-phase flows.....	9
Table 2-2 Measurement techniques for two-phase flows according to measurable properties	11
Table 6-1 Different timings used for spray morphology experiments	123
Table 6-2 Temporal evolution of heptane + absorber (left column) and gasoline (right column) penetration rate and cone angle at 30 bar for the delays in Table 6-1 starting from T1 (top row) and then down to T5 (bottom row)	123
Table 6-3 Temporal evolution of heptane + absorber (left column) and gasoline (right column) penetration rate and cone angle at 54 bar for the delays in Table 6-1 starting from T1 (top row) and then down to T5 (bottom row)	125
Table 6-4 Axial penetration in mm for heptane + absorber and gasoline at 30 bar	126
Table 6-5 Axial penetration in mm for heptane + absorber and gasoline at 54 bar	126
Table 7-1 Peak locking estimators for jet 1	164
Table 7-2 Peak locking estimators for jet 5	164

Chapter 1

INTRODUCTION

Motion estimation is fundamental in different engineering fields at both microscopic and macroscopic scale. One way to measure fluid motion is to image the pattern of point-like particles from which flow motion characteristics can be inferred; the images captured lead to two-dimensional information about the flow. However, a different approach is required when simultaneous information of two or more flows interacting is required. This thesis addresses the simultaneous measurement of two-dimensional motion across a full field of view of two interacting flows. The motivation for this research is shown in Section 1.1 describing a particular engineering application where simultaneous measurement of flows is desired. A short summary of the new contributions of this work is given in Section 1.2 and the structure of the thesis is outlined in Section 1.3.

1.1. Motivation

Emission levels are becoming a highly influential factor in automotive engine design due to strict legal regulations being applied. Similarly, engine efficiency is increasingly important with depleting energy resources. Whilst different technologies are being developed, the internal combustion engine will remain the selected choice for automotive vehicles over the coming decades hence it is important to improve and make more efficient use of existing technologies.

Gasoline Direct Injection (GDI) engines are showing the potential to achieve considerable improvement in fuel economy, power output and cold-start hydrocarbon emissions; this is achieved mainly by reducing throttling and heat losses during stratified combustion and a better control over fuel injection. This potential has led to a number of research projects aimed at having a better understanding of how these engines work as well as to develop and optimise their combustion systems which are complex and require careful control over parameters such as in-cylinder gas motion, injection control and ignition time over a wide range of operating conditions.

In order to understand the interaction mechanisms on GDI engines and therefore be able to generate improved designs, simultaneous 3-component (3C) velocity measurements in both phases (air – fuel) are required. These parameters need to be temporally and spatially resolved throughout the mixture preparation process and characterised over a range of temperatures and pressures consistent with the injection strategies (early and late fuel injection) to be used in GDI engines.

As it will be discussed with more detail in Chapter 3, there were no techniques available which provided simultaneous 3C velocity data for multi-phase air/fuel flows in macroscopic engineering rigs; for the 2-component (2C) velocity data published in the literature, assumptions were made to achieve phase separation. With particle imaging techniques the fundamental problem is to distinguish tracer particles or naturally occurring droplets between the multiple phases. Whilst different techniques have been proposed for multi-phase measurements, some of the approaches proposed are limited to there being differently sized tracers in the two phases; other approaches have been proposed where similarly sized tracers can be distinguished between the phases but are difficult to extend to 3C measurements due to the complexity of the setup. The technology reported in this thesis is generic and can also be applied to many macro and micro fluidic applications.

1.2. Aims and original contributions

This thesis presents a new imaging system which enables the simultaneous measurement of two-phase flows in macroscopic, ~100mm field of view,

applications. The method proposed is based on the use of a single colour camera which will enable simultaneous imaging of phases which are colour-tagged using fluorescent particles and multi-wavelength illumination. The primary aim of this thesis is to describe the use of fluorescent particles, the imaging systems developed and associated image processing and to demonstrate their applicability by measuring a multi-constituent gas phase flow and the two-phase air/fuel flow obtained from a high pressure gasoline injector. Additionally, a strong focus of this contribution is the flexibility and relative simplicity of the imaging system which allows its extension to stereoscopic imaging to give simultaneous two-phase 3C velocity measurements.

This thesis presents the following new contributions.

- Use of more efficient fluorescent tracers for 'flare' removal applications with their efficiency shown by two different case studies.
- A detailed description of a new imaging system consisting of a single 3CCD colour camera for simultaneous two-phase measurements.
- Use of more efficient fluorescent tracers for simultaneous multi-constituent measurements using colour imaging.
- Application of the colour imaging system for the simultaneous measurement of fuel and air in a gasoline direct injector spray.
- Use of an absorber in the fuel phase to reduce the effects of multiple scattering with penetration rate, cone angle and velocity measurements presented to validate the approach.
- Extension of the imaging system for simultaneous stereo measurement of air and fuel in a Gasoline Direct Injection spray.

1.3. Thesis format

The thesis is structured into three main parts: foundations (part I), experimental approach for multi-phase measurements (part II) and two-phase measurements in a GDI spray (part III). Part I presents the relevant background information and motivation which includes a review of multi-phase flows and Gasoline Direct Injection engines (Chapter 2). A comprehensive review of optical diagnostic techniques is presented with their current state-of-the-art for applications in multi-phase flows, particularly GDI injectors, and potential areas of improvement (Chapter 3). Part II describes the use of fluorescent tracers for gas flow applications and experiments are conducted to prove their use for flare removal (Chapter 4). A new approach to multi-phase imaging and processing is presented and its application to similarly sized tracers in multi-constituent gas phase flows is presented (Chapter 5). Part III presents an extension of the imaging system proposed for the simultaneous measurement of air and fuel in a Gasoline Direct Injection spray. First the modified experimental setup is described (Chapter 6) and then its application for 2C and 3C measurements is presented (Chapter 7). Finally, Chapter 8 summarises the main results obtained and presents suggestions for future work.

The individual chapters of the thesis are described below:

Part I: Foundations

Chapter 2 presents an overview of two-phase flows and their importance in different engineering applications. A description of the Gasoline Direct Injection concept is presented including history, combustion strategies, spray systems and current state of the art; the need for improved GDI fuel injectors is also presented.

Chapter 3 presents a thorough review of optical diagnostics techniques for quantitative flow visualisation. The review starts with some general considerations for motion estimation based on particle imaging to then briefly discuss single-point techniques. Full-field techniques are then reviewed in more detail and their application for measurements in multi-phase flows and GDI engines is discussed. Finally, a common experimental issue encountered when using laser illumination

for velocity measurement known as 'flare' is described as well as the approaches used to reduce its effects.

Part II: Experimental approach for simultaneous multi-phase measurements

Chapter 4 introduces the fluorescent tracers which are going to be used in all the experiments. The size of the tracers is measured and their visibility is then evaluated under typical flow visualisation conditions. The use of the tracers to reduce the effects of flare is presented and velocity measurements close to surfaces are performed. Finally the visibility of the tracers with a different type of camera (3CCD colour) is presented.

Chapter 5 describes a new imaging system for multi-constituent flow imaging and simultaneous velocity calculations. First the two fluorescent tracers used to seed the constituents are described. The selected camera for imaging is introduced along with the required corrective procedures and the approach for image processing. An application is then presented as proof of principle for a multi-constituent gas phase flow. The fluorescent tracers used in this project were developed at the University of Edinburgh by Mourad Chennaoui under the supervision of Dr Anita Jones as part of a collaborative project; however, the evaluation of the dyes and solvents as gas phase tracers was conducted by Mourad Chennaoui and the author at the Optical Metrology group, University of Leeds

Part III: Two-phase measurements in a GDI spray

Chapter 6 presents an extension of the imaging setup developed in Chapter 5 for two-phase measurements in a GDI spray. The experimental rig for the injector is described as well as the imaging system for phase discrimination. As part of the system novelty, the setup for three-component velocity measurements is described involving the use of two colour cameras in a stereoscopic arrangement requiring conventional stereo calibrating procedures.

Chapter 7 presents the results obtained from the experimental setup described in Chapter 6. Both instantaneous and average vector fields are presented and information derived from the velocity measurements such as turbulence intensity and vorticity are discussed. Finally, the results of the stereo measurements are presented including an assessment of the measurement accuracy. The chapter finishes with a discussion of the important features of the imaging system deployed and the results that have thereby been obtained.

The thesis concludes with a summary of the results and an outlook on further research is presented in Chapter 8.

Part I
Foundations

Chapter 2

MULTI-PHASE FLOWS AND GASOLINE DIRECT INJECTION ENGINES

The first part of this chapter introduces the basic principles of multi-phase flow systems, in particular air/fuel two-phase systems as well as current measurement techniques. The second part is dedicated to the development of Gasoline Direct Injection (GDI) engines: the discussion starts by pointing out how the need for improvements over the current port injection engines led to the introduction of the direct injection concept. This is followed by a description of the combustion and mixture formation strategies in GDI engines and the current research work on sprays for GDI injectors. The chapter closes by highlighting the potential areas of improvement for research on GDI engines, especially those areas where a better understanding of the mixing process is still required.

2.1. Multi-phase flows

The term multi-phase flow refers to a flow of two or more coexisting 'fluids' of matter in motion; the difference between the matter can be its thermodynamic state (phase) or the presence of multiple chemical components (Kleinstreuer 2003). The multi-phase flows discussed in this thesis are considered to have a level of phase (or component) separation at a scale above the molecular level.

Multi-phase flows are present in many aspects of our everyday life such as rain, snow, fog, mud slides and many more; additionally, virtually every processing

technology must deal with some multi-phase flow: from papermaking to the pellet form of almost all raw plastics (Brennen 2005). Multi-phase flows are used in a wide range of different industrial and engineering applications and can be categorised as shown in Table 2-1 below.

Table 2-1 Categories and examples of multi-phase flows (Source (Crowe et al. 1998))

Gas-liquid flows	Bubbly flows Separated Flows Gas-droplet flows
Gas-solid flows	Gas-particle flows Pneumatic transport Fluidized beds
Liquid-solid flows	Slurry flows Hydrotransport Sediment Transport
Three-phase flows	Bubbles in a slurry flow Droplets/particles in gaseous flows

2.1.1. Applications of multi-phase flows

Multi-phase flows are very common in different engineering applications such as power generation, chemical processes, steam generators, cooling towers, refrigeration systems and pipelines for transport of gases and oil mixtures. Different current industrial applications include:

- Spray drying: in this process a liquid material is atomised and then exposed to hot gases which dry the liquid into its powder form; this is used in the food and pharmaceutical industries.
- Pollution control: The removal of particles or droplets from industrial effluents or other emissions can be performed with special devices such as impactors which are used for inertial separation of particles from a stream of air.
- Pneumatic and slurry transport are a very important multi-phase flow application where either liquids or gases are used to transport other

materials. In the chemical industry air is used for the transport of cement and coal to furnaces and mixers.

- Power generation: both boilers and nuclear reactors use two-phase flow heat transfer as part of their energy generation processes.

2.1.2. Measuring multi-phase flows

When measuring a multi-phase system, parameters such as particle size, shape, concentration as well as the velocity of the two phases need to be measured. Multi-phase flows can be modelled numerically or their properties can be measured using several experimental methods. Numerical methods are out of the scope of this thesis but literature is readily available elsewhere: (Crowe 2005), (Prosperetti and Tryggvason 2009) amongst many others. Numerical methods usually include the use of Lagrangian approaches due to its simplicity and robustness; (Crowe et al. 1998) lists some industrial applications of Lagrangian methods on multi-phase flow modelling including spray dryers, coal fired furnaces and propulsion systems. Alternatively, flow models have been created, based on direct solutions of the Navier-Stokes equations, which include two-phase interaction by assuming dispersed particles as point forces acting on the fluids. The complexity of modelling the interactions between individual droplets or particles in multi-phase systems, combined with limitations on available computing resources, means that reduced models must often be used and hence validation of results with experimental data remains important.

Different methods are available to measure two-phase flows experimentally and have been summarised in Table 2-2; these can be broadly divided into sampling and on-line methods (Crowe et al. 1998). Sampling methods are still used in powder technology industries to characterise bulk solids; the analysis of the solids can be performed with a microscope or mechanical methods such as sieving and sedimentation. On-line methods are those which can be applied directly on a process line to analyse the properties of both dispersed and continuous phases and are widely used in two-phase flow research. As it will be explained in Section 3.5.1, these methods are usually limited to low concentrations in the dispersed phase.

Table 2-2 Measurement techniques for two-phase flows according to measurable properties (Source (Crowe et al. 1998))

Phase Property	Sampling methods	On-line methods
Size	Sieving Sedimentation Coulter Principle	Light scattering Laser diffraction Phase Doppler Anemometry
Concentration	Isokinetic Sampling	Isokinetic Sampling Fibre Optics Light scattering Laser diffraction Light absorption
Velocity	Not possible	Fibre Optics Laser Doppler Anemometry Particle Image Velocimetry Particle Tracking Velocimetry

Optical methods using laser illumination, such as Particle Image Velocimetry and Laser Doppler Anemometry, are of particular interest in this thesis. A detailed explanation of their principles and application on two-phase flows is presented in Chapter 3.

2.2. Gasoline Direct Injection Engines

A very important application of multi-phase flows is the interaction of air and fuel in internal combustion engines. Given the increasingly stringent emission regulations and the depleting energy resources, improvements and a more detailed understanding on current combustion systems are required. One of the proposed improvements in gasoline engines is the use of direct injection engines due to their potential for fuel economy and emissions reduction.

2.2.1. The need for direct injection technology

Under the Kyoto Protocol of the United Nations Convention on Climate Change, the European Union agreed to reduce greenhouse gas emissions by 8 % by 2008-2012 and at least 20% by 2020 compared to the level in 1990. As anticipated by the European Auto-Oil II Program, with the regulations that have already been

implemented, the emissions targets set for 2020 will be achieved. However, carbon dioxide (CO₂) emissions need to be dealt with actively (EuropeanUnion 2000).

Implemented regulations have targeted passenger cars as an area where emissions need to be significantly reduced given their impact on climate change and that they account for about 12% of the overall CO₂ emissions in the European Union (EuropeanUnion 2007). Consequently, the strategy adopted by the European Union in 1998 to reduce CO₂ emissions from passenger cars consisted of a voluntary commitment by the automotive industry on fuel economy improvements (ACEA Agreement) mainly through technological developments and the subsequent market changes. Targets of 140gCO₂/km on CO₂ average emissions were set for passenger cars by 2008 and 120gCO₂/km in 2012 by the European Commission in 2002 (EuropeanUnion 2002). However, later in 2007, studies forecasted that the 120gCO₂/km target will not be met by 2012 and a revised target of 130gCO₂/km reduction with improvements in vehicle motor technology plus an extra 10gCO₂/km with the use of other technologies (such as biofuels and more efficient air conditioning systems) was established to achieve the 120gCO₂/km target. A recently published regulation by the European Commission has established a target of 95gCO₂/km for the average emission of new car fleets from 2020 onwards (EuropeanUnion 2009).

The need for emission reductions in gasoline engines is evident due to the significant amount of European light duty passenger cars powered by gasoline. Given that CO₂ emissions are linked to fuel efficiency, different approaches have been proposed such as improvement in power train efficiency and aerodynamic performance and reductions in vehicle mass; however, changes in mass and vehicle drag often conflict with safety and comfort requirements (Turner et al. 2005). Amongst the different alternatives for more fuel efficient combustion systems, Gasoline Direct Injection (GDI) engines have seen increasing development and interest in the last 15 years due to their potential to achieve significant improvements in fuel efficiency. In Gasoline Direct Injection, fuel is injected directly into the combustion chamber at high pressure as opposed to conventional gasoline engines where the air/fuel mixture goes into the chamber through the inlet port.

2.2.2. History of Direct Injection

A brief summary of the main milestones in direct injection development is presented here. The interested reader is referred to (Zhao et al. 1999b) and (Zhao 2009) where the most important research, prototype and production GDI engines developed are reviewed.

The concept of direct injection had been used before the introduction of production GDI engines in the 1990's. Direct injection had been used as early as the 1920's when the Hesselman engine was introduced; the Hesselman was a spark ignition engine adapted to run on heavier petroleum products, such as diesel oil, and the fuel was injected directly into the cylinder. Later, different production aircraft developed during the Second World War used direct injection but were soon replaced due to progress on carburettor technology. The first passenger car using direct injection was the Gutbrod in 1951 and later in 1954 the Mercedes 300SL introduced a four-stroke engine with direct injection; this technology was quickly replaced once port injection systems had been improved and offered a less expensive solution due to GDI engines demand on materials and problems with their service life (Bosch 2006). It should be noted that the driving force behind the first systems was not necessarily to improve fuel economy but to achieve a homogeneous air/fuel mixture (Iwamoto et al. 2000). From the 1950s to the 1980s more GDI engines started being developed again targeting fuel economy. Different stratified combustion concepts were proposed with a narrow spacing configuration between the spark plug and the fuel spray cone. Several problems were obtained with these systems, which prevented them from being mass produced, such as: hydrocarbon emission deterring combustion, limited operating zone, spark plug fouling due to the presence of soot and a general poor performance (Iwamoto et al. 2000). These problems meant work in GDI development was again stopped.

In the 1990's the GDI concept was picked up again, with fuel economy being again the main driving force, given the need for energy saving and emissions reduction particularly CO₂; these are known as the third-generation GDI engines (Iwamoto et al. 2000). The first GDI engine in a passenger car was launched in 1996 by Mitsubishi; details of Mitsubishi's system can be found in (Kume et al. 1996) and (Iwamoto et al. 2000). Since then different automotive manufactures have adapted the GDI concept and models using GDI engines such as the Alfa Romeo 156,

Ferrari California and the latest generation of the Hyundai Sonata have been released.

2.2.3. Theoretical advantages over conventional port injection engines

The main difference between conventional port fuel injection (PFI) engines and GDI engines is in the mixture preparation strategies, shown schematically in Figure 2-1. In PFI engines fuel is injected into the intake port of each cylinder whereas in GDI engines fuel is injected directly into the engine cylinder.

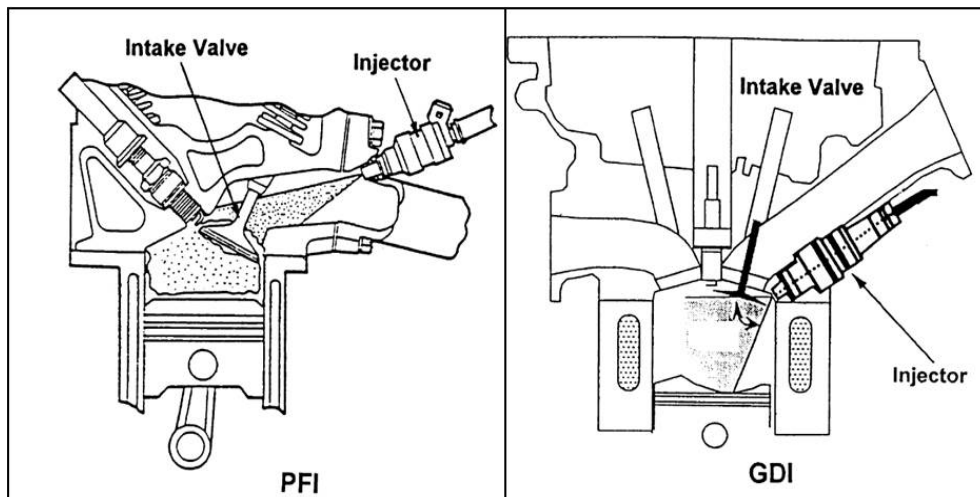


Figure 2-1 Comparison of PFI and GDI mixture preparation systems (Source Zhao et al., 1999b)

The theoretical advantages of GDI engines over PFI engines can be summarised as follows (Zhao et al. 1999b) (van Basshuysen 2009):

- Potential to reduce specific fuel consumption by 12-15%
- Quicker starting and a better control of the air/fuel ratio
- Fewer heat losses
- Higher compression ratio
- Lower octane requirement
- Increase of volumetric efficiency
- Improved transient response
- Reduction of start unburned hydrocarbon (HC) emissions
- Reduction of CO₂ emissions

On the other hand, there are some disadvantages which need to be overcome in order to achieve mass production of the GDI concept:

- Difficulty to control the stratified combustion over the required operating conditions range
- Complex injection control
- Excessive light load unburned hydrocarbons emissions and excessive high load NO_x emissions and soot formation
- Three-way catalysts are required for NO_x control but cannot be used to full capacity in all operating conditions

2.2.4. Combustion process in GDI engines

The main target is to build an engine that offers higher fuel economy compared to that of diesel engines at part-loads and better than that of port injected engines at full-load. At partial loads, the engine should be operated unthrottled in a lean condition by stratifying the charge and creating a rich air/fuel mixture around the spark plug. At light loads, the engine must generate a near stoichiometric mixture at the spark plug for good combustion reliability; it must also provide good mixing to avoid soot-producing rich zones without overmixing lean zones to avoid high hydrocarbons emissions. While working at high loads, the combustion system must completely mix the fuel and air to avoid fuel impingement on the walls and piston scuffing. On the other hand, to achieve the higher potential at high loads the engine should be operated under stoichiometric or slightly rich conditions; this mixture should be homogenous to avoid soot formation. Consequently, combustion processes in a GDI engine can be divided into homogeneous and stratified charge combustion processes.

2.2.4.1. *Homogeneous*

For homogeneous combustion, a stoichiometric mixture is usually formed with $\lambda=1$ (λ is the ratio of air/fuel ratio of a mixture relative to a stoichiometric mixture); for stoichiometric mixtures three-way catalytic converters will operate under the highest conversion rate for all pollutants hence homogeneous combustions processes are designed to be emission-reducing concepts.

2.2.4.2. *Stratified*

For stratified combustion, fuel is injected during the compression stroke and the stratified mixture can be transported to the spark plug by the shape of the piston (wall-guided), the air flow structures (air-guided) or the position of the injector (spray-guided). Figure 2-2 below shows the different stratification techniques in GDI engines. Wall systems inevitably lead to some of the fuel impinging on the piston surface producing wall wetting; this is undesirable given that fuel films burn with a low air/fuel ratio and are a source of soot emissions. Stratification systems usually work with a combination of the wall and air-guided approaches and use swirl injectors. Wall and air guided systems, however, have not completely met the requirements for stratified combustion particularly due a limited operating range for which the engine can be operated with stratified charge and the unfavourable shape of the combustion chamber which leads to most of the benefits at part load being outweighed at full load (Achleitner et al. 2007).

Recent studies have focused on spray-guided stratification as an alternative to the wall and air-guided modes. In spray-guided stratification the injector is situated at the top or on the side of the combustion chamber as shown in Figure 2-2. The main advantage of this method is that the fuel spray can be guided directly towards the spark plug without interaction with the piston or air flow reducing wall and piston wetting; on the other hand, given the short time available for combustion, higher injection pressures of up to 200bar are required. When the combustion process is properly configured, the spray-guided stratification systems can achieve greater fuel consumption savings compared to wall and air-guided stratification systems (van Basshuysen 2009). Comparisons on the performance of spray and wall-guided systems have been published such as (Drake and Haworth 2007) where a spray-guided system showed 4% better fuel economy, a factor of two lower unburned hydrocarbon emissions and lower smoke emissions compared to a wall-guided system.

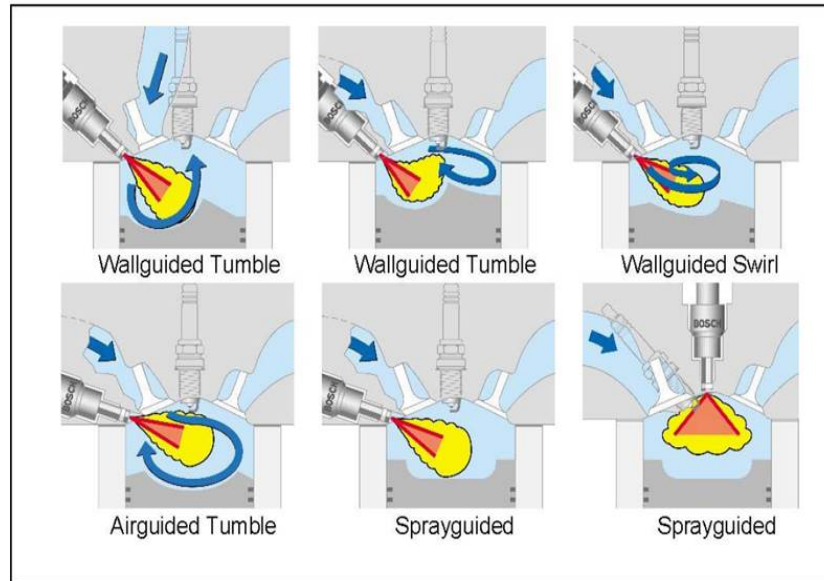


Figure 2-2 Combustion concepts in GDI engines (Source: (Ortmann et al., 2001))

2.2.5. Operating modes

The different operating modes in GDI engines have been compiled by (Bosch 2006) depending on the requirement of torque and speed and are shown in Figure 2-3. The main two operating modes are homogeneous and stratified (shown as A and C respectively in Figure 2-3) and there are some transition modes between them.

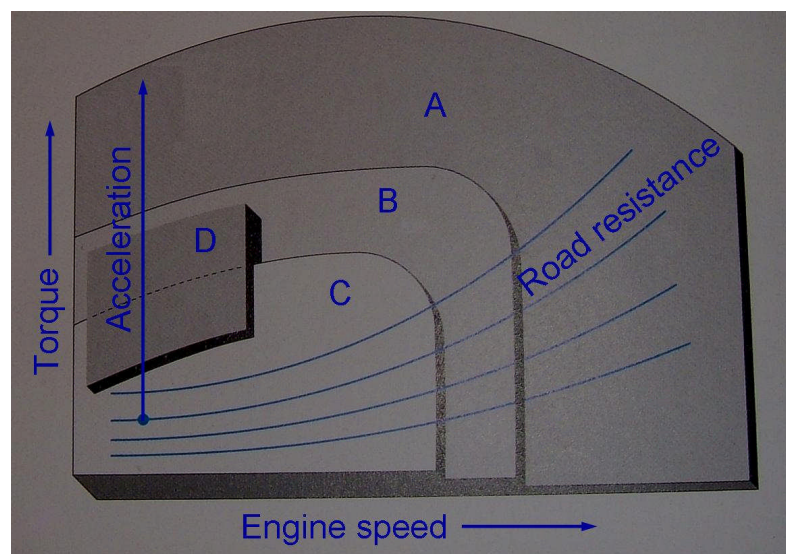


Figure 2-3 GDI operating mode map; Homogeneous (A), Homogeneous lean (B), Stratified Charge (C) and Homogeneous stratified charge (D). (Adapted from Bosch, 2006)

Homogeneous (A)

In this mode, fuel is injected into the air during the induction stroke to form a homogenised stoichiometric mixture; this mode is used when high levels of torque are demanded. Emissions in this mode are low and can be treated with a three-way catalytic converter.

Stratified charge (C)

In this mode, fuel is injected during the compression stroke with fuel only mixing with part of the air creating a stratified-charge cloud. This cloud needs to be sufficiently homogenised at the moment of ignition and close to the spark plug. Given the charge is stoichiometric only locally, the overall mixture is lean (when considering the surrounding air), requiring extra exhaust gas treatment since three-way catalytic converters are substantially less effective in reducing NO_x emissions in lean-burn operation (Bögner et al. 1995). For this mode, accurate control of the quantity and timing of fuel injection are required but it may improve efficiency up to 15% compared to PFI engines (Hentschel 2002). As shown in Figure 2-3, this mode is used at part and low loads.

Homogeneous lean (B)

This is the transition mode between stratified and homogeneous modes; fuel consumption is lower because the engine runs unthrottled reducing pumping losses. Despite reduced fuel consumption, NO_x emissions are increased due to the catalytic converter limitations for lean mixtures.

Homogeneous stratified charge (D)

This is another transition mode where dual injection is deployed. The entire combustion chamber is first filled with a homogeneous lean mixture with fuel injected during the induction stroke and again during the compression stroke creating a rich mixture near the spark plug. This mode is activated for a number of cycles during the transition between homogeneous and stratified-charge modes.

2.2.6. Fuel Injectors for GDI Engines

In this section a brief summary of fuel spray characterisation along with the requirements and development of GDI fuel injectors is presented.

2.2.6.1. Fuel atomisation

Atomisation is the process in which liquid is broken up to form droplets; liquid atomisation is controlled by the interaction of inertial, viscous and tension stresses as shown in Equations 2-1 to 2-3.

$$\text{Inertial Stresses} = \rho U^2 \quad \text{Equation 2-1}$$

$$\text{Viscous Stresses} = \frac{\mu U}{L} \quad \text{Equation 2-2}$$

$$\text{Surface Tension Stresses} = \frac{\sigma}{L} \quad \text{Equation 2-3}$$

where ρ is the liquid density, μ is the liquid dynamic viscosity, σ is liquid surface tension, L is the characteristic length (usually droplet diameter) and U is the droplet velocity. Non-dimensional parameters can be obtained as the ratio of these stresses and are used for the characterisation of sprays; commonly used parameters include Reynolds (Re), Weber (We) and Ohnesorge (Oh) numbers. The Reynolds number (Equation 2-4) is given as the ratio of the inertial stresses to the viscous stresses; it is used to characterise different flow regimes (laminar, turbulent or transitional). The Weber number (Equation 2-5) is the ratio between the inertial stresses and the surface tension stresses; it provides an estimation of the point at which liquid breakup will occur. The Ohnesorge number (Equation 2-6) is the ratio of the viscous stresses to the surface tension stresses; large values usually indicate breakup inhibition due to the increased effect of the viscous stresses.

$$\text{Re} = \frac{\text{Inertial}}{\text{Viscous}} = \frac{\rho U L}{\mu} \quad \text{Equation 2-4}$$

$$We = \frac{\text{Inertial}}{\text{SurfaceTension}} = \frac{\rho U^2 L}{\sigma} \quad \text{Equation 2-5}$$

$$Oh = \frac{\sqrt{We}}{Re} = \frac{\mu}{\sqrt{\rho \sigma L}} \quad \text{Equation 2-6}$$

The interaction between air and fuel is extremely important for fuel atomisation and droplet evaporation. Several studies have been published on jet breakup and it is still being studied due to the complexity of the phenomena involved. Different studies such as (Chigier and Reitz 1995) have been published on the interaction between a single-hole nozzle flow and stagnant gas. Fuel usually leaves an injector as a liquid film forming a wave due to disturbances on the liquid surface; at some characteristic frequency ligaments are formed (when the surface tension stresses are overcome by inertial stresses) which then break up into a chain of droplets as shown in Figure 2-4 .

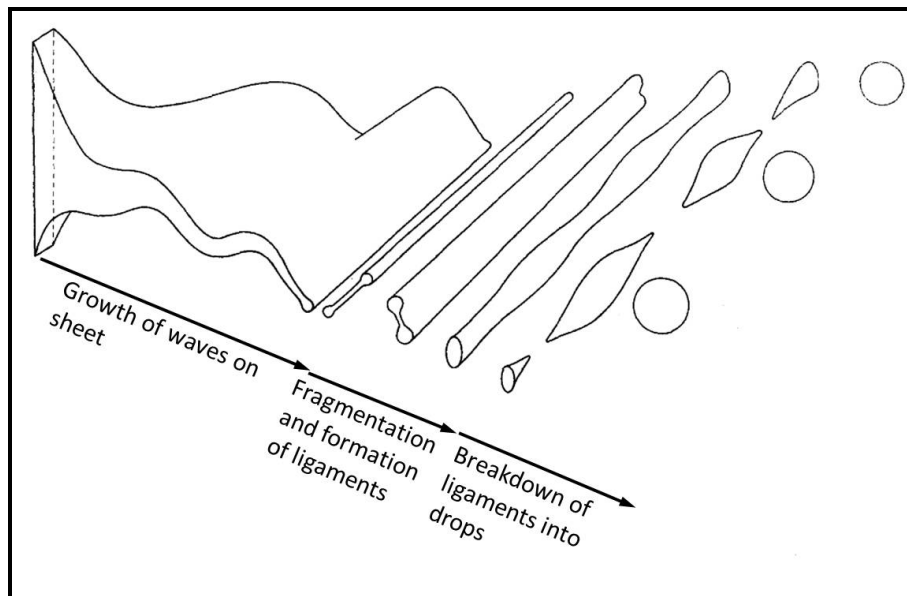


Figure 2-4 Liquid sheet breakup (Adapted from Dombrowski and Johns, 1963)

Whilst a detailed study of fuel characterisation and breakup processes is out of the scope of this thesis, a recent recommended practice published by the Society of Automotive Engineers provides a list of the most important parameters to be considered when working on the structural properties of GDI sprays (Hung et al. 2008). Figure 2-5 shows two general descriptors of GDI sprays; whilst these are

not characterisation metrics they will have an effect on the measured spray parameters. Figure 2-5 (a) shows the main observed regions in a GDI fuel spray including main spray and vortex formation. Figure 2-5 (b) shows the wetted footprint of a multi-hole injector.

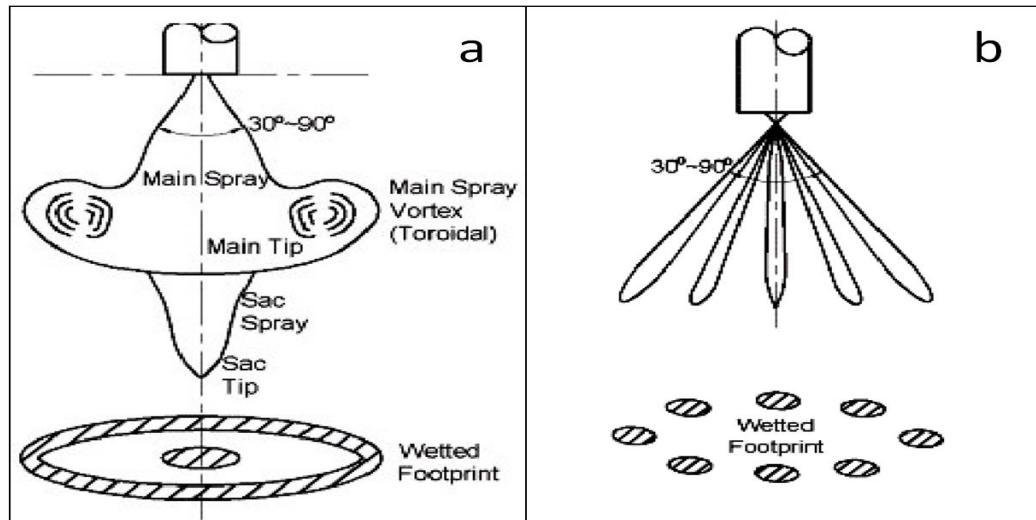


Figure 2-5 Description of observed regions in a GDI fuel spray (a) and multi-hole GDI wetted footprint (Source Hung et al., 2008)

According to the SAE J2715 recommended practice, the following parameters can be used to characterise a gasoline fuel spray

- Angular extent of the spray envelope (Cone angle)
- Fuel mass distribution within the spray
- Spray tip penetration
- Drop size distribution which includes the Sauter mean diameter (SMD) and the 90% cumulative volume diameter (D_{V90}). These are commonly accepted as the meaningful statistical parameters obtained from the drop size distribution of a spray. The SMD is defined as the diameter of a drop which has the same ratio of volume to surface area as the collection of all drops in the measured drop size distribution. The D_{V90} represents the diameter of a drop for which the volume of all smaller drops in the size distribution is 90% of the total volume of all drops in the size distribution.

Spray penetration rate and cone angle will be used to characterise the flow in the multi-hole GDI injector in Section 6.3.1.

2.2.6.2. *GDI spray requirements*

Fuel injection has a greater importance in GDI engines compared to PFI engines. Factors such as cone angle, penetration rate, mean drop size and delivery rate are critical and an optimum matching of these factors to obtain rapid fuel vaporisation is essential for the development of the GDI concept (Zhao et al. 1999a). As opposed to PFI engines, there is less time for mixture preparation on GDI engines thus it needs to be aided by the spray characteristics. Whereas most of the port injected engines can operate using a spray with 200 μm SMD, a GDI engine will require less than 25 μm SMD in order to achieve acceptable emissions levels (Zhao et al. 1999b). (Dodge 1996) evaluated the evaporation of in-cylinder droplets and concluded that a SMD of 15 μm or less is required to avoid excessive levels of unburned hydrocarbons. It is important to mention that a GDI injector also requires an even droplet distribution; if a spray produces a few large droplets these may be enough to increase the level of unburned hydrocarbons over the entire operating condition.

Some of the specific requirements for a GDI injector are the same as those for a PFI injector and include: good spray axisymmetry (symmetry about an axis) over the operating range, small pulse-to-pulse variation in fuel quantity and spray characteristics, good linearity between flow and pulse width and a minimal variation of these parameters from unit to unit (Zhao et al. 1995). For GDI injectors, the additional requirements include: enhanced atomisation level, expanded dynamic range, more control of spray penetration, greater emphasis on packaging constraints, ability to operate at higher injector body and tip temperatures and the ability to produce off-axis sprays in various inclined axes according to any particular combustion system (Zhao et al. 1999b).

2.2.6.3. *Development of GDI sprays*

Given the importance of fuel injection in GDI engines considerable research has been focused on the development of different fuel injectors. Overall studies have focused on injector performance under the two main operating regimes in GDI

engines particularly stratified charge where the fuel is injected late in the compression stroke. It is essential to assess how the injectors will perform under different conditions of nozzle design, chamber pressure and injection pressure; the effect of these parameters on tip penetration, cone angle, jet velocity and droplet size distribution needs to be understood.

Swirl injectors, usually referred to as first generation injectors, are used in the air and wall-guided combustion processes. Different studies have shown swirl injectors offer lower fuel consumption for stratified, overall-lean part load operation (20%) but not a significant improvement on HC and NO_x emissions (Fraidl et al. 1996). Other workers found that swirl injectors showed instability with back pressure leading to the collapse of injection. This is a very undesirable feature for stratified-charge operation, when the fuel is injected late, and is clearly inappropriate for the spray-guided configuration where the spark plug and injector are closely spaced and ignition starts at the recirculation zone formed at the spray periphery (Mitroglou et al. 2007). Figure 2-6 below shows how the structure of a single-hole GDI spray is affected due to the backpressure obtained during the compression stroke; images were taken at the same time after start of injection for chamber pressures of 1, 5 and 10 bar respectively.

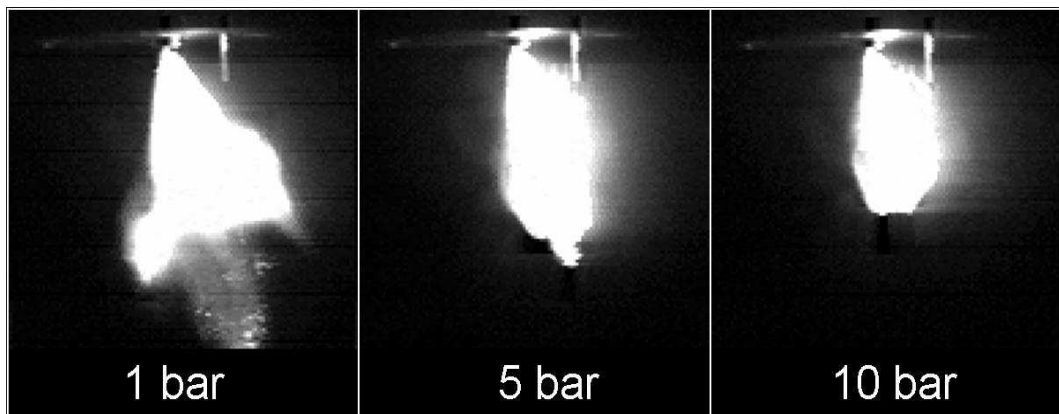


Figure 2-6 Effect of chamber pressure on a GDI single-hole spray. Images provided by David Towers, School of Mechanical Engineering, University of Leeds

Multi-hole injectors were proposed as a different alternative to be used in the spray-guided combustion process and also to provide more flexibility to adapt the spray pattern to a particular combustion chamber design (Kim and et al. 2007). Given their relatively recent introduction, there are not many published articles on their performance but the results obtained so far have shown they perform better

than swirl injectors for stratified-charge combustion. A review of the findings has been made by (Mitroglou et al. 2007) and can be summarised as follows:

- An improved stability, compared to swirl injectors, at elevated cylinder pressures
- Improved air entrainment due to a larger surface area produced by the separated spray jets
- Enhanced flexibility to direct the charge towards the spark plug allowing a better matching to particular combustion chamber designs
- Using injection pressures up to 200 bar and back pressures up to 12 bar, it was found that the spray cone angle is largely independent of injection and chamber pressure (Mitroglou et al. 2006)
- As expected, under higher chamber pressures, the penetration of the spray is reduced but the more compact spray can still be more easily directed to the spark plug.

2.2.7. Current and future GDI research

Research work on GDI engines is still ongoing and there are many aspects which still need to be improved. The current focus is on the development of multi-hole injectors; despite their initial positive results, there are still issues with the timing of the injection and different methods are still being studied (Mitroglou et al. 2006). Research is also being conducted in the use of piezo-injectors and their related issues such as cavitation (Giannadakis et al. 2008).

Overall, a more detailed understanding of the air/fuel interaction mechanisms in GDI engines is still needed in order to generate improved designs. Simultaneous three-component velocity measurements of air and fuel need to be obtained under the different operating regimes of GDI engines but have not been reported yet. These measurements can be used to understand the entrainment of gases produced by fuel injection given the important role it plays in vaporisation and mixing and are essential in stratified combustion processes.

2.3. Summary

This chapter presented a review of multi-phase flows and GDI engines. The importance of multi-phase flows in different engineering applications was established and the most commonly used measurement methods were briefly described. Similarly, GDI engines were introduced as well as the current need for such systems. A summary of the operating principle, combustion systems and especially the requirements on GDI fuel injectors was also presented. The GDI concept is still being developed and simultaneous air/fuel measurements are still required to increase the understanding of the different mechanisms involved on the different operating regimes.

A detailed review of optical diagnostics techniques for GDI engines and multi-phase flows is presented in Section 3.6.

Chapter 3

OPTICAL DIAGNOSTICS TECHNIQUES

Amongst the different techniques available for experimental studies in multi-phase flows, optical techniques are very appealing due to their non-intrusive nature. Advances in laser technologies as well as in imaging devices have allowed the development of optical diagnostics tools based on particle imaging for a wide range of applications. This chapter presents a review of the most commonly used optical techniques for multi-phase flows and gasoline fuel injectors; the current state of the art, as well as the limitations of the different approaches, is discussed. This review will be focused on particle/droplet based diagnostics since they are the most commonly used in velocimetry measurements. First, a brief introduction to single-point techniques is presented followed by a more in-depth discussion of full-field approaches. Details of the algorithm framework for the analysis of particle imaging data are also included. The chapter finishes with an overview of the techniques discussed and, based on the published literature, the potential areas of improvement for the application of optical diagnostics methods in multi-phase flows is presented. In particular, possible advances in the characterisation of the air/fuel interaction in GDI engines are discussed.

3.1. Light scattering from small particles

Understanding light scattering behaviour by small particles is of particular interest given that most of the optical diagnostics techniques for velocimetry

measurements use laser light scattered by small particles as the means of obtaining flow information. The light scattered by spherical particles is mainly a function of the ratio of the refractive index of the particle to that of the surrounding medium, particle size, shape, orientation, observation angle and light polarisation (Raffel et al. 1998). The light scattering properties of a particle can be characterised as a function of the size parameter x defined as:

$$x = \frac{\pi D_p}{\lambda} \quad \text{Equation 3-1}$$

where D_p is the particle diameter and λ is the wavelength of the illuminating light. For $x \ll 1$ (small particles compared to the wavelength), light scattering is commonly referred to as Rayleigh scattering which is normally too weak for full field velocity measurements using laser illumination. For larger values of x (large particles compared to the wavelength), the light scattered by the particles can be described by Mie theory (also referred to as Lorenz-Mie theory). Given that the optical diagnostics techniques used in this thesis are based on Mie scattering, Rayleigh scattering will not be discussed. The interested reader is referred to (Bohren and Huffman 1998) and (van de Hulst 1957) for a more detailed description of Rayleigh scattering.

3.1.1. Mie scattering

Mie theory is an analytical solution of Maxwell's equations for the scattering of electromagnetic radiation by small particles. An example of Mie scattering is shown in Figure 3-1 for a 10 μ m olive oil droplet in air (refractive index = 1.46) under an illumination wavelength of 532nm. The plot is the solution of the light scattered using the Lorenz-Mie solution to the Maxwell equations as given by (van de Hulst 1957) and compiled using a C++ code. Figure 3-1 shows there is a considerable difference in the scattering intensity (intensity is on a log scale and plotted radially) of the droplet depending on the scattering angle with higher intensities obtained in the forward direction (0-90 degrees). It would be advantageous for optical diagnostics techniques to record images in forward scattering angles since these will produce high scattering intensity; however, due to the limited depth of field when imaging at such angles, recording images at 90 degrees is more commonly used (Raffel et al. 1998).

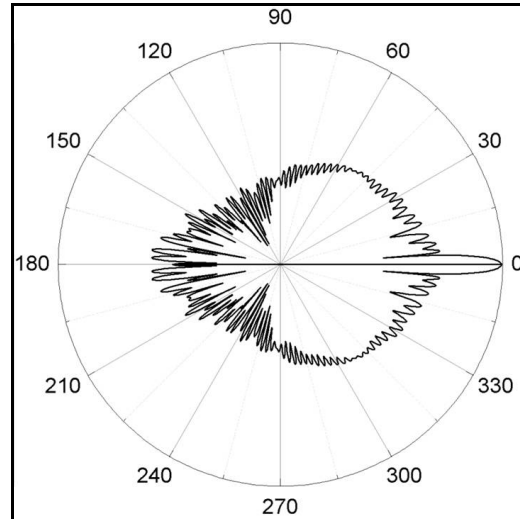


Figure 3-1 Mie intensity vs. scattering angle for a 10µm olive oil droplet in air

The light scattering distribution around 90 degrees shows rapid oscillations in the light scattered by the droplet. Spatial averaging over a finite aperture of the collecting optics will reduce the influence of these fluctuations (Melling 1997).

Several droplet sizing techniques have considered a simplified approach in which only the reflected and first order refracted rays are considered (Ragucci et al. 1990) (Glover et al. 1995). van de Hulst showed that the geometrical analysis is useful for $x \gg 1$ (large particles compared to the wavelength) and that the geometric solutions approach the Mie scattering solution asymptotically as the particle diameter increases (van de Hulst 1957). Figure 3-2 below shows the geometrical optics approach to ray tracing for light incident on a particle. The following equations can be used to describe the light beam as it goes through the particle:

For the reflected ray (Law of reflection):

$$\theta_i = \theta_r \quad \text{Equation 3-2}$$

For the refracted ray (Snell's law):

$$n_1(\sin \theta_1) = n_2(\sin \theta_2) \quad \text{Equation 3-3}$$

where θ_1 , θ_2 , θ_v , θ_i , θ_r are the angles of the different rays and n_1 and n_2 are the refractive indices of the particle and the surrounding medium respectively.

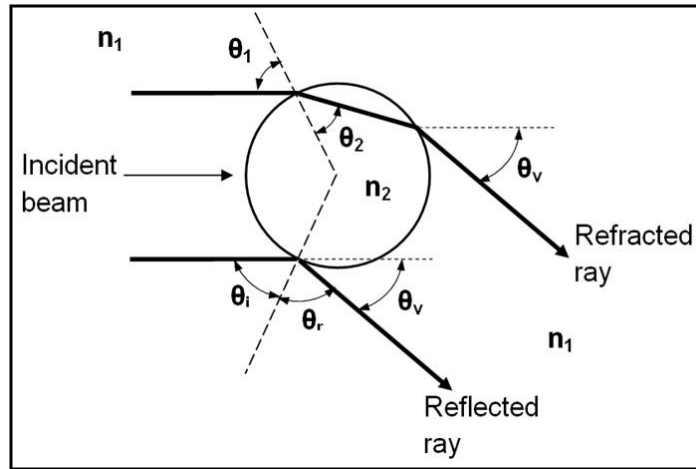


Figure 3-2 Geometrical ray tracing

An incident beam is partially reflected and partially refracted at the particle boundary. The refracted beam goes through the droplet until it meets the far surface. Here, part of the beam is internally reflected and part is refracted leaving the droplet at an angle θ_v (1st order refracted ray). The internally reflected ray will continue until it meets the droplet boundary where the light will be once again partially internally reflected and partially refracted leaving the droplet (2nd order refracted light). This process then continues but most of the beam energy is accounted for by the reflected, and 1st and 2nd order refracted beams. An interferometric particle imaging setup is described in Appendix A and is used in Chapters 4, 5 and 6 to measure droplet size distributions; in this approach droplet size is calculated by measuring the angular frequency of interference fringes (arising from the light directly reflected from the droplet surface and the first-order refracted beam) in defocused images.

3.1.2. Fluorescence

Fluorescence is a type of luminescence in which a molecule is excited to a higher atomic energy state, usually by the absorption of photons, and then decays to its ground state resulting in the emission of light of longer wavelength and lower energy. Figure 3-3 shows the energy levels of a molecule for the absorption and fluorescence processes.

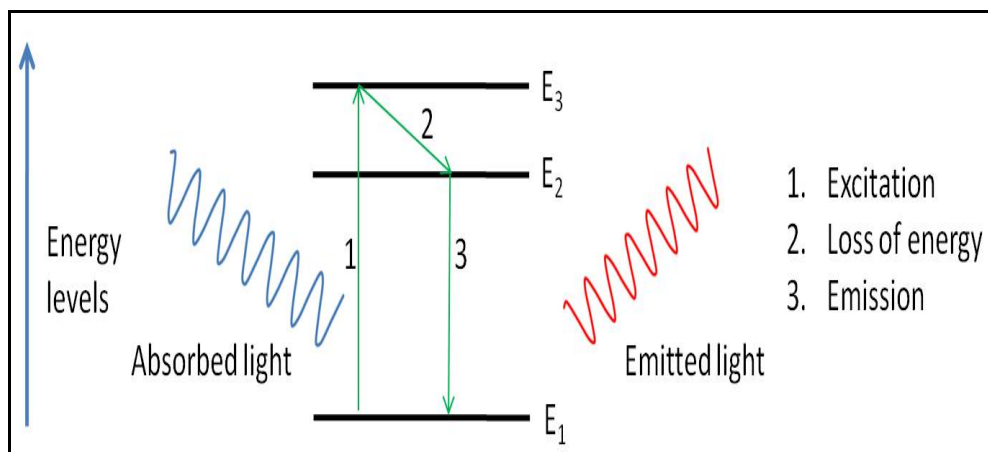


Figure 3-3 Energy levels of a molecule for absorption and fluorescence

A molecule, usually known as a fluorophore, is hit by a photon; the molecule then absorbs the light energy to reach a higher energy state known as the excited state (excitation). The energy level of the excited state is given by the quantum energy of the incident photon defined by Planck's hypothesis as:

$$E_{\text{absorbed_photon}} = h\nu \quad \text{Equation 3-4}$$

where ν is the photon frequency and h is Planck's constant (6.626068×10^{-34} J s). Hence, according to Figure 3-3

$$E_3 - E_1 = h\nu \quad \text{Equation 3-5}$$

The molecule is unstable at high energy levels and loses some energy to adopt a lower more stable energy state (loss of energy). Finally, the molecule rearranges to its original state with the excess energy released and emitted as light; the energy emitted is given by:

$$E_{\text{emitted_photon}} = E_2 - E_1 \quad \text{Equation 3-6}$$

The emitted light is of lower energy and longer wavelength than the light originally absorbed which effectively means that the colour of the emitted light is different to the colour of the absorbed light. Once the molecule is back to its original state, the process can be repeated with the particle absorbing light and emitting light until the point where the molecule can no longer fluoresce (photobleaching).

Fluorescent tracers have found widespread use in optical diagnostics techniques for flow tagging and Laser Induced Fluorescence (Section 3.6). The use of fluorescent tracers for Particle Image Velocimetry experiments is discussed in more detail in Section 3.5 and Chapters 4 and 5.

3.2. Single point measurement techniques

The invention of the laser in the 60's allowed the development of optical techniques that were previously impractical with other forms of illumination. Laser technology has enabled non-intrusive flow measurements by monitoring the light scattered by tracer particles immersed in the flow and from such measurements the fluid's velocity can be inferred. This entails the flow to be seeded with particles that have good light scattering characteristics and are able to follow the flow dynamics accurately. The requirements of the seeding particles for single point techniques are similar to those for full-field optical techniques; hence the details are discussed separately in Section 3.4.2.

Among the initial optical systems proposed, Laser Doppler Anemometry (LDA), also known as Laser Doppler Velocimetry (LDV), became established as an optical diagnostic technique given the high spatial and temporal resolution with which velocity measurements can be made. The technique has been successfully applied to laminar and turbulent flows, supersonic flows and high temperature flows. Initial work on LDA began in the early 60's by (Yeh and Cummins 1964) with considerable advances in the design of LDA systems over the last decades leading to fully integrated systems commercially available (Dantec 2010). Different arrangements have been developed (albeit with the same basic measuring principle) with a typical commercial LDA system consisting of a continuous wave laser, transmitting optics (beam splitter and focusing lens), receiving optics (focusing lens, photo detector), a signal conditioner and a signal processor. Figure 3-4 shows a schematic representation of a commercial LDA setup.

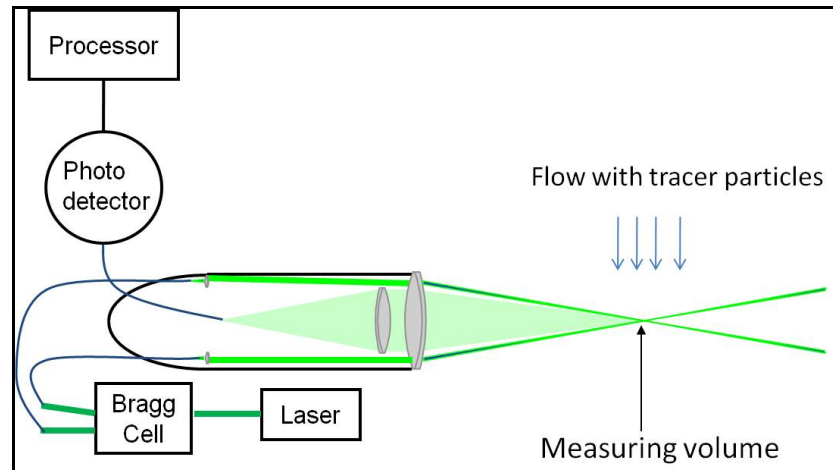


Figure 3-4 Schematic representation of a commercial LDA system (Adapted from Dantec 2010)

In an LDA system, a coherent light beam is split equally and the two resulting beams are then brought to a focused crossing forming the measurement volume which is typically a few millimetres long; at the crossing point, the two beams interfere with each other creating a fringe pattern. In some systems the beams are split using a Bragg cell creating two beams of equal intensity with a frequency shift which can be then used to distinguish between positive and negative velocities. The distance between the interference fringes can be calculated from the wavelength of the laser and the angle between the beams. Particles travelling through the measurement volume scatter light from both beams which is then collected by a receiving lens and focused on a photo detector; an interference filter placed in front of the photo detector lets only the required wavelength through in order to eliminate noise and other wavelengths. The photo detector converts the fluctuating light intensity into an electric signal known as the Doppler burst; using signal processing, the Doppler burst is filtered and amplified to then calculate the Doppler frequency using a Fast Fourier Transform algorithm. The Doppler frequency is effectively the time taken for each droplet to move between a pair of fringes ($\text{time} = 1/\text{Doppler frequency}$). Hence velocity is calculated dividing the known distance (fringe spacing) by the inverse of the measured Doppler frequency (Dantec 2010).

The setup depicted in Figure 3-4 allows for the calculation of one component of velocity; to measure two components, two extra beams can be added perpendicular to the first beams. For three component measurements, two

separate probes measuring one and two components respectively can be used. Moreover, different wavelengths should be used with 3 photo detectors recording the scattered light with one wavelength for each of the 3 velocity components measured. Commercially available LDA systems can generate up to 6 frequency shifted and unshifted beams of different wavelengths (Dantec 2010). However, as data are obtained only from a single point to map the entire flow field is a time consuming process, and coupled with the increased interests in techniques able to provide information simultaneously from different regions of the flow, led to the development of whole field techniques.

One of the main limitations of PDA systems is that their performance can be affected by particle non-sphericity. Although PDA commercial systems include non-sphericity detection, their accuracy when measuring non-spherical particles still needs to be assessed (Damaschke et al. 1998). An extension of the PDA setup was proposed for the measurement of arbitrary-shaped particles (Hardalupas et al. 1994); Shadow Doppler Velocimetry (SDV) consists of a classical PDA system supplemented by a shadow receiver. A shadow-like image is obtained from each illuminating beam and from the intensity levels of the pixels of the array the shape of the scattering particle can be reconstructed by processing a series of temporal slices (Fang Ren et al. 2003). The SDV technique has found extensive application due to its applicability to arbitrarily shaped particles with a list of recent applications and its extension to stereo measurements found in (Matsuura et al. 2004).

3.3. Full field measurement techniques

Whilst single point techniques such as LDA provide velocity data with high temporal and spatial resolution, velocities are measured at one single point which makes the system time-consuming and potentially expensive when full flow fields (such as the interaction of air and fuel in a GDI engine) need to be measured. On the other hand, advances on the quality of the illumination (short pulse duration and high-energy lasers) as well as the recording conditions (fast-frame and low-noise CCD cameras), have increased the number of global measurement techniques developed for simultaneous full-field velocity measurements in particular for experimental fluid mechanics. Two of the most commonly used

techniques include Global Doppler velocimetry and Pulsed-Light Velocimetry where flow fields are obtained by determining the changes of some kind of image features. Next, a description of such approaches is presented.

3.3.1. Global Doppler Velocimetry (Planar Doppler Velocimetry)

Global Doppler Velocimetry (GDV) is a full-field optical technique originally patented by (Komine 1990) and later reported in the literature by (Meyers and Komine 1991). This technique is also known as Planar Doppler Velocimetry and other variations to this name have been reported (Samimy and Wernet 2000).

Similarly to Laser Doppler anemometry, GDV estimates flow velocity by measuring the Doppler shift from particles in the field of view. Unlike LDA, only one beam is used in GDV and the absorption characteristics of molecular filters are used to determine the Doppler shift of the scattered laser light (McKeon et al. 2007). The main advantage of this principle over LDA is that a laser light sheet is used, instead of a beam, and a camera is used to record the light intensity through the filter over large areas (full field of view) instead of a photo detector examining light from a point source.

Figure 3-5 shows a schematic representation of the optical arrangement for GDV and the frequency to intensity conversion of a molecular iodine filter. When a single frequency laser is tuned to a point midway along the side of the absorption line of the filter, the absorption of approximately half of the light energy by the media is obtained. If the optical frequency is changed, by changing the Doppler shift in the light, the amount of energy absorbed by the media changes. Therefore, the absorption line acts as an optical frequency-to-intensity converter which is linear over a significant frequency range for a majority of absorption lines (McKeon et al. 2007).

The Doppler shift is related to the velocity of a particle scattering light by:

$$\Delta\nu = \nu_0 (\hat{o} - \hat{i}) \frac{\vec{V}}{c} \quad \text{Equation 3-7}$$

where $\Delta\nu$ is droplet shift of the light scattered by particles, ν_0 is the frequency of the light source, c is the speed of light, \vec{V} is the particle velocity, \hat{i} is the direction of the light source and \hat{o} is the imaging direction. Therefore, from the Doppler shifted light observed through the molecular iodine filter and recorded by the camera, real intensity variations will be obtained in the image plane which are in turn proportional to the particle velocity. A reference signal is usually required to normalise the percentage of light which goes through the filter for each particle; this signal is recorded before the light goes through the filter by imaging the flow directly. Signal normalisation (pixel wise) helps remove the effects of laser power variation and seeding density on the recorded signal (Nobes et al. 2004).

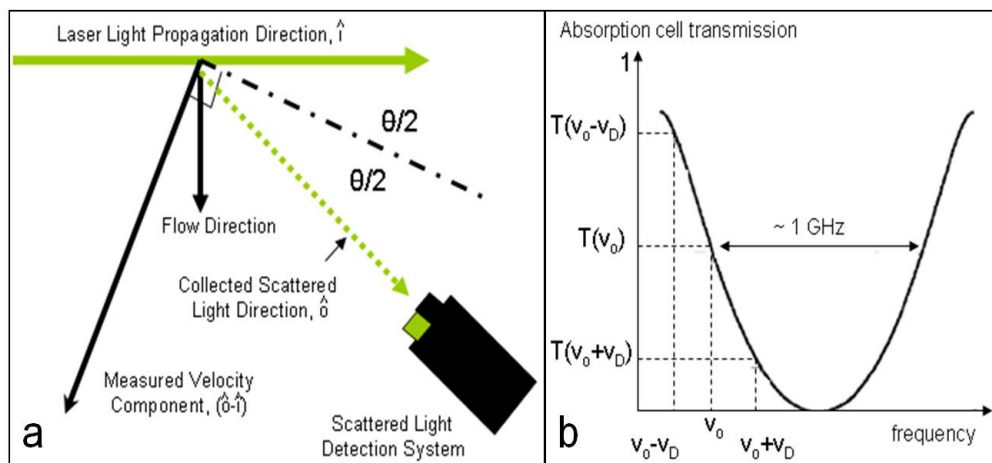


Figure 3-5 Schematic representation of the optical arrangement for GDV and the frequency to intensity conversion of a molecular iodine filter

The setup shown in Figure 3-5 can be used to obtain one velocity component; other components can be obtained by varying the viewing direction \hat{o} . The same principle can be applied to obtain three velocity components as first demonstrated by (Meyers and Komine 1991) and (Meyers 1995) who used a multiple-camera system to record images from different angles of the flow in a high speed jet on a wind tunnel.

A detailed review of the accuracy of GDV was presented by (Morrison and Jr 2001) and different sources of uncertainty were identified: filter cell stability, pixel

sensitivity calibration, laser frequency drift, image misalignment and observer \hat{o} laser \hat{i} orientations. It was also found that the biggest contributor to measurement uncertainty was the misalignment between the reference image and the filtered image since values that do not correspond to the same spatial location are processed. GDV is mainly used for higher speed flows (velocity $> 5\text{m/s}$) because of the discernible frequency shift and measurement uncertainties up to $\pm 5\text{m/s}$ reported (Morrison and Jr 2001). Therefore, given the slow velocities that can be present in the gas phase for the air/fuel interaction in a GDI spray, GDV is not appropriate for this application.

3.3.2. Pulsed-light Velocimetry

Pulsed-light Velocimetry (PLV) encompasses particle imaging techniques in which the velocity of the flow is analysed by tracking the motion of tracers added to the flow at two or more different times. PLV techniques use the basic definition of velocity to calculate the instantaneous velocity of the tracers from the known time difference and the measured displacement. The location of the tracers is obtained using short pulses of light to freeze their movement and then record the scattered light for each pulse on an imaging device. Since PLV techniques estimate flow velocity indirectly, by measuring the velocity of the tracers added to the flow, the accuracy of the measurements is mainly affected by the ability of the tracers to follow the flow faithfully. A compromise between tracking capabilities and scattering intensity is usually required; further details on tracer particles are presented in Section 3.4.2.

Adrian and Raffel et al., classify PLV in three different modes according to the image density of the particles recorded as shown in Figure 3-6 (Adrian 1991), (Raffel et al. 1998).

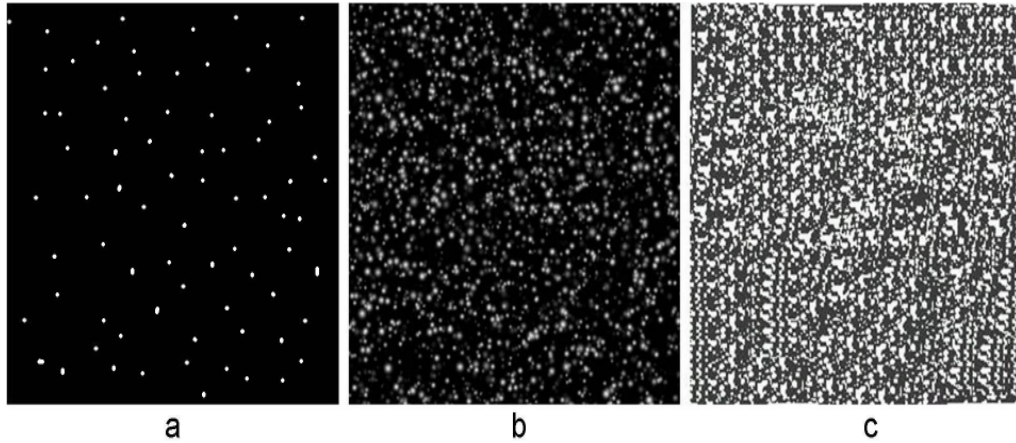


Figure 3-6 Three image density modes: a low (PTV), b medium (PIV), c high (LSV)

For the low seeding density case (Figure 3-6a) individual particles and their corresponding pairs can be visually identified for different illuminations; thus, tracking methods can be used for the evaluation of such images, and the approach is known as Particle Tracking Velocimetry (PTV). For medium image density (Figure 3-6b) particle pairs cannot be identified by visual inspection and statistical correlation methods are required for evaluation; thus this mode of operation is known as Particle Image Velocimetry (PIV). Finally, for high image density, it is not possible to identify individual particle images as the light scattered from the particles overlaps in the image plane to form speckles (Figure 3-6c) and this is referred to as Laser Speckle Velocimetry (LSV).

The next section provides a more detailed analysis of the PIV technique, which is the main focus of this thesis. A brief introduction to the principles of LSV and PTV is presented in Section 3.4.8.1. Should the reader require more information (Barker and Fournay 1977) (Kowalczyk 1996), (Meynart 1983) and (Adrian 2005) present a more in depth discussion of such approaches.

3.4. Particle Image Velocimetry

Particle Image Velocimetry (PIV) is a technique which provides instantaneous velocity measurements across a planar area of a flow field. In PIV, tracer particles added to the flow (in some applications, such as fuel sprays, the naturally occurring droplets act as tracers) are illuminated twice using a laser source which has been focused into a light sheet using an arrangement of cylindrical lenses. The light

elastically scattered by the particles is recorded by a CCD camera either within the same frame or in two separate frames. After correlation analysis, a 2-dimensional (2D) vector map of the fluid flow is produced (Westerweel 1997). Figure 3-7 shows a schematic representation of the experimental setup of a conventional PIV system.

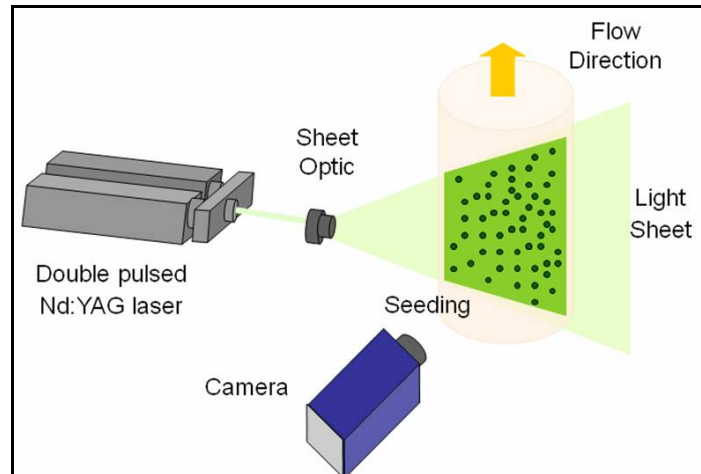


Figure 3-7 Schematic representation of a conventional PIV setup

PIV has developed considerably during the last 25 years and extensive research has been published on different areas such as image processing, error calculation and its applications in different fields. A detailed review of PIV history is out of the scope of this thesis hence only the main technical advances leading to its current state will be summarised here as listed by (Raffel et al. 1998). Comprehensive reviews on PIV history have been published and can be found elsewhere: (Westerweel 1993) (Grant 1994) (Grant 1997) (Raffel et al. 1998) (Adrian 2005).

Different factors have influenced the development of PIV during the last two decades such as.

- The use of digital techniques for image acquisition and analysis which have replaced conventional analogue recording and evaluation techniques. The use of double framing allows to capture independent images from the two pulses removing directional ambiguity.
- The use of pairs of frequency doubled Nd:YAG lasers to produce light in the visible spectrum with a wavelength of 532nm allowed the illumination of

a plane in the flow with two pulses of the same energy at any time delay. These lasers operate at frequencies of 10-20 Hz and can be synchronised to double-frame cameras for the acquisition of large amounts of data.

- Different aerosol generators have been developed to generate seeding tracers under controlled conditions to distribute the particles in the flow homogeneously.
- Advances have been made in image processing algorithms especially in the development of Gaussian peak finders which allowed the determination of the displacement peak location more accurately. (See section 3.4.5).
- Development in computer and hardware capabilities (memory size and processors) has allowed for a faster and more reliable handling and processing of large amounts of PIV data.

3.4.1. Light sources

Light sources in PIV experiments need to be sufficiently powerful for the light scattered by the tracer particles to be recorded in the imaging device. They also need to provide short light pulses (nanoseconds) so that the motion of the tracer particles can be frozen without blur.

Lasers are the most commonly used light source in PIV due to their ability to emit monochromatic light with high energy density which can be then formed into light sheets for the illumination of tracer particles in a plane. Pulsed lasers are usually preferred to continuous-wave lasers since the latter need a shutter mechanism to generate light pulses limiting their use to slow flow velocities.

Amongst the different types of lasers commercially available (Helium-neon, Copper-vapour, Argon-ion, ruby), Neodymium:YAG (Nd:YAG) are the most commonly used solid state laser for PIV illumination. Every laser consists of three main components: a laser material, a pump source and an oscillator. For Nd:YAG lasers, the laser material is a crystal where Nd^{3+} ions are incorporated in a YAG (yttrium-aluminium-garnet) crystal; the pump is a krypton flash lamp and the oscillator is a set of high reflectivity mirrors generating a Gaussian beam profile.

The strongest output wavelength for Nd:YAG lasers is 1064nm which can be frequency doubled to obtain 532nm and then tripled to obtain 355nm illumination commonly used for elastic scattering and excitation of fluorescent tracers respectively. Laser pulses are then focused into a light sheet to illuminate the area of interest; different lens combinations can be used depending on the type of laser with an expanding lens and a cylindrical lens the most commonly used combination for Nd:YAG lasers. A comprehensive review of laser technology is given by (Raffel et al. 1998).

3.4.2. Tracer particles for PIV

Tracer particle selection is essential in PIV since the velocity of the flow is estimated by measuring the velocity of the tracer particles added to it; tracer particles also need to scatter enough light to be recorded by the imaging device. The main factors influencing particle tracking capabilities in a fluid are: particle diameter, particle density and particle shape the fluid physical properties such as density, kinematic and dynamic viscosity. (Raffel et al. 1998) provides an estimation of the flow following capabilities of spherical particles in a viscous fluid at very low Reynolds numbers in the form of a velocity lag U_s given as:

$$U_s = U_p - U = d_p^2 \frac{(\rho_p - \rho)}{18\mu} a \quad \text{Equation 3-8}$$

where U_s is the Velocity lag, U_p is the particle velocity, U is the fluid velocity, d_p is the particle diameter, ρ_p is the particle density, ρ is the fluid density, μ is the fluid dynamic viscosity and a is the flow acceleration. Equation 3-8 shows that by matching as closely as possible the fluid density and the particle density the value of the velocity lag will be small and the particles will therefore follow the fluid motion appropriately.

In liquid flow applications it is not difficult to find particles with matching densities; solid particles can often be found (similar densities to most fluids) hence it is possible to use larger seeding particles to seed liquid flows. Tracer particles used for liquid flow applications include polystyrene and aluminium particles and glass spheres, among others (a list of commonly used tracer particles in liquid flows is

presented in (Melling 1997)). On the other hand, in gas flows the difference in densities is considerably larger. For example, if olive oil droplets are used to seed an air flow, the densities will differ by a factor of approximately 900 thus in order to have a low velocity lag value, the diameter of the tracer particles should be very small compared to that required for liquid flow applications.

More detailed theoretical descriptions of the relative motion of a particle in a fluid have been derived. When assessing the tracking capabilities of particles added to the flow, it is valid to assume particles to be spherical and the concentration used for gas flows is usually low enough to assume that each particle is suspended in a fluid of infinite extent making it possible to neglect particle interaction (Melling 1997).

The relative motion of the fluid is governed by the Navier-Stokes equations and the relative motion between a single particle and a fluid has been studied by (Ossen 1927) and (Tchen 1947) who derived an equation for the motion of a particle in a fluid with variable velocity. The equation of motion as formulated by (Durst and Melling 1981) is given below

$$\frac{\pi d_p^3}{6} \rho_p \frac{dU_p}{dt} = \frac{1}{2} C_D \rho_f (U_f - U_p)^2 A + \frac{\pi d_p^3}{6} \rho_f \frac{dU_f}{dt} + \frac{1}{2} \frac{\pi d_p^3}{6} \rho_f \left(\frac{dU_f}{dt} - \frac{dU_p}{dt} \right) + \frac{3}{2} d_p^2 \sqrt{\pi \rho_f \mu} \int_0^t \frac{\frac{dU_f}{dt} - \frac{dU_p}{dt}}{\sqrt{t-t'}} dt + F_e$$

Equation 3-9

where d_p is the particle diameter, ρ_p is the density of the particle, U_p is the particle velocity, ρ_f is the density of the fluid, U_f is the velocity of the fluid, μ is the fluid viscosity, C_D is the drag coefficient, t is time, A is the area of the particle and F_e is any external force present. The term on the left hand side represents the mass of the particle and its acceleration. On the right hand side: the first term represents a general expression for the drag force so that different approximations of the drag coefficient (C_D) can be used; the second term represents the pressure gradient applied to the particle (resulting in a force) due to the acceleration of the fluid; the third term is the force required to accelerate the added mass of the particle due to

the mass of fluid displaced by the particle's motion; the fourth term is the 'Basset history integral' which accounts for the drag force due to unsteadiness in the flow field and the final term accounts for any potential forces acting due to gravity, centrifugal or electrostatic fields.

Equation 3-9 is valid under the following conditions: the particle size is less than the turbulence scales in the fluid, the particle is surrounded by the same fluid molecules (the particle motion does not overshoot the motion of the fluid) and the turbulence is homogeneous and time invariant (Durst and Melling 1981). For PIV in gas flows (assuming no external forces) the ratio of the fluid density to the particle density, even for the least dense seeding materials, is ~ 0.001 . Hence the terms which are proportional to the fluid density are three orders of magnitude less than the other terms and can be neglected (Hinze 1959). Equation 3-9 can then be re-expressed as:

$$\frac{\pi d_p^3}{6} \rho_p \frac{dU_p}{dt} = \frac{1}{2} C_D \rho_f (U_f - U_p)^2 A \quad \text{Equation 3-10}$$

The Reynolds number of a particle relative to the fluid can be expressed as:

$$\text{Re}_p = \frac{|(U_f - U_p)| d_p}{\nu_f} \quad \text{Equation 3-11}$$

where ν_f is the fluid kinematic viscosity. Equations 3-10 and 3-11 can be combined, using $A = \pi(d_p^2/4)$, to obtain an equation for the motion of a particle in a continuous fluid:

$$\frac{dU_p}{dt} = \frac{3\nu_f \rho_f}{4d_p^2 \rho_p} \text{Re}_p C_D (U_f - U_p) \quad \text{Equation 3-12}$$

Different approximations for the drag coefficient have been proposed by different authors including Stokes' drag law, Melling's drag coefficient (Melling 1986), Neilson's drag coefficient (Neilson and Gilchrist 1969) and Meyers' drag coefficient (Meyers 1991). As an example, equation 3-12 can be solved using Stokes' drag law which is considered valid for particle Reynolds number $\text{Re}_p < 1$ (Durst and

Melling 1981) (Merzkirch 1987). The Stokes drag coefficient is defined by (Melling 1997) as:

$$C_{D,Stokes} = \frac{24}{\text{Re}_p} \quad \text{Equation 3-13}$$

Thus, Equation 3-12 becomes:

$$\left(\frac{dU_p}{dt} \right)_{\text{Melling}} = \frac{18\nu_f}{d_p^2} \frac{\rho_f}{\rho_p} (U_f - U_p) \quad \text{Equation 3-14}$$

It is important to notice that Equation 3.14 is analogous to Equation 3.8 and both can be used to assess particle response under any given experimental conditions. Equation 3.14 can be solved analytically to obtain an expression for the velocity of a particle in a fluid with velocity U_f as a function of time; this equation can be then integrated to obtain an equation for the displacement of the particle as a function of time. Displacement can be plotted against velocity (for the same time scale) to assess the response of different particles to a velocity change in air. Particle properties are assumed to be those of olive oil and a step change of velocity of 5m/s is assumed for air. Figure 3-8 shows the results of the particle displacement and its corresponding velocity for spherical particles of 0.5, 1, 2 and 3 μm in diameter. The results shown confirm that the smaller the particle, the faster it will acquire the continuous flow velocity.

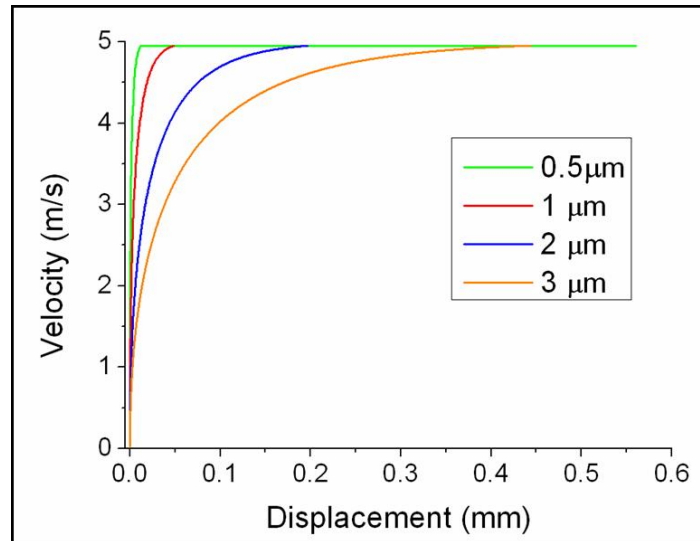


Figure 3-8 Olive oil particles response to a step change in air velocity of 5 m/s

In the gas phase, it is generally accepted that micron and sub-micron tracers are required for an adequate dynamic response (Melling 1997); on the other hand in liquid flows larger particles can be used which will also scatter more light ($\sim 20\mu\text{m}$).

3.4.3. Particle Imaging

For imaging of an object in air, as shown in Figure 3-9, the focal length, f , of the system is defined by the focus criterion as

$$\frac{1}{d_o} + \frac{1}{d_i} = \frac{1}{f} \quad \text{Equation 3-15}$$

where d_o is the distance between the object plane and the imaging lens and d_i is the distance between the image plane and the lens. The magnification of the system (M) is given by:

$$M = d_i / d_o$$

Equation 3-16

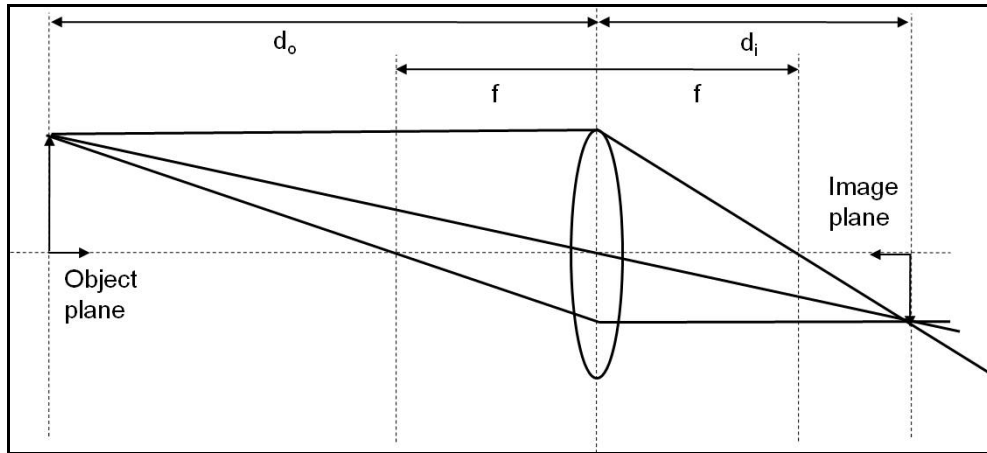


Figure 3-9 Geometric image reconstruction

The diameter of the image in the image plane is a function the diameter of the particle d_p , the magnification M , and the point spread function of the lens. For a diffraction limited system (an ideal system with no aberrations), its point response function is given as an Airy function with diameter (Adrian 1991):

$$d_{diff} = 2.44(1 + M)F_{\#}\lambda$$

Equation 3-17

where λ is the wavelength and the f number ($F_{\#}$) is defined as the ratio between the focal length (f) and the aperture of the imaging lens.

The image of a finite diameter particle is the convolution of the Airy function with the geometric image of the particle (Goodman 1968); therefore, the image diameter d_i can be estimated with the following equation (Adrian and Yao 1985):

$$d_i = \sqrt{M^2 d_p^2 + d_{diff}^2}$$

Equation 3-18

For full field imaging techniques, the minimum image diameter d_{diff} will only be obtained when recording small particles (few microns) at small magnifications. For larger particles and magnifications the influence of geometric imaging becomes more dominant and the particle image diameter will be mainly affected by the magnification of the imaging system (Raffel et al. 1998). The above equations will

be valid as long as the particles are within the depth of field d_z of the imaging system given by (Adrian 1991) as:

$$d_z = 4(1 + M^{-1})^2 f_{\#}^2 \lambda \quad \text{Equation 3-19}$$

3.4.4. Image acquisition

Different approaches to image acquisition have been reported in the literature since the early stages of PIV, but in general the light scattered by the particles is recorded via a high quality lens by an imaging device usually placed normal to the laser sheet. Until the early 90's photographic cameras were used to record PIV images, and therefore data evaluation and analysis could only be performed once the film had been developed. Nowadays the advances in electronic imaging have provided an alternative to photographic films with instantaneous image availability (thus feedback during recording) and the avoidance of chemical processing being its main advantages. Nevertheless photographic films are still used in some holographic applications. Amongst the different imaging devices, the charge-coupled device, CCD, has found the most widespread use (Raffel et al 1998). CCDs are electronic sensors which convert light (photons) into electric charge (electrons) based on the photoelectric effect. A CCD sensor consists of many individual CCDs arranged in a rectangular array; each individual CCD element is called a pixel (picture element) and its size is in the order of 5x5 to 10x10 μm . The light scattered by the particles can be recorded in either one single frame or in two consecutive frames (double frame); each acquisition approach will require a different processing method as explained in Section 3.4.5.

3.4.5. Image Analysis

When defining pulsed-light velocimetry (Section 3.3.2) it was established that for medium seeding levels, as it is the case in PIV, particle pairs cannot be identified by visual inspection hence statistical methods are required for velocity calculation. The main objective of statistical evaluation of PIV recordings is to determine the average displacement between two patterns of particle images which are stored as a 2D distribution of grey levels (Raffel et al. 1998). Each pattern is contained within small regions usually referred to as interrogation windows. Once the displacement

has been calculated, the velocity is obtained dividing the displacement by the known time separation between laser exposures.

Depending on how the images were acquired, two different processing methods can be distinguished. Early work on PIV reported the use of auto-correlation in which a vector field is calculated from a double-exposed image recorded on a single frame (Keane and Adrian 1990). Later studies expanded vector calculation to the use of cross-correlation in which the vector field is calculated based on two particle images recorded on separate frames (Keane and Adrian 1992). Cross-correlation has become the preferred form of analysis in PIV recordings since there is no directional ambiguity in the displacement.

3.4.5.1. Cross-correlation

In cross-correlation analysis two separate frames (corresponding to the two laser exposures) are divided into interrogation windows to estimate the average particle shift observed for the particles contained in each window. Given that the displacement calculated is averaged, a mathematical correlation procedure is used to extract the most probable displacement pattern. The maximum peak location in the correlation plane (Figure 3-10) indicates the particle displacement; therefore an instantaneous velocity can be calculated knowing the time difference between two successive frames.

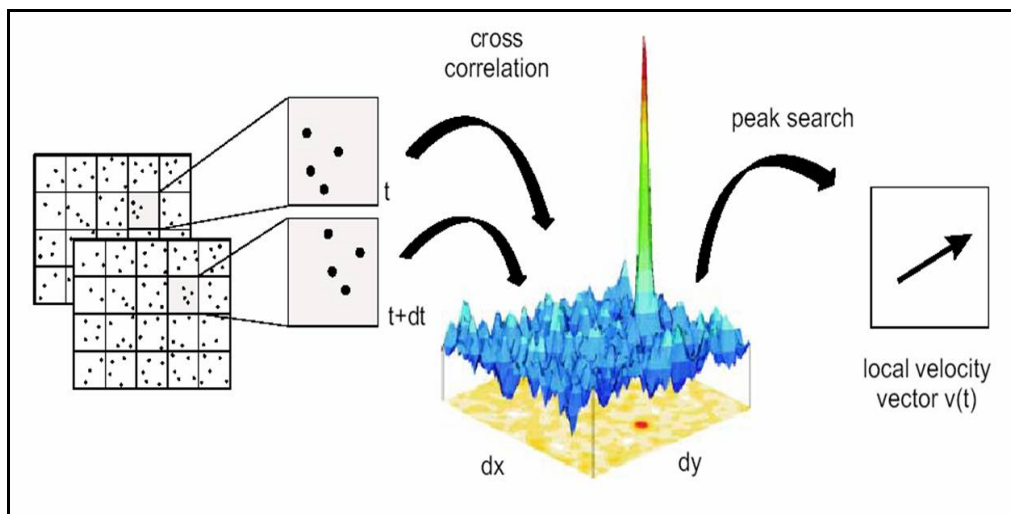


Figure 3-10. Cross-correlation process (Source: LaVision website <http://www.piv.de>)

Mathematically, two methods are used to compute the cross-correlation function: in the frequency domain using the Fast Fourier Transform (FFT) or directly in the spatial domain. The FFT provides a faster implementation but the direct spatial cross-correlation performs better with varying background intensity (LaVision 2007). Details on the mathematical background of each method can be found in (Raffel et al. 1998) and different studies comparing the performances of each method can also be found in the literature e.g. (Gui and Merzkirch 2000).

Keane and Adrian established that 10-20 particles are usually required in each interrogation area for reliable calculation (Keane and Adrian 1990); similarly (Coupland and Pickering 1988) introduced a definition of signal to noise ratio for PIV measurements which was analysed as a function of number of particle image pairs; it was found that the signal to noise ratio increased monotonically for up to seven particle pairs after which it remained approximately constant. To limit the loss of particle pairs due to in-plane motion the commonly known as one-quarter rule is generally accepted (the maximum particle shift should not exceed one quarter of the interrogation window size (Adrian 1991)).

3.4.5.2. *Particle displacement estimation*

Once the correlation function has been calculated, the particle displacement is given by the location of the highest peak in the correlation plane; since the data have been discretised, the peak displacement can only be determined with an accuracy of $\pm \frac{1}{2}$ pixel (Raffel et al. 1998). A more accurate measurement of the particle displacement can be obtained by fitting a function to the correlation peak. The most commonly used fitting function is the Gaussian peak fit (Willert and Gharib 1991) given that, when sharply focused, particle images are described by Airy intensity functions which can be approximated by a Gaussian intensity distribution. Other reported fitting functions include centroid and parabolic peak fits (Raffel et al. 1998) and more sophisticated methods have also been investigated including 2D interpolation or convolution reconstruction (Sugii and et al. 2000). The accuracy of each method has been studied analytically and with numerical simulations and accuracies from tenths of a pixels up to hundredths have been reported (Westerweel 1997) (Raffel et al. 1998).

Additional algorithms and techniques have been developed for improved results in PIV analysis and to reduce the effect of measurement errors (Section 3.4.6); these techniques are usually characterised by being iterative using the information from the initial iteration to adapt subsequent iterations. Some of the most commonly used techniques in commercial PIV software include the reduction of the window size and the introduction of a relative shift between correlation areas. Window overlap is used to improve the spatial resolution in cross-correlation by displacing each window a certain distance in both the x and y directions. This results in a higher number of matched particle pairs (due to sharing of particle information) and an increased signal to noise ratio in the correlation plane. In multi-grid approaches the vector field is calculated using an arbitrary number of iterations with a decreasing window size. For example, in the first iteration a reference vector field is calculated; in the next iteration the window size is halved and the reference vector field from the first iteration is used as the best-choice window shift (LaVision 2007). In this manner, vectors are calculated adaptively using the information from previous iterations to calculate the following steps more reliably. Other advanced techniques have been proposed such as second order correlation, local adaptive window shift (Fincham and Delerce 2000) and window deformation (Scarano 2002); additionally, the effect of the intrinsic spatial averaging nature of PIV (a set of discrete velocities is averaged to one value per interrogation window) on the calculation of second of second order statistics (such as turbulent kinetic energy) has been investigated and quantified (Spencer and Hollis 2005).

3.4.5.3. *Validation of velocity vectors*

Spurious vectors arise due to interrogation windows having insufficient particles or a low signal to noise ratio (Nogueira et al. 1997). It is important to remove spurious vectors from a vector field since calculations such as divergence and vorticity will be greatly affected by them. After spurious vectors have been removed it is usually desirable to fill the gaps using interpolation methods (Raffel et al. 1998). Whilst spurious vectors can usually be identified by visual inspections, this is not feasible for large amounts of velocity data. Spurious vector detection is generally performed using two methods: correlation peak quality (initially defined as detectability criterion by (Keane and Adrian 1992)) and vector field coherence.

The peak quality in each vector can be established by comparing the chosen peak to the other peaks in the correlation plane. A peak ratio is defined in DaVis 7.2 using the following equation:

$$Peak_ratio = \frac{P1 - \min}{P2 - \min} \quad \text{Equation 3-20}$$

where \min is the lowest value in the correlation plane, $P1$ and $P2$ are the peak heights of the first and second highest correlation peaks according to Figure 3-11. Therefore the peak ratio is calculated as a ratio relative to the common correlation background to compensate for background noise (LaVision 2007).

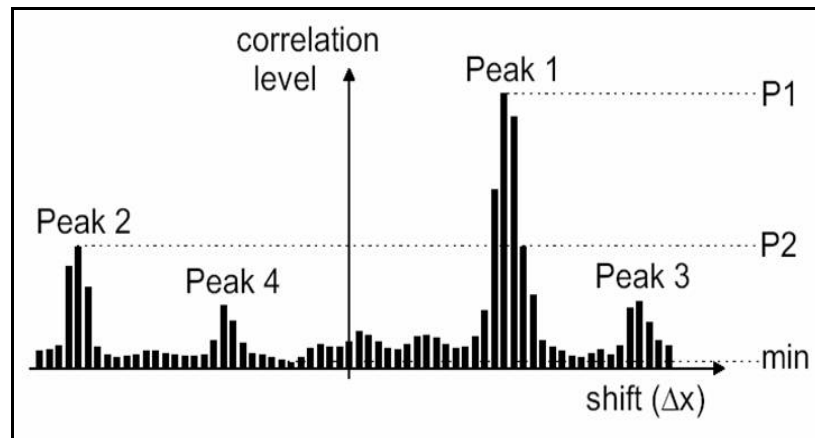


Figure 3-11 Peak ratio calculation (Source: (LaVision 2007))

In general, the higher the ratio the higher the confidence in the particular vector; a high peak ratio (1.5 – 2) indicates the vector is likely to be a valid vector with values down to 1.2 still considered valid (Keane and Adrian 1992). This calculation, however, will also remove good vectors whilst some outliers might also have a high peak ratio (LaVision 2007).

Spurious vectors can also be detected by comparing a particular vector with its nearby vectors (Westerweel 1994). Most of the approaches use median filtering where a box of 3x3 vectors surrounding a particular vector is used to compare the middle vector to the median and the RMS of the 8 surrounding vectors. The centre vector is rejected when it is outside the allowed range of deviation of the neighbouring vectors.

Different variations of the median filter have been developed and can be found in the literature (Westerweel and Scarano 2005). The algorithms implemented in DaVis 7.2 for median filtering are based on the algorithms proposed by (Westerweel 1994) and (Nogueira et al. 1997). Other more sophisticated approaches have also been proposed and are discussed in (Raffel et al. 1998).

3.4.6. Sources of error in PIV

Different sources of error need to be considered in PIV recordings. Extensive work has been done on error analysis for PIV but only the fundamentals will be discussed in this thesis as summarised by (Prasad 2000a). The effect of some of these sources of error can be reduced by careful selection of the experimental conditions for a given setup but others are inherent to the PIV technique.

3.4.6.1. Peak locking or bias error

The particle image diameter for PIV recording should be at least 2-3 pixels for curve fitting algorithms to accurately locate the centre of each particle or the centre of the correlation peak. If the particle image is one pixel or less, the centre of the particle will be located by the curve fitting function at the centre of the pixel. The practical effect of this is that particle displacement will not be estimated with sub-pixel accuracy and will be strongly biased to integer values.

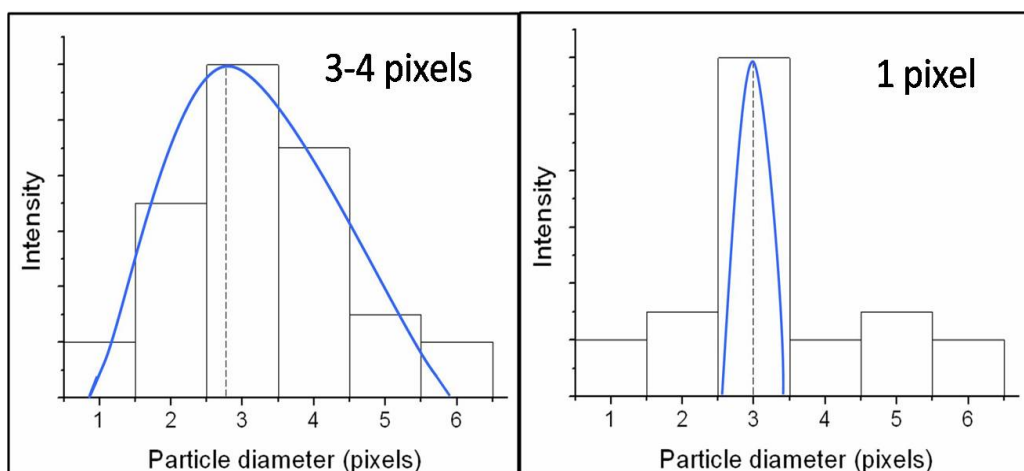


Figure 3-12 Intensity distribution of 2 particles with a Gaussian curve fitting

Figure 3-12 shows the intensity distribution of two particles and the Gaussian curve fitting with the calculated particle centre shown by the dashed line. For a particle image of 3-4 pixels across (left hand side), the calculated centre of the particle is located with sub-pixel accuracy; for a particle image of 1 pixel across (right hand side), the particle centre cannot be calculated with sub-pixel accuracy and the displacement will be strongly biased towards integer values. Peak locking effects can be estimated directly from vector fields within DaVis 7.2 using the following equation:

$$Peak_lock = 4 \times (0.25 - centre_of_mass) \quad \text{Equation 3-21}$$

where the centre of mass is calculated as follows: a histogram of the decimal part of the displacement for each vector (pixels) is plotted in the x and y directions with values larger than 0.5 plotted as 1 minus the value so that a range from 0 to 0.5 is obtained (effectively plotting the value to the nearest integer for each vector). When there are no peak locking effects, there is an equipartition of the decimal places and the centre of mass is expected to be around 0.25 (centre of histogram) hence peak lock estimator (Equation 3-21) ~ 0 . On the other hand, when there are strong peak locking effects, the centre of mass is shifted to zero hence peak lock estimator ~ 1 . Therefore the following values are given as indicators of peak locking effects in any particular vector field based on Equation 3-21.

- 0: No peak locking effect
- 1: strong peak locking effect
- < 0.1 : Peak locking effect is acceptable

A combination of particle size selection and imaging optics should be used to ensure particle images are at least 2-3 pixels across to reduce the effects of peak locking (LaVision 2007). The peak locator also affects the scale of peak locking with (Westerweel 1997) showing that the Gaussian peak locator outperforms both the centroid and parabolic fitting functions in terms of minimising peak locking errors. It should be noted that bias error can only be accounted for when it dominates over the other sources of error which are not deterministic. More detailed studies on peak locking and different methods to reduce its effects are

available in the literature (Cholemari 2007) including correlation mapping (Chen and Katz 2005), discrete window shifting (Westerweel et al. 1997) and continuous window shifting (Gui and Wereley 2002).

3.4.6.2. Acceleration error

In most fluid applications the particle streamlines are not straight but curved hence an error is incurred when the Eulerian velocity is approximated using Lagrangian particle displacements, (Prasad 2000a).

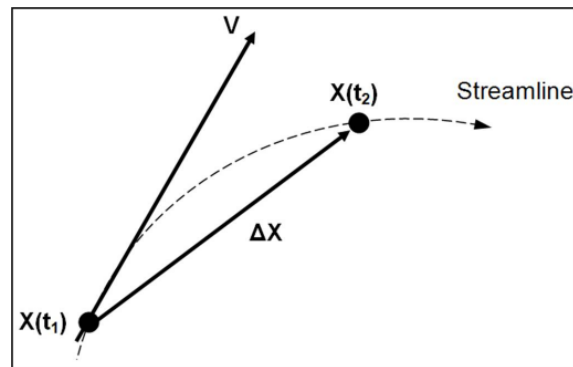


Figure 3-13 Acceleration error

Figure 3-13 shows Lagrangian particle displacements in a curved streamline. The deviation of the measured particle velocity ($\Delta x/\Delta t$) will be greater from the actual flow velocity V the larger the value of Δt ; hence the pulse separation Δt should be ideally short. However there is a point where for small pulse separations the calculated displacement may be too small and on a similar level to the random error (Prasad 2000a). A generally accepted compromise has been proposed as $\frac{1}{4}$ the interrogation window size for the maximum particle displacement (Section 3.4.5.1). (Melling 1997) and (Boillot and Prasad 1996) proposed an estimation of the optimal pulse separation accounting for the effects of random error:

$$\Delta t = \sqrt{\left(\frac{2\sigma_{random}}{Ma}\right)} \quad \text{Equation 3-22}$$

where σ_{random} is the measurement random error, M is the magnification of the optical system and a is the local acceleration of the particle (to be determined beforehand). Further optimisation of the pulse separation might be required if (as it

is the case for many applications) the flow does not have the same acceleration in all regions.

3.4.6.3. *Tracking error*

This error results from the failure of the tracer particles to follow the flow without slip. As discussed in Section 3.4.2, particle tracers need to be carefully selected according to the flow characteristics such that they follow the flow dynamics accurately minimising slip velocity.

3.4.6.4. *Gradient error*

This error results from the rotation and deformation of the flow within the interrogation area leading to loss of particle pairs and consequently changes in the correlation peak magnitude. A recent study by (Westerweel 2008) on the effect of local velocity gradients on correlation peaks concluded that local gradients can be ignored provided that the variation of the displacement within the interrogation domain does not exceed the mean particle image diameter.

3.4.6.5. *Perspective error*

This error arises due to the influence of out of plane velocity components when locating in plane (xy) image points; for some applications (especially in highly three-dimensional flows), the displacement in the z direction influences the particle displacement (as shown in Figure 3-14) introducing an uncertainty in the estimation of the in-plane velocity components. This error is unrecoverable and it is obtained in high magnification systems and at the edges of flow fields.

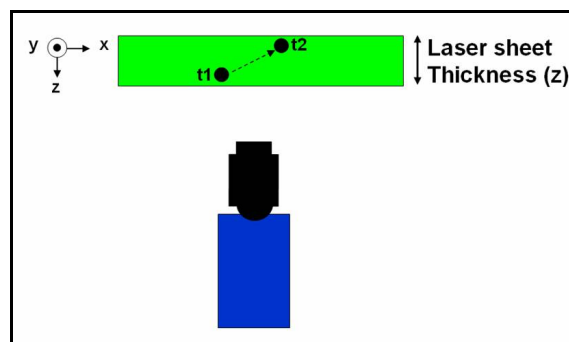


Figure 3-14 Perspective error

3.4.6.6. *Errors due to out of plane motion*

This is an extension of the perspective error and is also obtained in highly three-dimensional flows. When there is excessive out of plane motion, particles are lost from one of the images as they leave the illuminated area between laser pulses; this leads to uncorrelated pairs between the image pairs hence more noise in the correlation functions is obtained. To reduce the effects of particle loss, the out of plane displacement should be less than $\frac{1}{4}$ of the laser sheet thickness.

The effect of these errors on the accuracy of PIV measurements will depend on different experimental and processing conditions. Whilst measurement resolutions down to 0.01 pixels have been reported using synthetic test images, under experimental conditions the resolution is expected to be limited to at least 0.1 pixels due to variations in the intensity of individual particles (Nobach and Bodenschatz 2009). Unrecoverable errors have been quantified for the measurements presented in this thesis and can be found in Section 7.3.2; for the assumptions made, the worst case scenario considered produced an unrecoverable error of 18.3%.

3.4.7. Stereoscopic PIV (Stereo PIV)

One big disadvantage of the classical 2D PIV setup is that it only provides the projection of the velocity vectors in the same plane of the laser light sheet. The out of plane component cannot be measured and, as discussed in Section 3.4.6.5, produces an unrecoverable perspective error in the in-plane velocity measurements. There are different methods for recording the out of plane velocity component described in the literature such as holographic PIV (Coupland and Halliwell 1992) (Dadi et al. 1991), Dual-plane PIV (Raffel et al. 1996) and others as summarised by (Hinsch 1995) and (Arroyo and Hinsch 2008).

One of the approaches used to measure three components of velocity is an additional camera recording the image from a different viewing axis in what is known as Stereoscopic PIV (Prasad and Adrian 1993) (Gaydon et al. 1997). By using two cameras at two viewing angles, projections of the velocity vectors can be obtained in two different planes and then combined, after a careful calibration of the system, to extract all three velocity components. Figure 3-15 shows the basic

camera arrangement of a stereoscopic PIV system. The angle between the cameras (α) is usually ~ 45 degrees and the cameras should be arranged symmetrically in order to increase the accuracy in the vector calculation. The laser sheet should be arranged in such a manner that the main flow component is in-plane.

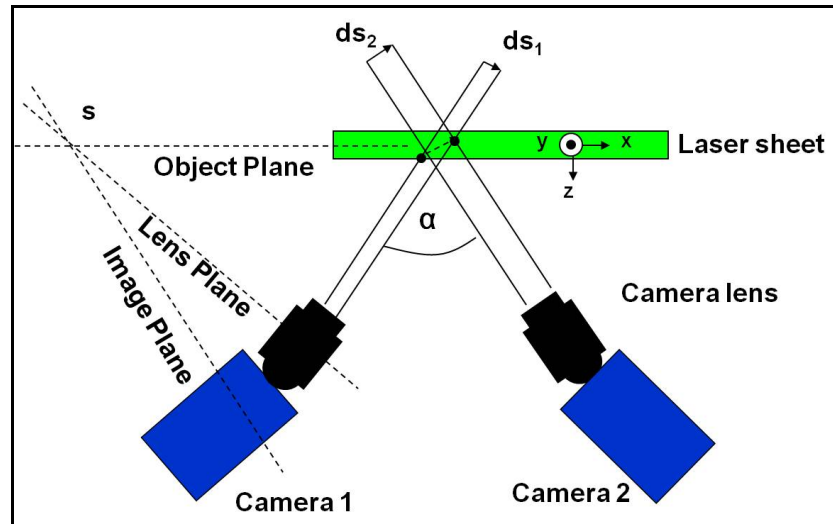


Figure 3-15 Camera arrangement for a Stereo PIV setup (backward-forward configuration)

Depending on the optical access to the area of interest, there are different arrangements for the cameras in a stereoscopic system. In the backward-forward arrangement, both cameras are on the same side of the laser sheet (Figure 3-15). Given the dependence of the light scattered by a particle on the viewing angle (Figure 3-1), there will be a significant difference between the light recorded by each camera (typically a factor of 10 for a backward-forward configuration). In order to ensure both cameras record similar light intensity levels, the camera recording in the backward position will require a larger lens aperture. Alternatively, both cameras can be positioned on different sides of the laser sheet either in a backward-backward or in a forward-forward configuration (see Figure 6-19 for an example of a forward-forward configuration). Although the backward-forward configuration is easier to calibrate (LaVision 2007), having the cameras in different sides of the laser sheet has the advantage that similar intensity levels will be obtained and therefore the same lens aperture can be used in both cameras. This is particularly useful in systems where it is required to have the same lens aperture in both cameras to ensure the same depth of field is obtained or when there is insufficient light intensity in the backward angles for a sufficiently high signal to

noise ratio of the particle images recorded. The advantages of a forward-forward configuration for certain applications are described in more detail in Section 6.6.1.

Given the cameras are positioned at an angle relative to the laser light sheet, only a part of the camera sensor is in focus. Due to oblique viewing, it is required to tilt the camera so that the sensor is covered by the tilted focal plane and all areas of the image plane are in focus. These conditions are usually met by arranging the imaging optics so that they comply with the Scheimpflug criterion using positioning adapters which are placed between the camera mount and the imaging lens (Prasad and Jensen 1995).

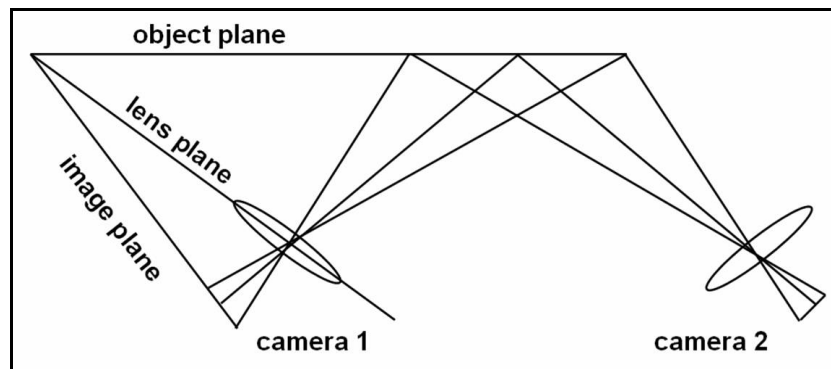


Figure 3-16 Scheimpflug criterion

Figure 3-16 shows the arrangement of the Scheimpflug criterion for which the image plane, the lens plane and the object plane for each camera have to intersect at a common point. The disadvantage of this arrangement is the introduction of a strong perspective distortion which requires additional calibration (LaVision 2007).

Reconstruction algorithms in stereo PIV use two 2D2-component (2C) vector fields (recorded by each camera) to be then combined to create a 2D3-component (3C) vector field; different reconstruction procedures have been summarised by (Prasad 2000a) and (Calluau and David 2004). After the computation of two 2C vector maps the displacement vectors are mapped (dewarped) from the image plane to the measurement plane using different mapping functions such as camera pinhole (Wieneke 2005) and other approaches such as the polynomial of 3rd order (LaVision 2007).

DaVis 7.2 employs an algorithm in which image dewarping and correction are applied on each step of the 2D vector multi-pass calibration scheme (this algorithm

is used throughout this thesis for vector calculation). The 3-dimensional (3D) reconstruction is then performed by solving 4 linear equations to calculate (u, v, w) from the 2C vector fields measured from each camera ($u1_{mes}, v1_{mes}$ and $u2_{mes}, v2_{mes}$). More details on the image reconstruction employed in DaVis 7.2 are available in the literature (Wieneke 2005) (LaVision 2007). Figure 3-17 shows an example of the combination of 2 2D2C vector fields to obtain a 2D3C vector field. Images from an acoustically-excited vortex ring generator have been taken with two cameras positioned in a forward-forward arrangement using the image reconstruction algorithm is DaVis 7.2. Images were taken using the same laser and imaging setup later used for the stereo multi-phase measurements described in Section 6.6.1.

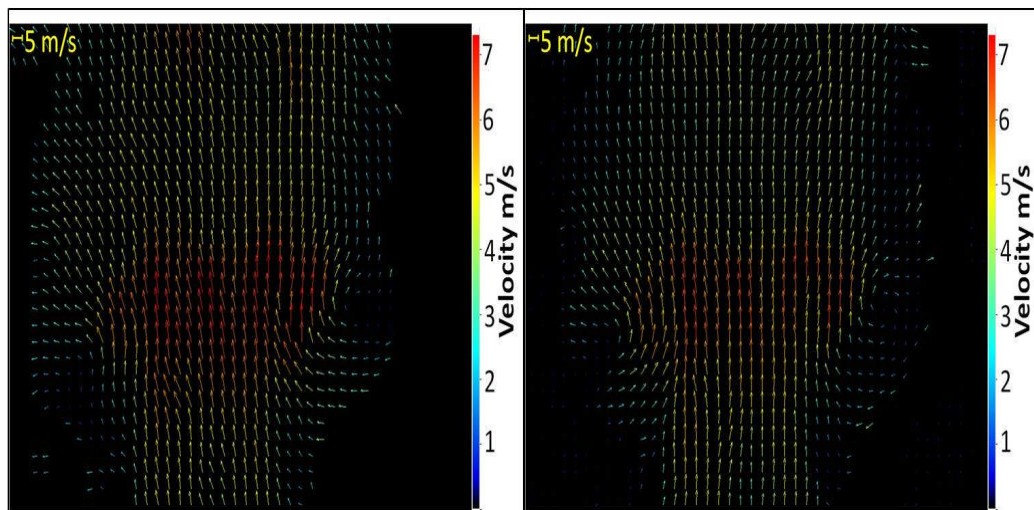


Figure 3-17 2C vector fields recorded from two cameras in a forward-forward Stereo PIV setup. The data for this figure were obtained by the author at the University of Leeds.

Figure 3-18 shows the combination of the two 2D2C vector fields in Figure 3-17 to produce a 3C vector field. The vectors indicate the conventional in-plane vector field and the out of plane velocity is shown as the background colour of the image with the corresponding velocity scale on the left hand side of the image. Red background indicates positive out of plane velocity and blue background indicates negative out of plane velocity. A toroidal vortex structure is observed with a change in sign of the out of plane velocity clearly shown in the centre of the vector field with the upper part (red background) coming out towards the camera.

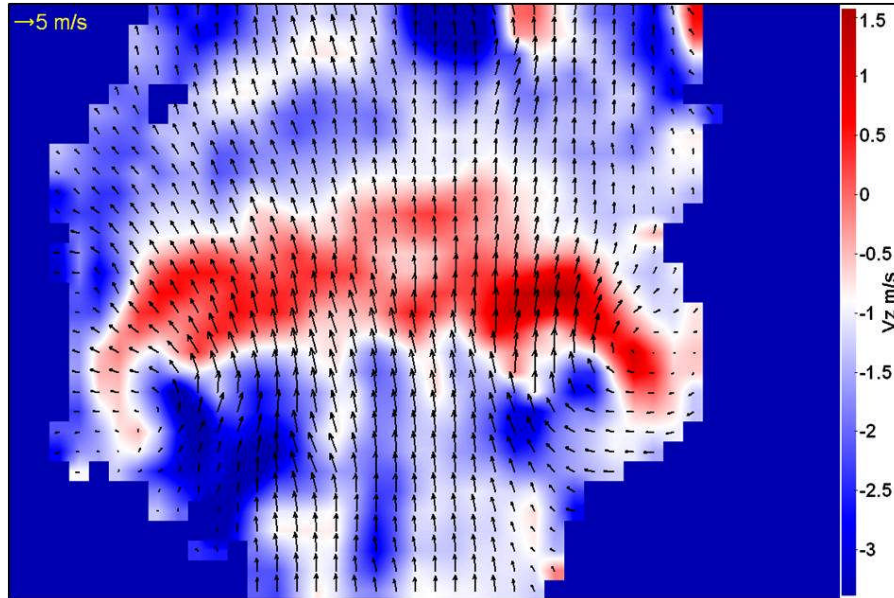


Figure 3-18 3C velocity fields obtained after combining 2 2C vectors fields shown in Figure 3-17. The out of plane velocity is shown in the background and side colour bar. The data for this figure were obtained by the author at the University of Leeds.

3.4.7.1. *Errors in Stereo PIV measurements*

Each of the 2C vector fields calculated by each camera contains the sources of error in standard 2C PIV including correlation noise, bias and peak locking. For the combined 2D3C image, various authors have discussed the different sources of error and their effect on the accuracy of the entire system e.g. (van Doorne and Westerweel 2007) and (Prasad 2000b). To balance the in-plane and out-of-plane error, it is desirable to have an angle between the cameras (α) of 90 degrees, however, the larger the angle the greater the non-uniformity in the magnification particularly in the x direction which leads to larger errors. A compromise is therefore required for adequate image quality and measurement accuracy with (Lawson and Wu 1997) suggesting a range of $20^\circ - 30^\circ$ (half angle, hence $\alpha = 40^\circ - 60^\circ$ in Figure 3-15).

Registration error has also been studied as a source of error which occurs when there is a mismatch between the two dewarped vector fields after they are projected back to the object plane. The main experimental variable controlling registration error is a misalignment between the laser and the calibration plate hence careful alignment is required when setting up the experiment. Whilst this error can be minimised, it is not possible to eliminate it completely (Prasad 2000b).

Stereo PIV setups become more sensitive to registration errors for very large and very small camera angles (Lawson and Wu 1997).

DaVis 7.2 provides an estimation of the stereo measurement accuracy in the form of a reconstruction error (LaVision 2007). Once the 3C velocity vector (u, v, w) has been calculated, it can be used to calculate the components $u1_{cal}, v1_{cal}$ and $u2_{cal}, v2_{cal}$ (two 2C vectors) and their deviation from the measured $u1_{mes}, v1_{mes}$ and $u2_{mes}, v2_{mes}$ (vectors originally calculated from the images in each camera) and thereby calculate the stereo reconstruction error. The reconstruction error can be calculated from each interrogation region and an error map created for the whole field of view as illustrated by (Voges et al. 2010) for their stereo measurements in a compressor rotor.

3.4.8. Other related PIV techniques

Since the origins of PIV related techniques have been developed simultaneously to extend its application to different fields. These mainly concern 3D measurements, volumetric measurements (3D3C velocities) and measurements at microscopic scales. A brief introduction to some of the most commonly used PIV-related techniques is presented next. More information on microscopic PIV measurements can be found in (Williams et al. 2010) and 3D measurements are reviewed in (Hinsch 1995), (Elsinga et al. 2006) and more recently in (Arroyo and Hinsch 2008).

3.4.8.1. Particle tracking velocimetry (PTV)

Different modes of pulsed-light velocimetry were defined in Section 3.3.2 in terms of image density. For low seeding density, individual particle pairs can be identified by visual inspection and it is referred to as Particle tracking velocimetry. Some applications require the individual tracking of particles either because the full motion of each particle needs to be characterised (biological applications), the out of plane velocity component is extracted from the processing of individual particle images (defocusing techniques) or because low seeding density is present due to experimental conditions which makes the use of statistical methods unfeasible (e.g. dispersed phase in multi phase flows as explained in Section 3.5).

The main advantages of PTV over PIV include a higher spatial resolution (in principle) since a velocity vector is calculated for each particle (no averaging effects) and the velocity processing is less computationally expensive than the statistical correlation process used in PIV. On the other hand, the main disadvantages of PTV are firstly its propensity to involve mismatched vectors in the velocity data due to particle overlap or fragmented particles and, secondly, the impossibility of calculating differential and integral values (such as vorticity) directly from instantaneous vector fields since the velocity vectors are randomly distributed (Ido and Murai 2006). Differential and integral values can still be calculated from averaged vector fields provided that flow characteristics do not change over a short time. As a result, research on PTV has focused on overcoming these limitations (Ido and Murai 2006) and on the use of 3D PTV as initially proposed by (Chang et al. 1984) and later followed by (Nishino et al. 1989) amongst others. This has led to newer approaches being developed including 3D scanning (Hoyer et al. 2005). PTV algorithms have also been used for dispersed phase processing in multi-phase PIV as described in Section 3.5.1.

3.4.8.2. *Microscopic scale PIV (Micro PIV)*

Micro PIV systems are intended to measure velocity fields of particle seeded flows with micron-scale spatial resolution using PIV techniques. The light source is usually a double pulsed or continuous wave laser which illuminates the flow seeded with fluorescent tracers (LaVision 2010). Micro PIV was first reported by (Santiago et al. 1998) where an epi-fluorescent microscope and an intensified CCD camera were used to record 100-300nm polystyrene seeding particles. Micro PIV has been widely used in different microfluidic devices by, amongst others, (Meinhart et al. 1999), (Sugii and et al. 2000) (Kim and Kihm 2004), and a review of the current advances and techniques for microfluidic devices has been compiled by (Williams et al. 2010). Similarly to macroscopic PIV, stereo measurements have been obtained by using two imaging cameras in the same epi-fluorescence setup (Lindken et al. 2006).

The main difference between the macroscopic and microscopic version of PIV is the size of the imaged tracers. Given the tracers are typically sub-micron and enclosed in narrow flow channels the illumination tends to scatter from the channel with greater intensity than that from the tracers. This problem is usually overcome

with the use of fluorescently labelled tracers and optical filters to separate the illuminating light from the light recorded in the CCD camera. As a consequence of the small tracer particles sizes, the effects of Brownian motion need to be considered as reviewed by (Olsen and Adrian 2000). Advanced simulations have been developed to predict errors in micro PIV measurements due to Brownian motion (Olsen and Bourdon 2007). Given the restricted optical access and diffraction effects in laser sheet forming optics, volume illumination is used and its effects have been reviewed by (Meinhart and et al. 2000).

3.4.8.3. *Holographic PIV*

Holographic recording of particles seeding in fluids has long been used since the 80's in full-field velocity measurements. It has found increasing applications given the phase and the amplitude of the light scattered by the particles are stored and can be then used to locate the positions of the particles at two or more instants in time (Barnhart et al. 2000). Holography was also used during the early stages of PIV development to remove the ambiguity obtained with the initial auto-correlation algorithms (Coupland et al. 1987).

In conventional Holographic PIV the entire flow field is illuminated with a suitably sized laser beam and the light scattered by the particles is recorded on a holographic recording medium (usually a photographic plate) after a reference wave is superimposed. After the interference pattern (hologram) has been developed, it can be illuminated by the same reference beam to create a virtual image of the particle field. A real image of the particle field can also be obtained by illuminating the hologram with the complex conjugate of the reference beam. Once the particle field image has been reconstructed, particle positions need to be extracted to estimate the velocity; several studies have focused on the extraction of velocity information and the aberrations of the imaging system given that the reconstructed particle field needs to be a faithful replica of the original. A detailed review of HPIV has been presented by (Hinsch 2002) where the different issues related to the technique are discussed including stereoscopic evaluation of particle positions.

3.4.8.4. *Tomographic PIV (Tomo PIV)*

Tomographic PIV was initially proposed by (Elsinga et al. 2006) and has undergone considerable development in recent years. In this technique, optical tomography is used to reconstruct the 3D particle light distribution from 2D images taken from 3 or 4 viewing directions simultaneously (optimal performance has been reported with 5 cameras). The experimental setup for the cameras requires a small lens aperture (to ensure the entire volume is focused) and for the cameras to be arranged in a Scheimpflug configuration (Figure 3-16). The intensity recorded by each pixel on the image represents a particle's intensity integrated along the pixels line of sight through the volume. The tomographic reconstruction is performed using the MART algorithm (Multiplicative Algebraic Reconstruction Technique), which is an iterative process where a multiplicative correction is applied to individual voxel intensities until it matches the intensities of the pixels that intercept at that voxel or in the neighbourhood of lines of sight. Other methods have been proposed in which the processing time is significantly reduced (Atkinson and Soria 2009).

The reconstructed tomogram pair is then analysed by means of 3D cross-correlation with an iterative multi-grid volume deformation technique, returning the three-component velocity vector distribution over the measurement volume. The largest source of error in the technique is the appearance of ghost particles i.e. when a larger number of particles are formed compared to those actually presented in the illuminated volume leading to reconstruction noise and therefore velocity uncertainties (Elsinga et al. 2006). The need for different viewing direction cameras restricts the application of the technique to flows with large optical access; furthermore the processing of the images is time consuming. Nevertheless, the technique has been increasingly used for 3D measurements.

3.4.9. Use of fluorescent tracers in PIV

Fluorescent tracers (Section 3.1.2) can be used as an alternative to elastic Mie scattering in PIV experiments. Seeding tracers can be mixed with a dye which absorbs laser light to then emit at a different wavelength (colour). This makes it possible to separate the tracer particles from other scattering objects such as walls, bubbles, droplets and other particles by using an optical filter to block the incident light (Tropea et al. 2007). Unlike Mie scattering (Figure 3-1), fluorescent

light emission is isotropic hence there is no dependence of fluorescent intensity on viewing angle. Fluorescent intensity is dependent on dye concentration and the particle diameter cubed whereas Mie scattering is proportional to the particle diameter squared and the viewing angle. Fluorescent tracers have been used for micro PIV experiments by different authors including (Meinhart et al. 1999) and (Shinohara and et al. 2004). The use of fluorescent tracers for multi-phase macroscopic PIV will be discussed in detail in Section 3.5 and Chapters 5, 6 and 7 and for flare removal applications in Section 3.7 and Chapter 4.

3.5. PIV in multi-phase flows

One of the most challenging areas in the development of PIV is the quantification of multi-phase/constituent flows (Hassan 1998). When conventional PIV is applied to multi-phase/constituent flows, images are obtained from the tracer particles in both constituents or phases and a vector field can be calculated. However, conventional PIV does not allow quantification and separation of the flow field for each component and parameters providing important information such as relative velocity and mixing cannot be quantified. Several approaches have been reported for the separation of the phases and a review of the most common approaches is presented here.

The approaches used in multi-phase flow PIV can be broadly divided into two main categories according to when the phases are discriminated. In the first category particles are discriminated when the images are recorded by means of fluorescent tracers, optical filters and multi-camera arrangements. The second category includes image separation by means of image post processing once the images for both phases have been acquired on the same frame; phases are discriminated by size, brightness and correlation peak properties.

3.5.1. Phase separation by image post processing

Phase separation by image post processing relies on a difference on the size of the particles in each phase which will produce a difference in the scattering properties on both phases. Phases can then be separated based on image size, light scattered by the particles or a combination of both. This can be applied in a

number of two-phase flows where one phase is naturally present as bubbles or solid particles (the dispersed phase, $\sim 100\mu\text{m}$) and the particles in the continuous phase are considerably smaller, $\sim 20\mu\text{m}$ for fluid flows and $\sim 1\mu\text{m}$ for gas flows. Some of the literature published adapting this approach is briefly discussed below.

One of the first experiments was presented by (Jakobsen et al. 1996) who performed simultaneous two-phase PIV measurements to study pneumatic conveyance of a solid phase. The solid phase consisted of particles with a diameter $50\text{-}200\mu\text{m}$ and the continuous phase (air) was seeded with $1\text{-}2\mu\text{m}$ droplets. Images from both phases were acquired on the same frame and image processing based on particle image size was used to separate the phases. Dispersed particles were removed from the frame and a new image was created with them; each phase was then processed using conventional PIV and PTV methods. The separation algorithm relied on the fact that the dispersed particles, due to their size, will scatter more light and their images will be bigger than those of the air tracers. Given that particle image size is dominated by the point spread function (see Section 3.4.3) for the air tracers, it is required for the dispersed particle images to be larger than the diameter of the point spread function. Laser energy and camera settings were adjusted to obtain a sufficiently high signal to noise ratio in the gas phase but this produced image saturation in the dispersed phase due to particle size differences. Background levels were increased (requiring some contrast enhancement) producing crosstalk between the phases and light re-scattering. The density of the dispersed phase was limited to reduce the effects of image saturation.

Kiger and Pan performed simultaneous measurements on a dilute two-phase flow in a water channel. Water was seeded with $15\mu\text{m}$ silver-coated glass spheres and particles of different sizes (45 to $360\mu\text{m}$) were used as the dispersed phase. Images for both phases were recorded on a single camera with 532nm illumination and a median filter (non-linear image processing) was then used to separate the phases. The median filter had been previously used in other applications to reduce image noise, hence the small tracers were considered as noise scattered over a uniform background for phase separation; it was found that a particle size ratio of ~ 5 was required for reliable processing (Kiger and Pan 2000). Subsequently, (Deen et al. 2002) showed that this median filter works well with synthetic PIV images where particles can be identified as single, solid entities. For real

experimental images in bubbly flows (where bubbles can have complex shapes and scattering patterns) the filter did not perform as well because the images were not continuous single entities and the separation was not successful.

Khalitov and Longmire performed PIV measurements on a fully-developed channel flow of air. Glycerine droplets ($1\mu\text{m}$) were used as tracers for the continuous phase and glass beads (53 to $75\mu\text{m}$) were added to the flow as the dispersed phase with particle images recorded simultaneously in the same frame. Image saturation was again obtained in the dispersed phase and the noise levels were increased due to 'coronas' (Hassan et al. 1992) around the dispersed particles. An algorithm employing second order gradients separated the images according to their size, brightness and centroid creating separate images for each phase. The dispersed phase velocity was calculated using PTV algorithms and the continuous phase velocity was calculated using conventional PIV processing. Whilst the separation algorithm worked well for solid dispersed particles, when bubbles were used as the dispersed phase there was crosstalk from the bubbles in the continuous phase images. The technique was again restricted to low dispersed phase particle densities and could not be applied close to walls due to higher RMS velocities and gradients (Khalitov and Longmire 2002). Cheng et al., continued the work started by Khalitov and Longmire in order to achieve separation of particles of similar size and also tried to reduce the effect of the noisy background levels previously obtained. PIV images were taken of a particle-laden jet; water was seeded with hollow glass spheres (8 - $12\mu\text{m}$) and aluminium oxide spheres ($150\mu\text{m}$) were used as the dispersed phase. Improved algorithms including intensity variation and a local minimum filter were used for phase separation and a FFT filter was used to filter background noise. The dispersed and continuous phases were processed with PTV and PIV algorithms respectively. A physical size ratio (dispersed phase size/continuous phase size) of 12 - 19 was obtained with a corresponding particle image size ratio of 3 - 6 (due to diffraction limited optics) which was an improvement over previous work (Cheng et al. 2010).

Muste et al., performed PIV measurements on a turbulent open-channel carrying dilute particle suspensions. Nylon spheres were used as water tracers ($20\mu\text{m}$) and the dispersed phase were 210 - $250\mu\text{m}$ sand particles. Images from both phases were separated using a similar algorithm to that of (Khalitov and Longmire 2002); after some image pre-processing was performed the phases were separated

based on their size and brightness level. Phase separation was aided by the difference in size of the two phases: dispersed particles ~10 times bigger than continuous phase tracer particles (Muste et al. 2009).

A similar approach consists of superimposing a digital mask on the image according to particle intensity. Gui et al., used such a technique to separate the phases in PIV measurements of the flow around systems of bubbles rising in water (similar to bubble column reactors); the mask is defined as a threshold based on particle size. The approach was tested in bubbly and solid dispersed particle flows where a mask was superimposed in the image which discriminated the dispersed particles based on their intensity. The technique required a substantial difference between the sizes of the two phases to obtain successful separation (Gui et al. 1997).

More recently (Zhang et al. 2008) used a similar masking technique to analyse two-phase flows in sand and wind-blown sands. Olive oil droplets with a mean size of $3\mu\text{m}$ were used as air tracers and sand grains ($100\text{-}125\mu\text{m}$) were added in a wind tunnel flow. Images were recorded simultaneously using 532nm illumination on the same image. Phases were then separated using a digital mask which removed the sand grain from the images and then filled the empty spaces with average background intensity. The dispersed images were processed using PTV and the continuous phase using PIV.

For the approaches described above, when a separate image is created with the dispersed particles, the empty spaces in the original frame are filled with an estimation of the local background; this might lead to an evaluation error in the interface of the two phases. A different approach uses shadowgraphy to produce shadows of the big dispersed particles with a different intensity range of that of the background and the continuous phase tracer particles.

Nishino et al., used shadowgraphy to obtain velocity measurements of dispersed particles in two-phase flows. Silhouetted particle images were acquired and an algorithm which detected both spherical and non-spherical particles was implemented. The accuracy of the particle detection algorithm was reported as $\pm 4\mu\text{m}$ for particles $10\text{-}50\mu\text{m}$ in diameter. The velocity of the particles was then calculated using PTV; the velocity of the particles in the continuous phase is not

calculated (Nishino et al. 2000). Tokuhiro et al., used two cameras side by side to combine shadowgraphy measurements and PIV measurements (Tokuhiro et al. 1998).

Lindken et al., combined the shadowgraphy technique with a digital mask for PIV measurements on the study of pseudo-turbulence in two-phase bubbly flows. The gas bubbles were imaged using shadow imaging; pulsed LED illumination was used for back illuminating the bubbles (producing shadows) and fluorescent tracers under 532nm illumination were added to the flow. A filter was placed in front of the camera to block Mie scattering allowing the fluorescence through. Given the dispersed phase images were shadows, there were no empty spaces in the image and a background higher than most PIV experiments was obtained. For this method, the signals of the two phases do not disturb each other. Dispersed objects up to 5m/s can be recorded without blur due to the LED illumination which does not produce pulses as short as those produced by a laser (Lindken et al. 2002).

Another method proposed relies on considerable differences in the motion of the two phases to discriminate them; this is carried out during the correlation process by identifying the two dominant correlation peaks: one representing the motion of the tracers and the other the motion of the dispersed phase. Delnoij et al., and Deen et al., applied ensemble correlation PIV to two-phase bubbly flows. In ensemble PIV the correlation of subsequent recordings is added up; if the flow characteristics do not change over a short time the peaks should then also add up. For two-phase PIV both phases were recorded on the same image and after applying ensemble PIV two peaks were obtained one for each phase. The limitation of this method is that instantaneous velocity and flow interaction information cannot be obtained and a difference in phase velocity is required for successful separation (Delnoij et al. 1999) (Deen et al. 2002).

3.5.2. Phase separation by optical arrangement

The methods presented in the previous section rely mostly on differences in size and velocity of the phases; a careful selection of particles, laser energy and imaging setup is required for the recording of images from both phases in the same frame. Although this is feasible for some applications, there are some multi-phase flows where mixing is important and the phases will have similarly sized

particles and velocities. In the case of sprays injected into the gas phase the particle size range of the droplets may extend from the sub-micron to 10's of microns and therefore overlaps the micron sized particles typically added to the gas phase (Melling 1997). Optically active tracers, normally producing a fluorescent or phosphorescent emission (Section 3.1.2) over a range of wavelengths different from that of the illuminating laser beam, provide a means of identifying the origin of a particular tracer particle. Fluorescent tracers were originally used by (Gharib et al. 1985) to determine flow direction from phosphorescent images. For multi-phase flow measurements, fluorescent tracers are used in one or the two phases and a pair of cameras are placed typically 180° opposite each other. The tracers emit light at a different wavelength of that used for illumination and, using optical filters, only the fluorescence emitted by the tracers is recorded. The light scattered by the particles in the dispersed phase (usually elastic scattering) is recorded on another CCD camera. Some of the published literature using this approach is discussed below.

Bröder and Sommerfeld analysed bubble behaviour and interaction in a bubble column. Rhodamine 6G tracers were added to the continuous phase (mean diameter 50µm) under 532nm illumination for emission at 585nm. A two-camera system recorded fluorescence and scattering from the particles separately. The cameras were placed at different angles (80° and 105°) to provide greater control of the scattering intensity of the phases by controlling the intensity of the scattering modes; at 105° the light intensity of the reflected beams in the bubbles is low. Phase separation was obtained by a combination of geometrical and optical means. There were problems because the light emitted by the tracers was reflected or refracted again by the bubbles (Bröder and Sommerfeld 2002).

Kosiwczuk et al., used fluorescent tracers for both phases and a two-camera system; optical filters were placed in front of each camera to prevent Mie scattering from being recorded. The dyes used were Stilbene 420 and Rhodamine 610 with 355nm illumination. The liquid phase was produced using an ultrasonic atomiser resulting in droplets in the 30-40µm range and the gas phase was seeded with particles in the 1-5µm range. Given the cubic dependence of fluorescent intensity on diameter (Le Gal et al. 1999), it is feasible that the images obtained from the gas phase tracers are dominated by the particles at the high end of the diameter range (Kosiwczuk et al. 2005).

Towers et al., proposed a colour two-phase system using rhodamine-doped droplets and conventional tracers illuminated with a first pulse at 532 nm and a second from a pulsed dye laser at ~640nm. Images were obtained on two monochrome cameras with filters such that one camera only imaged the 2nd pulse and fluorescence emission with the other recording the first pulse Mie scattering. The efficiency of the dyes prevented fluorescent droplets of $<5 \mu\text{m}$ from being imaged and the use of 532nm light as both fluorescence pump, requiring high energy $>100\text{mJ}$, and for Mie imaging, which only requires low energy 1-3mJ, created an inefficient optical system requiring dense filters to be used that generated image distortions (Towers et al. 1999).

Tóth et al., performed two-phase PIV measurements to characterise the airflow in presence of liquid droplets. A two-camera system was used with simultaneous 532 and 266 nm illumination from the same laser cavity. Two fluorescent dyes matching these wavelengths were selected (Rhodamine B and Butyl PDB). Given its relatively low fluorescence efficiency butyl was used in the dispersed phase (30 to $245\mu\text{m}$). No extra image processing was used to separate the images (Tóth et al. 2009).

All the gas phase multi-constituent and multi-phase flow work reported depends on image processing algorithms to separate the flow constituent information from the two cameras. Therefore, sub-pixel registration is important to increase the reliability of processing, but is experimentally difficult, owing to the different distortions introduced by the filters used on each camera. Furthermore, constituent discrimination errors are introduced when particle images from the two constituents overlap. The measurement of 3-component velocities (via stereoscopic arrangements) in a two constituent/phase flow using multi-camera setups for each view has not been attempted owing to the experimental complexity of the system.

Multi-phase flow measurements have been performed in GDI air/fuel systems using some of the approaches described above and will be discussed in Section 3.6.2.

3.6. Optical diagnostics in GDI air/fuel systems

There has been continuous and extensive research work on different aspects of GDI engines during the last 15 years. Work has been produced on different areas such as combustion strategies, combustion chamber design, combustion modelling and direct flow measurements as presented in Chapter 2. In order to produce improved GDI designs, insights into the in-cylinder processes are desirable and can be obtained through optical diagnostics. A review of the optical diagnostic techniques to be used in the following chapters to measure flow velocity and spray characteristics is to be presented here. For a more detailed summary of other optical techniques to measure vaporisation, mixing, combustion and pollutant formation and the use of Laser Induced Fluorescence and Raman scattering in GDI measurements the interested reader is referred to (Hentschel et al. 1999), (Hentschel 2000), (Solomon et al. 2000), (Hentschel 2002) and (Fansler and Drake 2006).

The most common approach for optical diagnostics in GDI engines is the use of engines/cylinders with optical access normally obtained with the use of quartz glass windows in a hollow piston and the use of full fused-silica barrels. Section 6.1 describes the use of a glass silica barrel for PIV and spray structure measurements.

One aspect which needs to be considered for GDI optical diagnostics is that fuel sprays are usually very dense. Consequently, clear particle images cannot be obtained under certain spray conditions and sometimes speckle patterns are formed due to particle overlap. The single scattering approximation is not valid in high density areas within the spray where some photons are scattered more than once, a situation usually referred to as multiple scattering. Other sources of error which can be obtained with dense sprays are laser light extinction (laser intensity reduction along its line of propagation) and signal attenuation (reduction of the signal between the laser sheet and the camera). Different approaches have been proposed to compensate for these errors including the use of bidirectional illumination and data post processing algorithms (Sick and Stojkovic 2001). Given the more complex nature behind multiple scattering, very few experimental approaches have been proposed to counter its effects. Berrocal et al., proposed the use of structured illumination to suppress multiple scattering; a laser sheet is

spatially modulated along the vertical direction and, through phase modulation shifting and post processing of successive recorded images, the effects of multiple scattering were mitigated (Berrocal et al. 2008).

3.6.1. Use of Mie imaging for GDI injector characterisation

Spray structure characteristics can be studied stroboscopically with high temporal resolution using a light source and the light scattered by the particles (Hentschel 2002). The light source (usually a laser but others such as xenon flash lamps are also used) is orientated along the central cross section of the spray and, given the current capabilities of laser systems, a strong signal is obtained. Different authors have used this technique to study GDI spray structure and identify the effects of parameters such as injection pressure and ambient pressure on important injector parameters such as cone angle and penetration rate which, as described in Chapter 2, are paramount for the design of new GDI injectors. In some cases, the cameras used for imaging can also be used to record PIV data hence imaging has also been used in conjunction with PIV, LIF and LDA. Some of the published papers on Mie scattering for GDI spray imaging are briefly summarised below.

Davy et al., al used Mie scattered images to analyse the temporal and spatial development of a high pressure swirling spray. A copper-vapour laser was used and the effect of parameters, such as injection pressure and air/fuel timing, on the spray structure was studied (Davy et al. 1998).

Wagner et al., used two-dimensional Mie and LIF to investigate spray propagation in a GDI swirl injector. An Nd:YAG laser was used for illumination and Mie scattered images were used to study spray propagation inside the engine. LIF was then used to study cyclic fluctuation in the fuel vapour distribution (Wagner et al. 1999).

Choi et al., combined Mie scattering imaging and Phase Doppler Anemometry (PDA) to obtain the structure and the velocity of the spray droplets. A wind tunnel was used to produce crossflows around the injector to model the in-cylinder flow when fuel is injected late during the compression stroke (Section 2.2.5). The effect of injection pressure and crossflow velocity on spray penetration was analysed and a PDA system was then used to measure droplet size and velocity (Choi et al.

2000). Hargrave et al., also used Mie scattering imaging and PDA to analyse the full field structure of GDI injectors. This work demonstrated that the full field Mie imaging and the single point PDA techniques are complimentary for analysis of the flow in GDI injectors (Hargrave et al. 2000).

High-speed imaging of GDI sprays has also been reported; (Towers and Towers 2008) reported high speed imaging of the spray from a single hole injector in an optical engine running at 2000rpm. Images were obtained over many engine cycles and spatial probability density functions evaluated to identify regions where the spray was always present and the regions where the spray varied from cycle to cycle.

Different light sources have been used for stroboscopic measurements to create shadow images in a similar way used for multi-phase measurements in Section 3.5.1. Gold et al., used LIF measurements along with shadowgraphic spray imaging to analyse air/fuel mixing in homogeneous charge conditions; a triggered halogen lamp was used for illumination. The effects of intake air and injection timing during homogeneous charge injection were analysed (Gold et al. 2001).

Similarly, (Pitcher et al. 2004) used backlit imaging to study the effect of variable valve trains (controlling the fresh inlet charge into the cylinder) on the fuel flow for a GDI swirl spray. A xenon flash lamp was coupled with a fibre optic cable to provide diffuse light intensity distribution. LDA measurements were also taken inside the combustion chamber under conditions of early inlet valve closing and late inlet valve opening.

Single-hole injectors have encountered problems when injected during the compression stroke in stratified operation (Section 2.2.6.3); consequently more recent studies have focused on multi-hole injectors. Kim et al., studied the effect of injector timing, in-cylinder air charge motion, coolant temperature and injection pressure on the flow of a high pressure multi-hole injector. Mie scattering images were acquired using a xenon flash lamp directed with optical fibres to the imaging area (Kim et al. 2007). Mitroglou et al., analysed the spray structure of two multi-hole injectors (11 and 6 holes) as a function of injection and chamber pressures. LDA was used to measure droplet velocities and spray visualisation was performed with a flash lamp (Mitroglou et al. 2007).

Laser sheet visualisation is used in Section 6.3.1. to characterise the spray structure of a multi-hole GDI injector and obtain penetration rate and cone angle.

3.6.2. Use of PIV for flow analysis

As an established full-field technique, PIV has been used extensively for internal combustion engine research. Several studies have been published analysing the air flow structures within the combustion chamber. Numerous papers have been published for the studies of air structures in conventional PFI engines; given this literature review is focused in PIV studies for GDI engines, the interested reader is referred to (Reuss 1993) and (Reeves et al. 1996) for some of the early PIV studies in PFI engines and (Li et al. 2002a) and (Li et al. 2002b) for more recent studies of in-cylinder flows.

For GDI engines, PIV has been used to measure in-cylinder flows, spray structures and, given this research project is mainly concerned with multi-phase flow interaction, special attention should be on PIV measurements of the fuel/air interaction.

Some of published literature using PIV to study in-cylinder flow include (Towers and Towers 2004) who analysed cyclic variation within an optical engine modelling a GDI chamber using high speed PIV. Kubo et al., measured the spray structures in GDI swirl nozzles using PIV to measure the spray velocity distribution to validate numerical predictions (Kubo et al. 2003). Sick et al., presented a comprehensive summary of the different high-speed diagnostics in GDI engines including PIV measurements on and Micro-PIV measurements of vertical structures in the boundary layer at cylinder heads (Sick et al. 2010)

Measuring air entrainment induced by the fuel flow is vital for GDI development as it enables the characterisation of processes such as fuel propagation, vaporisation and air/fuel mixing. Some of the strategies presented in Section 3.5.2 for two-phase measurements have been applied to measure air and fuel in GDI injectors with the use of fluorescent tracers for the gas phase.

Boedec and Simoens used a combination of PIV, LIF and Mie scattering to study spray discharge in the gas phase inside a cylinder. Two Nd:YAG lasers and two

cameras were used to record each phase separately. The air phase was tagged with Rhodamine 6G dye (emits at 575nm) and naturally occurring atomised droplets from the spray were used as tracers. One filter was placed in front of one of the cameras to block the Mie scattering and only record the fluorescence. The other camera recorded Mie scattering from both tracers and the fluorescence from the gas phase tracers. The PIV processing gave poor validation rates probably due to the two sets of particle images with different displacements on one of the cameras (Boedec and Simoens 2001).

Rottenkolber et al., used fluorescent tracers to study the interaction of fuel and air from a GDI injector. DCM tracers were used to seed the gas phase (diameter $<3\mu\text{m}$) under 532nm illumination and both phases were recorded on the same image. Filters were used to adjust the scattering levels in the fuel and the phases were separated using a mask and a peak separation technique. The peak separation technique required a high velocity difference between the two phases for successful separation. The mask technique overestimated the air velocities in areas where too many spray droplets were found (Rottenkolber et al. 2002).

Driscoll et al., performed simultaneous air/fuel phase measurements in a dense fuel spray. A two-camera system was used with a different laser used to illuminate each phase. Stilbene 3 was used for the air phase but the particle size of the tracers was not specified. A different pulse separation was used in each laser to account for the expected difference in velocity of the phases. A band pass filter and an interference filter were used to separate the emission from the Mie scattering; a small scattering signal from the fuel phase (due to its big particle size) was still obtained in the camera recording the air tracers; these particles did not correlate well (due to the large pulse separation for the air tracers). Hence the separation still required a difference in velocity to be completely successful (Driscoll et al. 2003).

Lee and Nishida measured the ambient air motion and the spray in a swirl-type GDI injector. A two-camera setup was used with 532nm illumination. Rhodamine B (emitting at 570nm) was used to seed the air tracers with relatively large particles (6-8 μm) used. A low transmittance filter was used in front of the camera to only transmit the scattering of the larger fuel particles hence the separation was also aided by droplet size (Lee and Nishida 2003).

Dankers et al., used DCM tracers to measure the fuel-spray interaction with the surrounding air. A single camera was used and the tracers were excited with 532nm illumination; gas phase and fuel phase images were recorded in separate experiments using a long pass filter to block Mie scattering when recording the gas phase and the pulse separation was adapted depending on which phase was being imaged. The air tracer droplet size was not reported (Dankers et al. 2008).

Even though measurements in both phases have been obtained using the approaches presented above, phases were not measured simultaneously (Dankers et al. 2008). Other approaches relied on a difference in phase velocity for successful separation (Rottenkolber et al. 2002) (Driscoll et al. 2003) or were aided by a difference in size of the tracers in each phase (Lee and Nishida 2003); this indicates the need for a priori information for phase separation. The multi-camera approaches presented provide simultaneous information but it is difficult to achieve pixel to pixel correspondence from the images recorded in each camera; additionally, the experimental setups implemented would make it difficult to obtain stereo measurements (due to the complexity of the system) hence it has not been attempted. The approaches presented in this section include similarly sized phases (as is the case for the flows measured in this thesis) for which simultaneous phase separation has not been achieved entirely satisfactorily.

To the best of the author's knowledge, no study has been published studying the interaction of air and fuel in a 'second generation' multi-hole injector in the form of full field multi-phase PIV measurements.

3.7. Flare

One of the major problems in experimental systems using laser illumination has been unwanted 'flare' in the recorded images. Flare is caused when the light used to illuminate the tracers also impinges on surfaces within the experimental setup. The light scattered from a solid surface is much more intense than that scattered from tracer particles producing overexposure in the recorded images leading to the loss of velocity information (Prasad 2000a). Moreover the local background intensity is increased near the intensity saturated regions reducing the signal to noise ratio of the tracer particles. Flare is particularly problematic in a number of

industrially-important applications such as turbomachinery and engine research. Figure 3-19 shows an example of flare obtained using 532nm illumination to image tracer particles flowing around a car valve. Large areas of overexposure are obtained and charge is leaked out to neighbouring areas of the CCD particularly at the bottom of the image. Particle images are lost and the flow interaction with the valve surface cannot be measured.

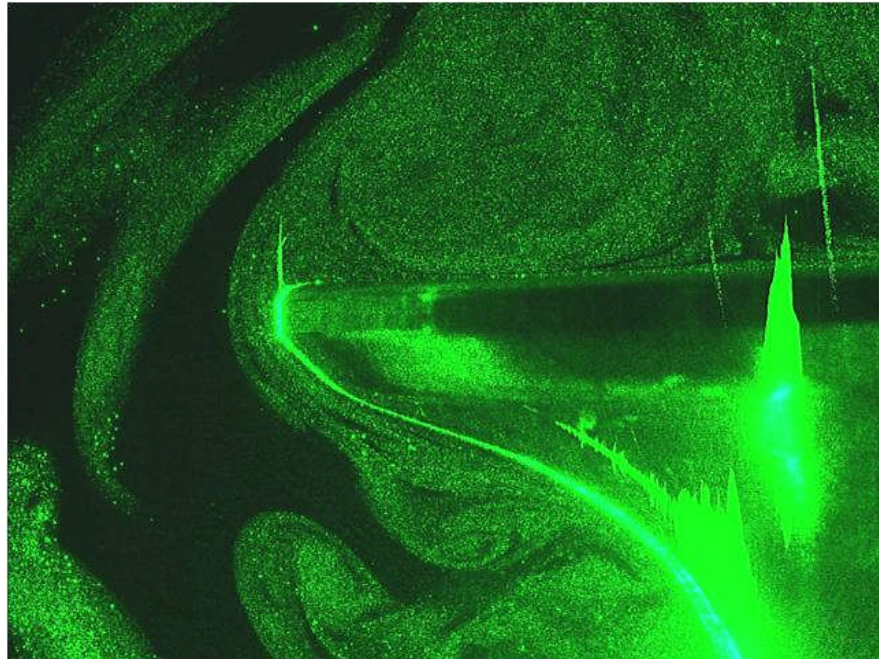


Figure 3-19 Flare obtained when illuminating the flow around a car valve using 532nm illumination. Image taken by the author and Matthew Orsmy at the University of Leeds

Different authors have encountered problems when using laser illumination and consequently various approaches have been taken to reduce the effects of flare.

Liu et al., and Yu and Liu performed stereo PIV measurements in axial compressors; their effective field of view for measurements in the blade passage was restricted due to strong flare light at the hub surface (Liu et al. 2006) (Yu and Liu 2007). Aleiferis et al., visualised cyclic variations of fuel droplet distribution in a spark ignition engine using laser sheet illumination. Strong background levels were obtained due to elastically scattered light from the walls of the combustion chamber; a correction procedure based on a PIV correlation algorithm was used to subtract the background from the particle images to increase their signal to noise ratio (Aleiferis et al. 2005).

Reeves et al., performed in-cylinder measurements in the tumble and swirl planes of a single cylinder engine. High levels of flare were obtained due to the close proximity of the laser sheet with the engine surfaces limiting the quality of the images obtained and contributing to data dropout. It was suggested to use larger particles, 4-10 μm , which would increase the scattering intensity. However, particle tracking capabilities would be compromised (Reeves et al. 1996).

Stansfield et al., performed in-cylinder PIV measurements in a Gasoline Direct Injection optical engine to analyse flow structures; when acquiring data for the intake flow field there were areas with missing vectors due to high laser flare from the cylinder head and valves. Tumble ratios (calculated using vector fields) were not obtained in the fields where the piston was visible due to flare from the piston window (Stansfield et al. 2007). Similarly, (Hentschel 2002) reported limitations in the field of view when measuring in-cylinder air flow due to strong reflections on the glass ring surface. Voges et al., used PIV to study the rotor blade casing interaction in a transonic compressor; the light sheet impinging on the moving blades of the rotor resulted in flare and overexposure over significant portions of the imaged area. Flare was reduced by shading the flare area with a piece of metal of similar size placed in front of the observation window (Voges et al. 2008). In a later study the same authors performed stereo measurements in a similar setup and found that flare from the casing also increased the stereo reconstruction error (Voges et al. 2010).

Arnott et al., performed PIV experiments inside a low speed wind tunnel over a wing model; matt black and self adhesive plastic foil were used to cover the wing surface reducing the effects of flare (Arnott et al. 2003). Wernet used PIV for velocity measurements on the blade passage region of a transonic axial compressor and the diffuser region of a high speed centrifugal compressor; care was taken when aligning the laser sheet to the blades and the diffuser was also painted black to reduce flare. Flare was still obtained leading to spurious vectors at the base of the blade, data dropout at the leading edge region and no measurements were obtained on the pressure side of the upper blade due to a combination of the viewing angle and flare from the surface (Wernet 2000). More recently, mirror-like paints containing optical absorbers have been reported for flare removal. Konrath et al., used PIV and pressure sensitive paint to study the flow around a delta wing. Several coatings were tested and a black acrylic paint with a

mirror finish doped with Rhodamine B was applied on the wing surface. The black pigments of the paint absorb some of the impinging laser light and Rhodamine B produces a wavelength shift in the light scattered from the surface which can be filtered out (Konrath et al. 2008). Whilst Matt black surface preparations can be beneficial for a short period, any surface layer can become rapidly ablated when using pulsed illumination.

An alternative approach to reducing flare is the use of fluorescently doped seed particles which emit light at wavelengths longer than that used for illumination. Provided sufficient chromatic separation exists between the excitation and emission wavelengths, filters can be used to prevent the intense light scattered from any solid surfaces from being imaged. The extremely high contrast ratio of commercially available bandpass filters (to $>10^5$) means that fluorescent tracers can be used to produce measurements in close proximity to surfaces and hence facilitate the study of boundary layers, flow-structure interactions and microfluidics. The development and use of fluorescent tracers for flare removal is explained in detail in Chapter 4.

3.8. Summary

This chapter has reviewed the most commonly used non-intrusive techniques for fluid flow measurements. Both single-point and full-field techniques were presented and in spite of the advantages of single point techniques, regarding temporal and spatial resolution available, in order to characterise GDI engines full field flow techniques are required both to reduce data acquisition time and study the instantaneous interactions between the phases across the field.

Current approaches available to provide 3-C velocity data for multi-phase flows in macroscopic engineering rigs have limitations in terms of the dispersed phase size and volume fraction. The multi-camera system normally used for 2C multi-phase measurements in GDI sprays has not been expanded to stereo measurements due to the complexity of the experimental system required. This thesis presents an alternative approach for multi-phase measurement consisting of a single, unmodified colour camera for 2C data which makes the extension to stereo measurements with a pair of colour cameras feasible.

Another problem commonly found in experimental systems is flare resulting from laser light impinging on solid surfaces and this is particularly limiting when velocities need to be measured close to surfaces. The effect of flare on PIV measurements and approaches for its reduction were discussed; the use of fluorescent tracers for flare removal is further discussed in Chapter 4.

Part II

Experimental approach for simultaneous multi-phase measurements

Chapter 4

FLARE REMOVAL IN GAS-PHASE PARTICLE IMAGE VELOCIMETRY

Chapter 3 introduced the problem of unwanted flare and its importance in some PIV experiments using laser illumination. Flare is produced when the light used to illuminate the seeding particles also impinges on surfaces within the experimental setup with the light scattered from the surface much more intense than the light scattered by the particles. Different techniques have been proposed for its removal as described in Section 3.7. One approach is to use fluorescently doped seed particles, which emit light at wavelengths longer than that used for illumination. Provided sufficient chromatic separation exists between the excitation and emission wavelengths, filters can be used to prevent the intense light scattered from any solid surfaces from being imaged.

This chapter presents a laboratory method to optimise and evaluate fluorescent tracers for flare removal in PIV experiments. Section 4.1 briefly presents the dye selection requirements and the analysis followed to select the most suitable dye solution for gas-phase PIV applications. The following sections describe the experimental setup used for the sizing of the tracers and the recording of PIV images. The chapter concludes with the application of the optimised fluorescent tracers in a common engineering application: flow is quantified around a gas turbine blade using 1 μ m tracer particles of o-xylene doped with Bis-MSB, in which

elastically scattered flare has been successfully removed from the images using an appropriate optical filter. Additional colour images of flare from a car valve are also included to show how the intense fluorescence of the tracers developed allows for the use of a different type of camera for image recording.

The development of the fluorescent tracers (including chemical analysis and fluorescence optimisation using micro-emulsions) was carried out by Mourad Chennaoui, School of Chemistry, University of Edinburgh. Tracer sizing, laser imaging (both greyscale and colour images) of flare removal images, PIV recording and analysis were a contribution of this research project by the author of this thesis.

4.1. Fluorescent dye Selection

The desired properties of a fluorescent dye for flare removal are: intense absorption at 355 nm, high fluorescence quantum efficiency, sufficient spectral separation between excitation and emission wavelengths and a fluorescence emission wavelength centred in the high-sensitivity range of silicon-based CCD cameras. For PIV experiments in multi-constituent and multi-phase flows, it is also desirable for the fluorescence emission bandwidth to be narrow and either contained within one of the primary colour bands, corresponding to a detection channel of a colour CCD, or located at a defined region within the visible spectrum.

Previously, Bis-MSB dye, which emits in the blue 400–470 nm when excited at 355 nm, was employed at concentrations up to 5×10^{-3} molar (M) (McGhee et al. 2005). An increased dye concentration has been achieved, improving the fluorescence intensity, by using o-xylene as the solvent as opposed to olive oil (Chennaoui et al. 2006). Dye concentrations up to 1×10^{-2} M have been achieved and are sufficiently stable for routine laboratory use and highly suitable for particle imaging using a frequency-tripled Nd:YAG laser. Thus, Bis-MSB tracers were chosen for application in a flare removal PIV experimental setup as presented next.

Further details on dye development, including chemical analysis and the laboratory procedure, which uses stabilised micro-emulsions to assess and optimise dye

fluorescence of dye-doped droplets through fluorescence spectroscopy, are out of the scope of this thesis but can be found elsewhere (Chennaoui et al. 2008).

4.2. Sizing of atomized tracers using interferometric particle imaging

Tracer particle sizing was performed in order to verify that the optimised fluorescently doped tracers were appropriate for a wide range of gas-phase flows where micron sized droplets are required to achieve adequate flow following (Melling 1997). The nebulisation solution, Bis-MSB in *o*-xylene at 1×10^{-2} M, was drawn through a pressure-driven medical nebuliser (Med2000 Andy Flow) into a 532nm light sheet. The seed density was controlled by a pressure regulated flow of nitrogen.

An interferometric particle imaging (IPI) setup was developed in which the light directly reflected from the droplet surface and the first-order refracted beam produce interference fringes across a defocused droplet image. Numerical analysis shows that the number of fringes across the image is proportional to the droplet size; more details on this technique can be found in Appendix A and in published literature (Damaschke et al. 2005) and (Glover et al. 1995). The experimental setup was formed to give approximately equal intensity of reflected and first-order refracted beams at a scattering angle of 70° and a camera (LaVision FlowMaster 3) was used with a Nikon Plan 20 0.4 ELWD microscope objective.

Conversion relationships between the number of interference fringes and the droplet size are available (Semidetnov and Tropea 2004) and have been applied to the imaging setup giving a value of approximately 1.5 fringes per micron. More details on the conversion relationships can be found in appendix A.

Bis-MSB-doped *o*-xylene tracers were nebulised using the same seeding pressure and experimental conditions as those later used for the acquisition of PIV images. For a population of 1000 droplets a mean drop size of $0.94 \mu\text{m}$ was obtained with the size distribution shown in Figure 4-1.

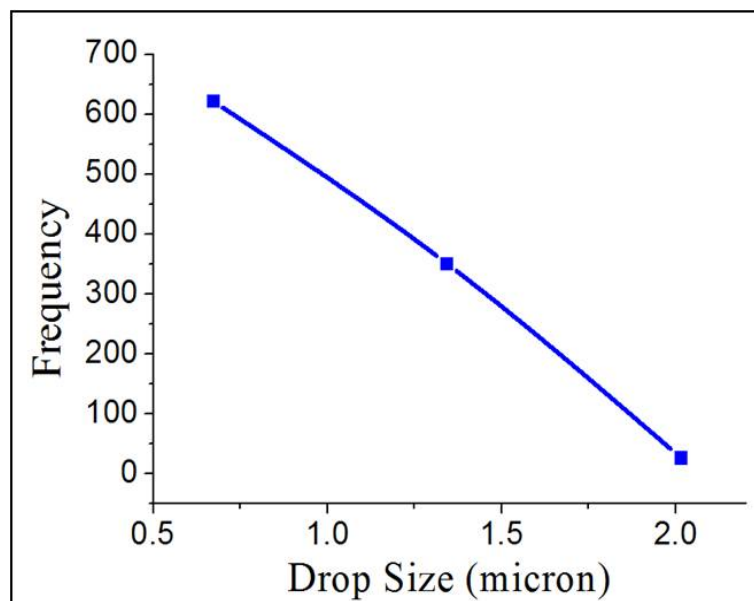


Figure 4-1 Bis-MSB droplet size distribution under experimental conditions

The visibility of these tracers was evaluated with a field of view of the same size as laser sheets typically used for PIV illumination (height circa 40 mm). It was found that satisfactory images of the fluorescence emission of micron sized tracers could be obtained with as little as ~30 mJ pulse energy of 355nm laser radiation at F#4, for Bis-MSB at 1×10^{-2} M, as shown in Figure 4-2. This compares very favourably with two previous studies in which another Stilbene derivative, Stilbene 3 (also known as Stilbene 420), was used in UV excited tracer droplets for two-phase PIV [(Driscoll et al. 2003), (Kosiwczuk et al. 2005)]. In both cases, 355nm pulse energies of 100 mJ were used. Driscoll et al do not indicate the size of their tracer particles, but Kosiwczuk et al state a diameter range of 1–5 μm . Given the cubic dependence of fluorescence intensity on diameter, it is feasible that the images reported in the latter study are dominated by particles at the high end of the diameter range.

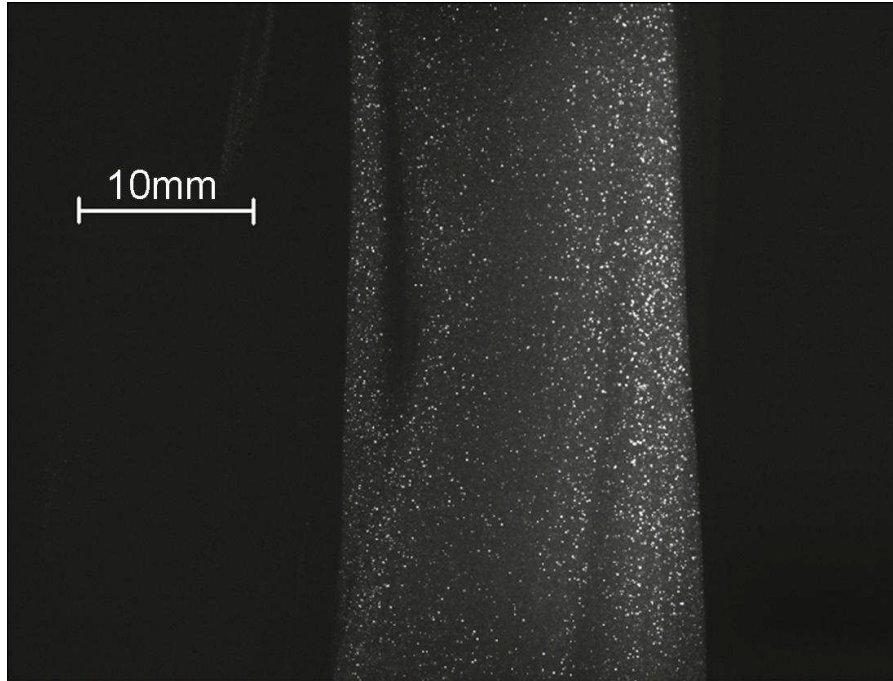


Figure 4-2 Emission from micron sized Bis-MSB fluorescent tracers.

4.3. Imaging of fluorescent tracers for PIV

To demonstrate the efficacy of the developed dye solution for gas-phase PIV, a laboratory experiment was performed to examine the flow against a turbine blade surface; the experiment setup is shown schematically in Figure 4-3. The blade tip is positioned towards the camera and the laser sheet impinges on the lower surface of the blade; a flow is generated vertically upwards over the blade surface, which is representative of turbomachinery applications for PIV.

A flow field was generated using three pressure-driven nebulisers (Med2000 Andy Flow) to ensure there is a high seeding density; their seeding pressure was set to 0.5bar with a regulator attached to a N₂ cylinder. The flow from the three nebulisers was collected in a flexible pipe, placed under the metal blade and then directed upwards using an extraction system. The blade was tilted such that its entire lower surface was directly visible to the PIV camera and was illuminated by the laser sheet. Figure 4-3 shows the blade position and tilt as well as the light sheet and flow directions; the green line on the lower blade surface shows the area where the laser sheet hits the blade.

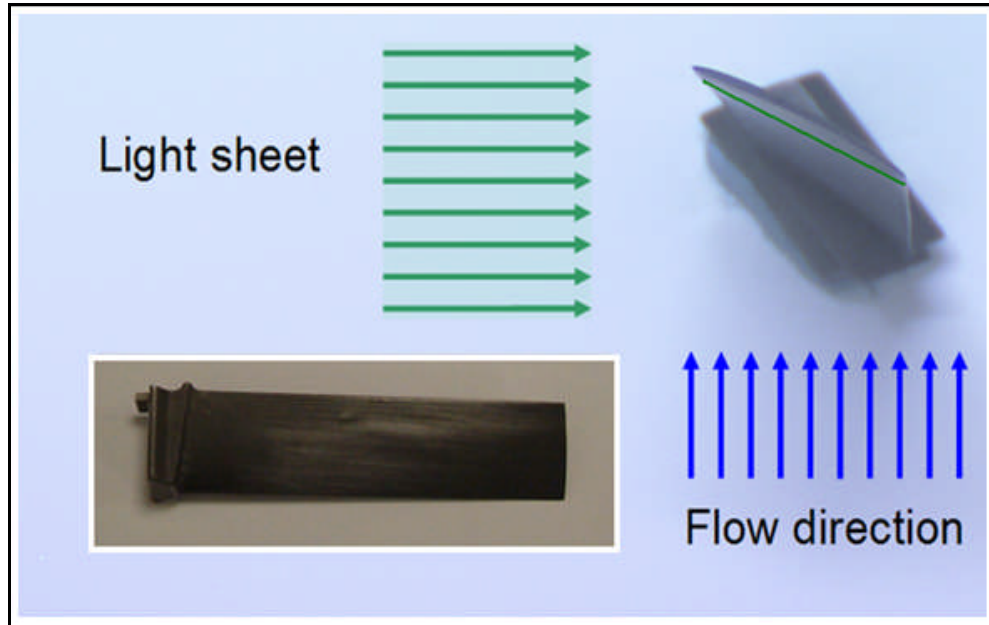


Figure 4-3 Schematic of the camera view and laser sheet orientation for a laboratory flare removal experiment; the inset (lower left) shows the gas turbine blade used

4.3.1. Seed imaging using 532nm illumination

The tracers were evaluated using two single-cavity pulsed Nd:YAG lasers (Continuum Surelite II-10). The first set of measurements was performed using conventional 532nm illumination by fitting doubling crystals to the laser cavities; the two laser beams were combined using a 532nm 50/50 beam splitter with two additional 532nm dichroic mirrors positioned on the beam path to remove any remaining 1064nm energy. The laser setup for 532nm illumination is shown schematically in Figure 4-4.

Laser beams were formed into light sheets with a height of circa 40 mm at the focus using an expanding plano-concave lens and a fused silica plano-convex cylindrical lens. The exact alignment of the laser sheets was critical to ensure that the same volume was illuminated by both the first and the second pulse. Correct alignment of the laser sheets was obtained by placing a JAI CVA50 ½ inch camera directly into the sheet protected by a suitable neutral density filter to prevent damage to the camera. This allowed measurements of the beam profile, thickness and sheet positioning.

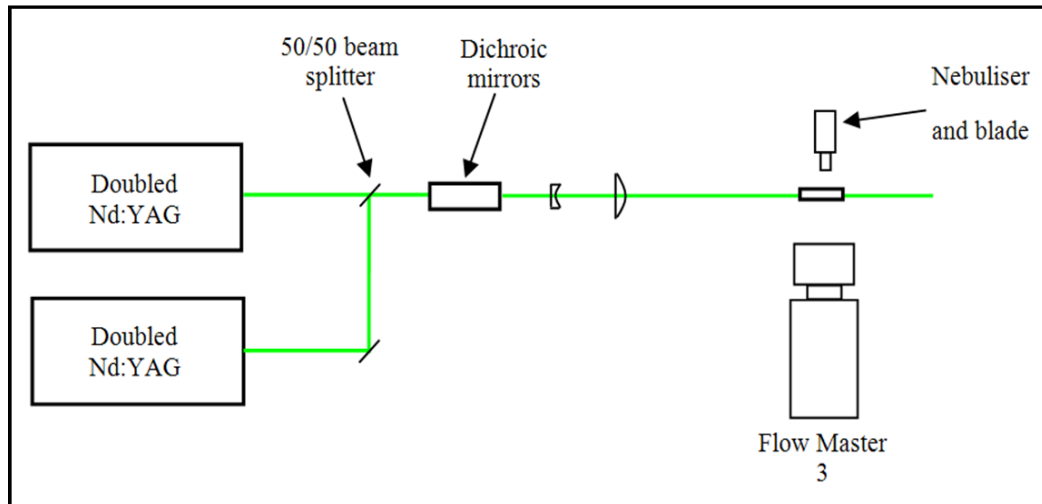


Figure 4-4 Schematic representation of experimental setup for 532nm illumination

An Imager camera (LaVision FlowMaster 3, cooled but not intensified) was used with a Nikon 105mm lens at F# 5.6. Images were recorded, corrected and processed using DaVis 7.2 from LaVision. Mie scattered light was recorded by the camera on double-framed images with a pulse separation of $70\mu\text{s}$ between laser pulses; laser energy of 6mJ per pulse was used for illumination of the flow. Under this configuration, flare was generated on the surface of the blade as shown in the white saturated (overexposed) areas of Figure 4-5. The laser light directly scattered from the blade surface is many orders of magnitude more intense than that scattered by the $1\mu\text{m}$ tracers causing the greyscale range of the detector to be exceeded.

Under saturation at particular pixels, charge is leaked out to the neighbouring area thereby generating a region of unusable pixels on the detector where the particle images cannot be observed and hence flow measurements are impossible.

The double-framed images were processed using the adaptive multi-grid cross-correlation algorithm in DaVis 7.2; lens aberrations were accounted for using the de-warping tool available in DaVis 7.2 using images taken of a white light illuminated target. A window size of 128×128 pixels was used for the first pass which was then decreased to 64×64 pixels with 25% overlap for the second pass; these parameters were selected to provide a clear visualization of both the low velocity vectors below the blade and the higher velocity vectors on the side of the

blade. The resulting vector field is shown in Figure 4-6 which has the seeding image (Figure 4-5) as background.

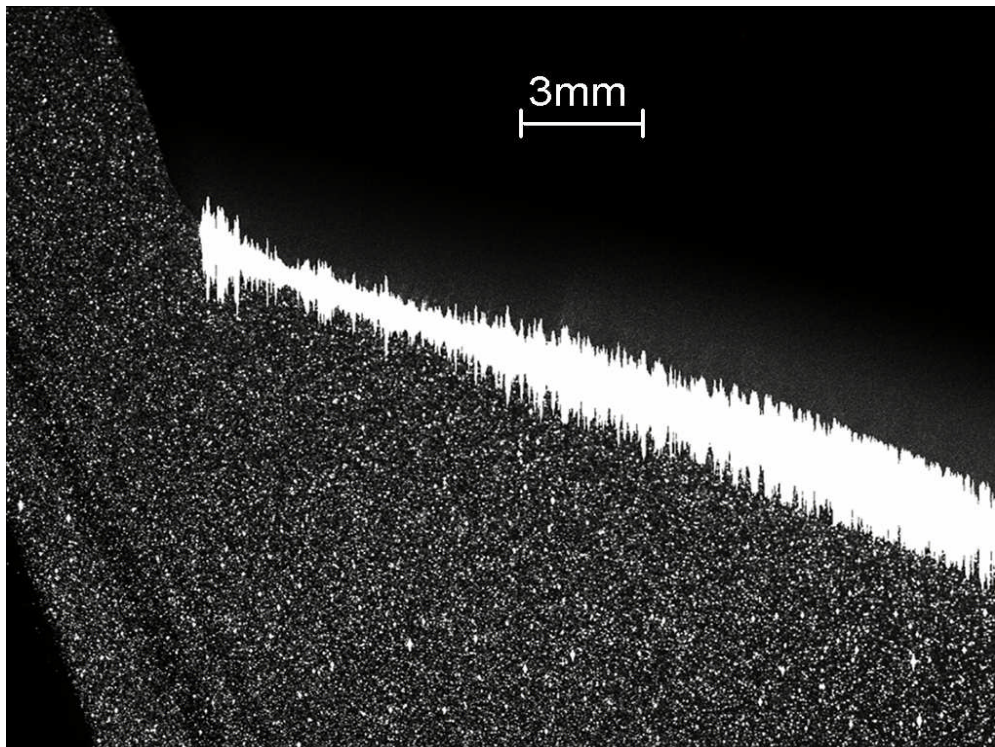


Figure 4-5 Mie scatter of Bis-MSB tracers under 532nm illumination

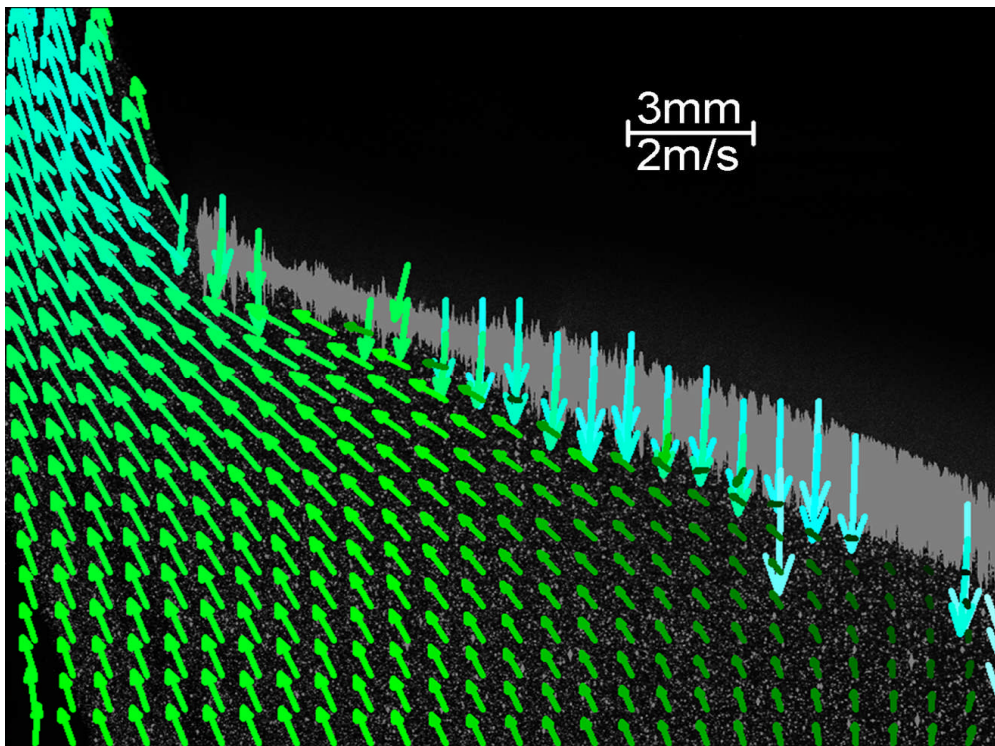


Figure 4-6 Vector field of Bis-MBS tracers under 532nm illumination

The resulting vector map shows that flare generated on the blade surface prevented seed imaging and velocity measurements within the region with saturated pixels, hence data reporting the interaction of the flow with the surface cannot be obtained. Similarly, light reflected from the surface also produced randomly located spurious vectors as shown in Figure 4-6.

4.3.2. Seed imaging using 355nm illumination

To achieve flare removal the Nd:YAG laser was frequency tripled to 355nm by adding tripling crystals to both laser cavities. It was found that standard high reflectivity dielectric mirrors did not remove all of the second harmonic (532nm) from the 355nm pulse. This problem was overcome using equilateral fused silica prisms on both beams to separate the harmonics by refraction. The two beams were combined using a combination of a 355nm half-wave plate and a polarization mixer. Light sheets were formed using an expanding plano-concave lens and a fused silica plano-convex cylindrical lens; their correct alignment was obtained following a similar procedure to that for the 532nm setup using the JAI CV-A50 1/2inch camera and a set of neutral density filters. The experimental setup for 355nm illumination is shown schematically in Figure 4-7.

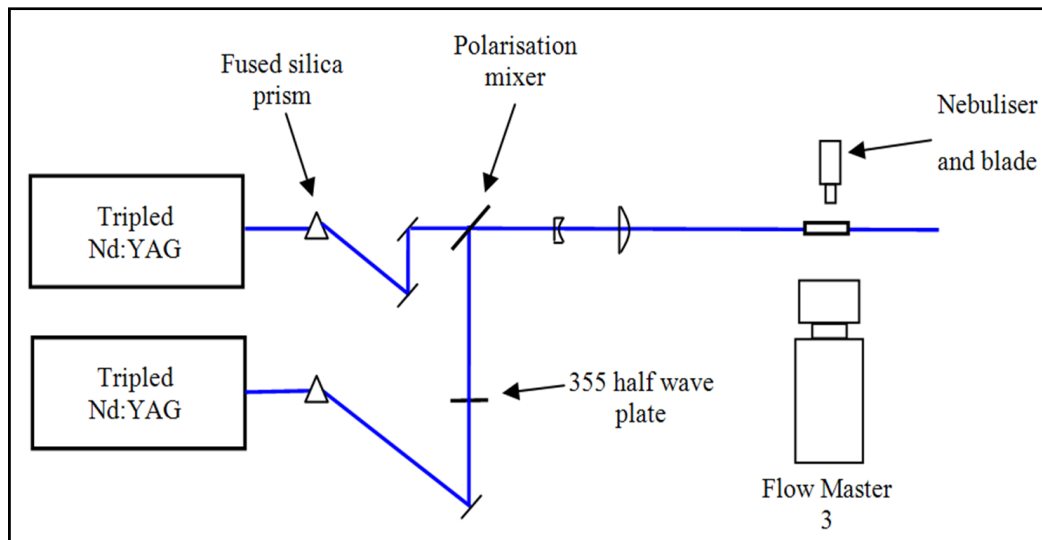


Figure 4-7 Schematic representation of experimental setup for 355nm illumination

Bis-MSB tracers were used at a concentration of 1×10^{-2} M in o-xylene; the flow field was again generated using a combination of pressure-driven nebulisers as

done in the 532nm setup. The imaging lens blocked any 355nm Mie scattered radiation hence no additional filtering was required.

Measurements on the blade were repeated using 30mJ UV illumination, acquiring double-framed images with a pulse separation of 70 μ s. In this case no flare was produced as shown in Figure 4-8. The lower surface of the blade, upon which the laser sheet is incident, is again visible. Blue fluorescence from the Bis-MSB doped tracers generated high contrast particles within the images. Such images could be obtained for several minutes before agglomeration of the tracers on the blade surface produced a detectable fluorescence.

After image correction, velocity vectors were calculated with the same cross-correlation parameters used for conventional 532nm illumination. The vector map obtained is shown in Figure 4-9. The inset figure demonstrates the ability to measure up to the blade surface by calculating vectors with a smaller window size in the area shown by the white square. Vectors are obtained within 75 μ m of the surface corresponding to one interrogation window size at 4 \times 4 pixels when the field of view is approximately 25mm.

The removal of the image flare has enabled velocity vectors to be obtained right up to the surface of the metal blade. It can also be seen that the continuity of the velocity field is considerably improved. With Mie imaging, the presence of flare results in the loss of the vectors from all interrogation regions containing some saturated pixels (see Figure 4-6) which increases the size of the region where the velocity information is lost. In contrast, with fluorescence imaging the velocity data show excellent continuity along the blade surface and around its left-hand edge.

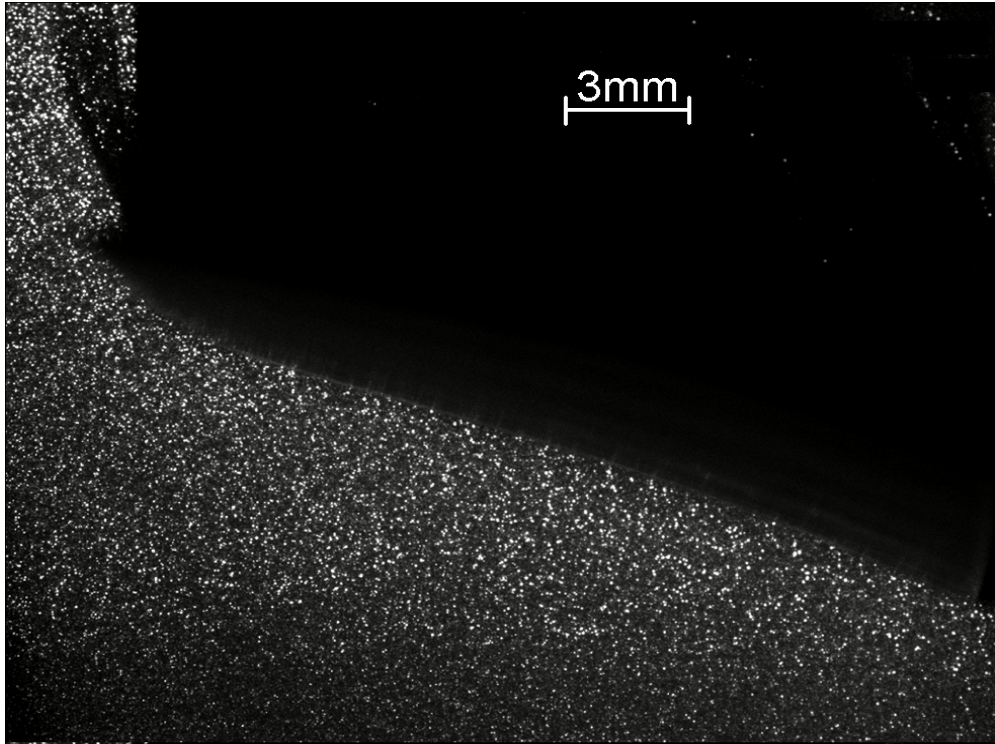


Figure 4-8 Fluorescence of Bis-MSB tracers with 355nm illumination

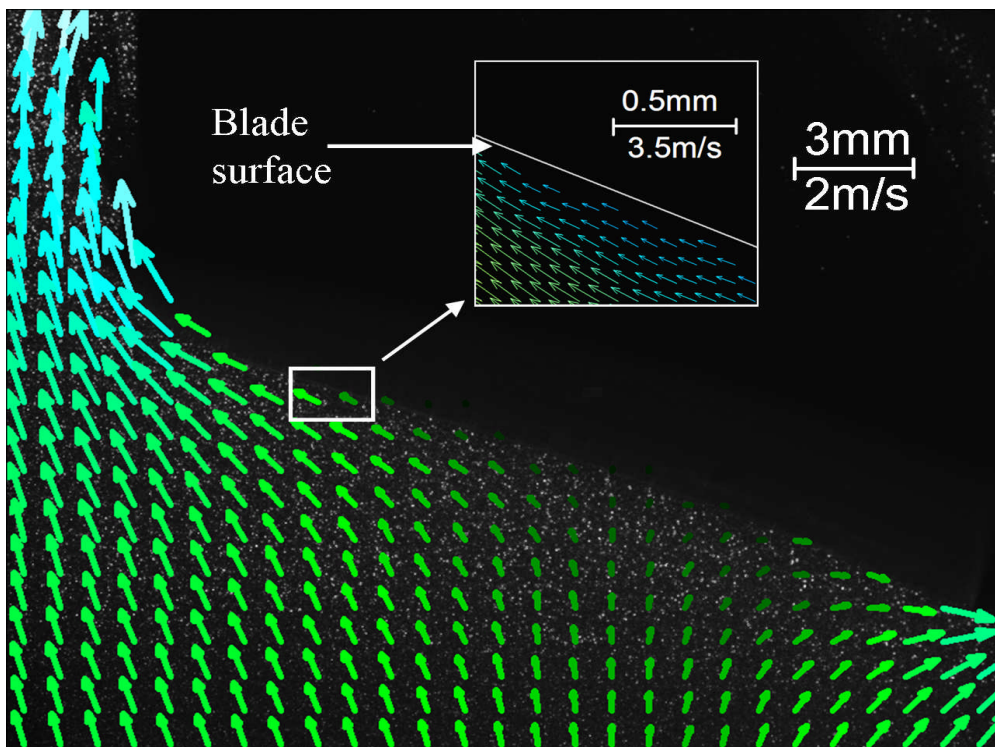


Figure 4-9 Vector field of Bis-MBS tracers under 355nm illumination

4.4. Colour imaging of flare

Using the same experimental setup of UV and green illumination, images have been recorded of the flare produced when imaging the flow against a car valve. The experiment was setup in the same way as described in Figure 4-3: the flow from 3 nebulisers (to increase the number density of tracers) was collected with a flexible pipe, placed under the valve and then directed upwards using an extraction system.

A Hitachi HVF22F 3CCD colour camera (which will be used extensively in the following chapters) and the same Nikon 105mm lens were used to record images of Bis-MSB tracers under the same conditions as those previously described in this chapter: first 532nm illumination and then 355nm illumination. Laser sheet orientation is the same as that in Figure 4-3.

No PIV image pairs have been obtained because the colour camera cannot record double-framed images (hence no velocity vectors have been calculated). The images are intended to provide a more detailed understanding of flare and its removal through colour images and also to show how the intense fluorescence of Bis-MSB tracers allows for the use of a conventional off-the-shelf colour camera (reduced sensitivity than the Imager Intense camera). However, it should be noted that PIV could be achieved with this camera if the flow is sufficiently slow (e.g. some Micro PIV applications) such that the frame rate of the camera was not a problem or by timing the laser pulses either side of the end of a frame.

Under 532nm illumination, Figure 4-10, flare is evident along the valve surface particularly on the lower section. Additionally, charge leak is also obtained on both the top and lower part of the valve and is, again, particularly bad in the lower part of the valve. No clear particle images can be obtained along the valve surface and therefore it would not have been possible to obtain velocity data in close proximity to the surface.

Under 355nm illumination, Figure 4-11, flare has again been removed, as well as charge leak, and clear particle images can be obtained along the surface making it possible to obtain velocity information in close proximity to the surface.

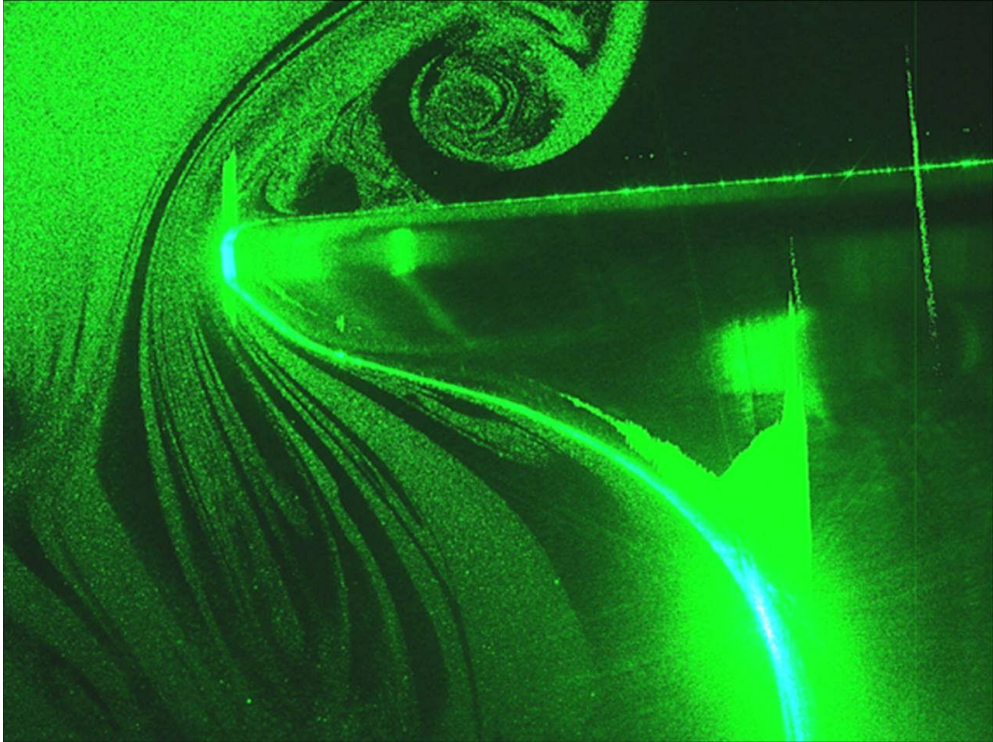


Figure 4-10 Colour image of Mie scatter of Bis-MSB tracers with 532nm illumination. Image taken by the author and Matthew Ormsby at the University of Leeds

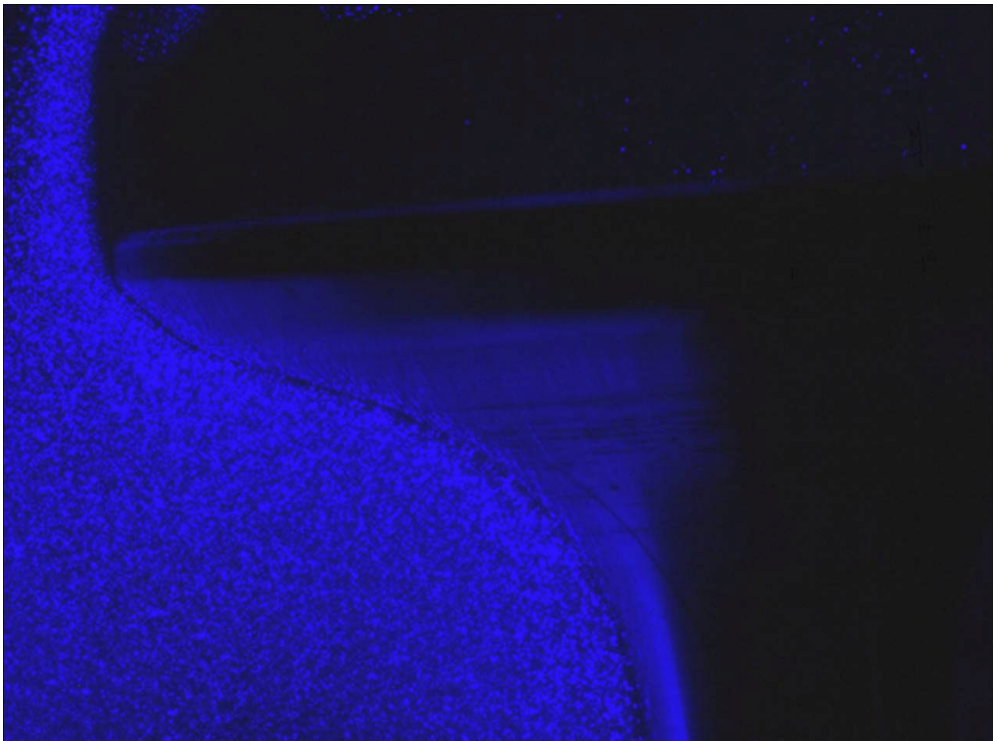


Figure 4-11 Colour image of fluorescence of Bis-MSB tracers with 355nm illumination. Image taken by the author and Matthew Ormsby at the University of Leeds.

4.5. Summary

A laboratory method to assess and optimise the fluorescence of micron-sized droplets of Bis-MSB in o-xylene has been developed; these tracers show intense fluorescence around 420 nm, when excited at 355nm, and are highly suitable for particle imaging using a frequency-tripled Nd:YAG laser. Concentrations up to 10^{-2} M have been achieved, producing a higher fluorescence intensity than that previously obtained using Bis-MSB in olive oil (Chennaoui et al. 2006). The fluorescence properties of Bis-MSB are such that double pulsed PIV experiments can be successfully conducted with standard solid-state lasers and silicon-based CCD cameras and off-the-shelf 3CCD colour cameras. Additionally, when imaging with a 3CCD colour camera additional external filters are not required with 355 nm illumination reducing the complexity of the experiment.

The optimised tracers are not only significantly smaller, $<1 \mu\text{m}$ mean diameter, than those developed previously (Kosiwczuk et al. 2005) but can also be imaged with a relatively low laser pulse energy of 30 mJ at 355 nm over a vertical field of view up to 40mm.

The effectiveness of these fluorescent tracers for flare removal in PIV experiments has been demonstrated, enabling measurements to be made in close proximity to reflective or scattering surfaces. This fluorescent PIV technique is expected to find applications in boundary layer studies and flow structure interactions in turbomachinery, automotive and chemical process industries.

Chapter 5

OPTICALLY EFFICIENT FLUORESCENT TRACERS FOR MULTI-CONSTITUENT PIV

The need for improved instrumentation to study mixing processes in multi-constituent and multi-phase fluid systems was established in Sections 3-5 and 3-6. Considering that no reliable PIV data has been obtained on two-phase flows with the available techniques, a new strategy for multi-constituent flow measurement in the gas phase is presented in this chapter.

Two fluorescent dopants with widely different emission spectra, solid state lasers and a 3CCD colour camera will be used. For each constituent of the flow, a fluorescent dye was chosen to emit light at a particular wavelength in order to discriminate between the types of tracer particle and hence flow constituent or phase. The adopted philosophy is to exploit the inherent co-registration offered by a 3CCD colour camera with the images recorded in the 3 colour planes enabling flow constituent / phase to be determined as well as pulse order; the addition of a second 3CCD camera in a stereoscopic arrangement would also enable the measurement of three components of velocity.

Dye selection requirements will be discussed along with the experimental setup and the image recording process. An image processing strategy to reduce the crosstalk between colour channels and also to account for chromatic and lens

distortions is also described. Two examples of multi-constituent flow will be shown and their results analysed.

The development of the Bis-MSB and DCM fluorescent tracers (including chemical analysis and fluorescence optimisation using micro-emulsions) was carried out by Mourad Chennaoui, School of Chemistry, University of Edinburgh. Everything else presented in this chapter is a contribution of this research project.

5.1. Fluorescent Tracers Selection and Imaging System

The desired properties of fluorescent dyes for gas phase PIV have been discussed in Chapter 4; these can be summarised as strong absorption at 355nm (frequency tripled Nd:YAG), high quantum efficiency, sufficient spectral separation between excitation and emission wavelengths and a fluorescence emission spectrum in the high sensitivity range of silicon based CCD cameras. For use with colour cameras, it is also desirable for the fluorescence emission bandwidth to be contained within one of the primary colour bands corresponding to a detection channel of the colour CCD camera, and for there to be sufficient chromatic separation between the illumination and the fluorescence and between the fluorescence and any wavelengths used for Mie scattering. It was found that dyes developed originally for dye lasers tend to offer higher solubility (to maximise fluorescent yield) in a range of solvents that are suitable for atomisation as gas phase seeding. Chapter 4 also described the development and properties of Bis-MSB tracers emitting in the blue, 400-470nm, when excited at 355nm, and concentrations up to 1×10^{-2} M were achieved using xylene as the solvent (Chennaoui et al. 2008).

Red fluorescent tracer particles have also been investigated, based on DCM dye dissolved in Dimethyl sulfoxide (DMSO), and similar concentrations of up to 1×10^{-2} M have been achieved. DCM has absorption bands conveniently located at both 355 and 532nm giving a wide range of applications. For single phase / constituent flows, the DCM tracers may be used with a filtered monochrome camera and a standard twin-cavity Nd:YAG laser with both outputs at 532nm in order to remove flare from the images (in the same way Bis-MSB tracers were used with 355nm illumination in Chapter 4 for the same purpose). The filter is selected to block the 532nm excitation whilst transmitting the fluorescence.

In multi-constituent flows, DCM tracers can be used in one flow constituent whilst the Bis-MSB tracers are used in the other. Simultaneous excitation of both dyes can be achieved using 355nm excitation from one Nd:YAG cavity, giving chromatically separate images in the blue and red channels of a colour camera, thereby achieving flow constituent discrimination. A low energy, 1-2mJ, pulse at 532nm will generate Mie scatter from both types of tracer in the green channel. This approach has the advantage that only solid state lasers are required for illumination.

A 3CCD Hitachi HV-F22F colour digital camera was selected for the experiments. This is an off-the-shelf readily available camera used for a wide range of applications (Hitachi 2010). The camera separated internally the imaged light into bandwidths of red, green and blue directing them to the appropriate CCD chip allowing three co-aligned images to be recorded simultaneously. Figure 5-1 shows an example of the experimental flow, where both the Bis-MSB and DCM doped tracer droplets are illuminated simultaneously using a sheet of laser light at 355nm.



Figure 5-1 Bis-MSB (left) and DCM (right) tracers excited by a 355 nm laser light sheet.

Qualitatively it can be seen that the emissions from the Bis-MSB and DCM droplets are obtained in the blue and red channels of the CCD, respectively. If the fluorescence emission is ideally matched to the CCD response, completely separate images of the two types of tracer are obtained in the blue and red image layers. A 532nm pulse can be then used to produce Mie scatter images of both

tracers in the green channel. Figure 5-2 shows pulse order and corresponding CCD exposure for this approach where the first constituent is seeded with DCM tracers and the second constituent is seeded with Bis-MBS tracers.

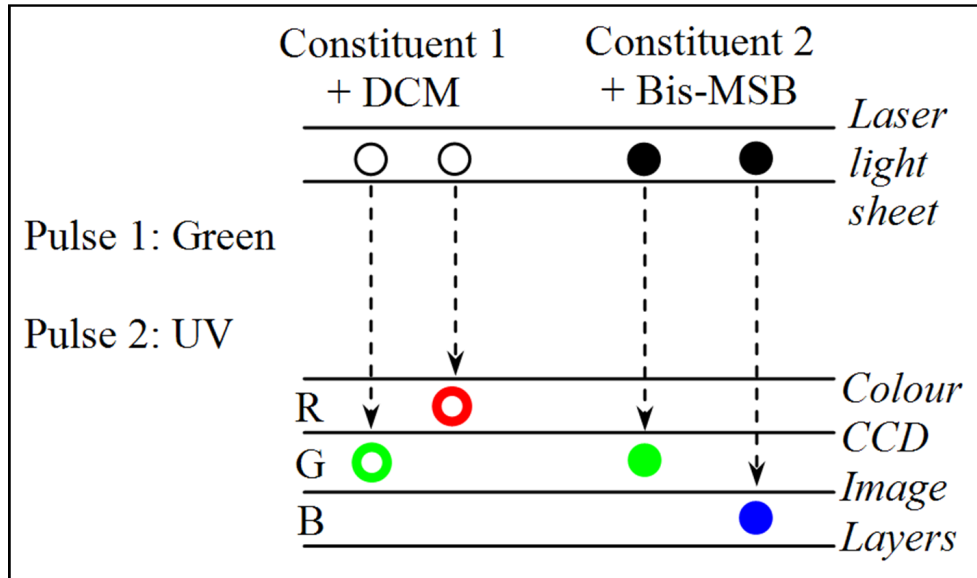


Figure 5-2 Pulse order and CCD exposure on 3CCD colour camera

Cross-correlation between the green and red channels should produce vectors for one constituent and between the green and blue channels the vectors for the other constituent. The extra green Mie images of the opposite flow constituent generate randomly located correlations and hence there is higher background noise in the correlation plane, but the velocity vectors can still be obtained reliably providing there are two or more tracers in each interrogation area.

5.2. Experimental setup

The dyes were evaluated using two single-cavity pulsed Nd:YAG lasers (Continuum Surelite II-10) which were fitted with frequency doubling and tripling crystals respectively, giving a first pulse of 532nm and a second of 355nm light. A fused silica prism was used to ensure all of the second harmonic was removed from the 355nm pulse (see Section 4.3.2) to avoid crosstalk between channels due to the absorption peak of DCM at 532nm. The experimental system is shown schematically in Figure 5-3. The laser beams were formed into light sheets to illuminate the flows using a combination of a negative spherical and positive cylindrical lens. In order to align the sheet foci of both wavelengths it was

necessary to expand each beam at different distances relative to the cylindrical lens. Expanding plano-concave ($f=-200\text{mm}$) lenses were positioned in each beam and mounted on micro-blocks, giving three axes of linear adjustment, to aid the alignment. The beams then met at a 532nm clear backed dichroic mirror allowing the 355nm beam to pass through unhindered. The co-aligned expanding beams were directed through a fused silica plano-convex cylindrical lens ($f=300\text{mm}$) to produce a laser sheet of height circa 30mm at the focus.

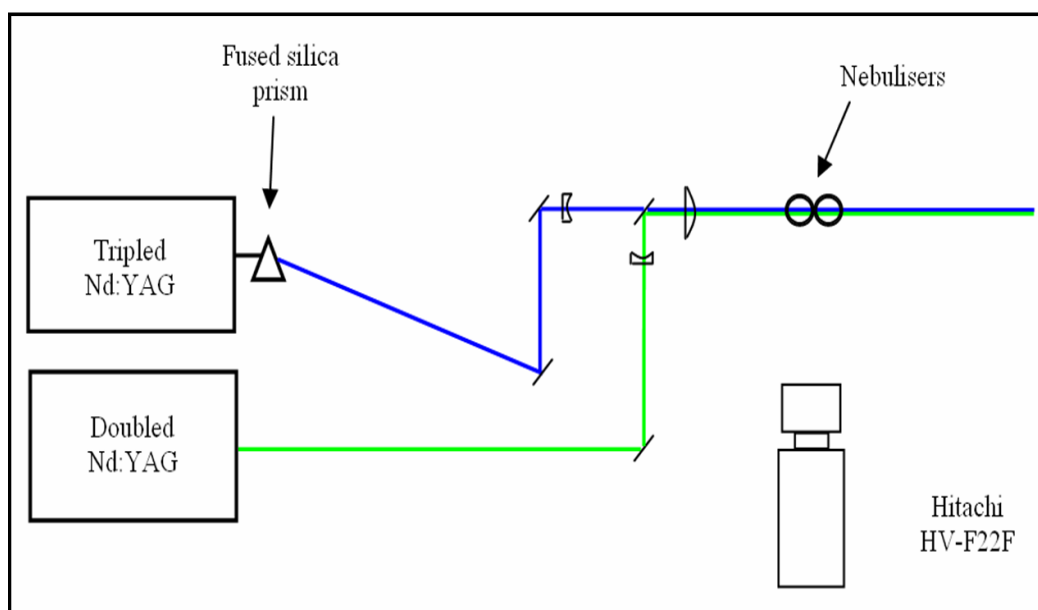


Figure 5-3 Schematic representation of experimental setup

The exact alignment of the two light sheets was critical and was obtained by placing a JAI CV-A50 1/2 inch camera, protected by a neutral density (ND) filter, directly in the sheet (see Section 4.3.1). This allowed measurements of the beam profile, thickness and allowed sheet positioning; a representative image is shown in Figure 5-4 including the horizontal intensity profile. In this image, both laser pulses are visible, the thicker sheet shown is the green pulse, inside which, is the 355nm sheet. The intensity of the laser sheets was significantly reduced to obtain this data and by different amounts (to prevent permanent damage to the camera). Allowing for the difference in camera sensitivity at the two wavelengths used, it is expected that the two laser sheets are more similar in thickness to one another whilst the use of the alignment camera ensured that the centre of each sheet was precisely co-aligned.

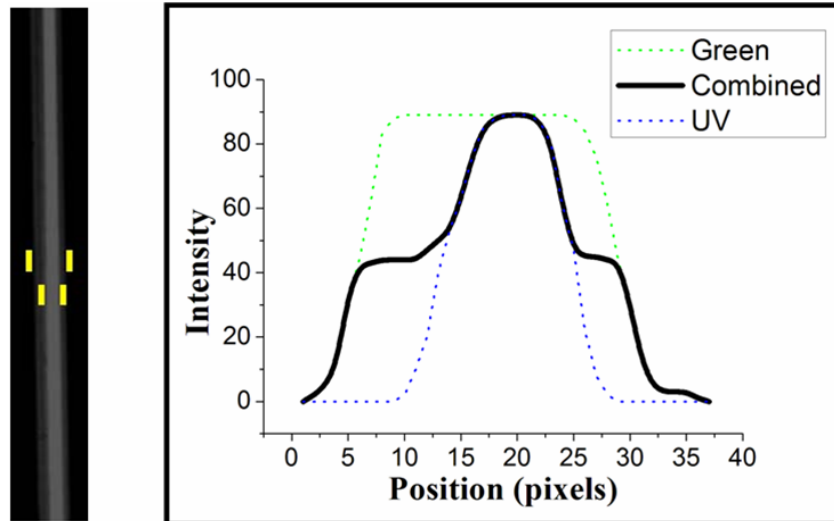


Figure 5-4 Laser Light Sheet imaged on JAI CV-A50 and UV, green and combined horizontal intensity profile. Marks show edges of 532 nm (outer) and 355 nm (inner) laser sheets

O-xylene and DMSO were used as solvents for the fluorescent tracers and solutions were drawn through separate pressure-driven medical nebulisers (Med2000 Andy Flow) into the sheet. A regulator attached to a N₂ cylinder allowed the pressure and hence seed density to be varied. The atomised droplets were removed from the laboratory environment using an extraction system which was also used to direct the flow upwards. Images were recorded onto the Hitachi colour camera and focused by a Nikon 105mm lens. Brightness and sharpness on the camera were adjusted to reduce background noise level and, due to a reduced sensitivity on the red channel (maximum of ~0.6 compared to green channel due to the presence of an IR blocking filter, see Figure 5-5), the red gain was increased with all the other options left unchanged. The camera was used with a resolution of 1280 x 960 pixels and the pixels are 4.65 μ m square.

The lens aperture was set slightly more closed than in most PIV experiments (F#11) to give sharply focussed images in all 3 colour channels simultaneously, i.e. to overcome any longitudinal chromatic aberration from the imaging optic and manufacturing tolerance on positioning of the CCD chips in the camera.

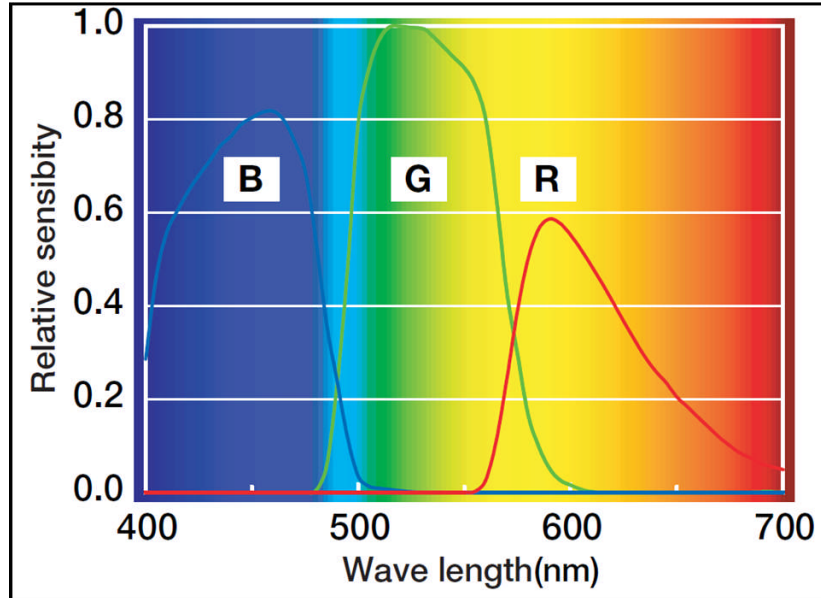


Figure 5-5 Hitachi HV F22F spectral response characteristics (Source (Hitachi 2010))

5.3. Droplet sizing

The fluorescence emission of micron sized droplets, typically used in gas phase PIV for adequate dynamic response (Melling 1997), was analysed by exciting both types of tracers simultaneously with a 355nm pulse. Initial examination of the images recorded showed that Bis-MSB (blue) tracers had sufficient signal-to-noise ratio whereas images from DCM (red) tracers did not due to the reduced sensitivity in the red channel (Figure 5-5). In order to ensure reliable vector processing, a wider drop-size distribution (larger mean drop size) was used for the red tracers by changing the nebulising conditions such that a higher fluorescence signal was obtained on the red channel.

The drop-size distribution for each type of tracer was determined using an interferometric setup in which droplet size is calculated by measuring the angular frequency of interference fringes from defocused images. The same setup used in Section 4.2 was used here giving a conversion relationship of approximately 1.5 fringes per micron. These conversion relationships are expected to be accurate within a few percent (Semidetnov and Tropea 2004). Drop sizes were measured under experimental conditions (seeding pressure 0.35 bar) for a population of 1000 particles for each type of tracer. Mean droplet sizes of 1.04 μm for Bis-MSB (blue

dye) and $2.25\mu\text{m}$ for DCM (red dye) were obtained. The droplet size distribution for each solution is shown in Figure 5-6.

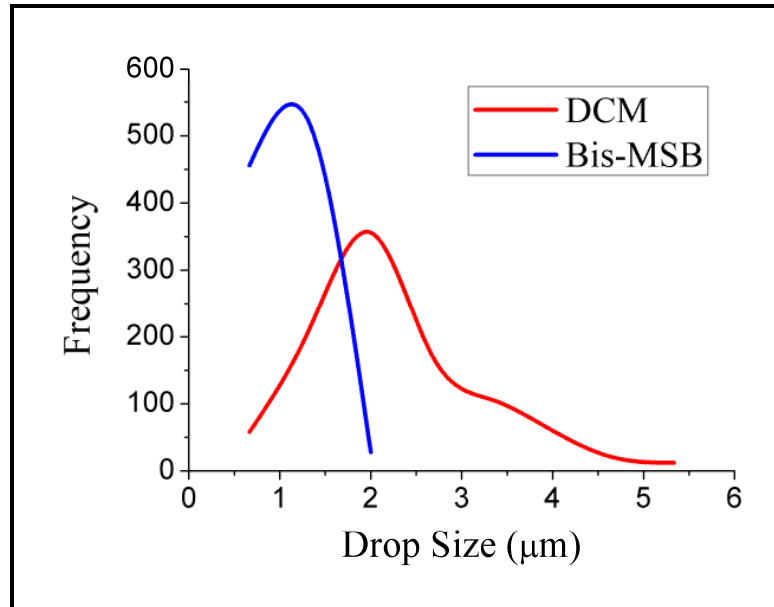


Figure 5-6 Drop size distribution under experimental conditions

The drop size distribution for the DCM (red) tracers spans from 1 to $5\mu\text{m}$ but it needs to be established which part of the size distribution is actually recorded by the colour camera on the red channel. Small particles ($<2\mu\text{m}$) will have a considerably lower fluorescence intensity than larger ones ($2\text{-}4\mu\text{m}$), due to the power law dependence on particle diameter of the fluorescence signal (expected to be between a quadratic and cubic relationship). For this range of tracer sizes the particle image size is dominated by the diffraction limited performance of the imaging optic, hence the particle image diameter is approximately constant at $18\mu\text{m}$ (approximately 4 pixels) for the magnification used (Equation 3-18). The particle images across the size range of all of the tracers therefore appear with an approximately uniform size and a Gaussian intensity profile of varying intensity for each colour channel. Furthermore, to remove crosstalk between the colour channels (see Section 5.4.1), particles with low signal-to-noise ratio will be removed so the bigger droplets are the ones actually contributing to the cross-correlation process.

To quantify the fraction of the DCM-doped tracers with detectable fluorescence, two sets of images of the tracers were recorded separately on the red (fluorescence, 355nm pulse) and green (Mie scattering, 532nm pulse) channels

using the same seeding pressure of 0.35bar. It is assumed that the 532nm laser sheet energy is sufficiently high to make the entire distribution of tracers visible in the green layer of the colour camera. A Matlab code was developed to count the number of particles visible in an image based on a recursive flood fill algorithm. A threshold level was defined and then the image was scanned looking for new pixels; once a new pixel was found it was flood filled around it to then check it was above a certain predefined minimum pixel number (to avoid counting noise as particles). This process was repeated across the image to produce a final particle count. The ratio of number of red to number of green particles is an indicator of the part of the droplet size distribution being recorded, as only the bigger, more intense red particles will be captured. Based on a particle count evaluated over 30 green and red images an average of 73% of the particles present have sufficient fluorescence intensity to be imaged, indicating that approximately three quarters of the DCM droplet size distribution is recorded on the red channel under experimental conditions. Figure 5-7 shows the cumulative distribution of DCM drop size, highlighting the part of the distribution that is being recorded. Hence the mean drop size of the visible DCM doped tracers was evaluated to be $2.65\mu\text{m}$.

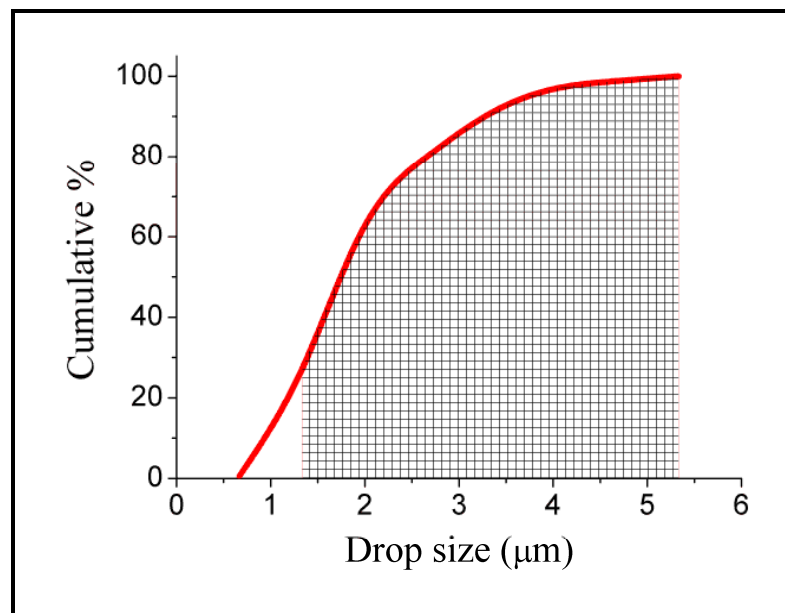


Figure 5-7 Cumulative drop size distribution for DCM tracers highlighting the size range visible on the red channel of a Hitachi HV-F22F 3CCD colour camera

Both the Bis-MSB (blue) dye and the DCM (red) dye were used at a concentration of 10^{-2} M. No additional filtering was required to block the 355nm Mie scattered light from reaching the CCD because it was out of the spectral range of the colour

camera (see Figure 5-5). To balance intensities between the Mie (1st pulse) and fluorescence (2nd pulse) images, neutral density filters were placed in the unexpanded green laser beam path to reduce its pulse energy to an appropriate level (this avoided beam profile variations found at reduced Q switch delay values). The 355nm pulse energy was 95mJ and only ~1mJ of 532nm was required for Mie scattering imaging into the green channel.

5.4. Data Processing

A typical image obtained from the system is shown in Figure 5-8. The two seeding streams are largely spatially separated, with the Bis-MSB-doped (blue) tracers on the right and the DCM (red) tracers on the left. The image was illuminated using a pulse of 532nm followed 50 μ s later by a 355nm pulse. Careful examination shows green to red particle pairs on the left hand side and green to blue image pairs on the right, with both flows going from the bottom to the top of the image (directed upwards using an extraction system). Figure 5-8 shows the original colour image (upper left) and the three separate colour channels shown in grey scales.

5.4.1. Crosstalk correction

In most colour CCD cameras the spectra of the red, green and blue channels are designed to overlap so that there are no colour-blind areas. For the Hitachi HV F22F used this is also the case as shown in the spectral response characteristics in Figure 5-5. There is an overlap of approximately 20nm with a maximum response of 0.22 (relative to a green response of 1) between the blue and green channels. The overlap is larger between the green and the red channels, ~50nm, with a maximum response of 0.34.

This overlap in spectral response can also lead to crosstalk between colour channels: for example a red fluorescent image produced a low signal in the blue and green channels. In this configuration the most damaging crosstalk is that between the red and blue images representing the separation of the images from the two flow constituents. The green channel still contains low level crosstalk from the other channels and the red and blue channels some low level crosstalk from the green Mie scattering. The potential for the DCM doped tracers to emit red

fluorescence from the 532nm pulse coupled with the green and red spectra overlap could also generate crosstalk between the green and red channels.

Crosstalk levels can be reduced using an approach initially applied in 3D surface contouring applications using colour imaging (Huang et al. 1999). This method was then adapted to obtain a quantitative evaluation of crosstalk between colour channels with 3CCD colour cameras for 3D shape measurements (Zhang et al. 2006). Using this approach the coupling effects can be estimated for each channel respectively as the percentage of the intensity from a particular channel that is detected in the other two channels. For example, for an image in the red channel, C_{rg} and C_{rb} represent the intensities detected in the green and blue channels expressed as a percentage of the intensity on the red channel. A similar process is used for the other two channels to define the coupling matrix as proposed by (Zhang et al. 2006):

$$\begin{bmatrix} C_{rr} & C_{rg} & C_{rb} \\ C_{gr} & C_{gg} & C_{gb} \\ C_{br} & C_{bg} & C_{bb} \end{bmatrix} \quad \text{Equation 5-1}$$

The first suffix for each term indicates the channel of the original image and the second suffix indicates the channel of the detected image. Elements along the diagonal are 1, i.e. $C_{rr}=C_{gg}=C_{bb}=1$.

Images were taken separately of fluorescence emission from both types of tracers (red and blue) and Mie scattering (green) under experimental conditions. Each colour image was split into its RGB channels and a pixel-wise background subtraction performed on each channel. Greyscale intensity of particles in each image was measured on the three channels to obtain the crosstalk coefficients and the coupling matrix in Equation 5-1:

$$\begin{bmatrix} 1 & 0.17 & 0.2 \\ 0.43 & 1 & 0.2 \\ 0.1 & 0.02 & 1 \end{bmatrix} \quad \text{Equation 5-2}$$

Equation 5-2 shows the coupling effects for the experimental setup used. There is a strong coupling effect between the green and the red channels which was expected given the overlap of the red and green spectral response and the

absorption peak of DCM at 532nm. By inverting the coupling matrix a set of corrected RGB intensities can be determined from a set of measured intensities pixel-wise across the image, thereby accounting for the crosstalk. The method was applied to a raw camera image and the results are shown in Figure 5-8 where crosstalk between colour channels has been considerably reduced. Care was taken in capturing the PIV images from the flow field and in measuring the coupling effects to ensure that the intensities were maintained within the linear range of the camera.

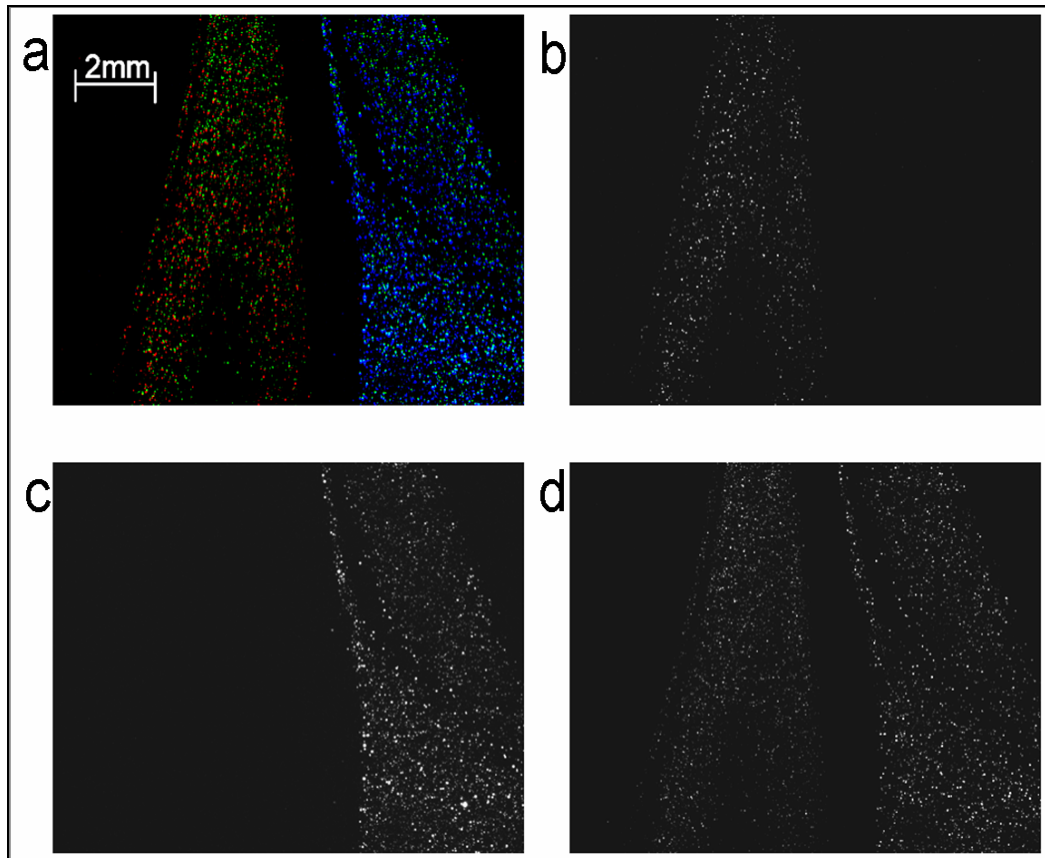


Figure 5-8 RGB image (a) of spatially separate flow streams seeded with DCM doped tracers (left side of image) and Bis-MSB doped tracers (right side). Crosstalk compensated RGB component images are given in greyscales, red: b, blue: c and green: d.

5.4.2. Chromatic and lens distortions

Chromatic and lens distortions were accounted for in two stages. Firstly, images taken of a white-light-illuminated calibration plate were used to remove the distortions in each colour channel independently with the image de-warping tool in DaVis 7.2. Secondly, it is also necessary to estimate the distortions due to the

combination of the offset between each of the 3 colour channels within the camera (given they are not exactly co-aligned) and chromatic lens distortions. For example, taking the green channel as the reference, there is a small offset from the green to the red and from the green to the blue images which produces false displacements on the vector maps.

A simple correction procedure was used in which images taken of a white-light-illuminated rough continuous surface were used to ensure that vectors would be obtained in every interrogation window across the whole field of view. Images were split into RGB channels and pairs of images (red to green and blue to green) were cross-correlated in DaVis 7.2 using the same calculation parameters as those later used for the vector calculation of the flow constituents.

The validity and repeatability of the correction procedure were assessed. Different surfaces were used under the same illumination conditions and the maximum difference in displacement in any interrogation region was found to be 20% with the overall offset pattern unchanged for different surfaces. Once a surface had been selected the repeatability was tested by using different light levels. The maximum difference of the average displacement was found to be 4% for different light levels. An average offset of 0.3 pixels was obtained between the red and green images and 0.75 pixels between the blue and green images. The displacements obtained in each interrogation window are then subtracted from the vector maps for the corresponding flow constituent to account for any false displacements.

5.5. Results

Following image distortion and crosstalk correction, the data were imported as double frames for green to red and green to blue. Background subtraction was performed and the adaptive multi-grid cross-correlation algorithm in DaVis 7.2 employed to obtain the velocity vectors for each flow constituent. Finally, the vector fields corresponding to the chromatic distortion and CCD positioning offsets were removed. The vectors were exported as text files from DaVis 7.2 and then plotted using Origin. The resulting vector fields are shown colour coded for each flow constituent in Figure 5-9 corresponding to the RGB image shown in Figure 5-8. In

this vector field it is clear that the crosstalk compensation has been successful and spatially separate regions corresponding to each tracer type have been obtained.

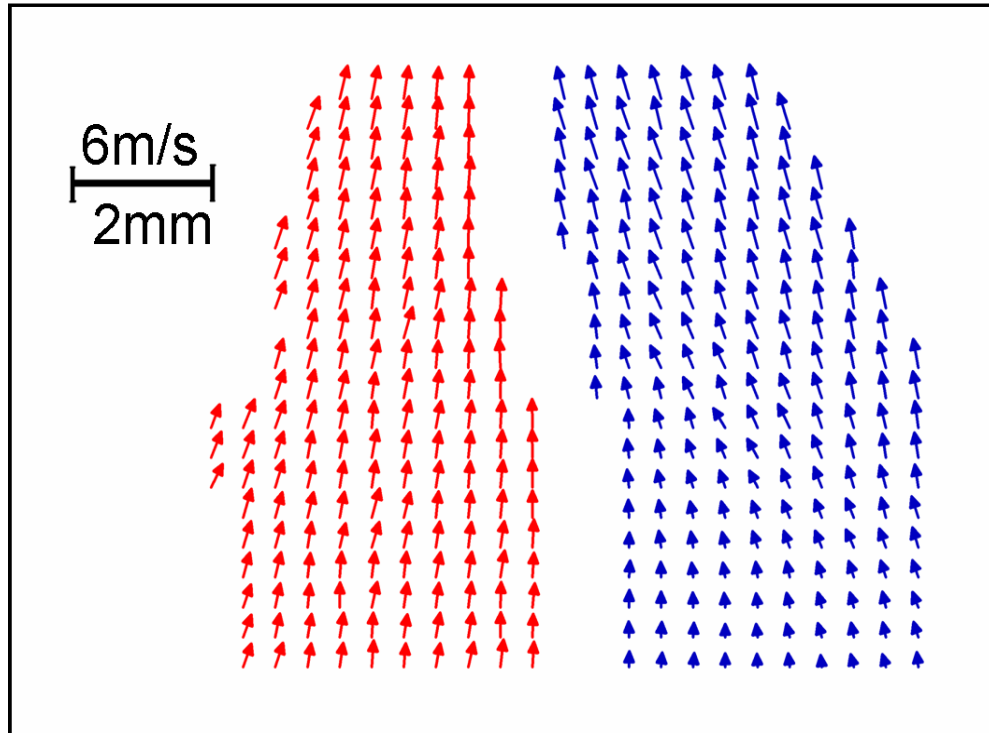


Figure 5-9 PIV vectors found from cross correlation of the data in Figure 5-8. Red vectors from DCM-doped tracers, blue vectors Bis-MSB-doped tracers

A second more interesting example is shown in Figure 5-10. Here the flow, generated using four nebulisers (2 for each type of tracer), was brought together using a suitable pipe before being imaged. This produced a densely seeded image with abundant constituent mixing throughout and the measured region is sufficiently downstream for the two constituents to be considered as well mixed. The RGB image was produced by illumination with 532nm and 355nm laser light sheets and a pulse separation of 50 μ s. The vector map obtained is presented in Figure 5-11 showing abundant clear regions of mixed flow where the blue vectors are thicker so that the interrogation regions with vectors from both types of tracers can be easily identified.

The validity of the vector fields obtained was assessed using the post processing stage in DaVis 7.2 in which a median filter and a ratio-threshold for the different peaks on the correlation plane were used to discard spurious vectors.

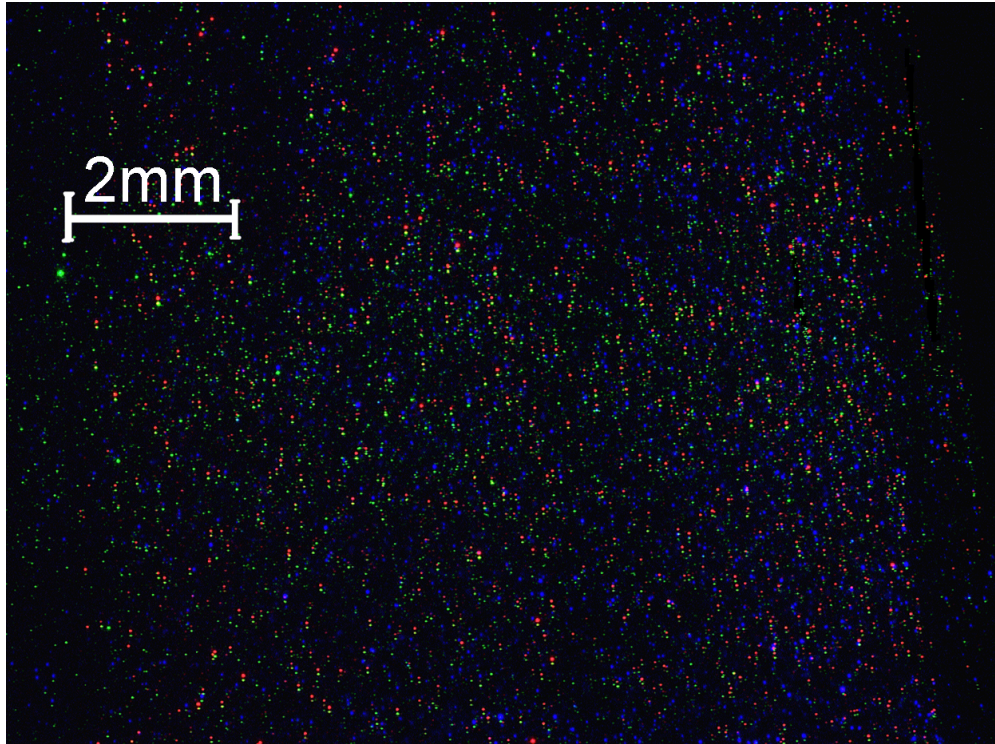


Figure 5-10 Second example of a multi-constituent flow

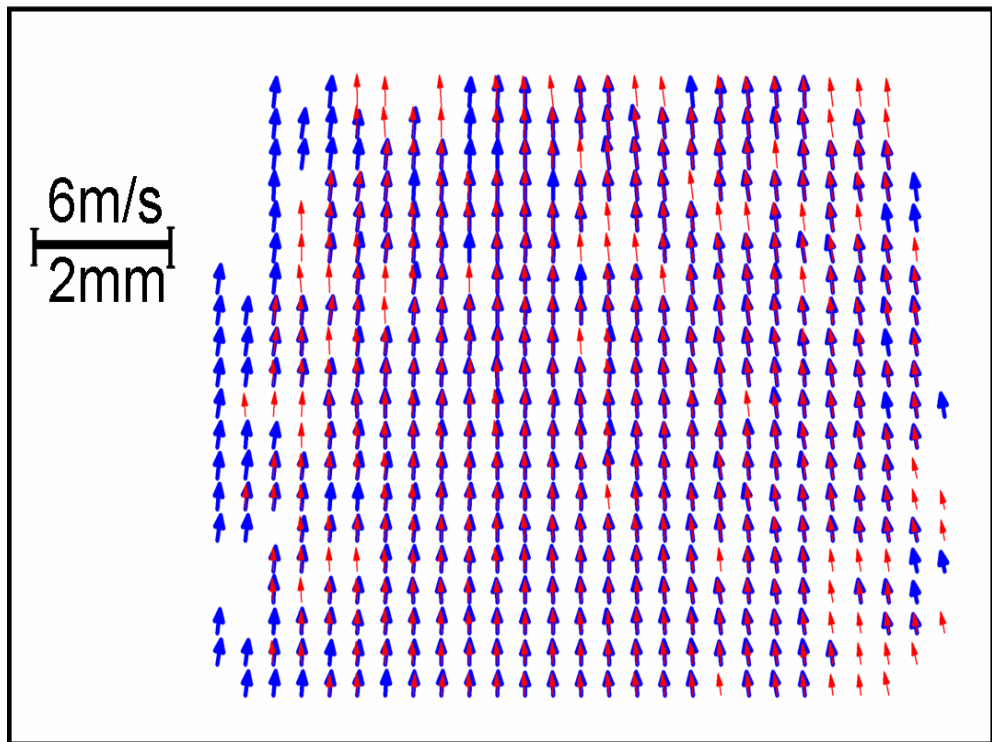


Figure 5-11 PIV vectors found from cross correlation of the data in Figure 5-10. Red vectors from DCM-doped tracers, blue vectors Bis-MSB-doped tracers.

The vector fields in Figure 5-11 were analysed to ensure they are not biased towards integer values due to peak locking effects. DaVis 7.2 provides a numerical estimation of the peak locking effect based on the histograms of the velocities in the x and y directions which were found to be well below the acceptable level of peak locking effects (Equation 3-20). Values of 0.024 and 0.03 were obtained for the Bis-MSB and DCM doped tracers respectively where a value of 1 indicates a strong peak locking effect.

Resultant velocities on each interrogation window were calculated and sorted in ascending order for the red tracers and plotted with the correspondent velocity calculated with the blue tracers as shown in Figure 5-12.

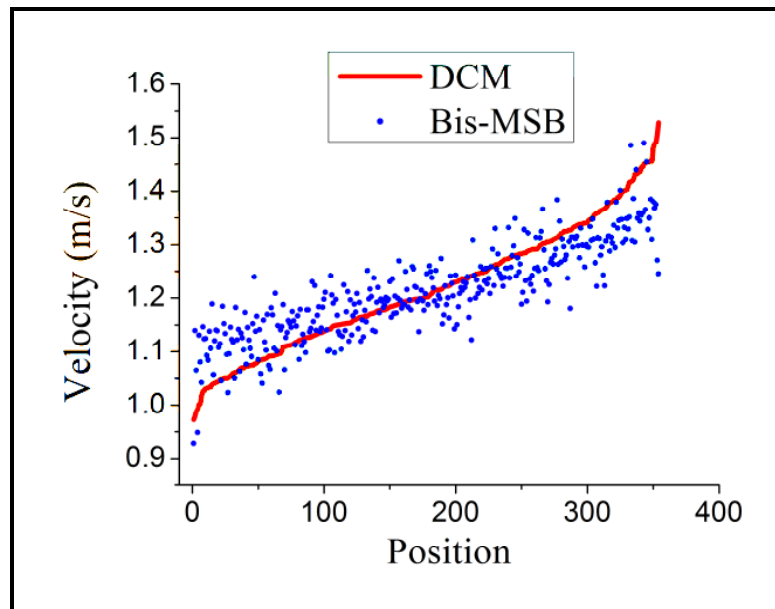


Figure 5-12 Resultant velocity comparison for vector field in Figure 5-11 with DCM-doped (red) and Bis-MSB-doped (blue) tracers

The average difference between the resultant velocity calculated from each type of tracer was found to be 0.25 pixels (0.046 m/s) equivalent to approximately 3.96% of the average displacement across the image. The velocity dynamic range could be improved by using longer pulse separation as necessary (producing a higher particle displacement within the interrogation windows) hence the noise floor of 3.96% could be reduced if required. The results shown in Figure 5-9 indicate that crosstalk can be completely compensated; given that the fully mixed flow in Figures 5-10 and 5-11 utilise the same image processing algorithms and optical setup as that of figure 5-9, it can be expected the same crosstalk compensation

performance will be obtained. Consequently the calculated difference of 0.25 pixels can be taken as the noise level for these experiments which is comparable to the minimum uncertainty of 0.1 pixels (Nobach and Bodenschatz 2009) for single phase PIV.

As previously discussed, larger droplets were required for DCM tracers (red) to ensure the data obtained were reliable. The limiting factors for the recording of red fluorescence are the reduced sensitivity on the red channel (compared to the blue and green channels) of the camera used and the aperture required (F# 11) for a sharp focus on the three colour planes. DCM tracers produced with a Laskin nozzle (monodisperse droplets, mean size $1\mu\text{m}$) were tested separately with an Imager Intense camera (see Chapter 4) and focused with the same Nikon 105mm lens. The particle images obtained were sufficiently bright to provide reliable PIV data.

5.6. Summary

Flow direction, displacements and associated velocity vectors have been measured successfully in a multi-constituent gas phase flow using a single 3CCD colour camera and solid state lasers. Direct quantification of the fluid mixing velocities has been achieved and pertinent correction procedures have been developed and implemented to reduce the effects of crosstalk and CCD offset. It is important to notice that the crosstalk compensation used is a linear process and therefore should not be affected by the presence of overlapping particles (this being the main difference between the flows in Figures 5-8 and 5-10).

The uncertainty in the velocity measurements has been estimated by comparing the data obtained using both types of fluorescent tracers in the same flow. The average difference in velocities was calculated to be <4%.

The use of a 3CCD camera for multi-constituent and multi-phase flows can also be extended to obtain three components of the velocity vector by adding a second colour camera in a stereoscopic imaging setup. This approach would be simpler to implement compared to the conventional method of multiple cameras for each stereo view with different optical filters (Section 3-5 and 3-6).

The use of UV excitation has the added benefit of spectrally separating the excitation wavelength from the imaging bandwidth to allow flare removal (see Chapter 4).

Part III

Two-phase measurements in a GDI spray

Chapter 6

TWO-PHASE MEASUREMENTS IN A GDI SPRAY – EXPERIMENTAL SETUP

Chapter 2 established the need of having simultaneous 3-component (3C) velocity measurements in both phases (air/fuel) in order to be able to generate improved GDI spray designs. However, as it was discussed in Chapter 3, none of the techniques currently available provide 3C velocity data for multi-phase flows in macroscopic engineering rigs without limitations on the dispersed phase size and volume fraction.

Chapters 4 and 5 described the development of fluorescent tracers and their application for flare removal and multi-constituent flows respectively. In particular, a methodology for multi-constituent/phase flow using a single colour camera was proposed along with procedures to account for crosstalk and chromatic aberrations. This chapter describes the use of this methodology for multi-phase air/fuel measurements in a high pressure multi-hole GDI injector. In the proposed approach, previously developed UV-excitabile Bis-MSB tracers are used to seed the gas phase with the naturally occurring droplets in the fuel used as tracers for the other phase. The co-registration offered by the selected 3CCD colour camera (Hitachi HV f22f) enabled images recorded in the three colour planes to give flow constituent as well as pulse order information using standard solid state lasers and a 532nm-pumped pulsed dye laser. Details of the experimental setup including fuel selection, spray rig, optical setup and the use of a second colour camera for stereo measurements are also included.

6.1. Fuel selection and injection system

It is a common practice during research and development of fuel injectors to use idealised fuels since these have a simpler and well documented chemical structure. Idealised fuels are also important in applications involving fluorescent tracers where the use of UV illumination could produce undesired fluorescence from some of the additives present in commercial gasoline. It is, by all means, necessary for these idealised fuels to have similar atomisation and spray break up properties to those of gasoline; consequently fuel selection needs to be done carefully.

Heptane was selected as the working fuel because previous published work comparing the dynamics of different fuels concluded that it best represents the spray morphology and droplet dynamics of gasoline in GDI injectors. Mie imaging and Phase Doppler measurements were reported from a GDI pressure swirl injector; different fuels were tested (including commonly used fuels in spray research such as heptane and iso-octane) and it was concluded that the spray dynamics of heptane, in terms of penetration rates and velocity profiles, were the closest match to those of gasoline (Wigley et al. 2006). Additionally, the Society of Automotive Engineers (SAE) has published a recommended practice for gasoline fuel injector spray measurement and characterisation in which n-heptane is listed as one of the test fluids (Hung et al. 2008).

The fuel delivery system consists of a high pressure 6-hole Bosch GDI injector (17.5cc/min, 0.5mm nozzle diameter) mounted in a rig with a fused silica barrel providing optical access. The glass barrel provides the same geometric boundary conditions as present in a conventional thermodynamic engine. Therefore, demonstration of the diagnostics in the rig implies that they can also be applied in a full optical engine. A multi-hole injector was selected over a single-hole injector given that, as established in Section 2.2.6, recent research on GDI injectors has focused on the development of multi-hole injectors to be used in spray-guided combustion systems. The fuel injector and the glass barrel are shown in Figure 6-1.

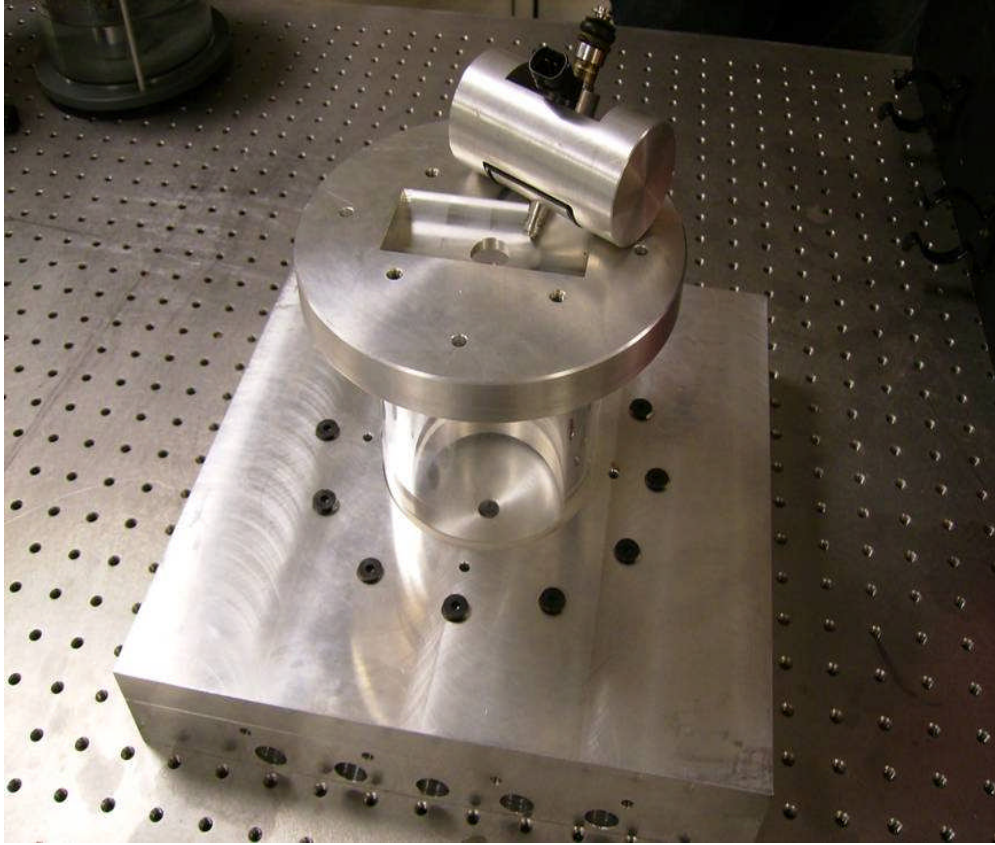


Figure 6-1 Fuel injector and spray rig system

Fuel was pressurised using a sphere which is part of the hydropneumatic suspension used in Citroën cars. A diaphragm in the sphere is expanded under pressure from a regulated flow of nitrogen which then pressurises the fuel; a pressure gauge is attached to the sphere to have an initial estimation of fuel pressure. A pressure transducer (General Electric PMP 1400) was also used to give more accurate control over fuel pressure (compared to that from the pressure gauge attached to the sphere). The transducer has a range of 0 to 250 bar for a 0 to 5 volts output which covers the entire required operating range for the experiments; the output voltage was displayed on a Keithley 179 A TRMS multimeter.

A deadweight tester was used to calibrate the transducer in the 0-70 bar range; Figure 6-2 below shows the calibration line obtained.

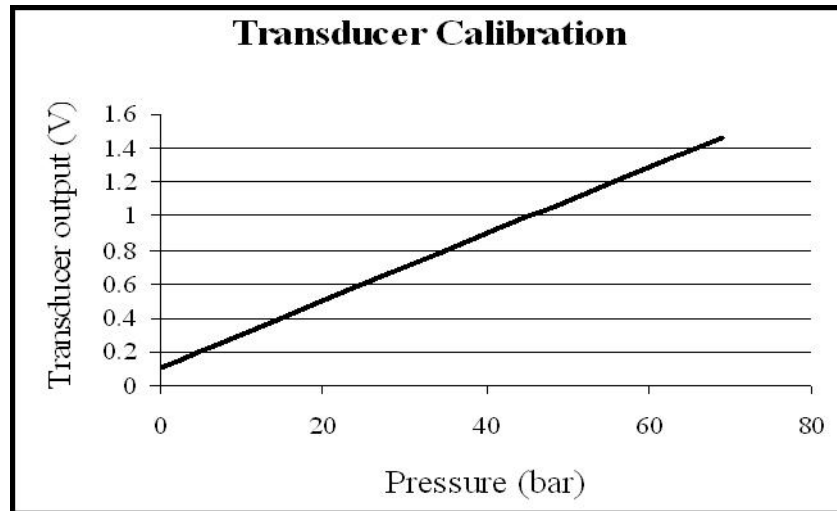


Figure 6-2 Calibration line for pressure transducer

Injector opening time was controlled by sending a negative 10V pulse to the control unit. The width of this pulse was the injection duration; in practice, however, actual fuel delivery time may not be equal to the injection pulse width due to mechanical opening and closing of the injector (Hung et al. 2008). A 555 monostable timer circuit with a tactile switch was implemented to obtain single injections to avoid quick accumulation of fuel on the glass barrel surface which would be obtained if the injector was open continuously for every laser pulse; this also allowed the synchronisation of each individual injection with the repetition rate of the lasers (10Hz) and the camera.

6.2. Use of an absorber in the fuel

The use of a wavelength selective absorber is presented in this chapter as a means of reducing the effects of multiple scattering within the dense spray (Section 3.6) and reducing the intensity of the light scattered by the larger fuel droplets. Advice in the selection of fuel absorber was provided by our collaborators at the School of Chemistry, University of Edinburgh (Mourad Chennaoui and Dr Anita Jones). Flow constituent identification in the fuel/air system was achieved by adding micron sized UV-excitable Bis-MSB tracers (emitting in the blue colour channel) to the gas phase and the naturally occurring fuel droplets acted as tracers for the liquid phase. More details on the properties of Bis-MSB, its emission, efficiency and applications have been discussed in Chapters 4 and 5 and can also be found elsewhere [(Chennaoui et al. 2008) and (Angarita-Jaimes et al. 2008)].

Red and green Mie scattering was used to identify the fuel (the optical setup is described in Section 6.5.1).

The difference in the particle size of the two phases (up to $\sim 30\mu\text{m}$ for the fuel and $\sim 1\mu\text{m}$ for the gas phase) produces a substantial difference in Mie scattering intensity levels (approximately proportional to the square of the particle diameter) and exceeds the dynamic range of the 3CCD, 8-bits per channel colour camera (up to 255 greyscale intensity values). Hence to balance the scattering levels an absorber was added to the fuel to reduce its scattering intensity. The addition of the absorber allowed images with a sufficiently high signal to noise ratio to be obtained from the gas phase seeding whilst avoiding over exposure in the fuel phase or, in the dense area of the spray where fuel is not fully atomised, obtain clear particle images.

6.2.1. Required characteristics for the absorber

The desired characteristics for the absorber are a strong absorption in the 500 – 650 nm range (green to red Mie scattering) and a high solubility in heptane (a non-polar solvent) which rules out several commercially available dyes/absorbers best suited to be mixed with polar solvents.

Due to the reduced sensitivity of the Hitachi HV f22f camera in the red channel (0.6 relative to green as previously discussed in Section 5.2) higher red energy, when compared to green, will be required for the scattering of the air tracers. Whilst the energy can be obtained from the laser source, this has the disadvantage of further increasing the multiple scattering in the fuel phase and the range of intensities present due to the quadratic relationship between particle diameter and Mie scattering. Hence it is also desirable for the absorber to have a higher absorbance in the red spectrum to account for this difference in channel spectral response.

Different commercially available dyes were considered and the BASF Sudan 673 dye was selected. This dye is commonly used to colour petroleum derivatives and is supplied as a highly concentrated solution in xylene to ensure optimum solubility in organic solvents.

The Sudan 673 dye was mixed with heptane resulting in a solution consisting of 1 part of dye per ten parts of heptane. This ratio was obtained empirically by mixing the heptane and the Sudan 673 (gradually increasing Sudan 673 volume) until it was found, after putting the mixture in an ultrasonic bath for 30 minutes, that some of the Sudan 673 remained unmixed hence no more dye could be added to the heptane. The absorbance of the new solution was measured using an Ultraviolet-visible spectrophotometer; hexane was used as the solvent with 5 different concentrations measured: 5, 15, 25, 35 and 50ppm; the results are shown in Figure 6-3 below. The absorbance measurements were carried out by Mourad Chennaoui from the University of Edinburgh.

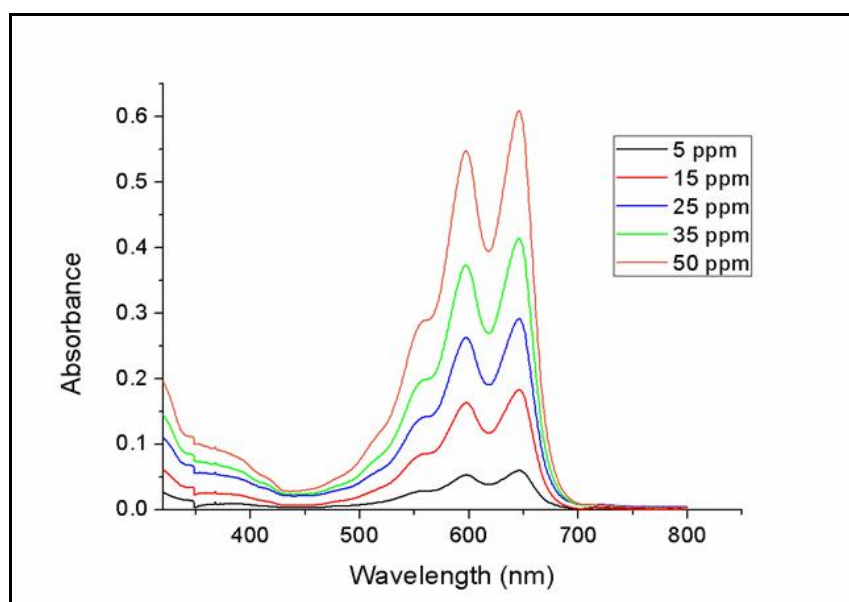


Figure 6-3 Absorbance measurements for Sudan 673 dye in hexane. Data obtained by Mourad Chennaoui, School of Chemistry, University of Edinburgh

The absorbance from the new mixture shows that it absorbs in the required red/green range; whilst the absorption peaks do not exactly match the peak emission of the dye laser (see Figure 6-14) the absorption properties of the new mixture will help match the scattering intensities of the two dyes since it still covers the required range. Figure 6-4 shows red Mie scattering of heptane before and after it is mixed with the absorber; both images were recorded using the same camera and laser energy settings. It is clear how the Mie scattering intensity has been considerably reduced making it possible to use higher laser energy for illumination and also being able to obtain sharp images in regions that were previously saturated.

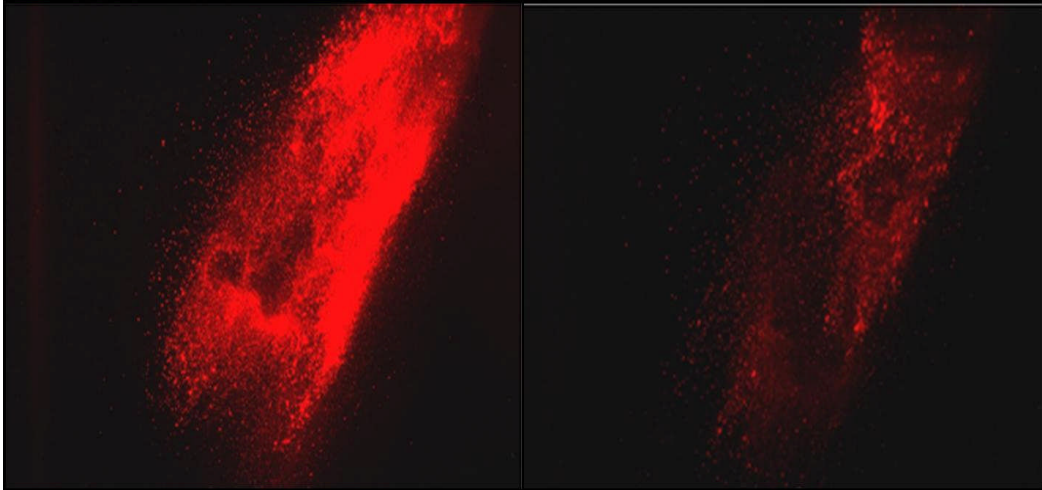


Figure 6-4 Heptane Mie scattering before (left) and after being mixed with the Sudan 673 absorber

Figure 6-5 and Figure 6-6 show the new scattering levels of both the gas phase tracers used to seed the air and the atomised fuel droplets (the vertical lines in the gas phase tracer images are from internal reflections generated by the glass barrel that encompasses the experiment). Fuel corresponds to the mixture of heptane + absorber and the air phase corresponds to the Bis-MSB tracers under experimental conditions. The images were taken consecutively using the same laser energy and camera settings for red and green lasers respectively: first the seed was drawn into the glass chamber to take the first image (left) then the flow was stopped to subsequently inject the heptane + absorber mixture.

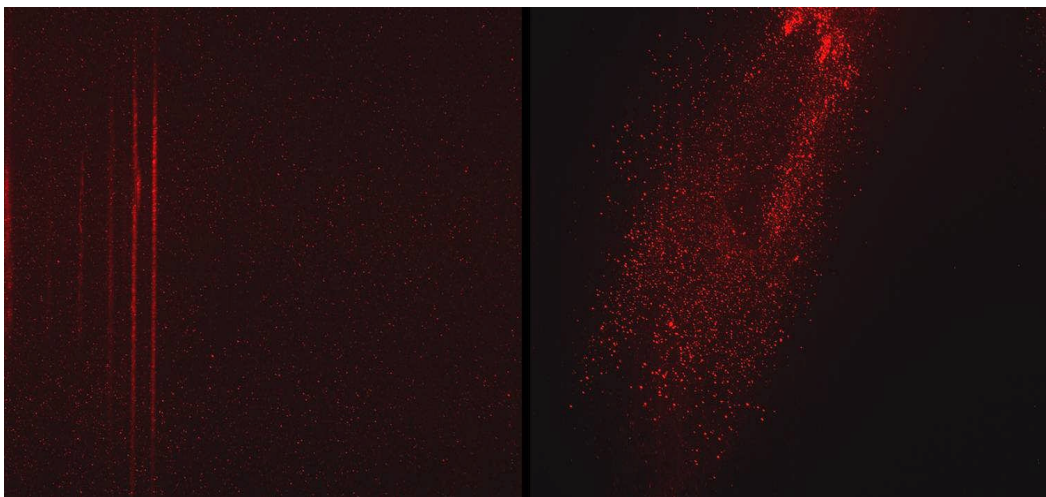


Figure 6-5 Scattering of gas (left) and fuel phase (right) in the red channel

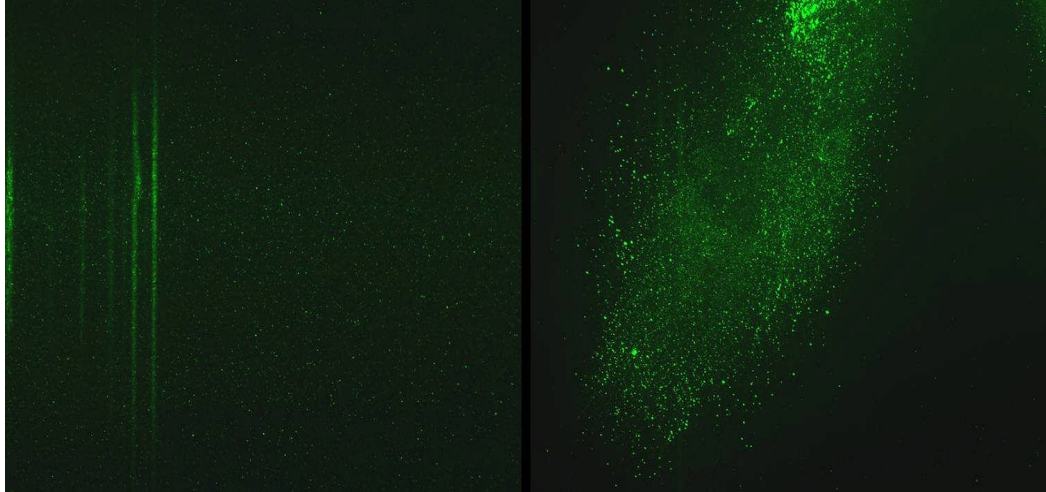


Figure 6-6 Scattering of gas (left) and fuel phase (right) in the green channel

From Figures 6-5 and 6-6 it is observed that the scattering intensity in the fuel has effectively been reduced; it is now possible to obtain a sufficiently high scattering intensity from the air tracers and also clear particle images in the fuel phase. Some image saturation was still obtained in certain areas of the fuel particle images, however it was still possible to obtain vector maps from these images using the cross correlation algorithm in DaVis 7.2.

6.3. Spray morphology and velocity measurements

Spray morphology (penetration rate and cone angle) and velocity measurements were performed on the new mixture (heptane + absorber) to ensure it still correctly modelled gasoline dynamics in a GDI injector.

6.3.1. Penetration rate and cone angle measurements

Penetration rates and cone angle were measured for a commercial gasoline and the mixture of heptane + absorber under the injection pressures to be used in the multi-phase experiments: 30 and 54 bar. Images were taken at 5 different timings after the start of the injection and until the jets were fully developed. A frequency doubled Nd:YAG laser was used for illumination and a Hitachi HV f22f camera focused with a Nikon 55mm lens was used to record the scattered light. Distortions (mainly astigmatism) in the images introduced by the glass barrel were corrected

using a meniscus cylindrical lens ($f=4030$ mm) placed in front of the camera (Reeves 1995).


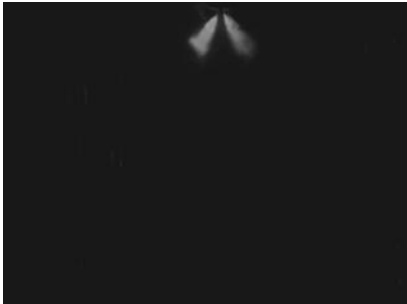
The different timings (delay between start of injection opening and laser pulse) used for each injection pressure are summarised in Table 6-1 below.

Table 6-1 Different timings used for spray morphology experiments

Pressure	Injection duration (ms)	T1 (ms)	T2 (ms)	T3 (ms)	T4 (ms)	T5 (ms)
30 bar	1.34	0.456	0.681	0.906	1.131	1.356
54 bar	1.46	0.456	0.731	1.006	1.281	1.556

Fifty images were recorded for each injection pressure and at each time delay for both gasoline and the heptane + absorber mixture; the images were then averaged and the results are shown in Table 6-2 for 30 bar and in Table 6-3 for 54 bar injection pressures for heptane + absorber (left column) and gasoline (right column) respectively.

Table 6-2 Temporal evolution of heptane + absorber (left column) and gasoline (right column) penetration rate and cone angle at 30 bar for the delays in Table 6-1 starting from T1 (top row) and then down to T5 (bottom row)

Absorber 30 bar	Gasoline 30 bar
	

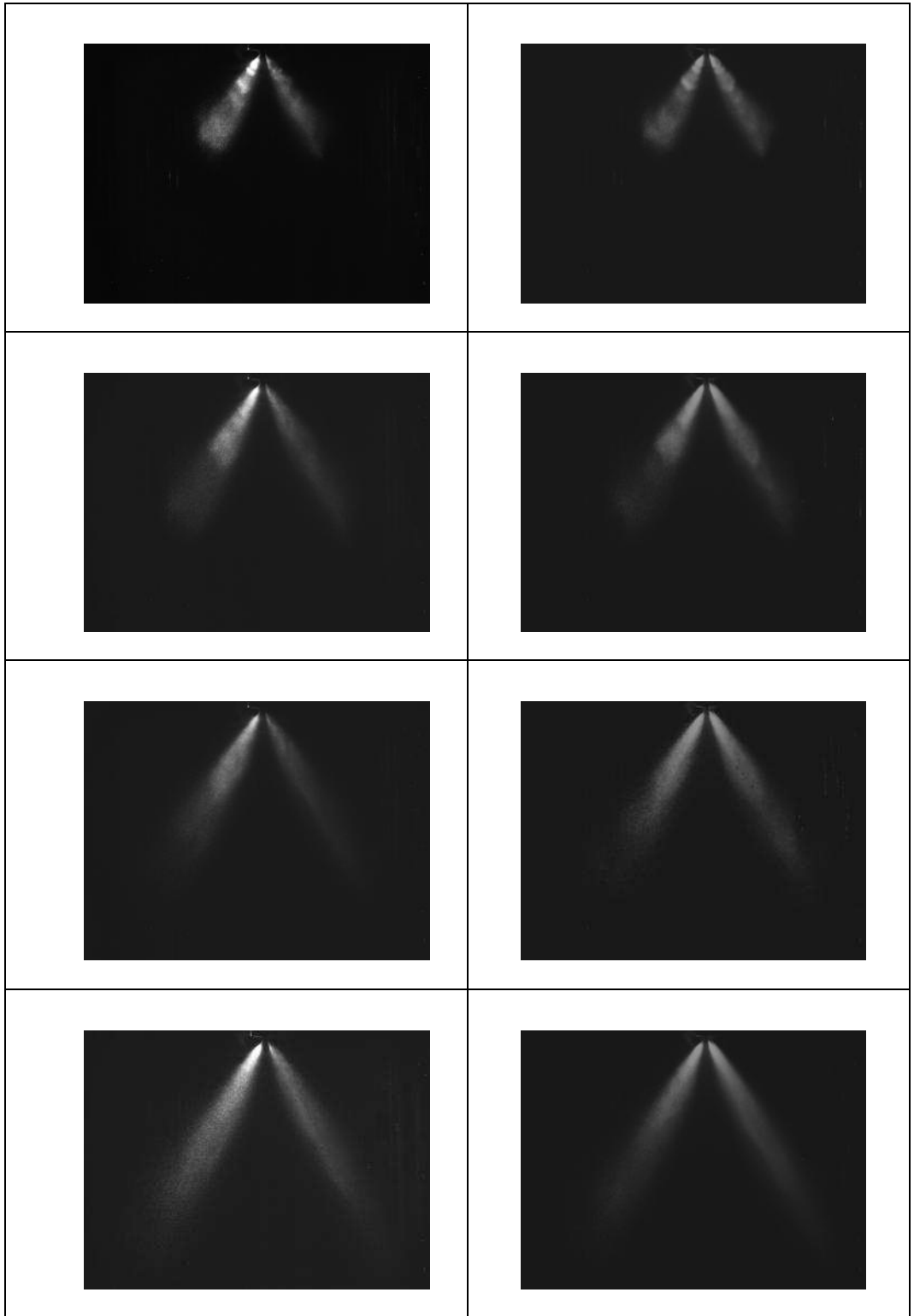








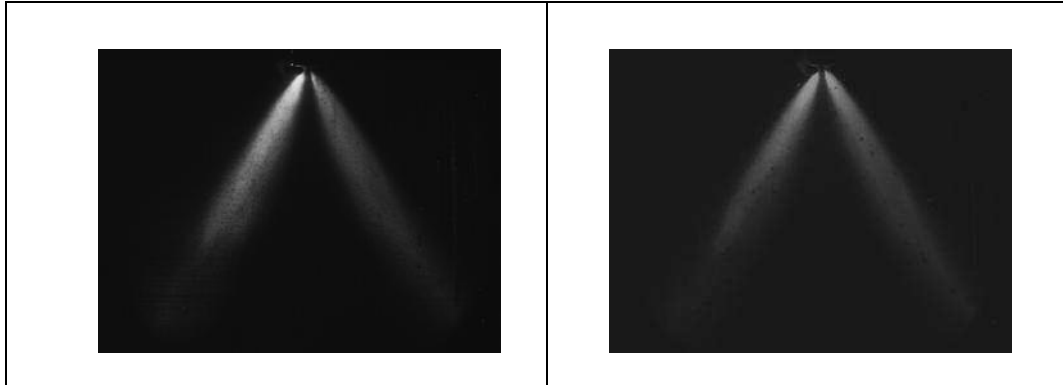


Table 6-3 Temporal evolution of heptane + absorber (left column) and gasoline (right column) penetration rate and cone angle at 54 bar for the delays in Table 6-1 starting from T1 (top row) and then down to T5 (bottom row)

Absorber 54 bar	Gasoline 54 bar
	
	
	
	



Axial penetration and cone angle (left spray half angle according to the recommended practice of (Hung et al. 2008)) were measured directly on each of the images above for the left hand side jet aligned to the laser sheet (see Section 6.4). Results are summarised in Table 6-4 and Table 6-5 below and the penetration is plotted against time in Figure 6-7.

Table 6-4 Axial penetration in mm for heptane + absorber and gasoline at 30 bar

	T1	T2	T3	T4	T5
Gasoline	5.9	17.5	25.9	32.1	38.4
Heptane+Absorber	6.5	16.8	26.1	31.8	38.8

Average cone angle: 22.83 degrees for gasoline and 21.14 degrees for heptane + absorber.

Table 6-5 Axial penetration in mm for heptane + absorber and gasoline at 54 bar

	T1	T2	T3	T4	T5
Gasoline	7.7	23.1	33.0	38.4	42.2
Heptane+Absorber	7.8	22.2	32.0	38.1	42.7

Average cone angle: 22.54 degrees for gasoline and 21.48 degrees for heptane + absorber.

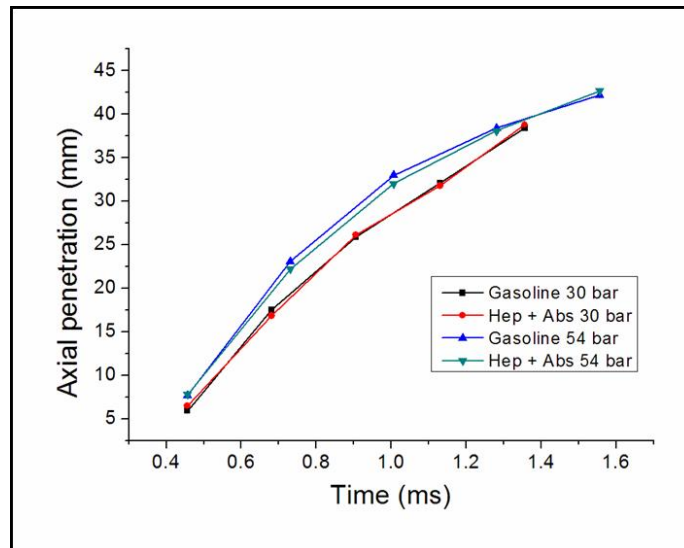


Figure 6-7 Axial penetration for heptane and gasoline at 30 and 54 bar

The difference in average cone angle measured for gasoline and heptane + absorber is approximately 1 degree. The resolution of the cone angle data is limited by the pixel size in the captured images. It is estimated that with an uncertainty in estimating the edge of the cone at 1 pixel and over a distance from the nozzle of 50 pixels, the uncertainty in cone angle is approximately 1 degree. Therefore, the difference in data for the two fuels is not significant.

The results obtained agree with previously obtained data (Wigley et al. 2006) and the penetration for gasoline and heptane + absorber are virtually the same (gasoline penetrates slightly faster than heptane + absorber which is more evident at 54 bar). Hence it can be concluded that the new combination of heptane + absorber atomises in a sufficiently similar manner to commercial gasoline for it to be used in these experiments.

6.3.2. Velocity measurements

PIV measurements have been taken under the same injection pressures to compare the dynamics of gasoline and the heptane + absorber mixture and to complement the penetration and angle measurements performed in the previous section. Fifty images were taken for a delay corresponding to end of injector

opening and vectors were processed using DaVis 7.2 from LaVision. An average vector field was calculated from the 50 instantaneous realisations for each condition and the results are shown in Figure 6-8 for 30bar and Figure 6-9 for 54bar. For each set of images the first vector map (A) corresponds to absorber + heptane, the second (B) to gasoline and the third (C) is the result of subtracting the gasoline vector map from the absorber vector map.

The mean velocity of the valid vectors in each field has been used to calculate the difference between the two vector maps at each condition defined as follows:

$$diff = \frac{mean_{absorber} - mean_{gasoline}}{mean_{gasoline}} \times 100 \quad \text{Equation 6-1}$$

The following results have been obtained after applying Equation 6-1 to the vector fields shown in Figure 6-8 and Figure 6-9:

- 30bar: 7%
- 54bar: 1%

The difference velocity fields (vector field C in Figure 6-8 and Figure 6-9) show two different patterns. For 30bar there is a near uniform low velocity across the entire vector field (Figure 6-8) which indicates the velocity distribution is similar for both heptane + absorber and gasoline. On the other hand, for 54bar there is a near zero velocity across the middle (Figure 6-9) with higher velocities on either side. There are two possible explanations for this; one would be a difference in injection angle with the heptane + absorber mixture but, as it was found in Section 6.3.1, the cone angle is virtually the same for both fuels. The difference in velocity may also be explained by a small lateral shift which can be obtained during the change of fuels and rig cleaning given it needs to be disassembled to clean the glass barrel after several injections; hence it cannot be guaranteed that the camera image will be exactly in the same position after it is assembled again and a small lateral shift may be obtained which may explain the difference velocity field in Figure 6-9 C. Nevertheless, from a visual inspection of the vector fields, the mean differences and the cone angle and penetration results, it is concluded that the heptane + absorber mixture presents atomisation and velocity properties which enable it to be used as a substitute of gasoline for these experiments.

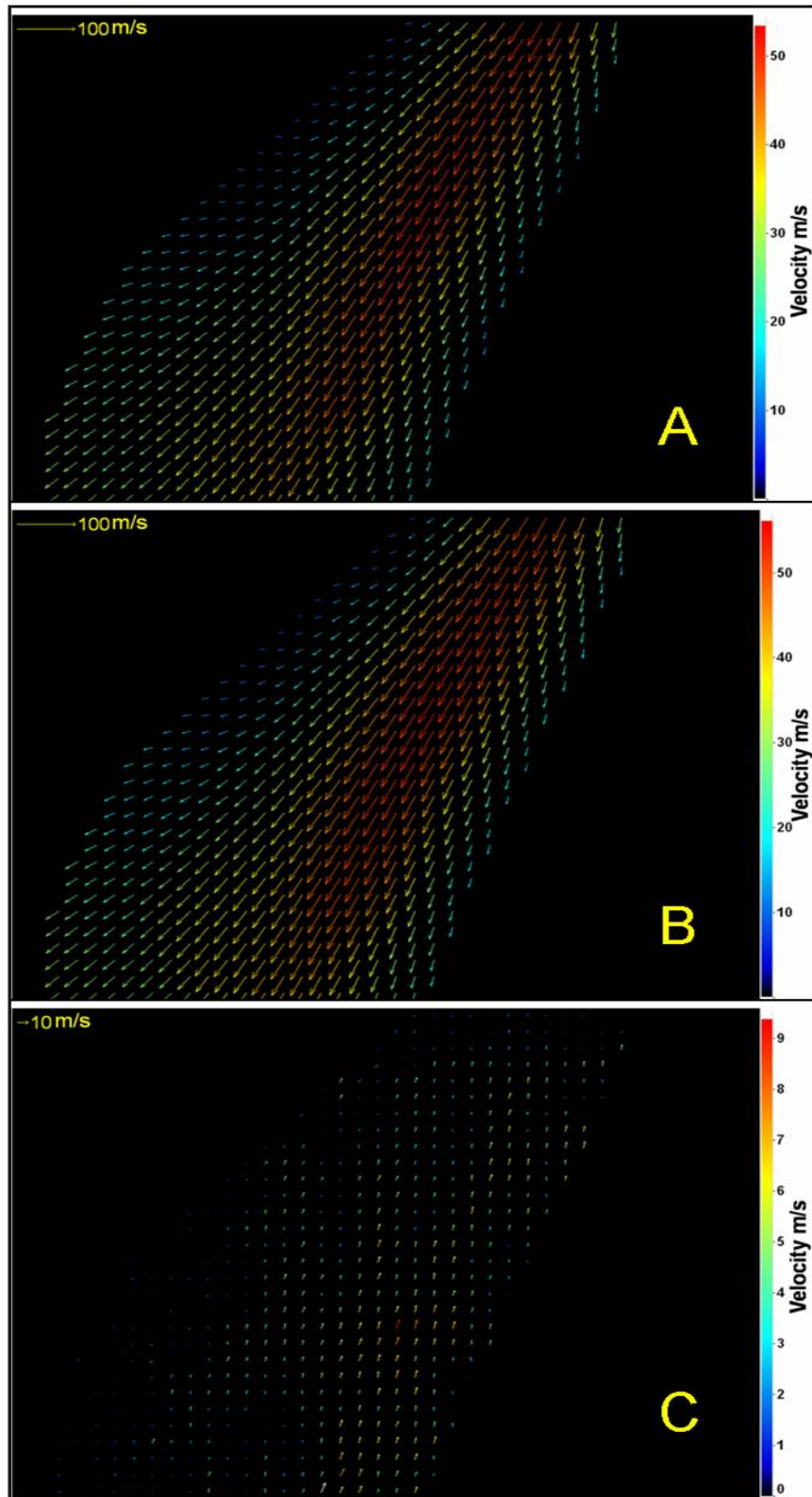


Figure 6-8 Vector fields for absorber (A), gasoline (B) and difference A-B (C) at 30 bar full injection

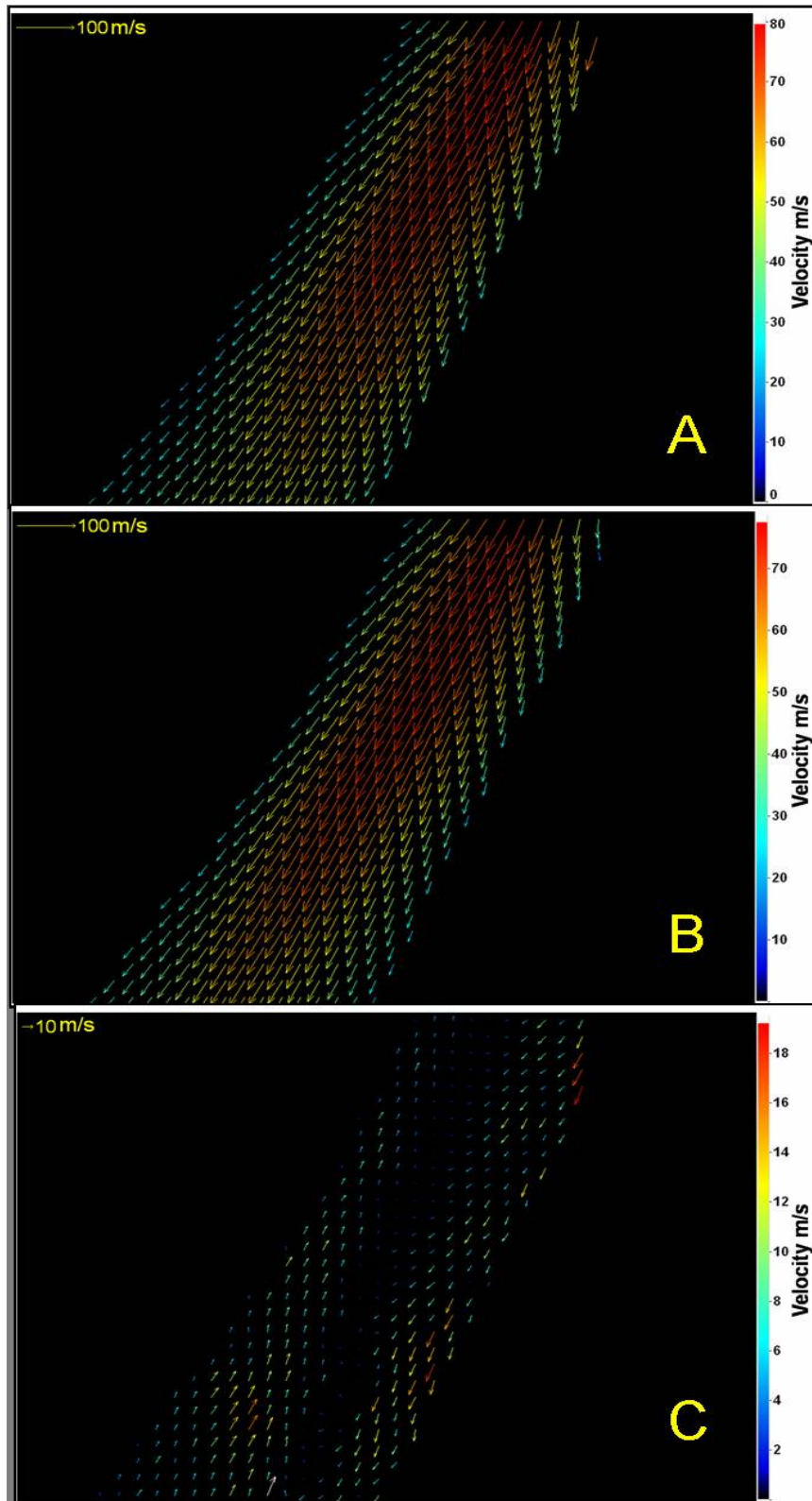


Figure 6-9 Vector fields for absorber (A), gasoline (B) and difference A-B (C) at 54 bar full injection

6.4. Characteristics of fuel jets

Figure 6-10 shows in detail the characteristics of the 6-hole injector used for the experiments.

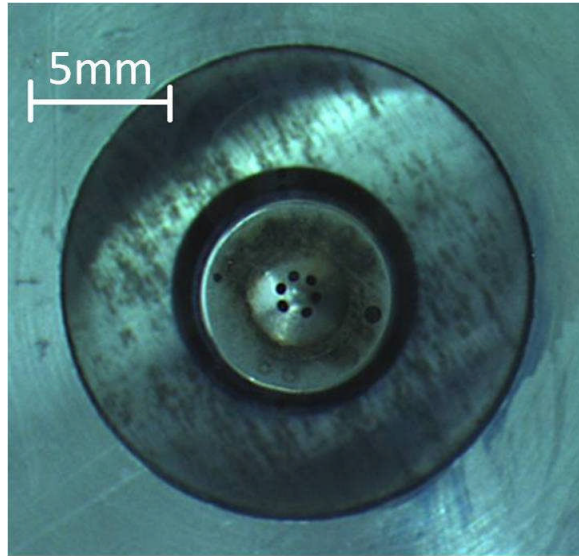


Figure 6-10 Detailed view of multi-hole GDI injector

Although the 6 holes in the injector do not seem to be overly asymmetrical, the six jets produced are directed mainly towards $\frac{3}{4}$ of a circle (or $\frac{3}{4}$ moon shape as referred to by (Aleiferis et al. 2010) in their work on a similar injector) in the fused silica barrel (thinking of the fused silica barrel as the engine cylinder). This pattern, in principle, is advantageous because the laser can be aligned to the first jet for illumination. Figure 6-11 shows a schematic representation of the spray pattern and the 'wetted footprint' (Hung et al. 2008) from below the injector tip. The six jets have been numbered starting from the jet to which the laser was aligned as shown in Figure 6-11 on the right hand side image. The objective of Figure 6-11 is to show the circumferential position of each jet relative to one another below the injector tip given this will influence subsequent measurements.

One of the requirements of GDI injectors is to have a good spray axis symmetry over the engine operating range (Zhao et al. 1999b); from Figure 6-11, an imaginary black dotted line between jets 3 and 4 and going through the injector tip represents the axis of symmetry for the injector with three jets on either side.

Given the symmetry axis of the injector lies in between two jets (rather than through the middle of them), if one jet is aligned to the laser sheet and the injector tip, the other jet being illuminated in the same vertical plane will not be totally aligned with the laser sheet (the laser will not go through the middle of the jet). Therefore if the laser is aligned through the middle of jet 1 and the injector tip, it will not go through the middle of jet 5 but this jet will still be illuminated. Multi-phase PIV measurements were taken in two fuel jets on the same vertical plane, jets 1 and 5 on Figure 6-11; the 3 red, green and blue lines through jets 1 and 5 show the plane illuminated by the laser sheet.

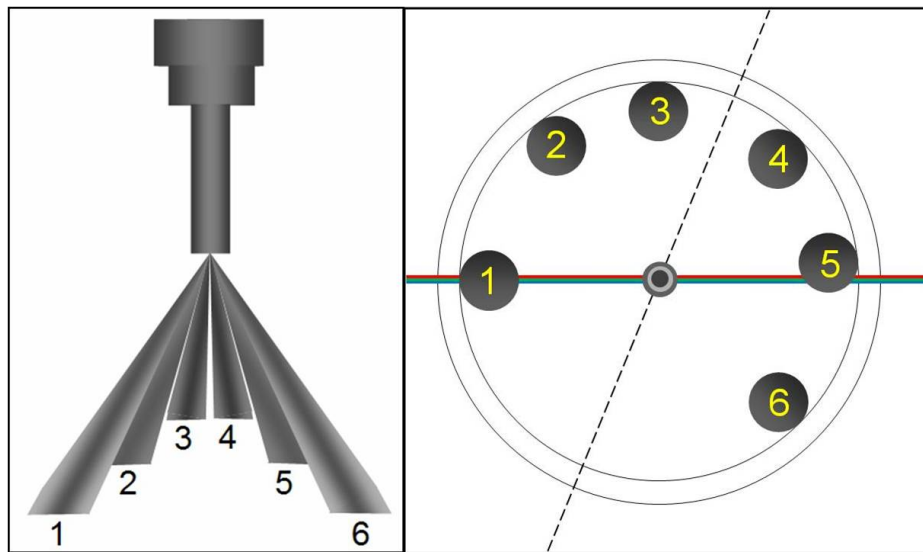


Figure 6-11 Fuel jets from multi-hole GDI injector and wetted footprint showing axis of symmetry

The effect of the absorber colour also needs to be considered; the Sudan 673 dye is dark blue in contrast to the yellowish colour of gasoline and transparent of heptane resulting in a dark blue heptane + absorber mixture. In the plane where the measurements were taken, when jet 5 was illuminated, jet 6 obstructed the viewing path and therefore reduced the quality of the recording (the dark colour of the dye obscured the image).

Images have been recorded of jets 1 and 5 in the same vertical plane where velocity measurements were later taken for a commercial gasoline (Figure 6-12) and the heptane + absorber mixture (Figure 6-13). For the heptane + absorber mixture, jet 5 is slightly dimmer (foggy appearance), and with fewer clear particle images when compared to gasoline, due to jet 6 being in front of it.

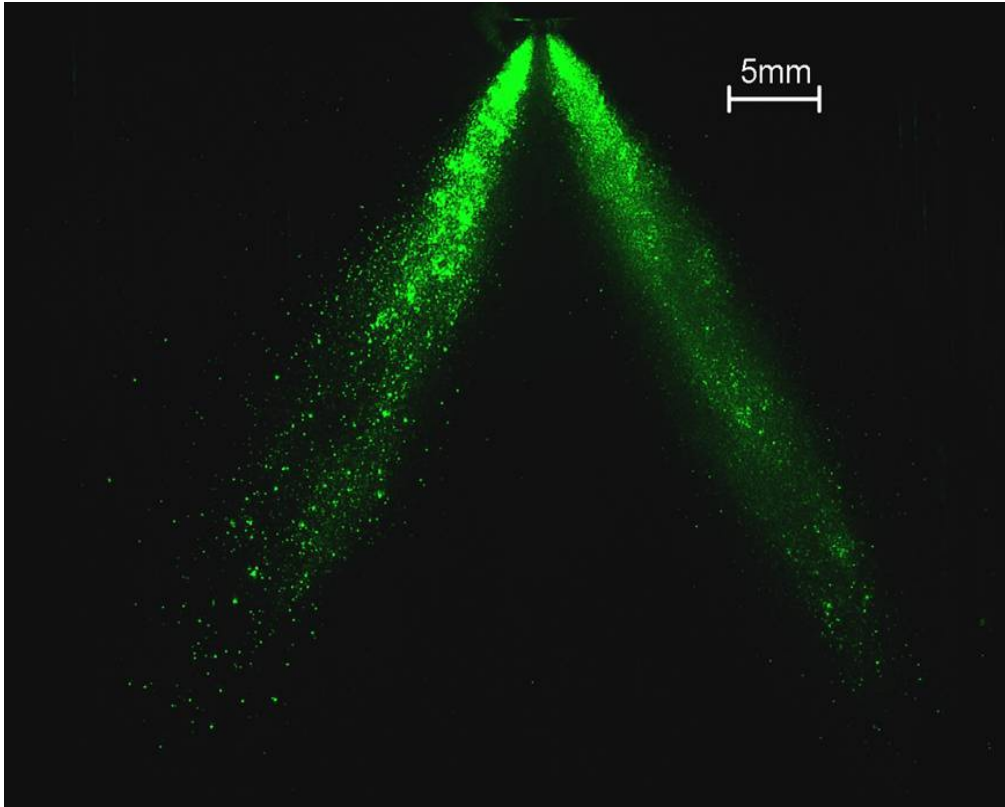


Figure 6-12 Gasoline jets 1 (left) and 5 (right) under 532nm illumination

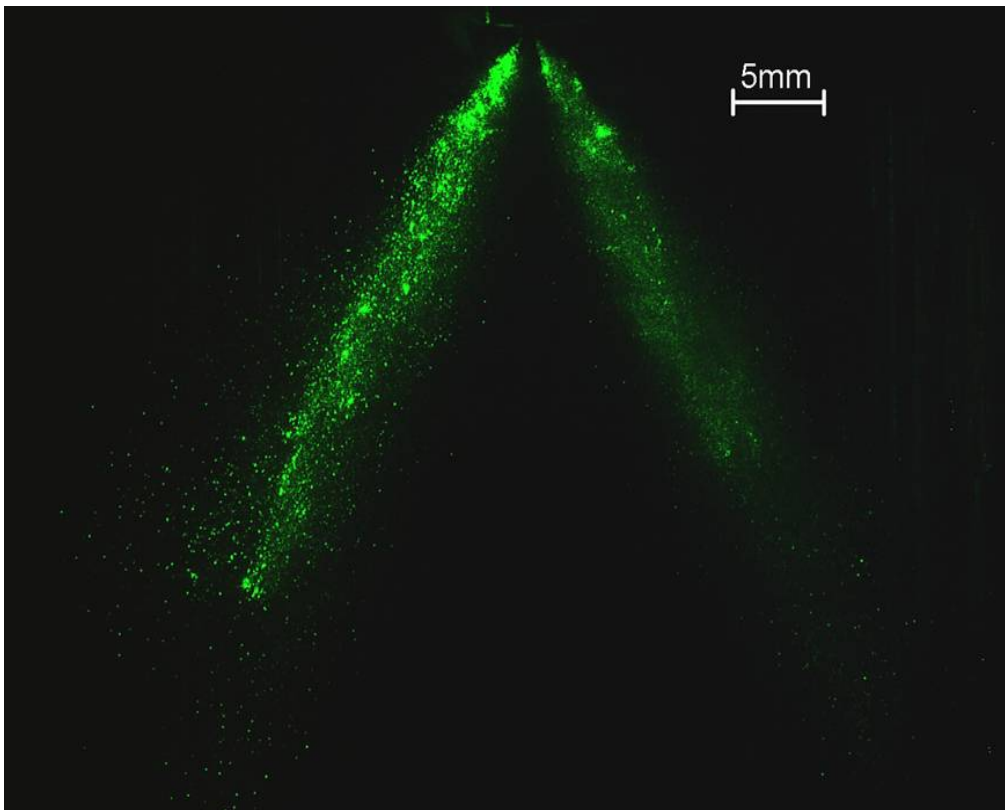


Figure 6-13 Heptane + absorber jets 1 and 5 under 532 nm illumination

It was still possible to obtain velocity data in jet 5 but there were fewer valid vectors in each instantaneous vector field compared to those for jet 1.

6.5. TWO PHASE AIR/FUEL EXPERIMENTS

6.5.1. Optical Setup

Experiments were performed using a combination of a solid state laser and a dye laser. An Nd:YAG laser (Continuum Surelite II-10) fitted with a doubling and tripling crystal provided both 532nm and 355nm wavelengths in a single spatially overlapping beam; a 532-pumped Quanta-Ray Pulsed Dye Laser with DCM dye (ethanol as the solvent) gave a pulse with an emission peak at 628nm .

The emission range from the 532-pumped dye laser was measured using a high resolution fibre optic spectrometer (Ocean Optics HR2000) and the result is shown in Figure 6-14 below; the peak in the spectrum is at approximately 628nm and the full width at half maximum (FWHM) range is 10nm .

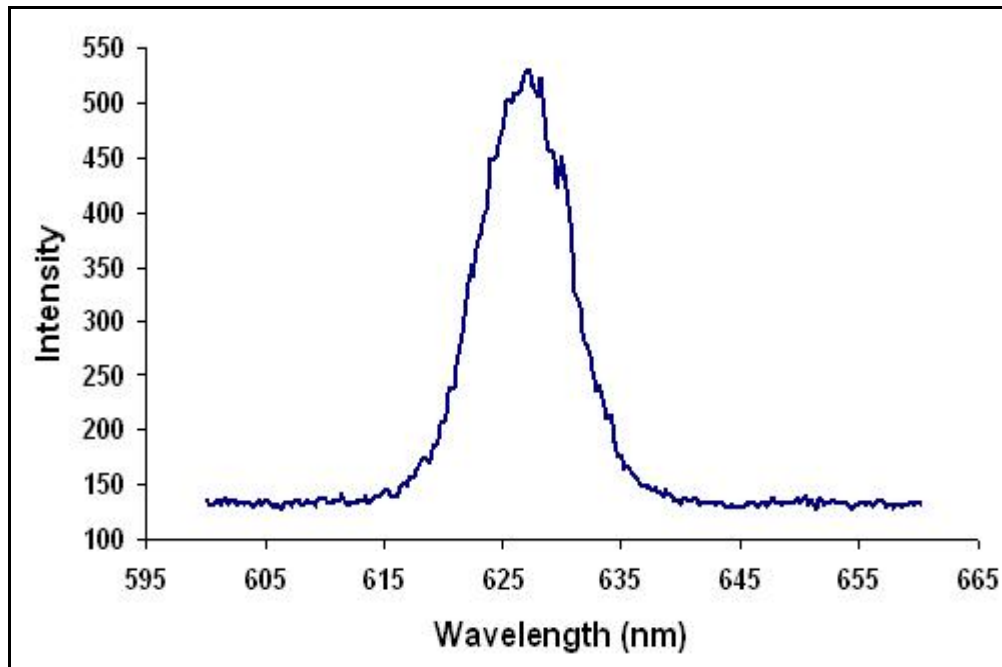


Figure 6-14 Emission spectrum from 532-pumped red dye laser

A dispersive fused silica 15 mm equilateral prism was used to separate the harmonics of the first pulse by refraction with the 532nm and 355nm components

subsequently realigned at the laser sheet focus. In order to align the foci of the 3 laser sheets it was required to expand each beam using separate plano-concave lenses at different distances relative to the common cylindrical lens. The three lenses ($f = -200\text{mm}$) were positioned in each beam and mounted on micro-blocks giving 3 axes of linear adjustment, to aid the alignment.

As previously detailed in Chapters 4 and 5, the correct alignment of the three laser sheets was obtained by placing a CCD camera (protected with a suitable ND filter) directly in the beam path thus giving a visual indication of their spatial overlap. This was also used to ensure the 3 beams were focusing on the same plane given that each beam was expanded using a separate plano-concave lens.

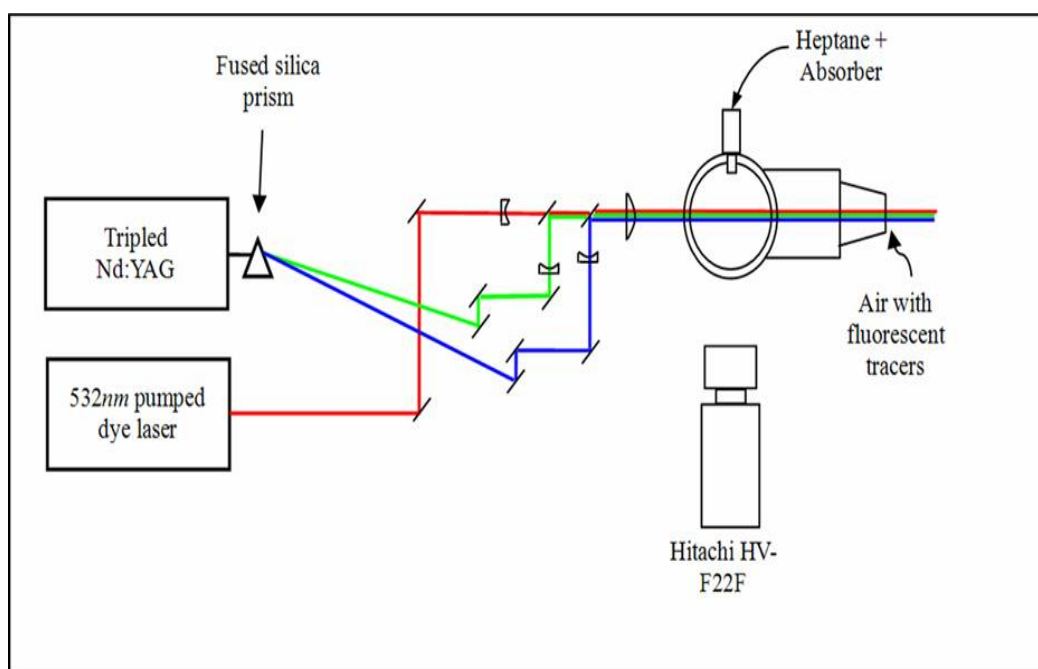


Figure 6-15 Schematic representation of experimental setup

Images were recorded using a Hitachi HV-F22F 3CCD colour camera (the same camera as used in the multi-constituent experiments in Chapter 5). A Nikon 60mm lens was used with the aperture set at F#11 to obtain a sharp focus on the three colour planes simultaneously. Brightness and contrast on the camera were adjusted to control noise levels with the red gain increased to compensate for the reduced sensitivity of the camera on the red channel. All the other parameters were left unchanged. Images were recorded at a resolution of 1360 x 1024 pixels.

Distortions in the images introduced by the glass barrel (mainly astigmatism) were corrected using a meniscus cylindrical lens ($f=4030$ mm) placed in front of the camera; its position and rotation relative to the camera were adjusted to obtain sharp images of the particles on the three channels.

6.5.2. Pulse order and exposure on CCD channels

The first pulse was red from the 532-pumped dye laser producing Mie scattered images from both types of tracers on the red channel. The second pulse was the overlapping 532nm and 355nm from the Nd:YAG laser; non-fluorescent (fuel + absorber) droplets produced images on the green layer and fluorescent particles (Bis-MSB droplets) produced images on the blue channel and the green channel. Figure 6-16 shows the exposures on each channel in the 3CCD colour camera.

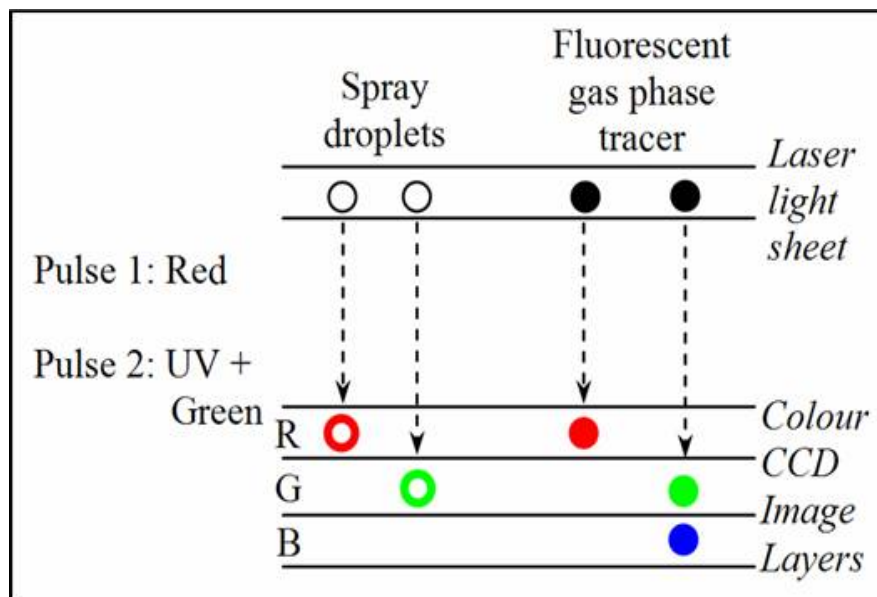


Figure 6-16 Pulse order and CCD exposure on colour camera

Any Mie scattered light from the UV laser sheet is blocked by a 400 nm long pass wavelength filter placed in front of the camera and is out of the colour spectrum of the Hitachi HV f22f camera shown in Figure 5-5.

6.5.3. Seeding Particles

A pressure-driven medical nebuliser (Med2000 Andy Flow) was used to generate Bis-MSB droplets (with the dye at a concentration of 10^{-2} M using *o*-xylene as the

solvent) to seed the gas phase; the droplets were fed into the glass chamber at a pressure of ~ 0.5 bar. More details on dye efficiency and its emission can be found elsewhere [Chapters 4, 5, (Chennaoui et al. 2008), (Angarita-Jaimes et al. 2008)]. A separate nitrogen cylinder and pressure regulator were used for the atomisation of the Bis-MSB droplets because it was found that using the same cylinder for the pressurisation of both fuel and seed would produce a fluctuation in the fuel injection pressure (shown in the digital readout of the transducer). By having separate nitrogen cylinders for fuel and seeding particles it was ensured that the fuel injection pressure would have a maximum variation of ± 0.5 bar (effectively $\pm 1.6\%$ for 30bar and $\pm 0.9\%$ for 54bar).

The droplet size of the Bis-MSB + o-xylene mixture was measured under experimental conditions using the same interferometric setup as that used in Chapters 4 and 5 giving a conversion relationship of 1.5 fringes per micron. Figure 6-17 shows a histogram (expressed as percentage) of the droplet size; an average droplet size under experimental conditions was calculated as $1.8 \mu\text{m}$.

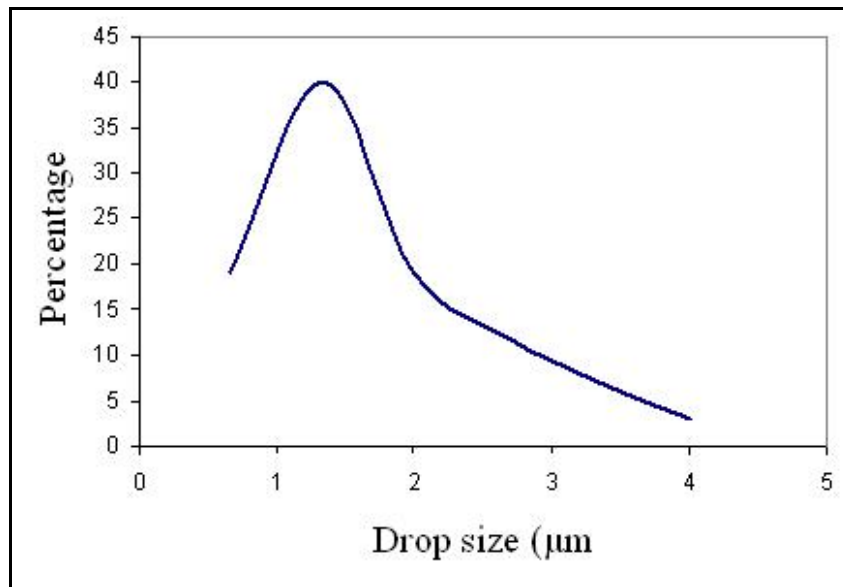


Figure 6-17 Bis-MSB droplet size distribution under experimental conditions

Gas phase PIV relies on tracer particles following the flow accurately (Melling 1997) hence the Bis-MSB particle response to the velocity changes expected in the experiments was analysed. Previous literature on air/fuel measurements (Dankers et al. 2008) found that the maximum velocity obtained in the gas phase was approximately 10 m/s with the majority of the vector field showing an average

velocity of 3-4 m/s. Naturally, air velocity will be affected by different experimental conditions such as injection pressure, injection duration and temporal development of the jet (early injection, end of injector opening and fully developed jet).

The capability of the experimental Bis-MSB droplet distribution to follow the air motion accurately can be assessed by solving the equation of motion (Equation 3-12) for a particle in a continuous fluid as described in section 3.4.2 for a step change in velocity of 10m/s:

$$\frac{dU_p}{dt} = \frac{3}{4} \frac{\rho_f}{d_p \rho_p} C_D (U_f - U_p)^2 \quad \text{Equation 6-2}$$

Where U_f and U_p are velocities of the fluid and the particle, ρ_f and ρ_p are the density of the fluid and the particle, C_D is the drag coefficient and d_p is the particle diameter. The Reynolds number for a particle relative to the fluid is defined as (Durst and Melling 1981):

$$\text{Re}_p = \frac{|(U_f - U_p)| d_p}{\nu_f} \quad \text{Equation 6-3}$$

Where ν_f is the kinematic viscosity of the fluid. The drag C_D coefficient has been evaluated using different approximations. The Stokes approximation is valid for spherical particles under the condition $\text{Re}_p < 1$ (Durst and Melling 1981) (Merzkirch 1987); for spherical particles in air at room temperature ($\nu_f = 15.68 \times 10^{-6} \text{ m}^2/\text{s}$), this approach is restricted to a maximum velocity change of 15.68 m/s for a $1\mu\text{m}$ particle, 7.84 m/s for a $2\mu\text{m}$ and 5.22 m/s for a $3\mu\text{m}$ particle. In the case of a change in velocity of 10m/s (assuming the tracer particles are quiescent before the change in fluid velocity), the Stokes approximation will not be valid immediately after the velocity change. (Melling 1986) developed a drag coefficient based on the Knudsen number Kn_p defined as:

$$C_{D,Melling} = \frac{24}{\text{Re}_p (1 + 2.7 Kn_p)} \quad \text{Equation 6-4}$$

where the Knudsen number is defined as:

$$Kn_p = l/d_p \quad \text{Equation 6-5}$$

where l is the molecular free path ($\sim 0.1\mu\text{m}$ for air).

The equation for the motion of the particle then becomes:

$$\left(\frac{dU_p}{dt}\right)_{Melling} = \frac{18\nu_f \rho_f}{d_p^2 \rho_p} \frac{1}{(1 + 2.7Kn_p)} (U_f - U_p) \quad \text{Equation 6-6}$$

which can be rearranged as:

$$\left(\frac{dU_p}{dt}\right)_{Melling} = C(U_f - U_p) \quad \text{Equation 6-7}$$

$$\text{where } C = \frac{18\nu_f \rho_f}{d_p^2 \rho_p} \frac{1}{(1 + 2.7Kn_p)} \quad \text{Equation 6-8}$$

Equation 6-7 can now be solved analytically to obtain an equation for the velocity of the particle (assuming $U_p(0)=0$ for the particles):

$$U_p(t) = U_f - U_f e^{-Ct} \quad \text{Equation 6-9}$$

Equation 6-9 can be then integrated to obtain an equation for the displacement of the particle (assuming $X_p(0)=0$ the particles):

$$X_p(t) = U_f t + \frac{U_f}{C} e^{-Ct} - \frac{U_f}{C} \quad \text{Equation 6-10}$$

The properties of the tracer particles are those of o-xylene which is the solvent used for the Bis-MSB fluorescent dye and the properties of the fluid are those of air at room temperature. Figure 6-18 shows o-xylene particle velocity against its corresponding displacement for a fluid velocity step change of 10 m/s (U_f) and a range of drop sizes. A displacement axis has been used in Figure 6-18 (rather than

a time axis) to assess velocity lag in terms of displacement so that it can be compared to the size of the interrogation window.

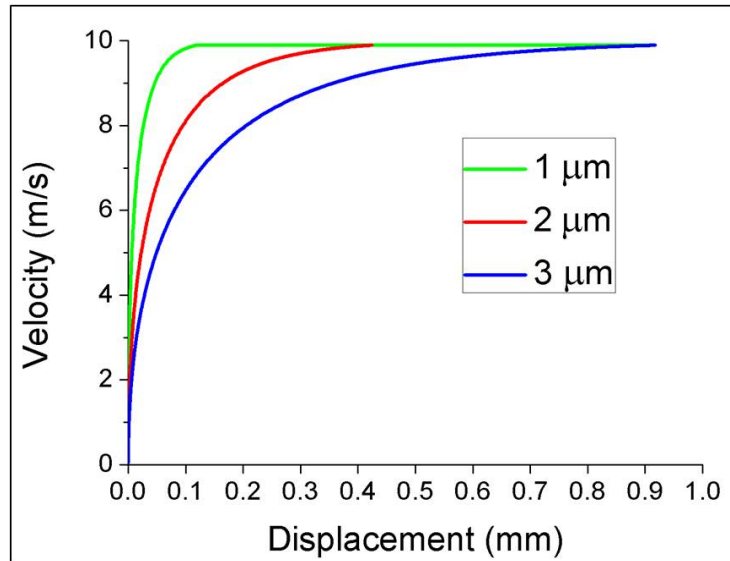


Figure 6-18 Bis-MSB particles response to a 10m/s velocity change

For the majority of the particles present, i.e. $< 2 \mu\text{m}$ there is very little difference in the particle response for hence it can be assumed that the particle distribution obtained in Figure 6-17 will follow the air motion appropriately for the expected velocities usually obtained in fuel injection measurements; this is also confirmed in Chapter 7 where gas phase velocities in the range plotted above are obtained. The velocity lag is $\sim 0.4\text{mm}$ for particles up to $2\mu\text{m}$ which is small compared to the size of the interrogation window later used in the PIV processing in Section 7.1.2.2 (128 pixels, $\sim 2.5\text{mm}$).

6.5.4. Image processing

Images were processed following the same procedure used in Chapter 5 for the multi-constituent measurements using the same colour camera. Crosstalk was accounted for as described in section 5.4.1. Separate images of blue fluorescence and red and green Mie scattering under experimental conditions were recorded; each image was then split into its RGB channels and the intensity of the particles was measured on the three channels to obtain the crosstalk coefficients in equation 5-1. These are shown in equation 6-11 below for the camera settings used under experimental conditions.

$$\begin{bmatrix} 1 & 0.18 & 0.2 \\ 0.18 & 1 & 0.2 \\ 0.19 & 0.2 & 1 \end{bmatrix} \quad \text{Equation 6-11}$$

Whilst the crosstalk from the blue channel to the red and green channel increased compared to equation 5-1 (to a still acceptable level) the other values remain similar. The crosstalk from the green to the red channel was significantly reduced primarily because no DCM tracers (red fluorescence) are used here hence there is no fluorescence emission from the 532nm pulse. Equation 6-7 was then inverted and the corrected intensities calculated across the images thus accounting for the crosstalk.

Chromatic and lens distortions were also corrected following the procedure described in section 5.4.2. Here instead of using a white-light-illuminated surface, images of the air tracers were taken with no pulse separation ($dt=0$, the 3 overlapping beams in one single laser pulse). The tracers were seeded into the chamber for a few seconds and then the nebuliser flow was stopped to then record the images; this was done to ensure tracers would be present everywhere across the image. The images were then corrected for crosstalk, split into their RGB channels and then processed in DaVis 7.2 using the same settings later used for to calculate the 2-phase vectors. For stereo measurements (see Section 6.6) the same procedure was repeated for the two colour cameras by taking images of air tracers for each camera separately because it was found the distortions showed a different pattern in each colour camera.

6.6. Stereo PIV Measurements

It is desired to have simultaneous 3-component velocity measurements in order to have a better understanding of the air/fuel interaction in GDI sprays. One of the main advantages of using a single camera approach for multi-constituent measurements is that it can easily be extended to stereo measurements by adding a second colour camera. Using the same experimental conditions described above, stereo measurements were taken on the same fuel jets.

6.6.1. Stereoscopic optical setup

The setup consisted of two Hitachi HV f22f 3CCD colour cameras in a stereoscopic arrangement. Each camera was positioned on a different side of the laser light sheet in order to obtain similar scattering levels (forward/forward configuration). This is due to the relatively small aperture (F#11) used to ensure the three colour planes were sharply focused simultaneously. If the conventional forward/backward configuration (both cameras on the same side of the laser sheet) was used, due to the differences in scattering level, the aperture in one of the cameras would need to be changed. If a larger aperture was used in one camera to balance the scattering levels, the three colour planes would not be sharply focused; on the other hand if a smaller aperture was used, there would be less light being recorded so the signal to noise ratio of the images would be reduced for the air tracers. Hence to maintain a high signal to noise ratio and similar light levels recorded by each camera, the 2 cameras were positioned on either side of the laser sheet (forward/forward configuration).

Scheimpflug lens arrangements were used on both cameras to ensure all areas of the image were in focus due to the imaging angles required. Imaging through the glass cylinder introduced additional aberrations which were partially compensated by the use of the corrective lens as previously described in section 6.5.1. The remaining aberrations were accounted for using a polynomial mapping function (van Doorne and Westerweel 2007) and (LaVision 2007). Figure 6-19 below shows a schematic representation of the stereoscopic experimental setup.

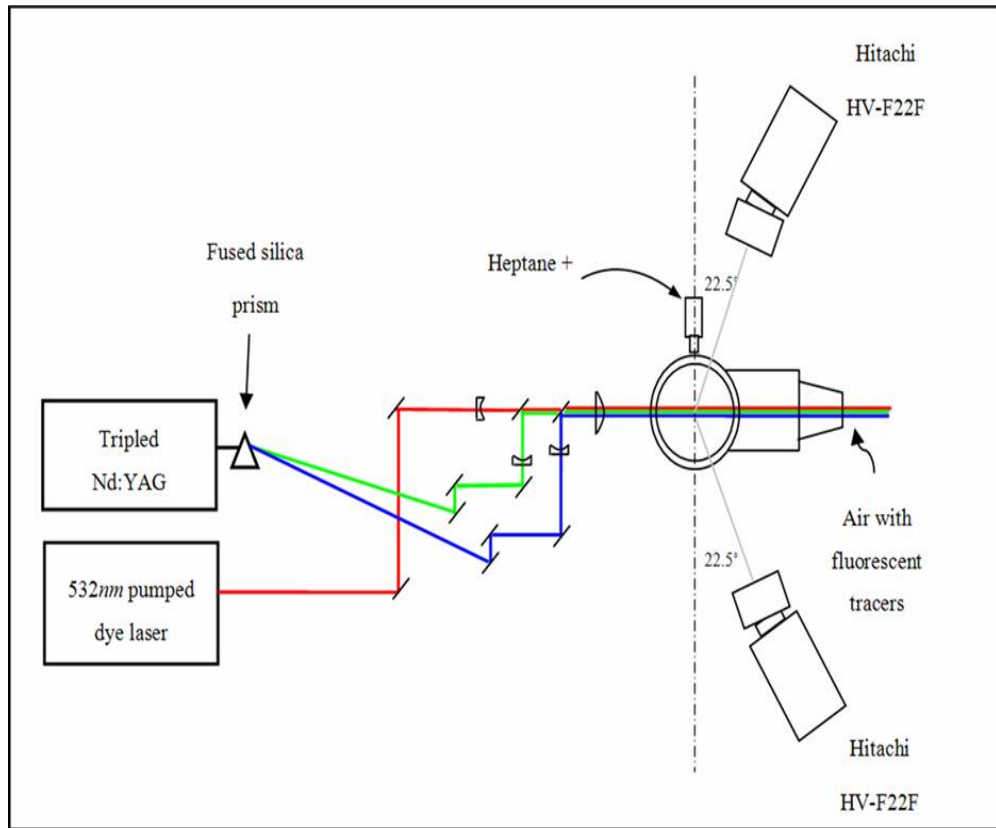


Figure 6-19 Schematic representation of Stereo PIV setup

6.7. Summary

This chapter has described the required experimental setup for multi phase air / fuel simultaneous measurements in a GDI spray.

New developments such as the use of an absorber in the fuel phase to reduce its scattering intensity have been introduced. Velocity measurements on top of the conventional penetration rate / cone angle measurements have been presented to ensure that the modified fuel, heptane + absorber, can be used as a replacement for gasoline in the experiments.

The single camera approach was then applied to obtain 3-component measurements by adding a second colour camera in a stereoscopic arrangement. The proposed setup has the advantage of being simpler than that which would have been required in the multi-camera approaches for 2C velocimetry reviewed in Section 3.5.2. Due to the experimental complexity of the

system, 2C multi-camera approaches have not yet been extended to stereo measurements.

Chapter 7 presents the results of the multi-phase air / fuel experiments obtained with the setup described in this chapter.

Chapter 7

TWO-PHASE MEASUREMENTS IN A GDI SPRAY - RESULTS

A new experimental setup for the simultaneous acquisition of multi-phase air/fuel data was described in Chapter 6 based on the imaging approach presented in Chapter 5 for two-constituent gas phase flows. The results obtained for a GDI multi-hole injector are presented in this chapter. First, 2C vector fields for air and fuel are presented; parameters derived from the 2C velocity fields velocity such as vorticity and turbulence intensity are presented and analysed. Stereo PIV results are also presented to then finish the chapter with a discussion of the imaging system and the results.

7.1. Two-phase Air/fuel vector fields 2D

Data were acquired at two injection pressures, 30 and 54bar, for two different injection timings (referred to as early injection and half injection from this point onwards) under conditions corresponding to injection on the induction stroke. For both injection pressures images were taken 0.60ms (early) and 0.76ms (half) after start of injection. Images were acquired with a pulse separation of 8 μ s which was chosen to ensure, considering the difference in velocities for the phases, that the gas phase tracers would have a displacement higher than the noise floor hence displacements up to 4 pixels were obtained. Consequently, there will be large displacements in the fuel phase but acceleration error (Section 3.4.6.2) will not

affect the results since the motion of this phase is mostly unidirectional. An additional set of images were taken (under one injection condition) of another injector of the same specifications to establish if there are any differences between nominally identical injectors; it was established in Section 2.2.6.2 that one the desired characteristics for both PFI and GDI injectors is minimal variation of the spray characteristics from unit to unit.

7.1.1. Two-phase RGB images

A typical image obtained with the colour system is shown in Figure 7-1 for jet1 and Figure 7-2 for jet 5 following the notation established in Section 6.4. Some areas in the images of the fuel phase are saturated but this is not at a high level hence problems reported from previous two-phase measurements such as higher background level, particle re-scattering and other aberrations (as discussed in Section 3.5.1.) were not observed. Simultaneous phase imaging was considerably aided by the addition of the absorber to the fuel phase such that sharply focussed images of individual fuel droplets of varying sizes can be seen even in the very dense parts of the spray. As discussed in Section 6.4, images for jet5 present a 'foggy' appearance due to the illumination for this jet being slightly off-axis and jet6 being in the path between the laser and the camera (Figure 6-11).

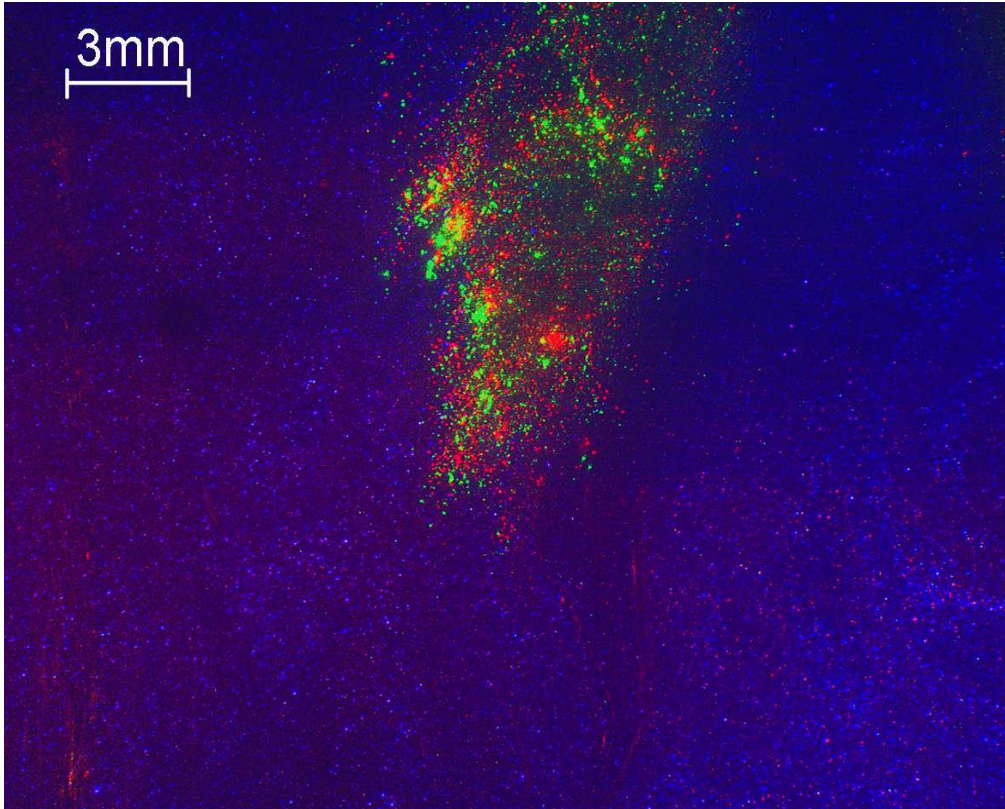


Figure 7-1 RGB multi-phase image for jet 1 – 30bar half injection

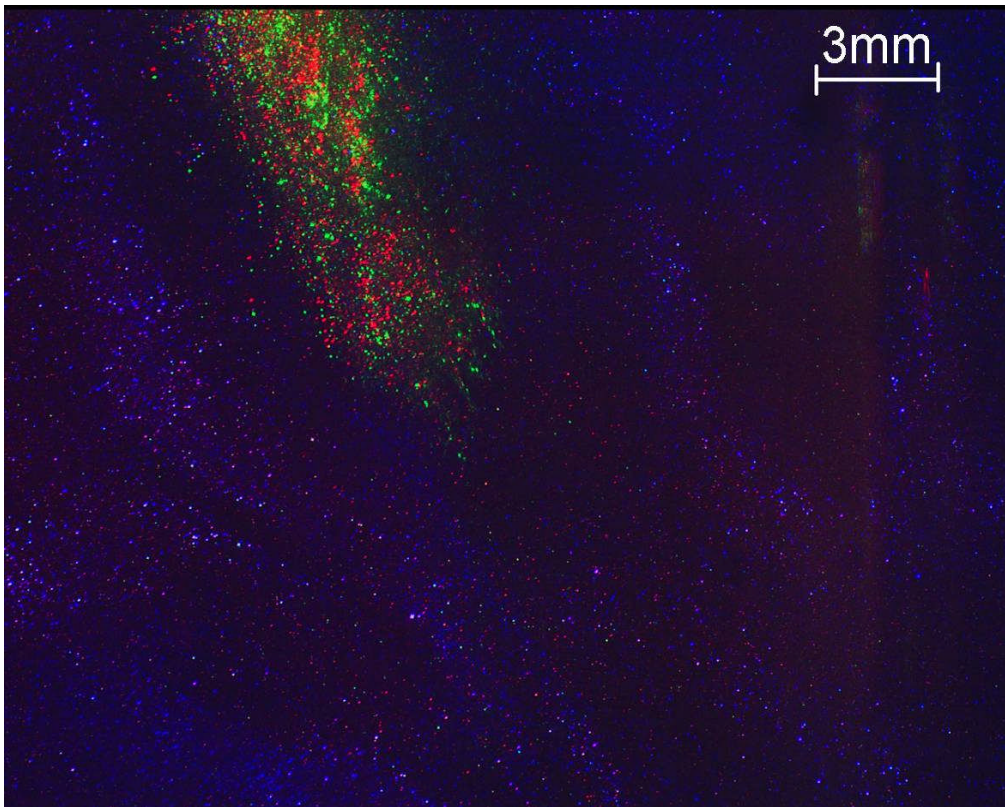


Figure 7-2 RGB multi-phase image for jet 5 – 30bar half injection

7.1.2. Vector field computation

After crosstalk correction (Section 6.5.4), RGB images were split into their component images and phases were identified as explained in Figure 6-16: blue and red channels are left unchanged and the blue channel is subtracted from the green channel to obtain the second image pair for the fuel phase (effectively removing gas phase particles from the green channel). The obtained component images are shown in Figure 7-3 in greyscales where a and c are the original red and blue components and b is the result of removing gas phase images from the green channel for the RGB image shown in Figure 7-1.

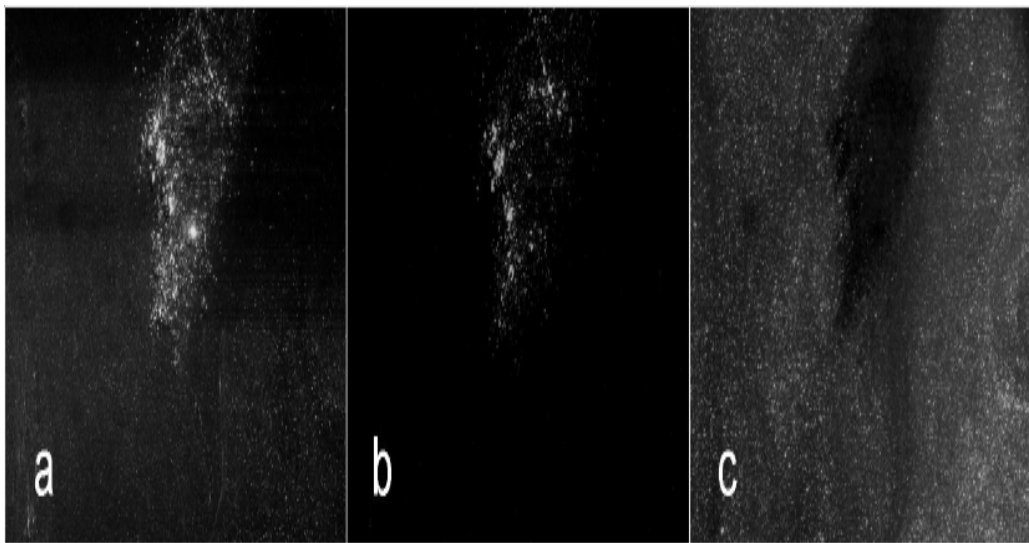


Figure 7-3 Red (a), green – blue (b) and blue (c) component images in greyscales for the multi-phase image shown in Figure 7-1

Gas phase vector fields were calculated by cross correlating images a and c; fuel phase vectors were calculated by cross correlating images a and b according to the pulse order shown in Figure 6-16.

7.1.2.1. Image Pre-processing:

Depending on the injection conditions, different image pre-processing settings were used; the main pre-processing function used was the subtraction of a sliding background which helped remove the differences in background noise which were more pronounced in the blue channel. A constant background level was also subtracted from each channel.

7.1.2.2. *Vector calculation parameters*

The adaptive multi-grid cross-correlation algorithm in DaVis 7.2 was used to calculate the vector fields. For the fuel phase, an initial window size of 128 pixels (50% overlap) was used due to large displacements in the fuel phase (up to 30 pixels). A final window size of 32 pixels was used with 25% overlap and two passes were used for each interrogation size. The size and overlap (25% instead of 50% again) for the final window size were chosen to provide a clear visualisation of the velocity vectors presented here (considering the restrictions in space). For the gas phase the same settings were used for the initial passes because of the possible high velocity vectors which can be obtained due to the air/fuel interaction within the spray; a final window size of 64 pixels with 50% overlap was employed with two passes used again for each interrogation size. A larger final window size was selected for the air vectors as there were some images in which most of the air tracers are pushed out due to the high pressure in the fuel spray; a final window size of 64 pixels ensures enough particles were present in each window size to obtain a high signal to noise ratio for each vector and therefore reliable gas phase velocities.

7.1.2.3. *Vector post-processing*

Vectors post-processing was used to validate the obtained vector fields using the post-processing options available in DaVis 7.2. A minimum peak ratio of 1.5 was necessary to accept a vector (Equation 3-20). A median filter was employed to remove vectors which varied more than twice the RMS of their eight neighbouring vectors. Finally distortions due to the offset of the 3 colour CCDs inside the camera (Section 5.4.2) were accounted for by subtracting vector fields of seed with pulse separation $dt=0$ as explained in Section 6.5.4.

7.1.2.4. *Average vector fields calculation*

Instantaneous vector fields were used to calculate the flow average. Average vector fields were calculated using 50 instantaneous realisations for each injection condition. A minimum of 10 validated vectors at each interrogation window were required to calculate the mean and only values within the range $AVG \pm 2RMS$ are included so that spurious vectors far outside the average are removed. It was found that, as expected, images for jet 5 are not as clear as images for jet 1 and

fewer valid vectors were obtained hence more instantaneous realisations were used for the calculation of the mean for jet 5 (a total of 65 were used).

7.1.3. Instantaneous and average vector fields

Figures 7-4 to 7-12 show the instantaneous and average vector maps obtained under the conditions described above. For each image the fuel phase is on the left hand side and the gas phase on the right hand side; the first 3 rows show instantaneous vector fields and the last row show the average vector fields for each phase. Images are presented this way so that different instantaneous vector maps can be compared to the average. A side colour bar is included on the side for each phase and it is scaled from 0 to the maximum velocity in each vector field. The vector fields from jet 5 have been inverted for the vectors to be orientated in the same direction as those of jet 1. Figures 7-4 to 7-7 show the multi-phase vectors for jet 1; Figure 7-8 shows the multi-phase vectors for jet 1 in the second injector from the same batch and Figures 7-9 to 7-12 show the multi-phase vectors for jet5.

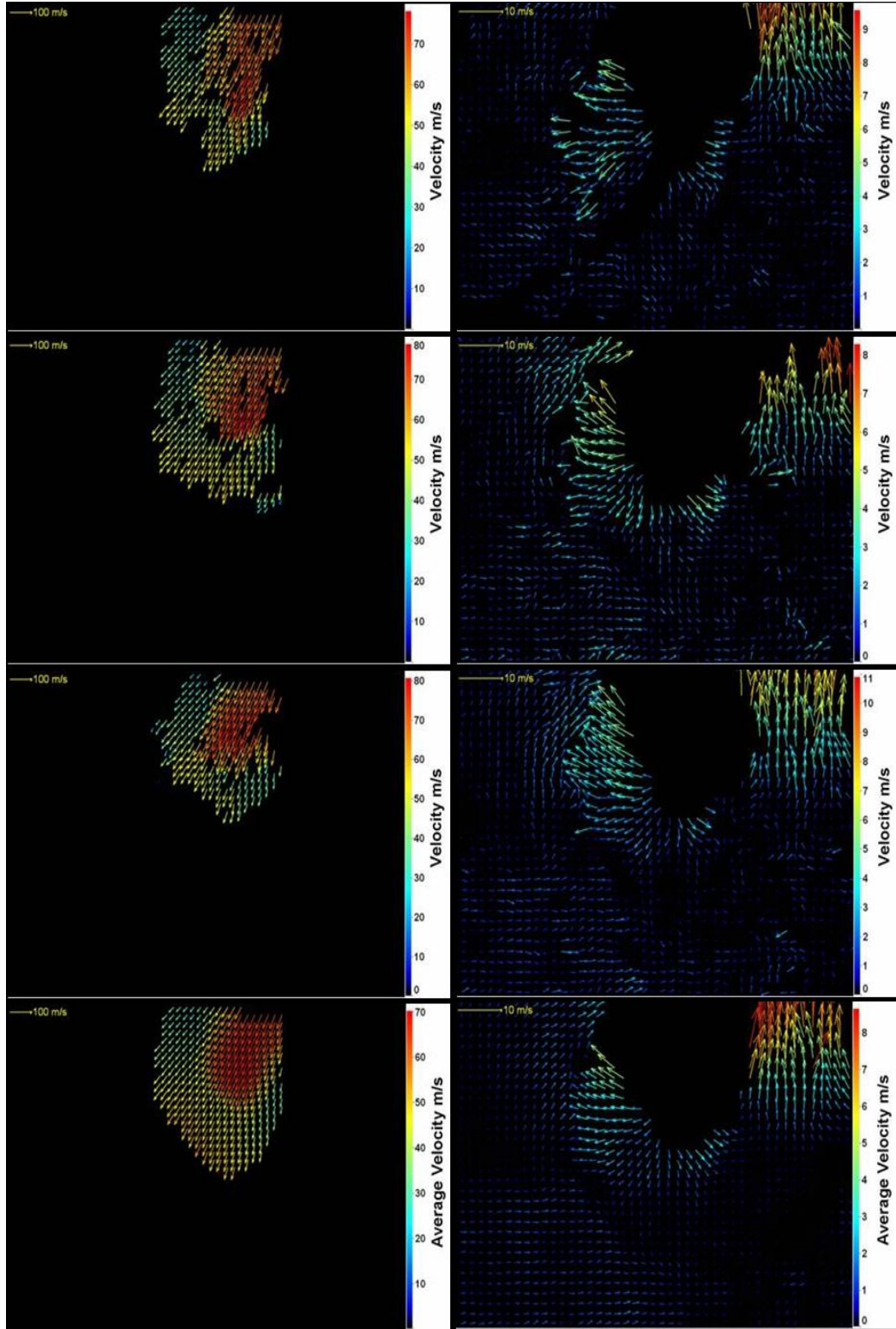


Figure 7-4 Instantaneous and average vector fields for fuel and air at 30bar, jet 1 – early injection

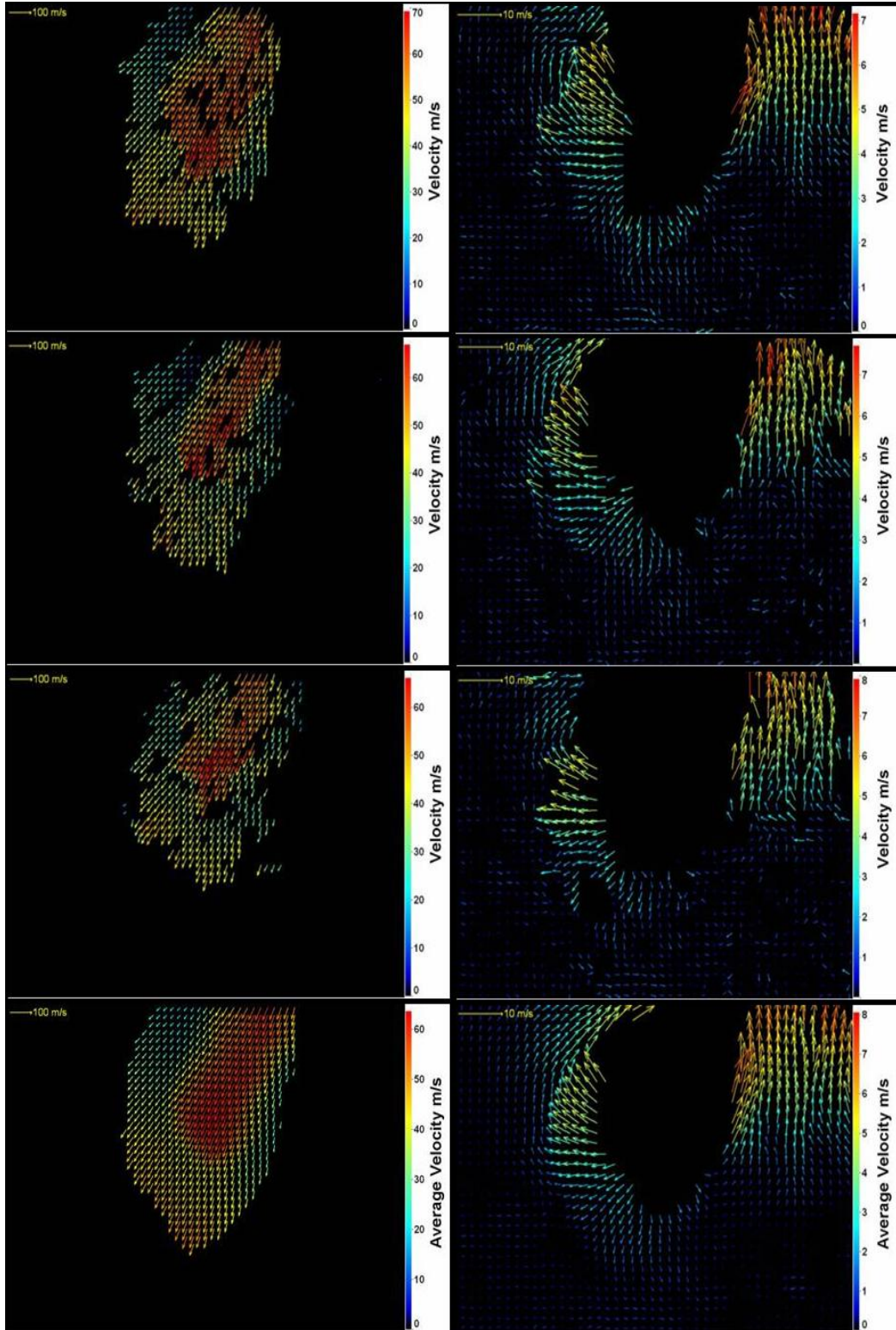


Figure 7-5 Instantaneous and average vector fields for fuel and air at 30bar, jet 1 – half injection

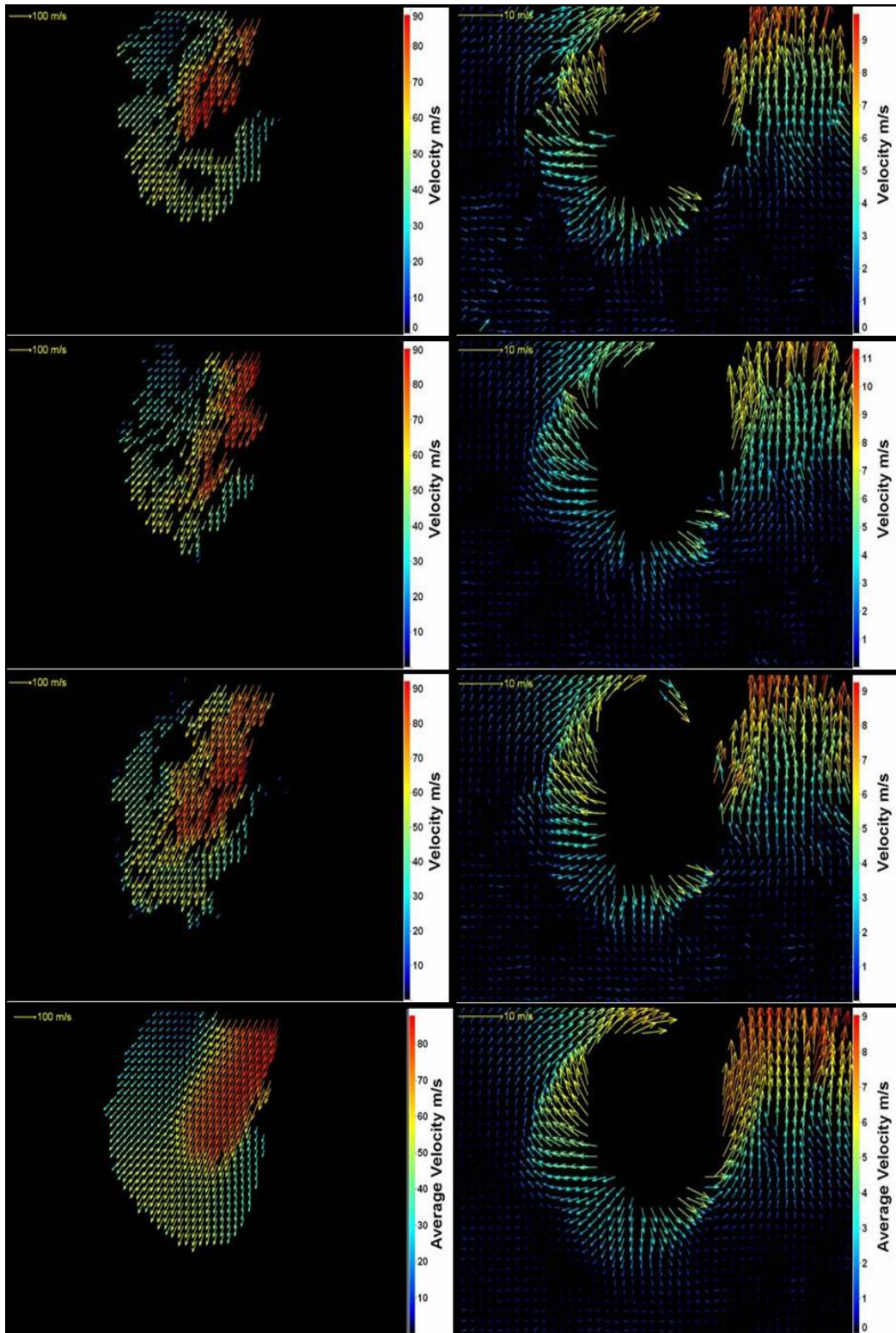


Figure 7-6 Instantaneous and average vector fields for fuel and air at 54bar, jet 1 – early injection

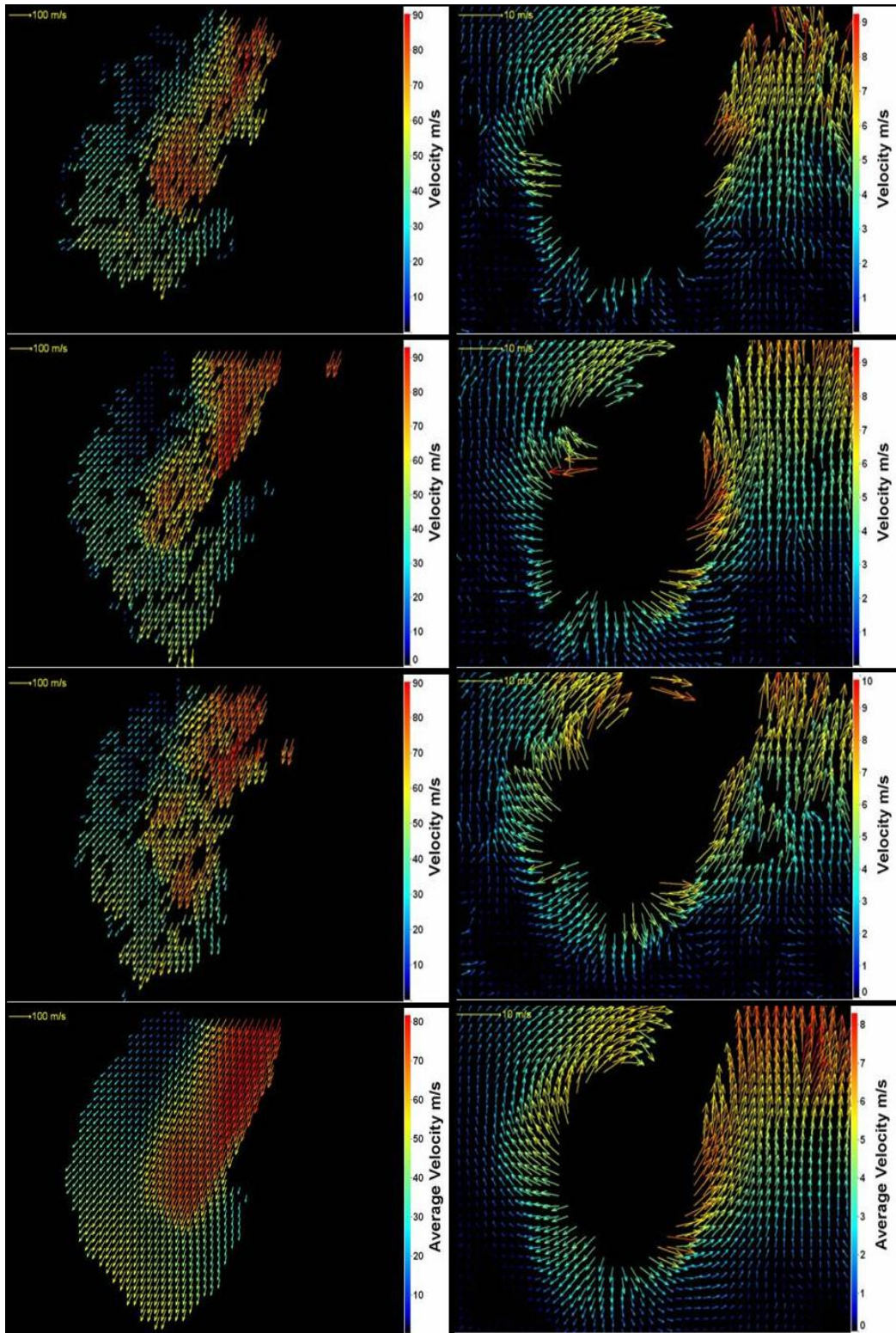


Figure 7-7 Instantaneous and average vector fields for fuel and air at 54bar, jet 1 – half injection

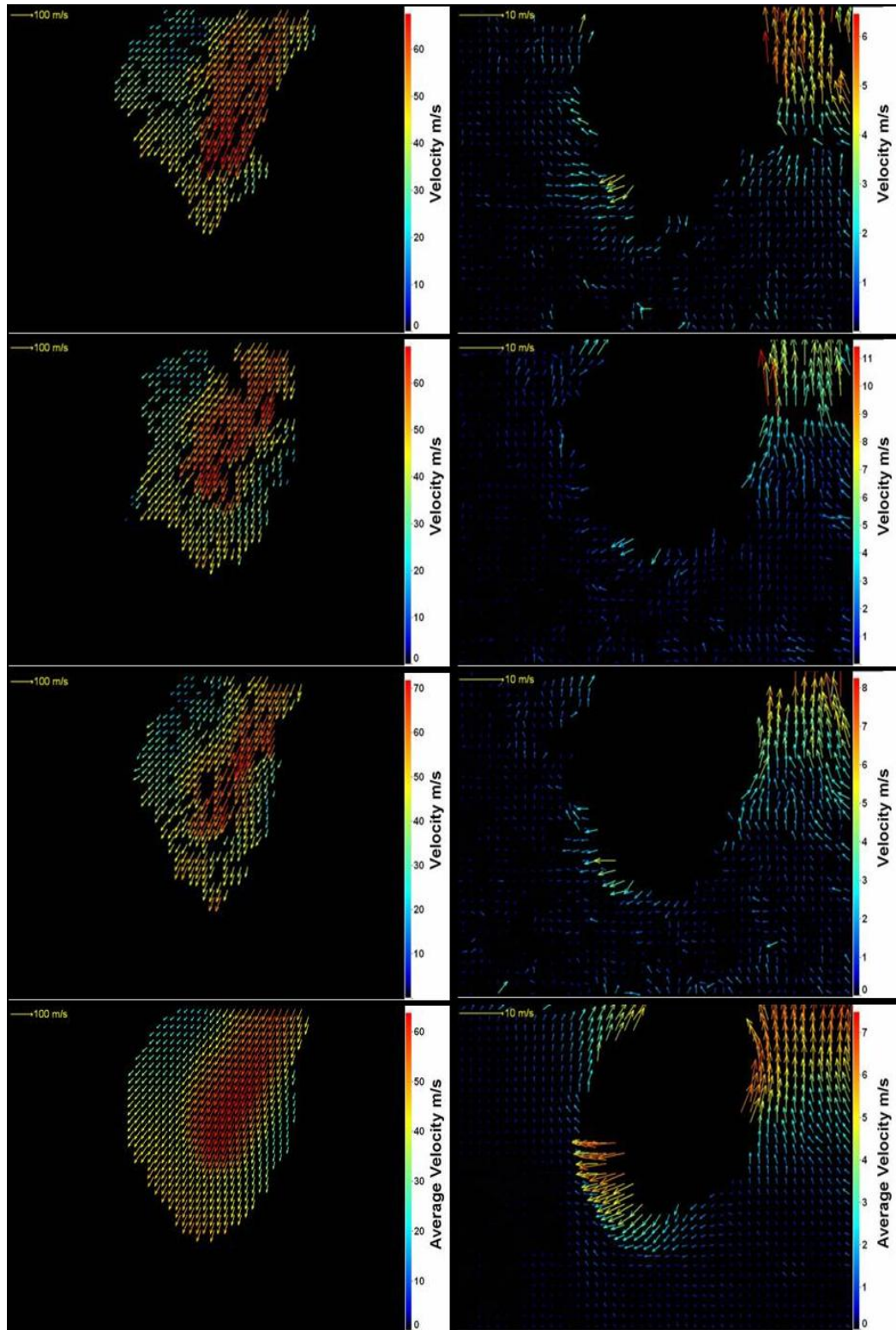


Figure 7-8 Instantaneous and average vector fields for fuel and air at 30bar, second injector
– half injection

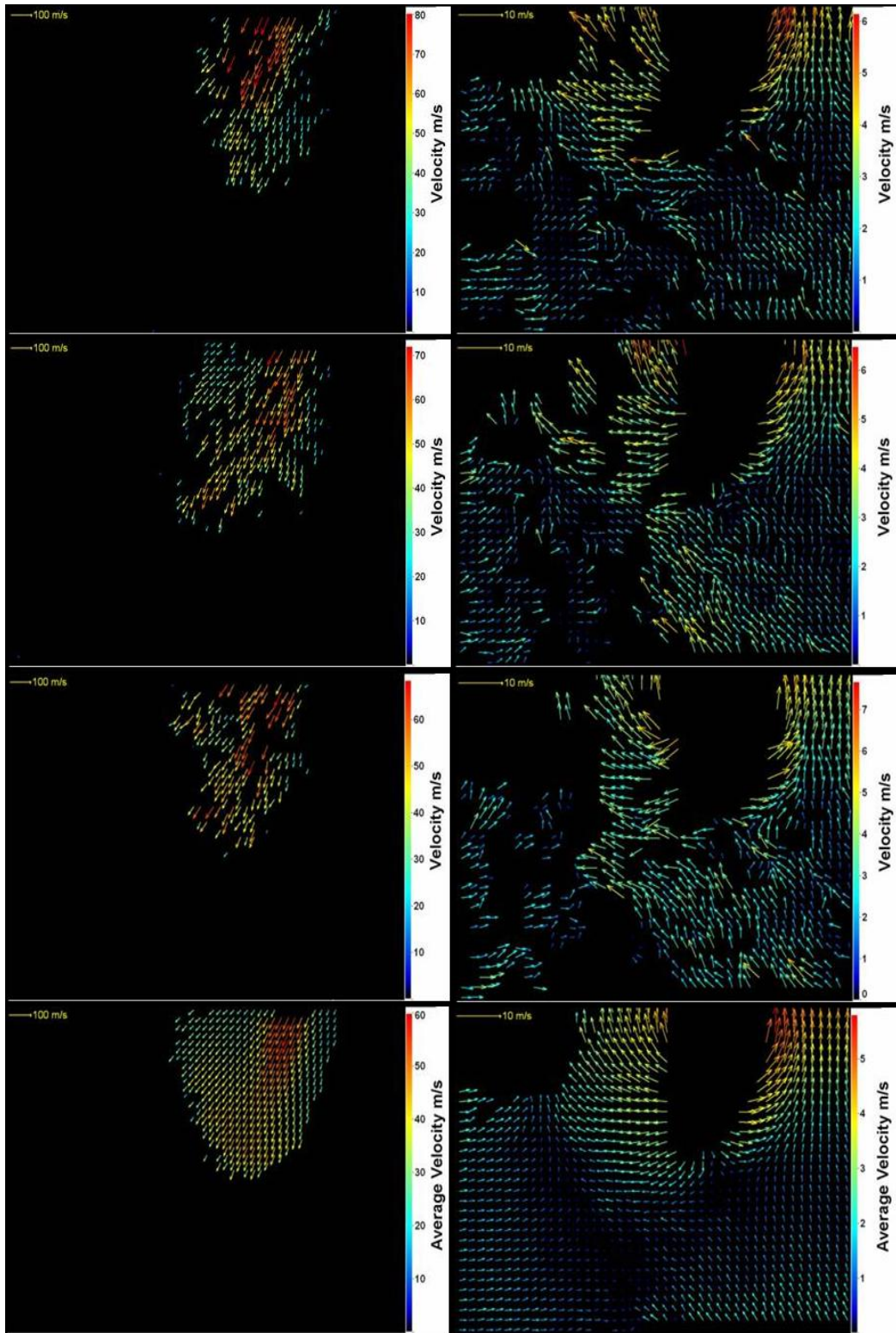


Figure 7-9 Instantaneous and average vector fields for fuel and air at 30bar, jet 5 – early injection

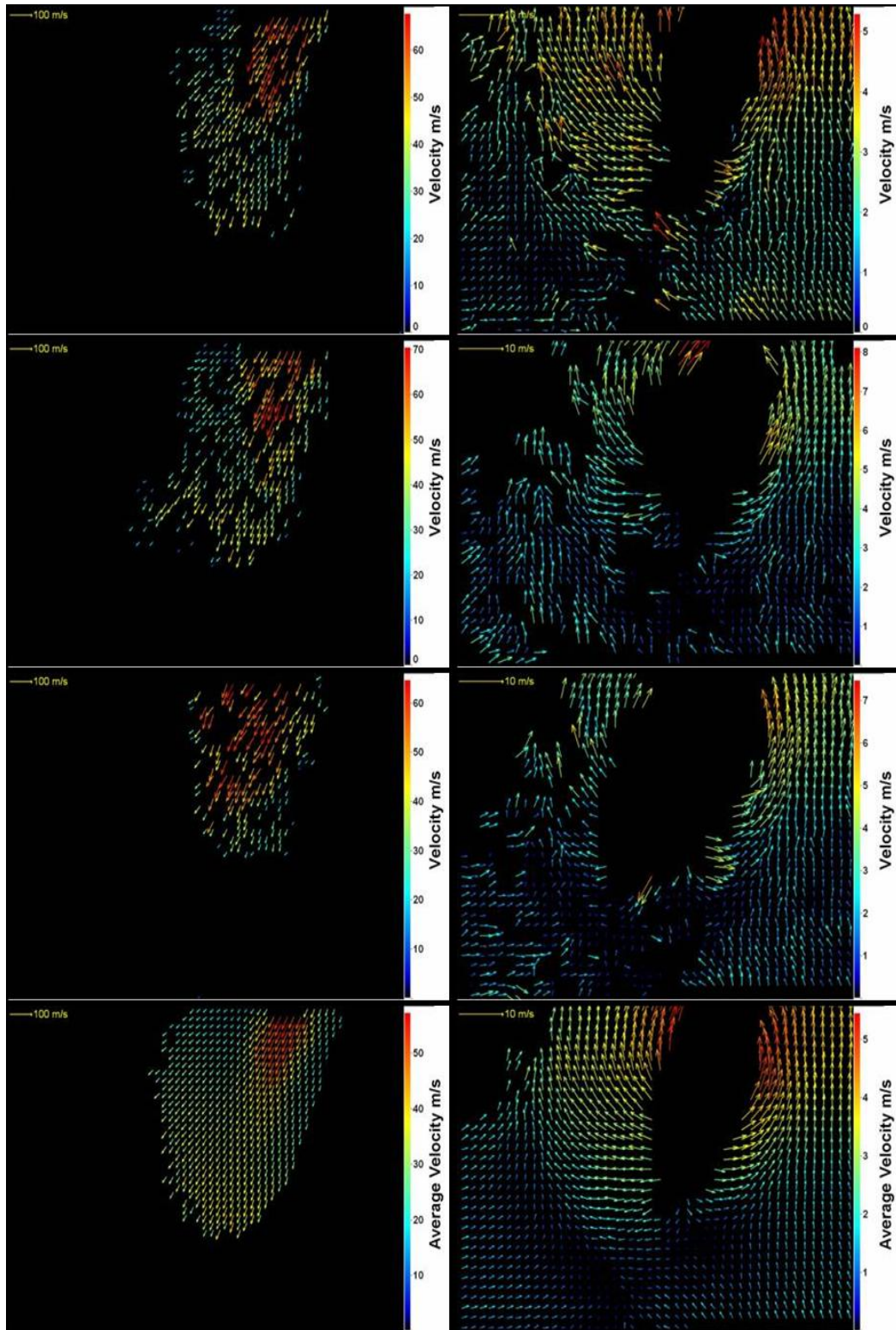


Figure 7-10 Instantaneous and average vector fields for fuel and air at 30bar, jet 5 – half injection

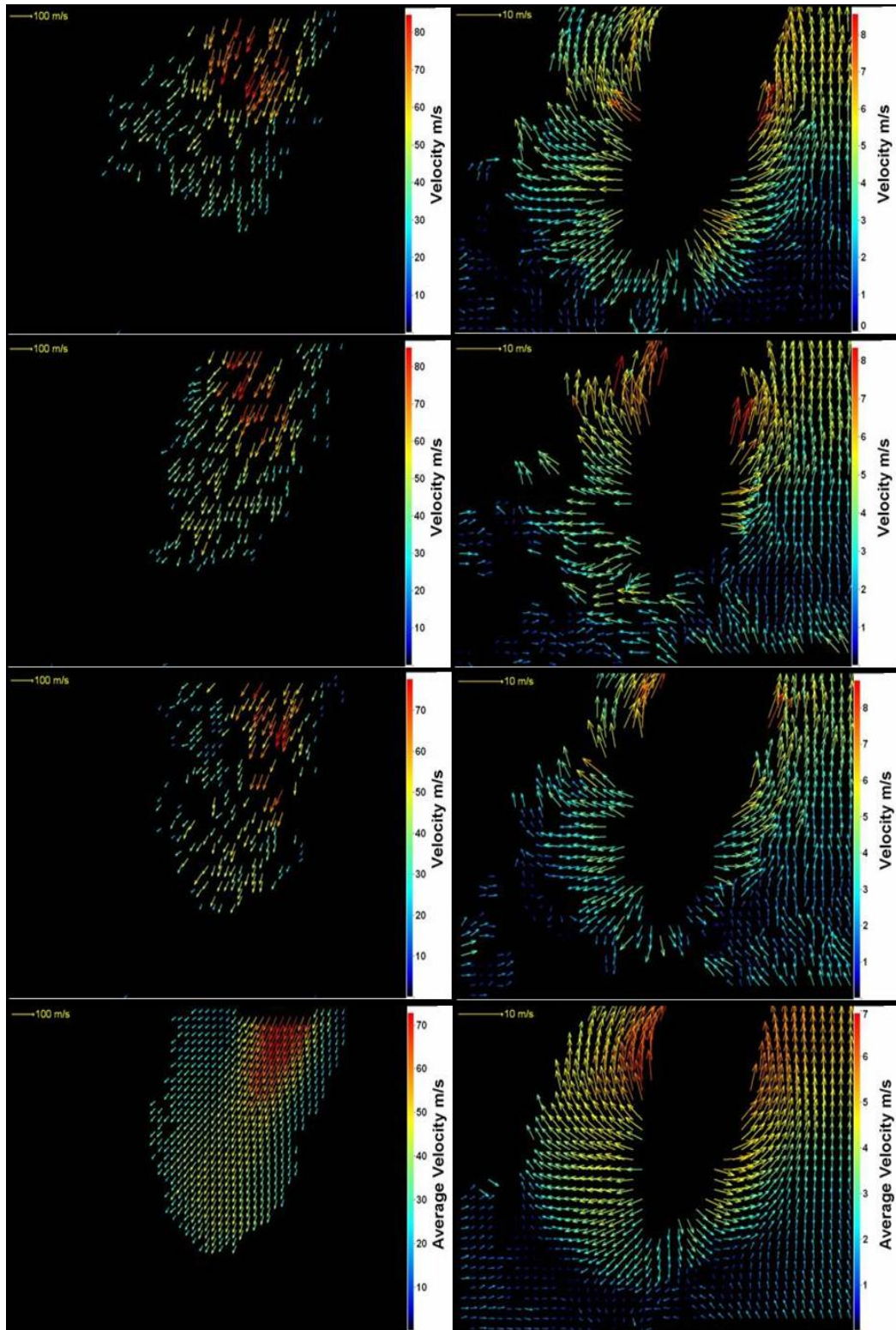


Figure 7-11 Instantaneous and average vector fields for fuel and air at 54bar, jet 5 – early injection

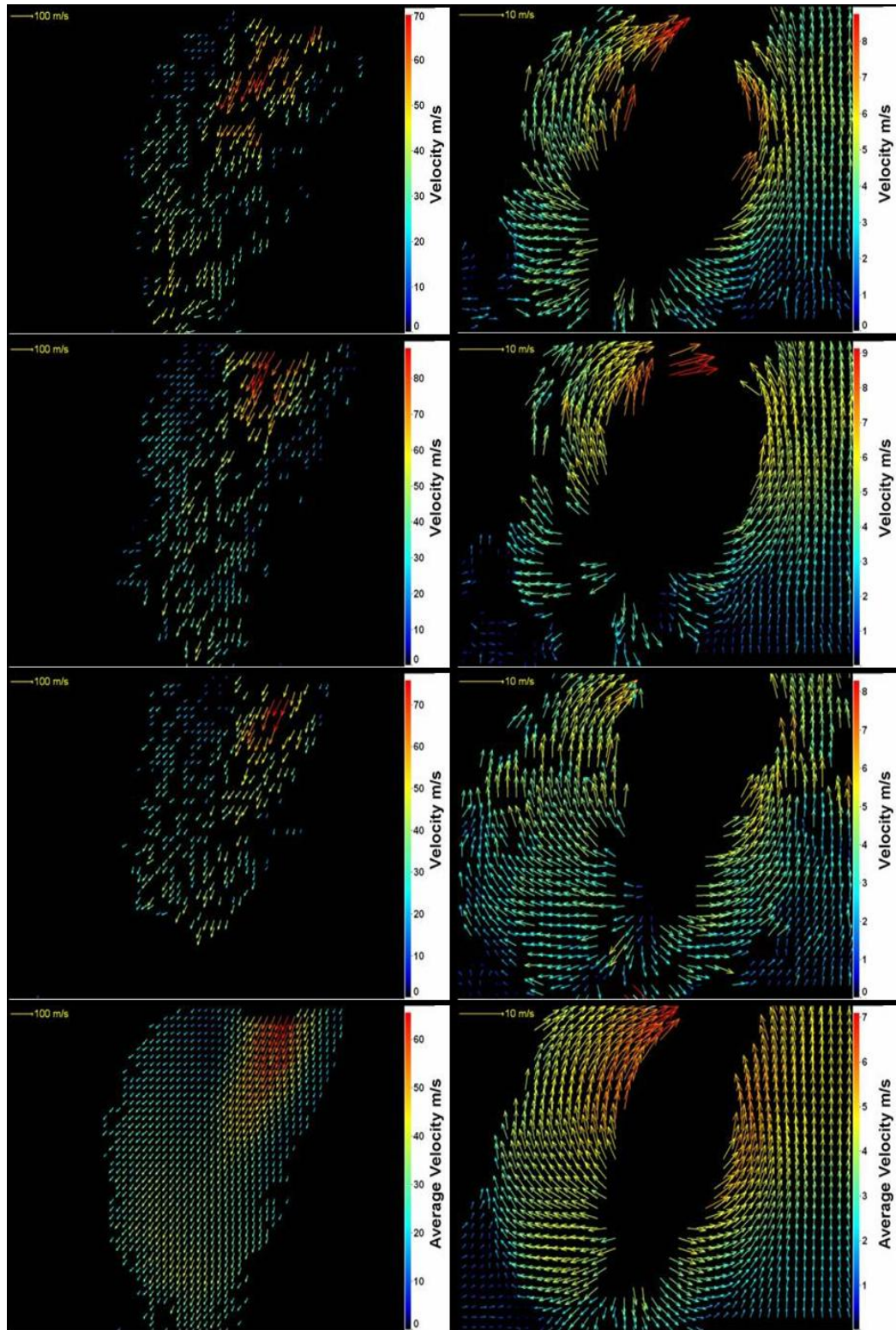


Figure 7-12 Instantaneous and average vector fields for fuel and air at 54bar, jet 5 – half injection

The differences between the fuel phase vector fields for jet 1 and jet 5 are significant. Whilst the maximum velocities obtained are similar (up to 90 m/s for jet 1 and 80 m/s for jet 5), larger areas of high velocity are obtained in jet 1 which was expected since the laser sheet illuminated through the middle of this jet as shown in Figure 6-11.

Figures 7-13 to 7-21 show the vectors for the 2 phases plotted in the same figure (using Origin 8). The length of the gas phase vectors has been increased by a factor of 10 compared to the length of the vector from the fuel phase. The overlap between the two sets of vector maps is now more evident with areas of vectors from both phases around the spray edge. Air entrainment into the spray is also evident particularly in the top left hand side for an injection pressure of 54 bar Figure 7-16. The combined vector fields from jet 5 show a different entrainment pattern compared to that for jet 1. The shape of the spray is different between jet 1 and jet 5 in that jet 5 has a narrower high velocity region. Furthermore, the 2-phase jet 5 vector field, e.g. figures 7-19 and 7-21, show larger regions of overlapping vectors than jet 1, corresponding to figures 7-14 and 7-16. These structural differences are consistent with the laser sheet being parallel but a small distance from the spray axis. Greater levels of interaction would be expected away from the spray axis which is what is seen in the data for jet 5.

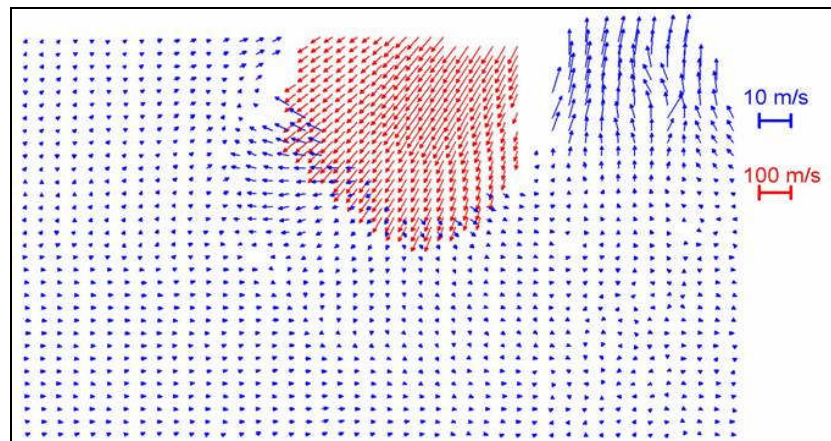


Figure 7-13 Averaged vector fields for fuel and air and an injection pressure of 30 bar, jet 1 early injection

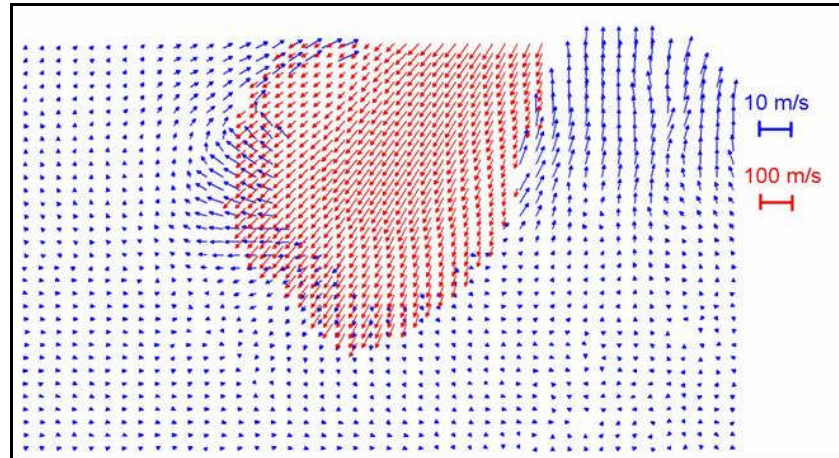


Figure 7-14 Averaged vector fields for fuel and air and an injection pressure of 30 bar, jet 1
- half injection

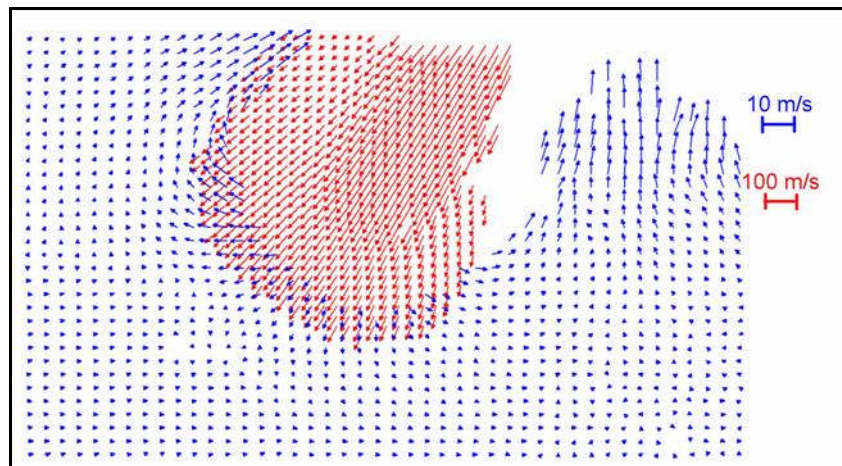


Figure 7-15 Averaged vector fields for fuel and air and an injection pressure of 54 bar, jet 1
- early injection

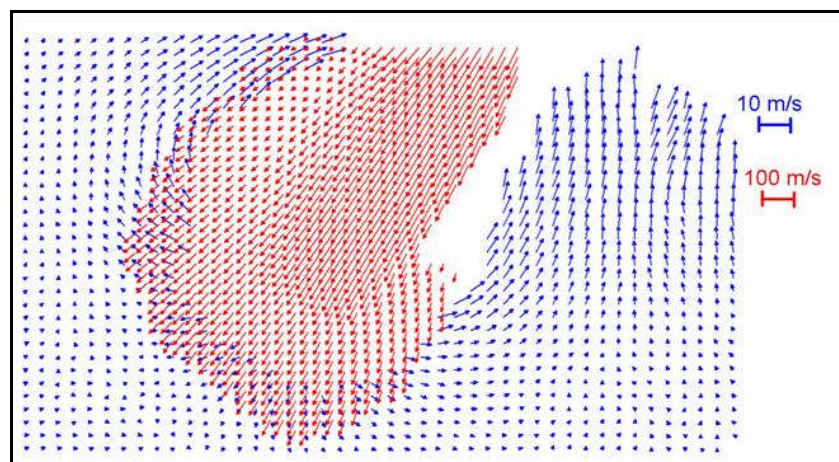


Figure 7-16 Averaged vector fields for fuel and air and an injection pressure of 54 bar, jet 1
- half injection

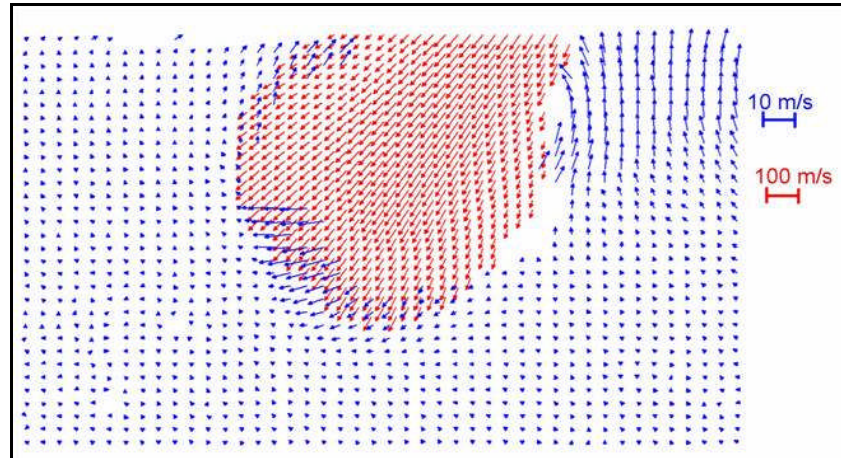


Figure 7-17 Averaged vector fields for fuel and air and an injection pressure of 30 bar, second injector - half injection

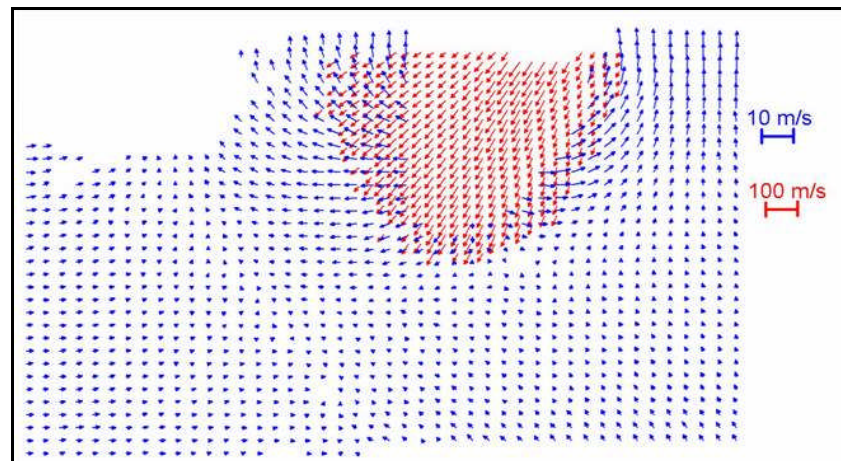


Figure 7-18 Averaged vector fields for fuel and air and an injection pressure of 30 bar, jet 5 - early injection

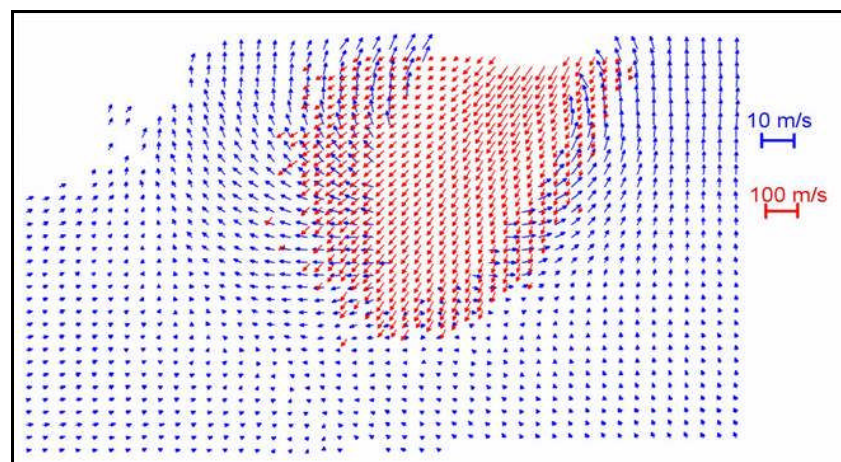


Figure 7-19 Averaged vector fields for fuel and air and an injection pressure of 30 bar, jet 5 - half injection

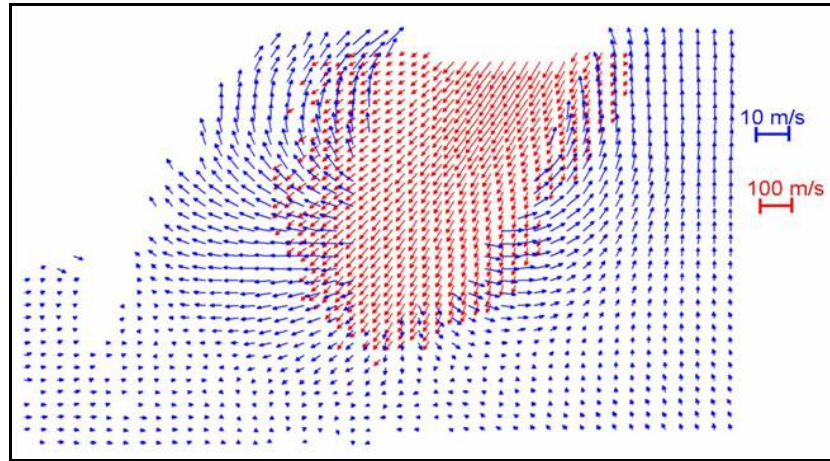


Figure 7-20 Averaged vector fields for fuel and air and an injection pressure of 54 bar, jet 5
- early injection

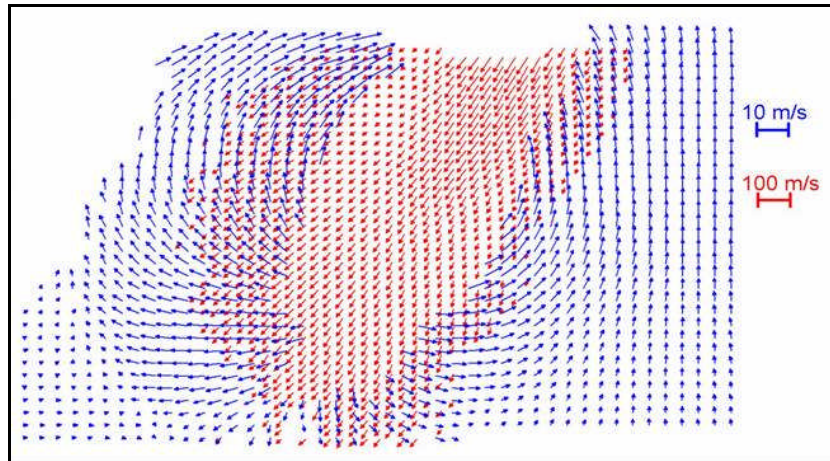


Figure 7-21 Averaged vector fields for fuel and air and an injection pressure of 54 bar, jet 5
- half injection

7.1.4. Average vector field statistics

Average vector fields were analysed to ensure they were not biased towards integer values due to peak locking effects. DaVis 7.2 provides a numerical estimation of the peak locking effect based on the histograms of the velocity values in the x and y directions. Using Equation 3-21, peak locking effects were estimated for the average vector fields shown in Figures 7-13 to 7-21 and the results are summarised in Table 7-1 for jet 1 and Table 7-2 for jet 5.

Table 7-1 Peak locking estimators for jet 1

	30 bar early	30 bar half	54 bar early	54 bar half	2nd injector
Air	0.00675	-0.03605	0.00943	0.06582	-0.06816
Fuel	0.01065	-0.00527	0.0228	-0.0038	0.010429

Table 7-2 Peak locking estimators for jet 5

	30 bar early	30 bar half	54 bar early	54 bar half
Air	-0.06374	-0.04162	0.0252	0.04272
Fuel	-0.02308	0.00409	-0.00152	0.00515

As mentioned in Section 3.4.6.2, 1 indicates a strong peak locking effect hence from the data above, it can be concluded the calculated velocity data are not affected by peak locking. It should be noted that instantaneous vector fields were also analysed and no peak locking effects were observed.

7.1.5. Gas phase vectors within the spray

Velocity vectors from air tracers have also been obtained further inside the spray. It is not possible to calculate a robust average for these vectors given that they rarely occur in the same location (same interrogation region) on the instantaneous vector maps since most of the air tracers are displaced by the fuel. Figure 7-22 shows different instantaneous vector maps where velocity vectors have been obtained inside the spray. The vectors' direction show they are following the spray direction and their velocity is very high compared to the rest of the vector map (each vector map is scaled from 0 to maximum velocity). Nevertheless, the air phase velocity inside the spray is low in comparison to that of the fuel droplets in the same location indicating the high levels of shear between the two phases.

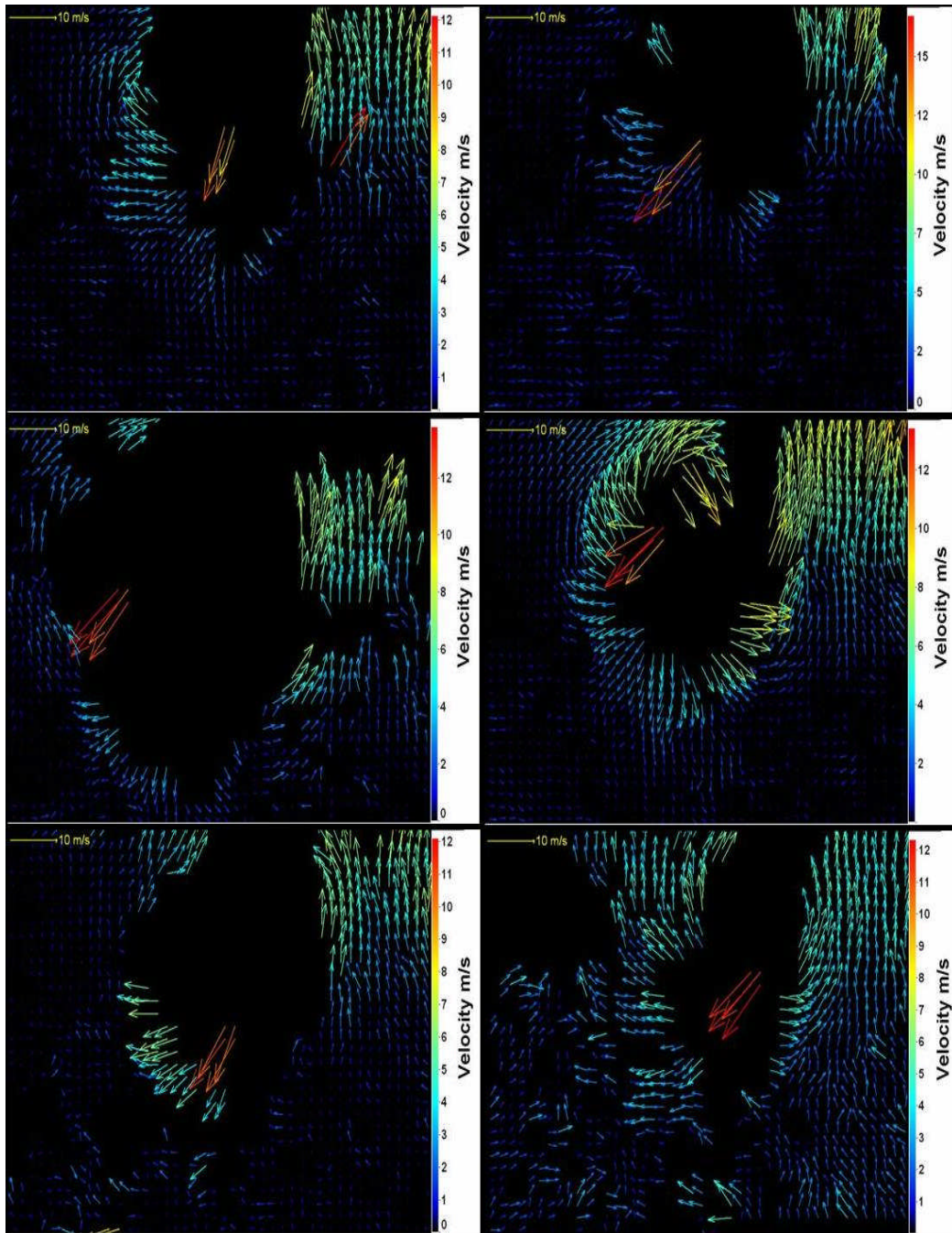


Figure 7-22 Instantaneous gas phase vector fields showing velocity vectors obtain with the spray.

7.1.6. RMS vector fields

RMS has been obtained for the fuel phase from the average vector fields calculated as described in Section 7.1.2.4. For each average vector field, RMS

(m/s) values are shown in the background and in the side colour map which is scaled from 0 to maximum.

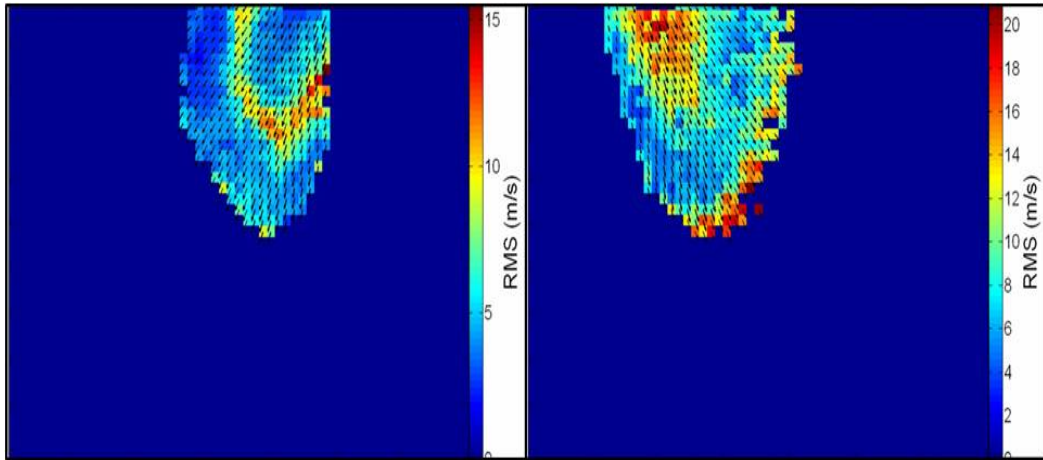


Figure 7-23 RMS for jet1 and jet5 for at 30 bar - early injection

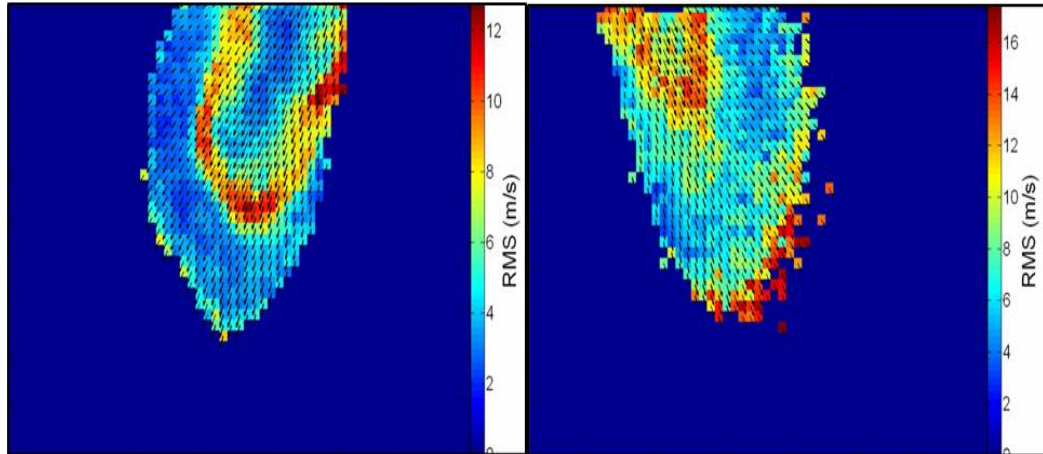


Figure 7-24 RMS for jet1 and jet5 for at 30 bar - half injection

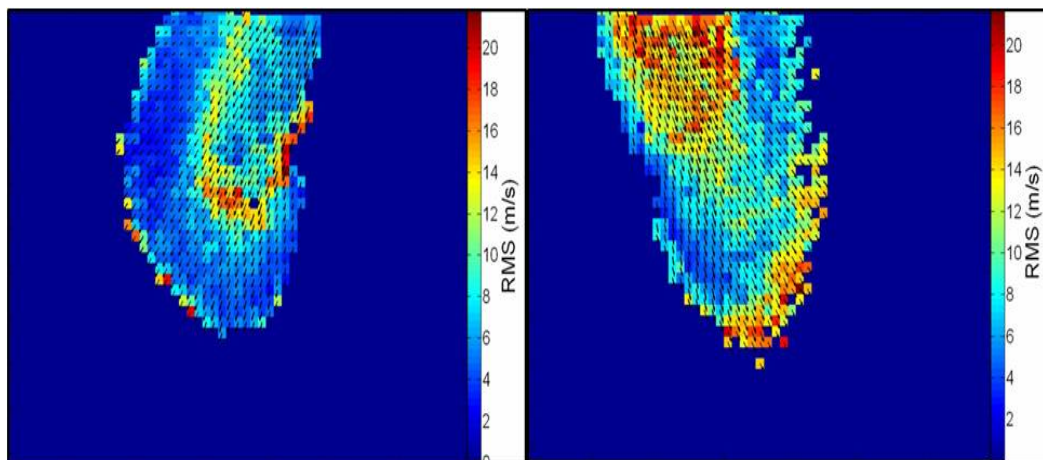


Figure 7-25 RMS for jet1 and jet5 for at 54 bar - early injection

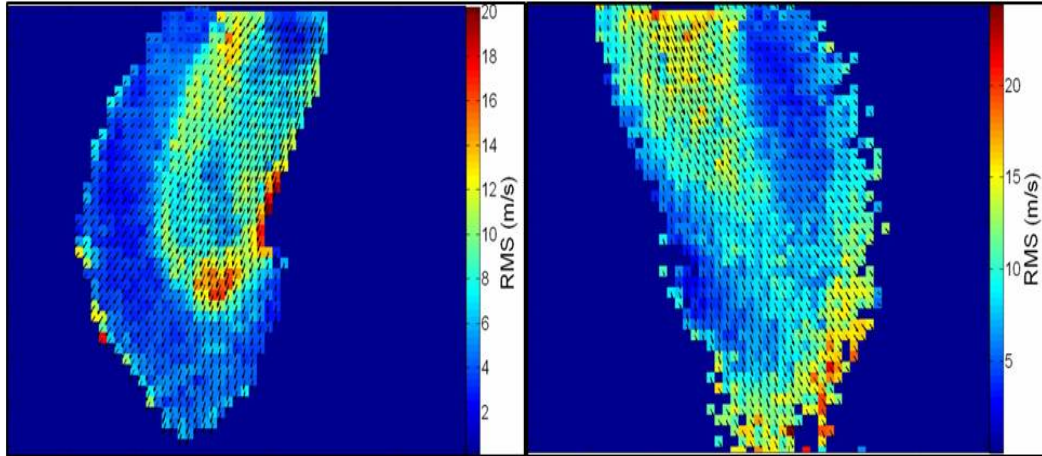


Figure 7-26 RMS for jet1 and jet5 for at 54 bar - half injection

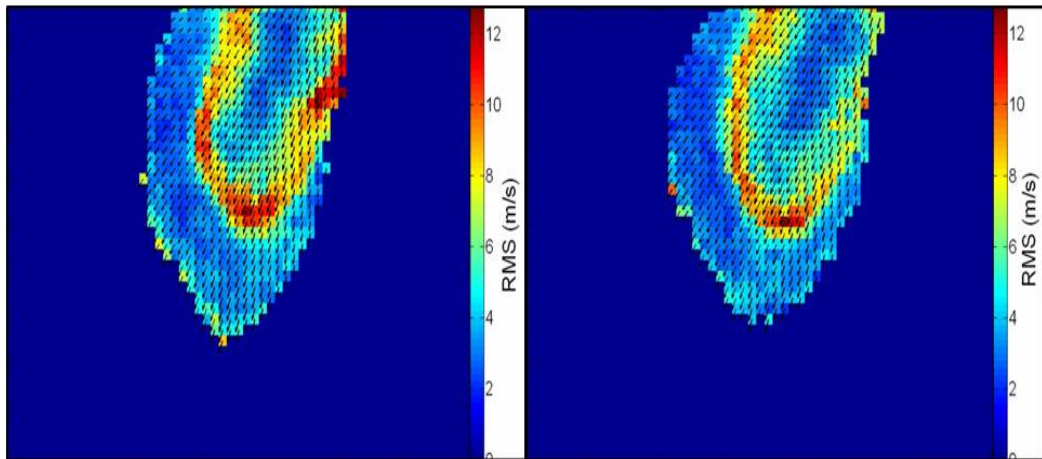


Figure 7-27 RMS for jet1 for two nominally identical injectors – half injection

7.1.7. Turbulence intensity

Turbulence intensity (defined here as the local RMS divided by the local mean for each vector and given as a percentage) has been calculated for the vector maps in the fuel phase; for each average vector field, turbulence intensity is shown in the background and in the side colour map which is scaled from 0 to maximum.

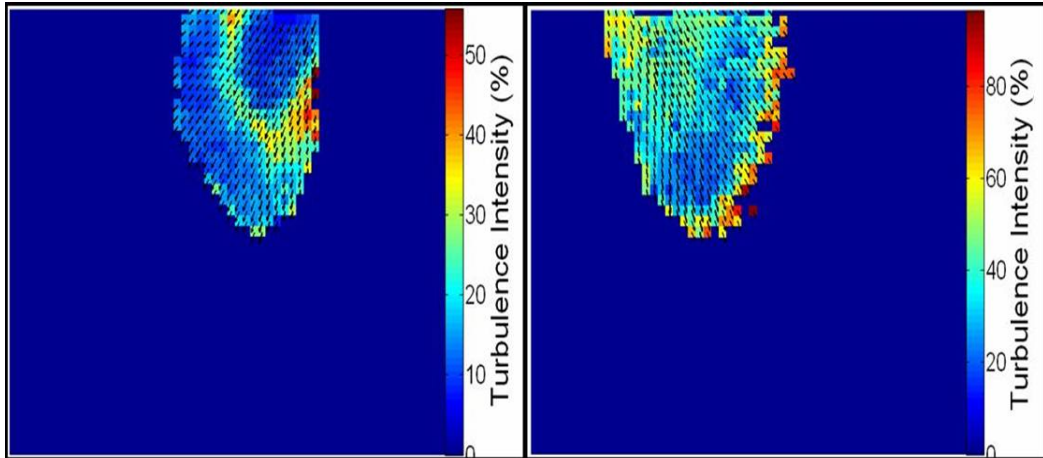


Figure 7-28 Turbulence intensity for jet1 and jet5 for at 30 bar - early injection

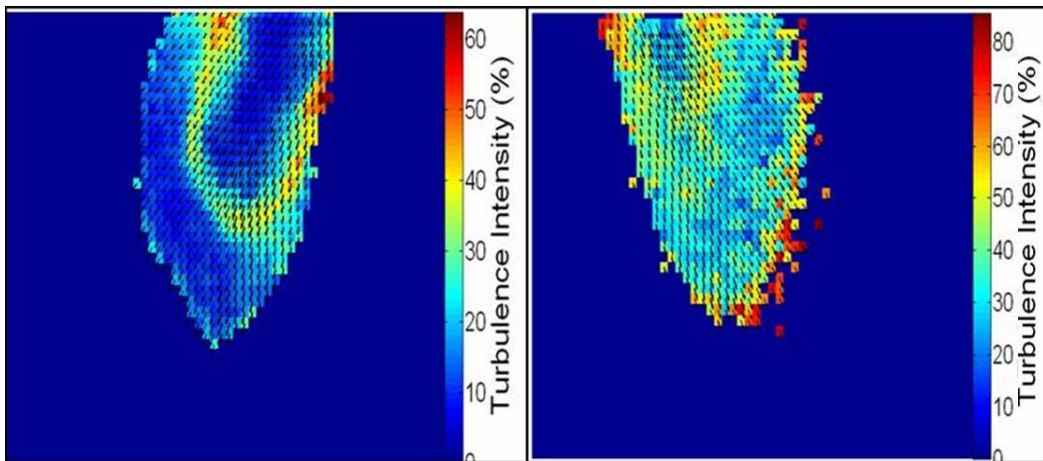


Figure 7-29 Turbulence intensity for jet1 and jet5 for at 30 bar - half injection

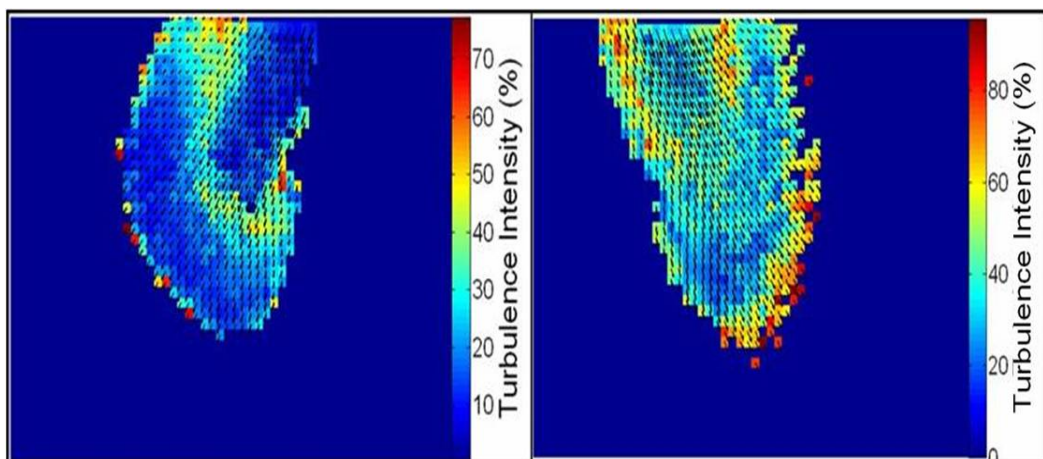


Figure 7-30 Turbulence intensity for jet1 and jet5 for at 54 bar - early injection

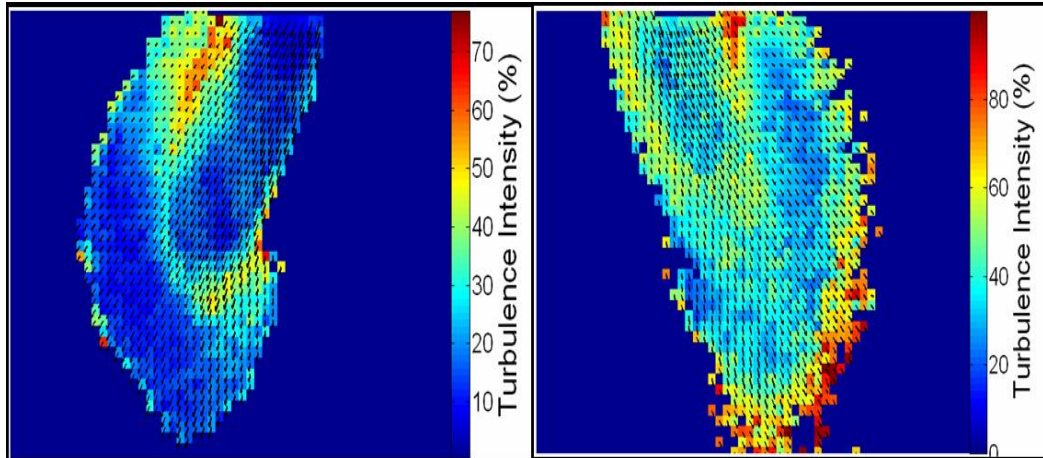


Figure 7-31 Turbulence intensity for jet1 and jet5 for at 54 bar - half injection

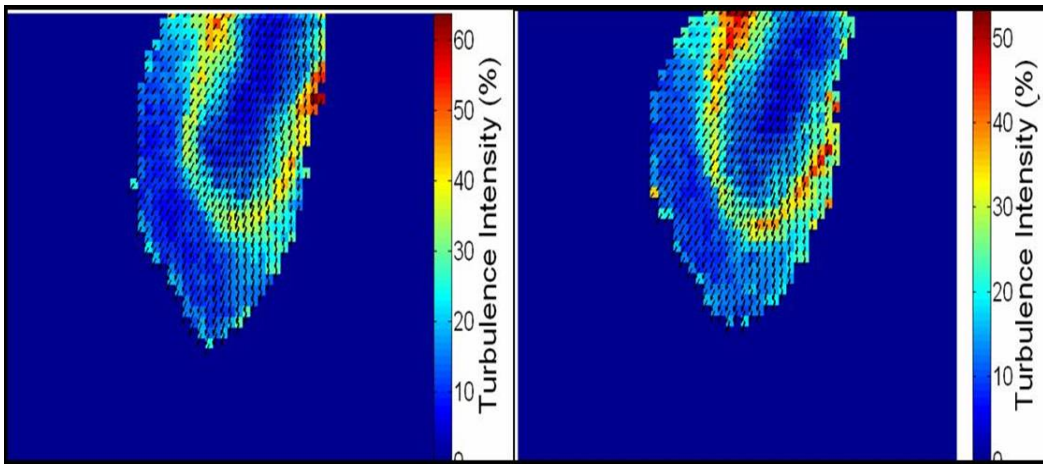


Figure 7-32 Turbulence intensity for jet1 for two nominally identical injectors – half injection

7.1.8. Vorticity

The basic definition of vorticity is the tendency of a vector field to rotate about a point; for a two dimensional field, vorticity is a vector quantity perpendicular to the vector field plane. Out of plane vorticity can be calculated from in-plane vector fields directly in DaVis 7.2 using the central difference scheme which is a point approximation to rotation. Equation 7-1 below was used to calculate vorticity (given as the rotation in the z direction from an xy vector field) following the notation shown in Figure 7-33:

$$Rot_z(X, Y) = \frac{V(X + \Delta, Y) - V(X - \Delta, Y) - U(X, Y + \Delta) + U(X, Y - \Delta)}{2\Delta}$$

Equation 7-1

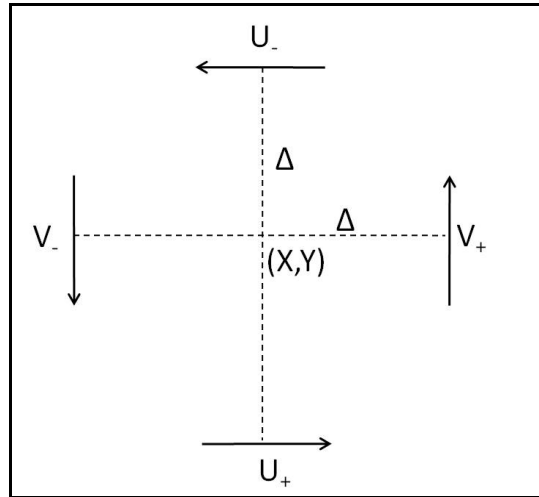


Figure 7-33 Notation for vorticity calculation

Figures 7-34 to 7-38 show the vorticity (units: s^{-1}) for all the injection conditions. Vectors have been arranged side by side with jet 1 on the left hand side and jet 5 on the right hand side. Vorticity is shown in the background with the corresponding colour map on the right hand side scaled \pm max so that positive vorticity (anti-clockwise) is shown red, negative vorticity (clockwise) is shown blue and areas with low vorticity are shown white.

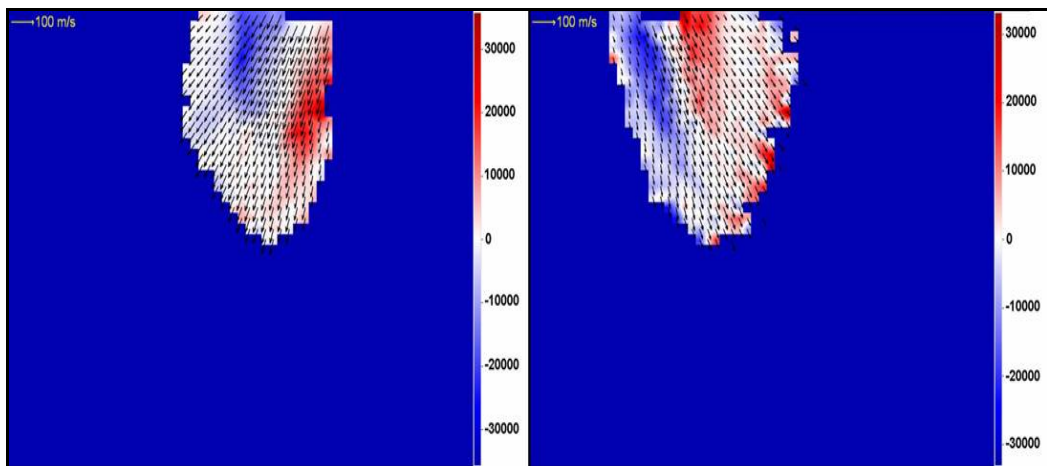


Figure 7-34 Vorticity for jet1 and jet5 for at 30 bar - early injection

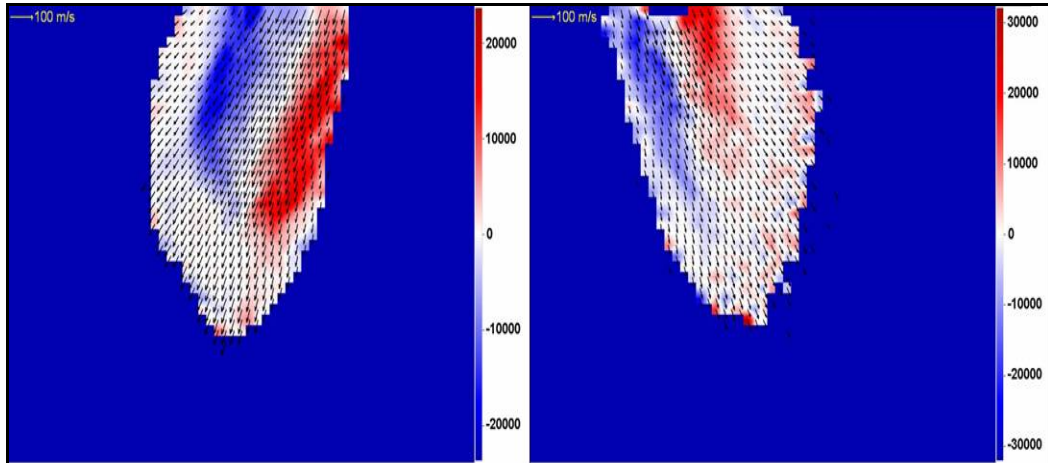


Figure 7-35 Vorticity for jet1 and jet5 for at 30 bar - half injection

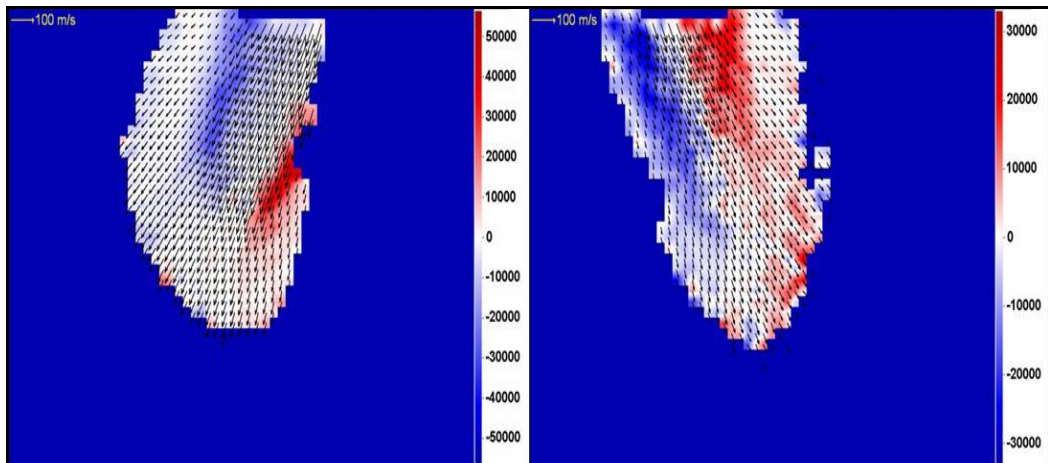


Figure 7-36 Vorticity for jet1 and jet5 for at 54 bar - early injection

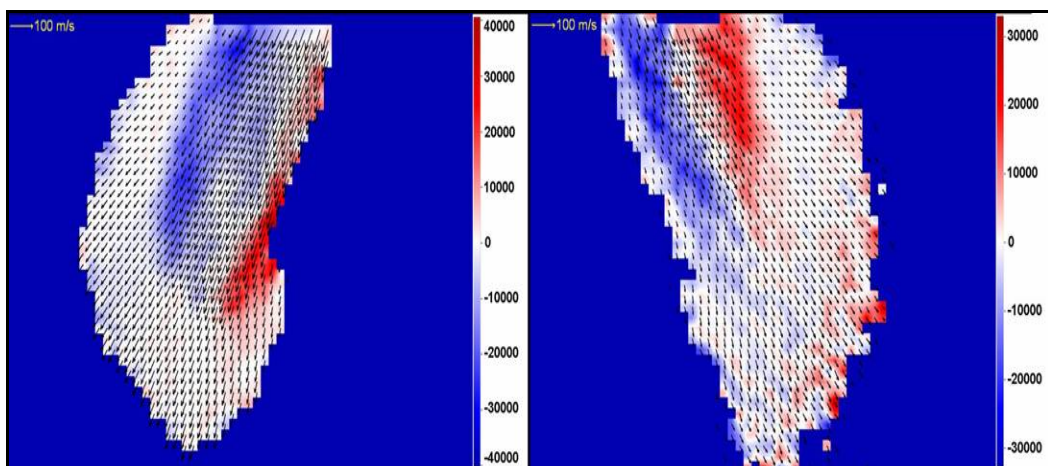


Figure 7-37 Vorticity for jet1 and jet5 for at 54 bar - half injection

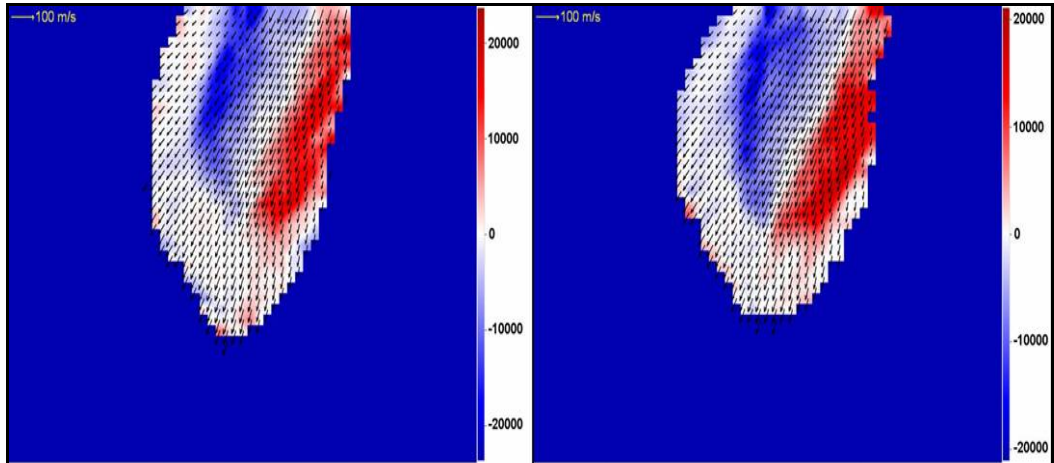


Figure 7-38 Vorticity for jet1 for two nominally identical injectors – half injection

For all the conditions there seems to be a pattern where two clear areas of rotation are identified in the high velocity region of each field clearly indicating swirling motion on either side of a low rotation area in the centre (indicated by the white background). The high vorticity values obtained are explained by the high velocities in the fuel phase (up to $\sim 90\text{m/s}$ at 54bar) and the small values of Δ used in Equation 7-1.

7.2. Stereo PIV results

Using the setup described in Section 6.6.1 and under the same experimental conditions, 3C stereo measurements were performed in jet 1. An example of the RGB images obtained with the stereo setup (Figure 6-19) is shown in Figure 7-39 for camera 1 and Figure 7-40 for camera 2; the same instantaneous image is shown viewed from the two cameras.

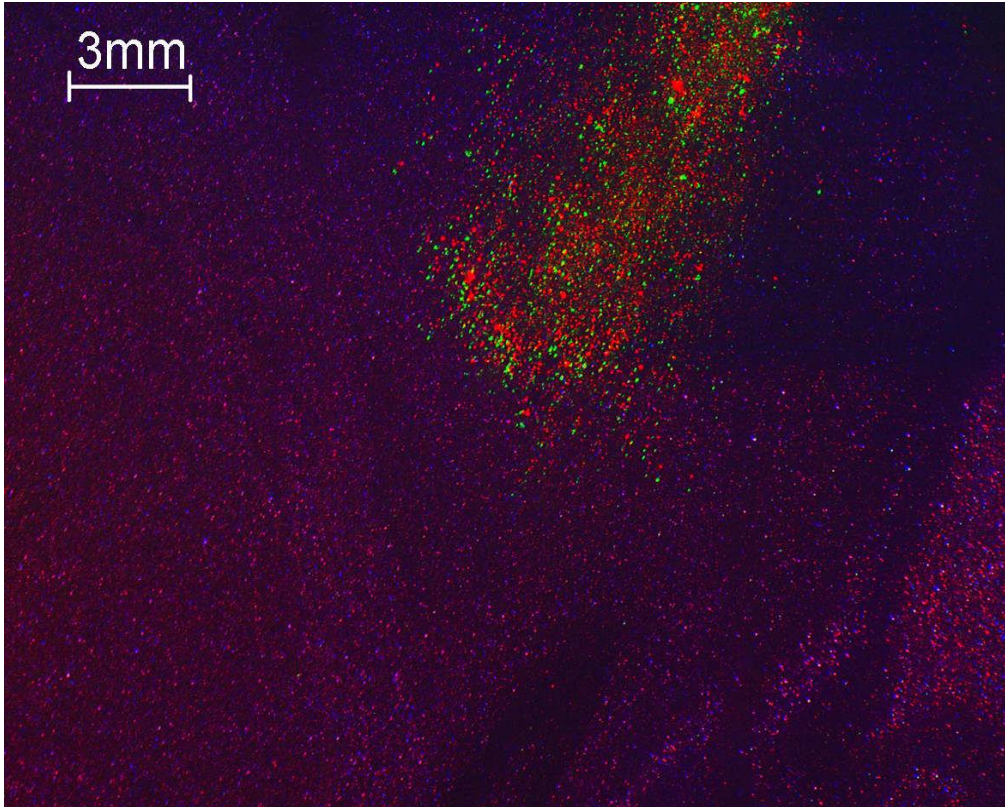


Figure 7-39 RGB stereo multi-phase image for jet 1 and camera 1 – 30bar early injection

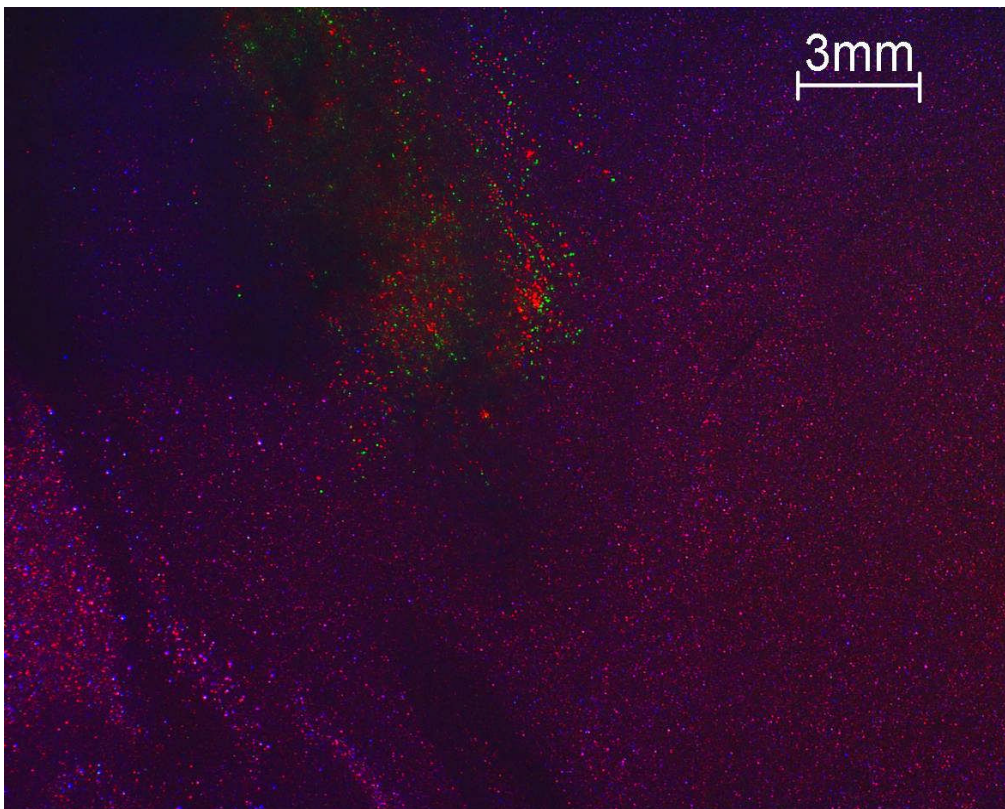


Figure 7-40 RGB stereo multi-phase image for jet 1 and camera 2 – 30bar early injection

It is observed from Figures 7-39 and 7-40 that due to the restricted optical access for camera 2 (due to other jets in the way as shown in Figure 6-11), image quality is better for camera 1 than for camera 2. Nevertheless it was possible to obtain velocity data from images from camera 2.

7.2.1. Stereo vector field calculation

Images were processed using a similar procedure to that used for 2C velocities. After crosstalk correction and phase identification, buffers with 4 frames were created (an image pair for each camera) and were processed using the same settings used in Section 7.1.2. It should be noted here that after vector calculation, the distortions due to CCD offset still need to be accounted for by subtracting vectors with a pulse separation $dt = 0$; it was found that CCD offset was different for each camera and a different vector field should be subtracted for each camera before the 2D3C vector field is reconstructed. Therefore, the sequential cross-correlation mode in DaVis 7.2 was used, where the two 2D2C vectors fields are produced, and the offset was subtracted for each camera view separately. The two 2D2C corrected vector maps were then combined and the final reconstructed 2D3C vector field was obtained.

7.2.2. Stereo PIV average vector fields

Average vector fields were calculated using 50 instantaneous realisations for each condition. The vectors indicate the conventional in-plane vector field and the out of plane velocity is shown as the background colour of the image with the corresponding velocity scale on the right hand side of the image. Out of plane velocity has been scaled from $-$ maximum to $+$ maximum so that red background indicates positive out of plane velocity and blue background indicate negative out of plane velocity. For each condition, the average fuel phase vector field is shown first followed by the average gas phase vector field.

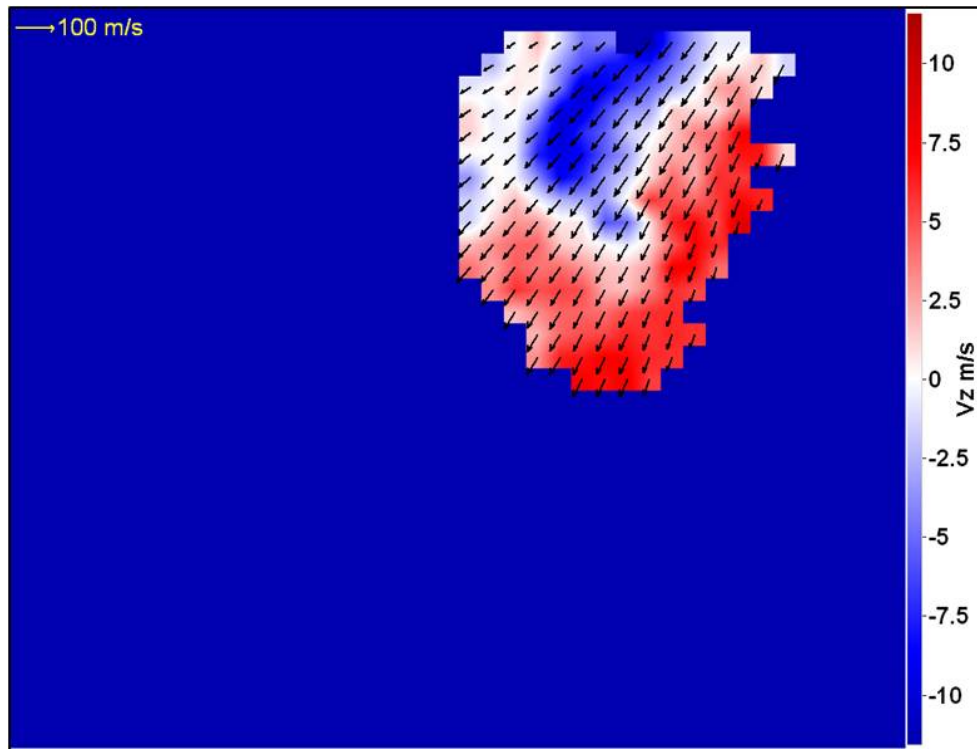


Figure 7-41 Stereo vectors of fuel phase at 30 bar – early injection; background and side colour bar show out of plane velocity

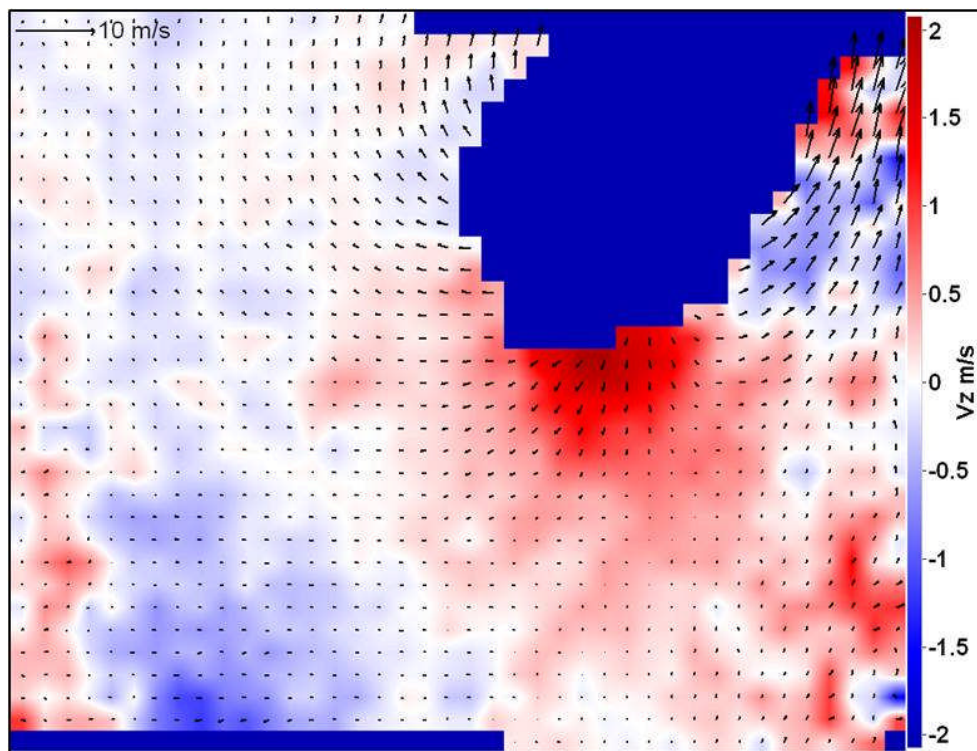


Figure 7-42 Stereo vectors of gas phase at 30 bar – early injection; background and side colour bar show out of plane velocity

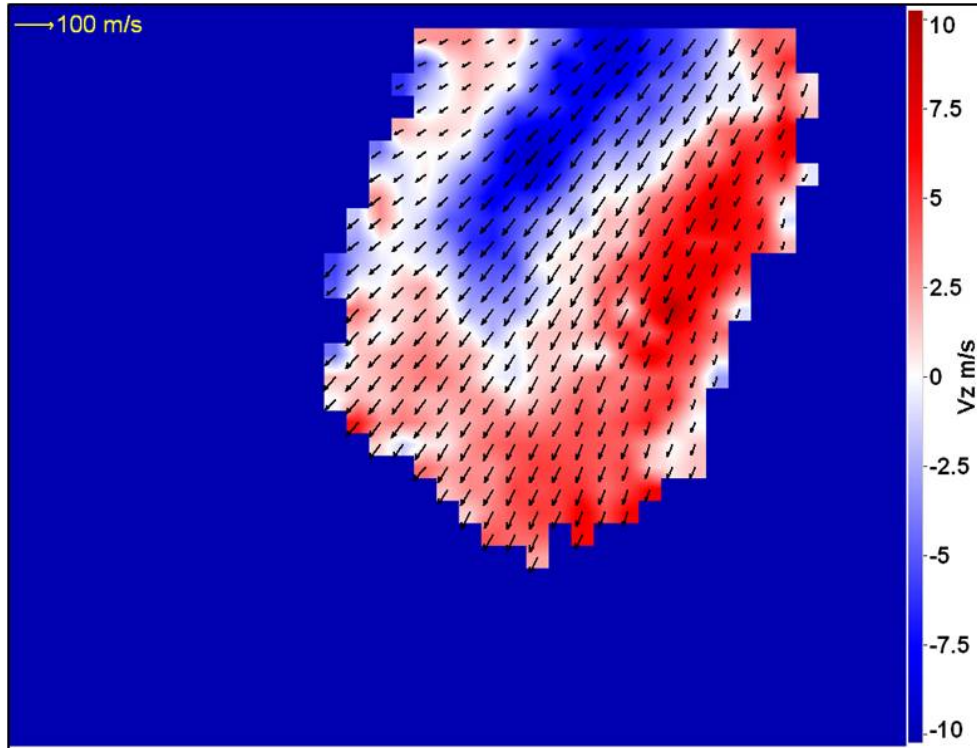


Figure 7-43 Stereo vectors of fuel phase at 30 bar – half injection; background and side colour bar show out of plane velocity

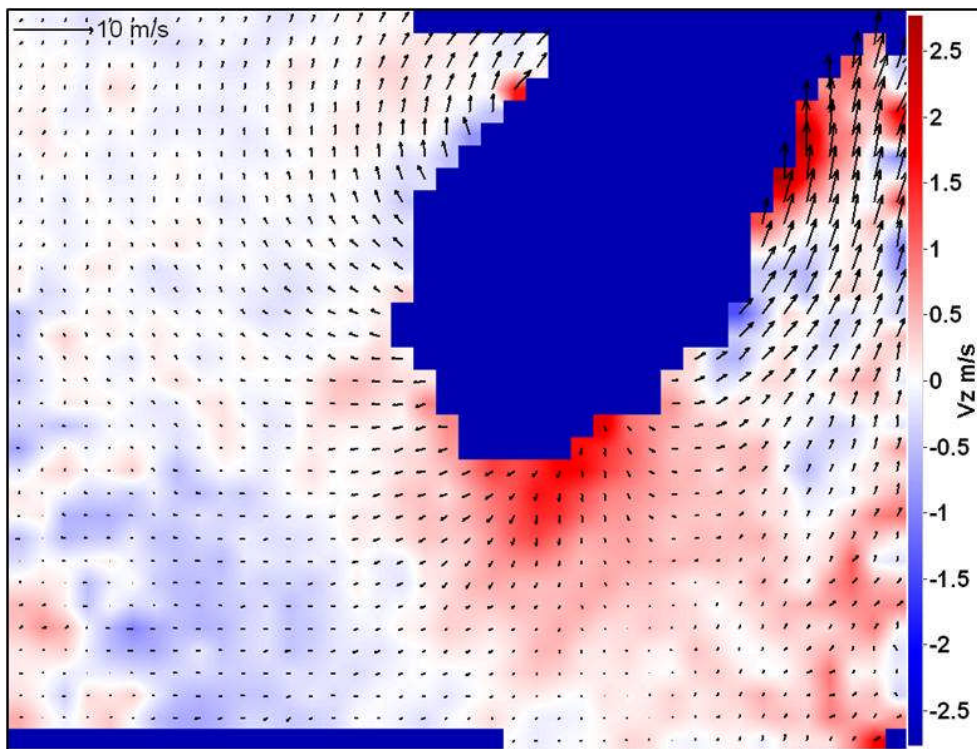


Figure 7-44 Stereo vectors of gas phase at 30 bar – half injection; background and side colour bar show out of plane velocity

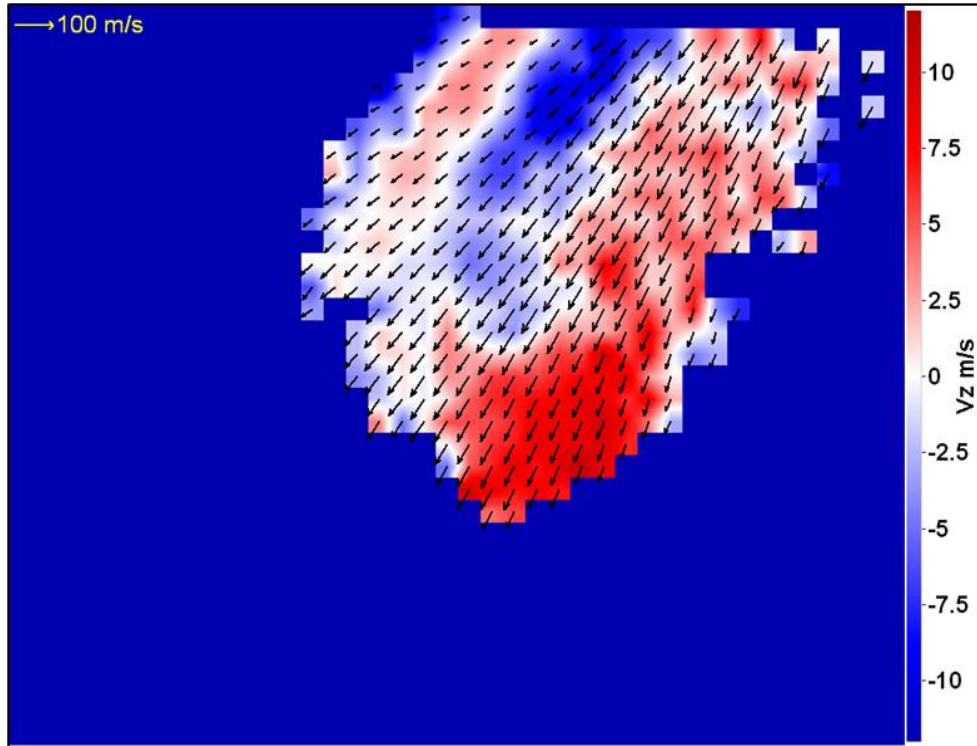


Figure 7-45 Stereo vectors of fuel phase at 54 bar – early injection; background and side colour bar show out of plane velocity

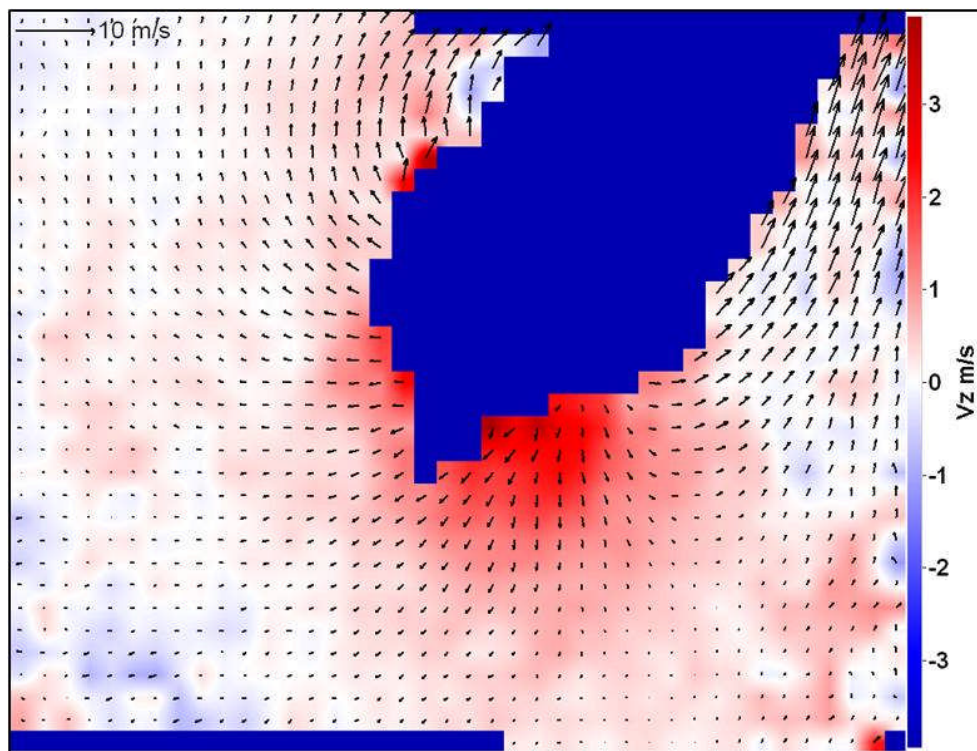


Figure 7-46 Stereo vectors of gas phase at 54 bar – early injection; background and side colour bar show out of plane velocity

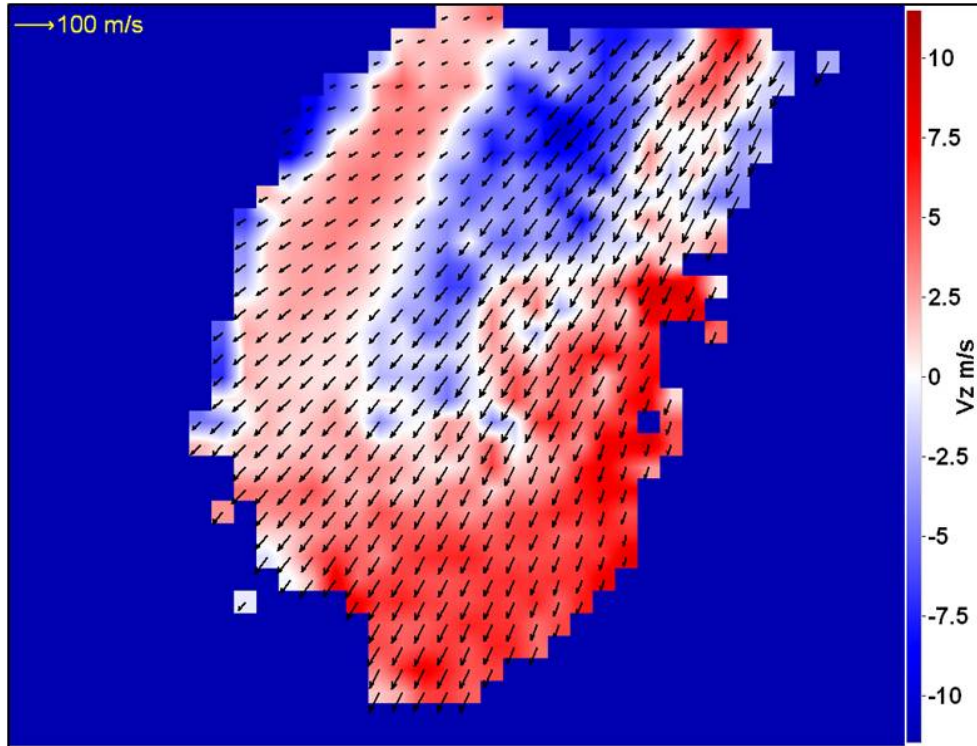


Figure 7-47 Stereo vectors of fuel phase at 54 bar – half injection; background and side colour bar show out of plane velocity

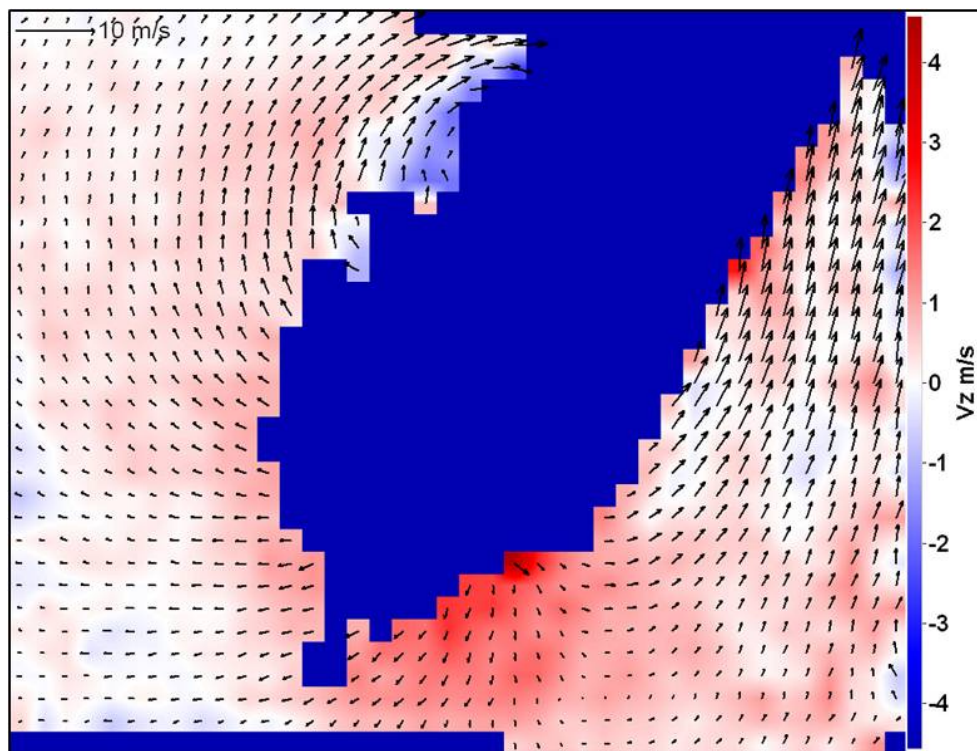


Figure 7-48 Stereo vectors of gas phase at 54 bar – half injection; background and side colour bar show out of plane velocity

The out of plane velocity shows different patterns which had not been observed from the 2C velocity fields. The spray phase shows a rotation in the near nozzle region. In the gas phase, strong out of plane effects are observed in spatially localised regions around the edge of the spray which appear in the same direction as the local spray velocity. Comparing the gas phase vector fields, it is evident that the out of plane velocity is higher at 54bar due to higher pressure. Positive out of plane velocities (red background) extend over large areas at 54 bar indicating a strong out of plane motion in both phases, the gas phase presumably being driven by the spray, even though the laser light sheet is approximately on the centre line of the spray from the particular nozzle of the injector. The highest out of plane velocities are obtained in the lower part of the air vector fields (just where the fuel terminates) with the highest in-plane velocities in the area below the injector tip (the top right hand corner of the vector field).

7.2.3. Stereo vector fields statistics

The error of the stereo measurements presented can be assessed in the form of a reconstruction error (Section 3.4.7.1.). DaVis 7.2 provides an estimation of the reconstruction error both as a vector post-processing filter and also as a contour map once the 3C vector field has been calculated. However, due to the way vectors were calculated, a combination of two 2C vector maps after offset correction, the option of an error map was not available in DaVis 7.2 under this correlation mode (sequential cross-correlation) hence an estimation of the reconstruction error was only available as a post-processing option when converting two 2D2C vector maps into 2D3C. In this mode, however, it was not possible to plot the reconstruction error hence only a qualitative assessment was possible. The maximum error obtained for fuel phase was 1.4 pixels (for a maximum displacement of ~30 pixels) but the majority of the vectors presented an error well below that. Similarly, the maximum error for the gas phase was 0.4 pixels (for a maximum displacement of ~4pixels) and most of the vector field presented an error below that level.

7.3. Discussion of results

7.3.1. Optical system

- The proposed optical system has been successfully used for the simultaneous measurement of fuel and air in a 6-hole GDI spray. Compared to the other systems previously used for GDI two-phase measurements, the system proposed here is simpler with only one 3CCD colour camera required for 2C measurements. The proposed approach requires an extra laser pulse to obtain the three exposures on the RGB channels. It has been shown that a twin cavity Nd:YAG system in combination with a dye laser can produce the required illumination.
- The proposed imaging system was successfully extended to obtain stereo two-phase velocity measurements by adding a second colour camera in a stereoscopic arrangement.
- The use of an absorber in the dispersed phase allowed the simultaneous imaging of the two phases with different tracer sizes (1.8 μm for air and up to $\sim 30\mu\text{m}$ for fuel) without observing the previously reported problems such as 'coronas', excessive background levels and inability to image fuel droplets in the middle of the dense spray. Whilst it could be argued that an 8-bit resolution camera is limiting in this application, the fact that sharp images are obtained even in the densest spray regions is indicative of the contrast reduction achieved through use of the absorber.
- Previous studies had reported crosstalk from the fuel phase with multi-camera arrangements, e.g. (Driscoll et al. 2003), for 2C measurements. The absorber reduces the intensity of the light scattered from the fuel phase with the benefit increasing with drop-size due to the increased path length in the droplet over which the absorber can act. Hence the combination of reduced intensity and the image processing algorithms described has enabled crosstalk to be removed from the colour based imaging system. Phase discrimination was performed in the experiments reported here without relying on particle size or particle velocity differences between the phases.

7.3.2. Spray measurements

- The spray and cone angle measurements presented in Section 6.3.1 confirmed one of the previous reported features on multi-hole GDI injectors (Mitroglou et al. 2006); it was found that the cone angle of each individual jet was independent of the fuel injection pressure and, as expected, fuel penetrates further with a higher injection pressure.
- Chapter 2 established that efforts in GDI spray injectors are being focused on the development of multi-hole sprays hence the results obtained in this chapter are relevant for the current state of GDI spray development.
- Given the characteristics of the fuel injector used for the measurement (6 axisymmetric jets), access was restricted hence the reduced quality of the images obtained for jet5 in 2C measurements; it should be noted that similar problems would be experienced with conventional monochrome cameras. For other proposed configurations of GDI injectors, such as three-hole injectors, better access to each individual jet will be obtained and similar image quality will be obtained from both cameras in stereo measurements.
- Similarly, due to out of plane effects obtained from the illumination plane being a small distance from the spray axis, the validation of vectors for jet 5 is worse than that for jet 1; this led to more instantaneous realisations required for the calculations of a reliable average vector field.
- The resolution of the 2C measurements is expected to be similar to that calculated in Section 5.5 where the average velocity uncertainty was 3.96%.
- Sharp velocity changes (direction) can be observed in the gas phase between the flow being entrained further up towards the nozzle and the flow pushed out from the spray (e.g. Figure 7-6). These are resolved very well probably because the maximum magnitude of the velocities in the gas phase is similar to the width of the correlation peak and hence what is being resolved is different locations of the centre of the peak rather than

separate peaks themselves. This perhaps makes it easier for the peak finding algorithms to find robust correlation peaks in all cases. The disadvantage of this is that the resolution of the velocities is limited.

- An interesting combination of features has been observed regarding vorticity, out of plane velocity, RMS and turbulence intensity in the fuel phase as exemplified in Figure 7-49 for an injection pressure of 30bar at half injection. There are correlations in the spatial positions of high levels of vorticity (a) and high out of plane velocity (b) with opposite signs of both quantities on the two sides of the individual jet. This combination of patterns implies a vortical structure propagating toroidally around the fuel phase. The high out-of-plane velocities may arise because of swirl in the channel built into the injector nozzle. Another mechanism maybe due to the high vorticity that is present, probably due to spray droplet break-up into smaller droplets, and the energy associated with the vorticity feeds the out-of-plane velocity. These positions are also correlated with areas where high RMS values (c) and turbulence intensity (d) are obtained.

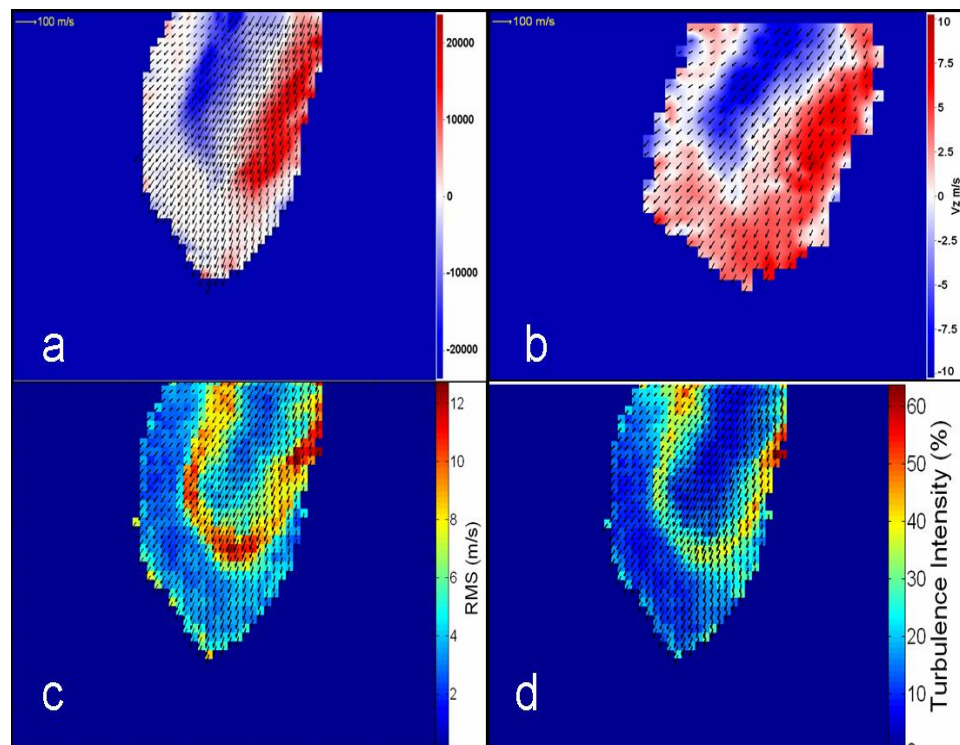


Figure 7-49 Vorticity (a), out of plane velocity (b), RMS (c) and turbulence intensity (d) for fuel phase at 30bar half injection

- Measurements were obtained from two injectors of the same specifications. Velocimetry (Figures 7-5 and 7-8), RMS (Figure 7-27), turbulence intensity (Figure 7-32) and vorticity (Figure 7-38) data show minimal variations between the two injectors which is one of desired characteristics for both PFI and GDI injectors as established in Section 2.2.6.2.
- Amongst the different errors in PIV measurements described in Section 3.4.6 the effect of peak locking, tracking and acceleration errors have already been discussed for the two-phase measurements presented in this thesis. The effect of other unrecoverable errors, however, needs to be assessed for the measurements presented here with the main quantifiable unrecoverable errors being due to out of plane and perspective effects. For the fuel phase, the worst case scenario is assumed to be when the highest out of plane velocity is obtained and its correspondent 3C velocity magnitude; the highest out of plane velocity measured was 12m/s for a velocity of 100m/s. Assuming $V_x=0.5V_y$, $V_z=12$ and $|V| = 100$ then

$$|V| = \sqrt{V_x^2 + V_y^2 + 12^2} = 100 \text{ m/s}$$

hence $V_x=44.4$ m/s and $V_y=88.8$ m/s. If the z component was not measured, the following velocity magnitude would be obtained from considering V_x and V_y only:

$$|V| = \sqrt{44.4^2 + 88.8^2} = 99 \text{ m/s}$$

hence the maximum unrecoverable error for the fuel phase under the conditions assumed is 1% given by the difference of including the out of plane component when calculating the velocity magnitude. This value is low due to the high in-plane velocities obtained. Given the gas phase is likely to be more isotropic the effect of out of plane/perspective errors is expected to be more significant. For the worst case scenario, an isotropic vector ($V_x=V_y=V_z=V$) is assumed to then calculate the magnitude when 3 and 2 components are measured respectively. For a 3C vector the velocity magnitude would be:

$$|V| = \sqrt{(V_x^2 + V_y^2 + V_z^2)} = \sqrt{3}V$$

For a 2C vector the magnitude would be:

$$|V| = \sqrt{V_x^2 + V_y^2} = \sqrt{2}V$$

hence the highest unrecoverable error is approximately the ratio of the 2C and 3C velocities:

$$1 - \sqrt{2} / \sqrt{3} = 18.3\%$$

this value contrasts with the calculated maximum error of 1% for the fuel phase. Whilst this maximum error is relatively large, it is inherent to classical 2D PIV where a vector field is obtained in the same plane of the laser light sheet. This thesis has produced 3C measurements where the out of plane component has been calculated hence the effects of perspective and out of plane errors should have been considerably lower than 18.3% for 2C measurements.

7.3.3. Significance of measurements

- Spray droplets have been imaged within the dense breakup region of the spray; this was achieved with the use of an absorber which has reduced the effects of multiple scattering normally obtained when imaging dense sprays.
- Structural differences have been obtained for the velocity fields of jet 1 and jet 5; a difference in the internal flow channels in the injector for these jets was observed experimentally in the wetted footprint (Figure 2-5) obtained on the glass barrel surface. This difference may also generate a change in fuel swirl on exiting the nozzle between the two jets and coupled with the off-axis illumination in jet 5, would be expected to lead to differences in the measured swirl level of the fuel and therefore differences in the velocity structure.

- The combined data obtained through these experiments: out-of-plane velocity, vorticity and turbulence intensity provides insights as to the conditions within the spray and entrainment of air. The spray contains regions going down each side of the jet with opposite vorticity and out-of-plane velocity indicating a strong rotation of the spray about its axis.
- The multi-phase data obtained in these experiments can also be used when assessing the interaction of air and fuel; air entrainment by fuel sprays has been investigated quantitatively using 2C mean gas phase velocity fields to measure the mass flow rate of entrained gas (Han and Mungal 2001) (Sepret et al. 2010). These references assume axisymmetric conditions and hence zero out-of-plane velocities on a plane through the centre of the spray. The data presented in this thesis shows that even when a jet is illuminated on the spray axis, e.g. jet 1, there can be significant out-of-plane velocities in the gas phase. Hence, the use of 2C data will provide over-estimates of the mass flow rate of entrained gas. Gas phase entrainment cannot be fully quantified from the 3C data presented in this thesis as imaging was not performed up to the injector nozzle. However, it is clear that 3C data should be used in the future to accurately quantify entrainment and thereby compare injectors and injection strategies.

7.4. Summary

Multi-phase air/fuel measurements have been produced from a high pressure GDI injector system. Flow phase and pulse order have been determined from a single 3CCD colour camera for 2-component velocimetry. Stereo velocity measurements have been obtained using a pair of 3CCD cameras providing previously unavailable simultaneous information on the multi-phase (fuel/air) interaction with three velocity components.

The initial, average vector fields presented here show significant structure in the out of plane velocity component. The spray phase shows a rotation in the near nozzle region. In the gas phase, strong out of plane effects are observed in

spatially localised regions around the edge of the spray which appear in the same direction as the local spray velocity.

Chapter 8

CONCLUSIONS AND FUTURE WORK

In this thesis a new imaging approach for simultaneous multi-phase velocity measurements was presented. The study included an explanation of the motivation for improved approaches, the description of the imaging system and its application to multi-constituent and multi-phase air/fuel flows.

The major achievements presented in this thesis are described in the following sections.

8.1. Use of fluorescent tracers for flare removal

- Bis-MSB fluorescent tracers which emit in the blue over the wavelength range 400-470 nm were presented using a new solvent, o-xylene, which allowed higher concentrations up to $1 \times 10^{-2} \text{M}$ to be achieved. The tracers were atomised using medical nebulisers giving a narrow size distribution and an average size of $0.94 \mu\text{m}$ which ensures that the tracers are appropriate for gas-phase PIV applications.
- The visibility of the tracers was evaluated using a 40mm light sheet and 30mJ pulse energy at F#4 in conditions representative of typical PIV experiments. Satisfactory images of fluorescence emission were obtained which compared very favourably with previous studies in which higher

pulse energy and bigger tracers had been used. The visibility of the tracers was also evaluated with an off-the-shelf 3CCD colour camera; high contrast particle images were obtained which also allowed the removal of flare around a car valve.

- Bis-MSB tracers were used to reduce flare in an experiment consisting of flow around a gas turbine blade. Under 532nm illumination flare was obtained due to strong laser light reflection from the blade surface generating a region of unusable pixels; velocity information was lost in different areas of the flow and randomly located spurious vectors were also obtained. Under 355nm illumination flare was successfully removed and high contrast particles were obtained up to the blade surface. Velocity vectors were then obtained within 75 μ m of the blade surface for an image with a field of view of \sim 30mm and the continuity of the velocity field was considerably improved.

8.2. Imaging system for multi-phase measurements

- A novel approach for multi-constituent imaging was presented using a single off the shelf 3CCD colour camera exploiting the co-registration of the three (R, G and B) colour images which are recorded simultaneously. A coupling matrix was used to obtain a quantitative estimate of crosstalk between the colour channels. By inversion of this matrix it was possible to correct for the crosstalk between the colour channels to obtain new corrected R, G, B images that identified flow phase and pulse order. Chromatic and lens distortion were accounted for first with the use of conventional calibration targets and CCD offset was estimated quantitatively from experimentally captured images with zero displacement and then subtracted from each calculated vector field.
- Two fluorescent tracers were introduced which can be illuminated simultaneously with 355nm illumination producing fluorescence emission in the red and blue channels. Bigger particles, mean diameter 2.65 μ m, were required for the red tracers for a sufficiently high signal to noise ratio due to reduced camera sensitivity in the red channel and the required F#11

aperture; the visibility of the red tracers was evaluated with a conventional monochrome camera and it was found that $1\mu\text{m}$ particles were sufficiently bright to provide reliable PIV data.

- A proof of principle experiment was presented in which two spatially separated streams were imaged with the 3CCD colour camera. The crosstalk and chromatic aberration corrective procedures were implemented and, after the vectors for each phase were calculated, separate regions corresponding to each tracer type were obtained indicating that the proposed imaging system discriminated the flow phases successfully.
- A second proof-of-principle experiment was presented in which the two constituents were brought together and then imaged sufficiently downstream to be considered well mixed. Similar correction procedures were implemented and the resultant velocities obtained from each constituent were compared. An average difference of 0.25 pixels from the displacement for each type of tracer was obtained. Additionally, the well mixed vector fields were analysed and it was ensured that they were not affected by peak locking effects.

8.3. GDI multi-phase measurements

- An absorber was added to the fuel phase and it successfully reduced the effects of multiple scattering in the dense GDI spray. The approach was complimented with measurements of spray cone angle, penetration rate and full field velocity to ensure the new mixture of heptane + absorber correctly modelled gasoline dynamics for the fuel injector selected. The measured values for penetration rate were approximately the same for both fuels and the measured cone angle only differed by one degree which, given the experimental measurement error, can also be assumed to be the same. The velocity fields were determined using conventional single phase PIV producing the same overall pattern for the gasoline and heptane + absorber. The difference between the average vector fields could be

explained by a lateral shift of the image that could easily have occurred during rig assembly.

- A system consisting of a conventional Nd:YAG laser producing both 532 and 355nm pulses and a 532nm-pumped dye laser was proposed for multi-phase illumination. Whilst an extra illumination wavelength was needed, it was shown that the alignment of the three beams was relatively straightforward and the spatial alignment and foci position could be obtained by placing a camera directly in the beam path.
- The relative simplicity of the imaging system proposed allowed its extension to obtain simultaneous measurements of the 3-component vector fields in two-phase systems. This was achieved by the addition of a second colour camera in a stereo arrangement requiring the same calibration procedure which has been fully established for conventional monochrome cameras applied to single phase flows. To the best of the author's knowledge, simultaneous full-field stereo measurements in two phase flows have not been reported previously in the literature.
- The use of stereo measurements showed that entrainment calculations will be affected by the out-of-plane velocity component which is not normally taken into account when assessing air entrainment in air/fuel systems. Additionally, the error in the multi-phase stereo measurement was assessed through the calculation of the reconstruction error. Maximum errors of 1.4 pixels (for a maximum displacement of ~30 pixels) and 0.4 pixels (for a maximum displacement of ~4pixels) were obtained for the fuel and gas phase 3C vectors respectively.

8.4. Outlook

From the main focus of this thesis, the following areas of future work have been identified

8.4.1. PIV System Improvements

- The results presented used a single pulse separation for two flows with highly different flow velocities. It may be feasible to use an additional laser pulse to be captured on a separate frame (frame straddling using a colour camera) in order to obtain better resolution in the gas phase velocimetry results. This would require an additional laser cavity and timing electronics synchronised to the camera frame rate.
- Further measurements may be taken with an imaging system with a smaller magnification so that the entire gas phase vector field can be quantified around the fuel spray. From this information, the full entrainment of air can be estimated accurately when using 3-component velocity data.
- It may be possible to obtain additional gas phase velocity data from within the spray, where only sparse velocity vectors were obtained in these experiments. This may be achieved by significantly increasing the time over which seeding is introduced in the cylinder.
- Similar principles maybe applied to multi-constituent mixing analysis in Micro PIV in order to separate the vector fields from two types of liquid flows brought together in a mixing device.

8.4.2. Measurements on the two-phase fuel / air flow from an injector

- Given the current needs in GDI development and the interest in multi-hole injectors further measurements of the air and fuel interaction under different conditions are required as follows.
 - Assessment of the injector under conditions corresponding to stratified combustion in which fuel is injected during the compression stroke. The effect of increased pressure in the combustion chamber can be evaluated in the existing experimental facility by pressurising the cylinder.

- Using the optical system developed, air and fuel interaction measurements can be obtained using multi-hole injectors with different numbers of holes as reported in the literature (11, 6 and 3 holes). In this way it will be possible to establish which configuration is desirable for stratified operation. With a larger number of holes the interaction between the entrained flows for each jet will become stronger which is ideally suited to the 3C multi-phase diagnostic developed in this thesis.
- Novel injection strategies, e.g. the use of multiple injections, are also well suited to the type of multi-phase measurements that are now possible. With multiple injections the in-cylinder flow is significantly modified by the first injection and hence the second injection experiences the 'wake' created by the first. Such phenomena have not been studied in detail and multi-phase full-field imaging methods would provide a large amount of data in a short space of time.
- All the fuel / air data presented in this thesis are obtained from when the spray is injected into a quiescent chamber. As the methods have been demonstrated whilst imaging through a curved glass barrel the techniques should be directly usable on a motored optical engine and hence the fuel / air interaction studied under the actual conditions present in an engine.
- Air entrainment can be estimated quantitatively including the out of plane velocity components provided the PIV data recorded extends to the injector nozzle.

Appendix A

INTERFEROMETRIC PARTICLE IMAGING FOR DROPLET SIZING

Interferometric particle imaging was first applied with a laser light sheet by (Ragucci et al. 1990) and (Glover et al. 1995); in this technique droplet size is calculated by measuring the angular frequency of interference fringes (arising from the light directly reflected from the droplet surface and the first-order refracted beam) in defocused images.

When a droplet is illuminated by a laser, its in focus image consists of glare points (from the reflected and first order refracted rays) whose separation is related to the refractive index of the particle, the observation angle and the particle size (Damaschke et al. 2005). When the particle is imaged out of focus, the two glare points merge into a single image with interference fringes arising from the two glare points; the size of the defocused images depends of the level defocusing.

It is required to find an observation angle for which the intensity of the two scattering orders creating the interference fringes (reflective and refractive) is approximately equal in intensity; this consequently limits the choice of observation angles for this technique to ensure highly scattered intensities and limits its application to non-opaque particles since at least one of the scattering orders must be refractive. An approximately equal intensity of reflected and first-order refracted beams can usually be obtained at a scattering angle of 70° , relative to forward scattering, hence producing high contrast interference fringes.

Figure A-1 below shows interference fringes obtained from a flow of olive oil droplets with a 10x microscope objective and a Hitachi HV-F22F camera.



Figure A-0-1 Interference fringes from olive oil droplets and a 10x microscope objective

For spherical particles the angular frequency of the fringes shown above is related to the particle diameter; it is also dependant on wavelength on light, observation angle and refractive index.

Different approaches have been proposed to determine the angular frequency of the interference fringes. One method consists of estimating the spatial frequency of the fringes and the size of the defocused image; however, it was found that if the image was not a true far field image (near or middle field) the fringes could exhibit curvature and lead to incorrect spatial frequency estimates (Hess 1998). The second method proposed for angular frequency estimation is to count the number of fringes directly from the defocused image; with this method different expressions have been derived (based on geometrical optics) relating the number of fringes on the defocused image to the particle size (Maeda et al. 2002). A more recent publication provides different relationships between angular fringe frequency and particle size including their limits of validity (Semidetnov and Tropea 2004).

The following derivations are based on geometrical optics in which the geometrical path-length difference between a reflected ray and a refracted ray is calculated; the equations presented here are those used to calculate droplet size in Chapters 4, 5 and 6. The interested reader is referred to (Semidetnov and Tropea 2004) for the derivation of the equations presented below.

The number of fringes across a defocused image is given by:

$$N_f = \frac{\Lambda}{\Delta\varphi} \quad \text{Equation A-1}$$

where Λ is the diameter of the receiving optics and $\Delta\varphi$ is the angular spacing between fringes. The diameter of the receiving optics is given by:

$$\Lambda = 2 \arctan \frac{D_a}{2S} \approx \frac{D_a}{S} \quad \text{Equation A-2}$$

where D_a is the diameter of the receiving aperture and S is the measured distance to the particle. The angular spacing between fringes is given by:

$$\Delta\varphi = \frac{2\lambda_b}{d_p n_1} \left(\cos \frac{\theta_r}{2} + \frac{m \sin(\theta_r / 2)}{\sqrt{1 + m^2 - 2m \cos(\theta_r / 2)}} \right)^{-1} \quad \text{Equation A-3}$$

where λ_b is the wavelength of illuminating light, d_p is the particle diameter, n_1 is the refractive index of the surrounding medium, θ_r is the scattering angle (respect to forward direction) and m is the refractive index ratio of droplet to surrounding medium. Hence from the angular spacing between the fringes (dependant on droplet diameter) and the diameter of the receiving optics, droplet size is calculated.

For the droplet size measurements performed in this thesis, the setup was formed to give approximately equal intensity of the reflected and first-order refracted beams at a scattering angle of 70°. A Nikon Plan 20 ELWD microscope objective was used; its working distance is 10mm and numerical aperture 0.4. For o-xylene (Bis-MSB droplets) the refractive index m is 1.5 and the refractive index of the

surrounding medium n is 1 (air); an illuminating wavelength λ_b of 532nm is used. For such configuration, a conversion relationship of 1.5 fringes per micron is obtained.

The validity of these results is given by the validity of geometrical optics to describe the scattered light from small particles. The used relations can be considered to be accurate to within about 1%. A possible source of error during the experimental setup is the alignment of the imaging system relative to the laser sheet with a 70 angle required for a maximum contrast of the interference fringes; this was found to have little effect considering a range of ± 5 degrees in which the conversion relationship does not change much (less than 1%) and can still be considered as 1.5 fringes/micron.

References

- Achleitner E, Bacher H, Funaioli A (2007) Direct Injection Systems for Otto Engines. SAE Technical Papers
- Adrian RJ (1991) Particle-Imaging Techniques for Experimental Fluid-Mechanics. Annual Review of Fluid Mechanics 23:261-304
- Adrian RJ (2005) Twenty years of particle image velocimetry. Experiments in Fluids 39 (2):159-169
- Adrian RJ, Yao C-S (1985) Pulsed laser technique application to liquid and gaseous flows and the scattering power of seed materials. Appl Opt 24 (1):44-52
- Aleiferis P, Hardalupas Y, Taylor A, Ishii K, Urata Y (2005) Cyclic variations of fuel-droplet distribution during the early intake stroke of a lean-burn stratified-charge spark-ignition engine. Experiments in Fluids 39 (5):789-798
- Aleiferis PG, Serras-Pereira J, van Romunde Z, Caine J, Wirth M (2010) Mechanisms of spray formation and combustion from a multi-hole injector with E85 and gasoline. Combustion and Flame 157 (4):735-756
- Angarita-Jaimes DA, Ormsby MP, Chennaoui M, Angarita-Jaimes NC, Towers CE, Jones AC, Towers DP (2008) Optically efficient fluorescent tracers for multi-constituent PIV. Experiments in Fluids 45 (4):623-631
- Arnott A, Schneider G, Neitzke KP, Agocs J, Sammler B, Schroder A, Kompenhans J Multi-window PIV for high-lift measurements. In: Instrumentation in Aerospace Simulation Facilities, 2003. ICASF '03. 20th International Congress on, 25-29 Aug. 2003 2003. pp 44-53
- Arroyo MP, Hinsch KD (2008) Recent developments of PIV towards 3D measurements. In: Particle Image Velocimetry: New Developments and Recent Applications, vol 112. Topics in Applied Physics. Springer-Verlag Berlin, Berlin, pp 127-154
- Atkinson C, Soria J (2009) An efficient simultaneous reconstruction technique for tomographic particle image velocimetry. Experiments in Fluids 47 (4):553-568. doi:10.1007/s00348-009-0728-0
- Barker DB, Fourney ME (1977) Measuring fluid velocities with speckle patterns. Opt Lett 1 (4):135-137

- Barnhart DH, Halliwell NA, Coupland JM (2000) Holographic particle image velocimetry: analysis using a conjugate reconstruction geometry. *Optics & Laser Technology* 32 (7-8):527-533
- Berrocal E, Kristensson E, Richter M, Linne M, Alden M (2008) Application of structured illumination for multiple scattering suppression in planar laser imaging of dense sprays. *Optics Express* 16 (22):17870-17881
- Boedec T, Simoens S (2001) Instantaneous and simultaneous planar velocity field measurements of two phases for turbulent mixing of high pressure sprays. *Experiments in Fluids* 31 (5):506-518
- Bögner W, Krämer M, Krutzsch B, Pischinger S, Voigtländer D, Wenninger G, Wirbeleit F, Brogan MS, Brisley RJ, Webster DE (1995) Removal of nitrogen oxides from the exhaust of a lean-tune gasoline engine. *Applied Catalysis B: Environmental* 7 (1-2):153-171
- Bohren C, Huffman D (1998) *Absorption and Scattering of Light by small particles*. Wiley Inter-Science,
- Boillot A, Prasad AK (1996) Optimization procedure for pulse separation in cross-correlation PIV. *Experiments in Fluids* 21 (2):87-93
- Bosch R (2006) *Gasoline-Engine Management*. Wiley,
- Brennen C (2005) *Fundamentals of Multiphase flow*. Cambridge University Press, New York
- Bröder D, Sommerfeld M (2002) An advanced LIF-PLV system for analysing the hydrodynamics in a laboratory bubble column at higher void fractions. *Experiments in Fluids* 33 (6):826-837
- Callaud D, David L (2004) Stereoscopic particle image velocimetry measurements of the flow around a surface-mounted block. *Experiments in Fluids* 36 (1):53-61
- Chang TP, Wilcox NA, Tatterson GB (1984) APPLICATION OF IMAGE-PROCESSING TO THE ANALYSIS OF 3-DIMENSIONAL FLOW-FIELDS. *Optical Engineering* 23 (3):283-287
- Chen J, Katz J (2005) Elimination of peak-locking error in PIV analysis using the correlation mapping method. *Measurement Science and Technology* 16 (8):1605
- Cheng Y, Pothos S, Diez F (2010) Phase discrimination method for simultaneous two-phase separation in time-resolved stereo PIV measurements. *Experiments in Fluids*

- Chennaoui M, Angarita-Jaimes D, Ormsby MP, Angarita-Jaimes N, McGhee E, Towers CE, Jones AC, Towers DP (2008) Optimization and evaluation of fluorescent tracers for flare removal in gas-phase particle image velocimetry. *Measurement Science & Technology* 19 (11)
- Chennaoui M, McGhee EJ, Towers CE, Jones AC, Towers DP Flare removal in gas phase PIV: Optimization of fluorescent tracers. In: 13th International Symposium on Applications of Laser Techniques to Fluid Mechanics, Lisbon, Portugal, 2006.
- Chigier N, Reitz R (1995) Regimes of Jet Breakup and Breakup Mechanisms (Physical Aspects). In: Kuo K (ed) *Recent Advances in Spray Combustion: Spray Atomization and Drop Burning Phenomena Volume I*. Progress in Astronautics and Aeronautics. Reston, Virginia,
- Choi J, Lee S, Shin H, Bae C (2000) Fuel-spray Characteristics of high pressure Gasoline Injection in flowing fields. *JSME international journal Series B, Fluids and thermal engineering* 43 (4)
- Cholemari M (2007) Modeling and correction of peak-locking in digital PIV. *Experiments in Fluids* 42 (6):913-922
- Coupland JM, Halliwell NA (1992) PARTICLE IMAGE VELOCIMETRY - 3-DIMENSIONAL FLUID VELOCITY-MEASUREMENTS USING HOLOGRAPHIC RECORDING AND OPTICAL CORRELATION. *Applied Optics* 31 (8):1005-1007
- Coupland JM, Pickering CJD (1988) Particle image velocimetry: Estimation of measurement confidence at low seeding densities. *Optics and Lasers in Engineering* 9 (3-4):201-210
- Coupland JM, Pickering CJD, Halliwell NA (1987) Particle image velocimetry: theory of directional ambiguity removal using holographic image separation. *Appl Opt* 26 (9):1576-1578
- Crowe C, Sommerfeld M, Tsuji Y (1998) *Multiphase flows with droplets and particles*. CRC Press, Boca Raton, Florida
- Crowe T (2005) *Multiphase Flow Handbook*. CRC Press,
- Dadi M, Stanislas M, Rodriguez O, Dymont A (1991) A STUDY BY HOLOGRAPHIC VELOCIMETRY OF THE BEHAVIOR OF FREE SMALL PARTICLES IN A FLOW. *Experiments in Fluids* 10 (5):285-294
- Damaschke N, Gouesbet G, Gréhan G, Mignon H, Tropea C (1998) Response of Phase Doppler Anemometer Systems to Nonspherical Droplets. *Appl Opt* 37 (10):1752-1761

- Damaschke N, Nobach H, Nonn TI, Semidetnov N, Tropea C (2005) Multi-dimensional particle sizing techniques. *Experiments in Fluids* 39 (2):336-350
- Dankers S, Gotthardt M, Stengler T, Ohmstede G, Hentschel W (2008) Two-phase PIV: Fuel-spray interaction with surrounding air. *Particle Image Velocimetry: New Developments and Recent Applications* 112:333-343
- Dantec (2010) Dantec Dynamics. Laser Optical Measurement Systems and Sensors. <http://www.dantecdynamics.com/>.
- Davy MH, Williams PA, Anderson RW (1998) Effects of injection timing on liquid fuel distributions in a centrally injected four-valve, direct injection, spark ignition engine. SAE Technical Paper Series
- Deen NG, Westerweel J, Delnoij E (2002) Two-Phase PIV in Bubbly Flows: Status and Trends. *Chemical Engineering & Technology* 25 (1):97-101
- Delnoij E, Westerweel J, Deen NG, Kuipers JAM, van Swaaij WPM (1999) Ensemble correlation PIV applied to bubble plumes rising in a bubble column. *Chemical Engineering Science* 54 (21):5159-5171
- Dodge L (1996) Fuel preparation requirements for direct-injected spark ignition engines SAE Technical Paper Series
- Drake MC, Haworth DC (2007) Advanced gasoline engine development using optical diagnostics and numerical modelling. proceedings of the Combustion Institute 31:99-124
- Driscoll KD, Sick V, Gray C (2003) Simultaneous air/fuel-phase PIV measurements in a dense fuel spray. *Experiments in Fluids* 35 (1):112-115
- Durst F, Melling A (1981) Principles and Practice of Laser Doppler Anemometry. Whitelaw, J. H. Academic Press Inc,
- Elsinga G, Scarano F, Wieneke B, van Oudheusden B (2006) Tomographic particle image velocimetry. *Experiments in Fluids* 41 (6):933-947. doi:10.1007/s00348-006-0212-z
- EuropeanUnion (2000) The Auto-Oil II Programme - A Report from the services of the European Commission.
- EuropeanUnion (2002) Implementing the Community Strategy to Reduce CO2 Emissions from cars: Fourth annual report on the effectiveness of the strategy. Brussels

- European Union (2007) Setting emission performance standards for new passenger cars as part of the Community's integrated approach to reduce CO₂ emissions from light duty vehicles. . Brussels
- European Union (2009) Setting emission performance standards for passenger cars as part of the Community's integrated approach to reduce CO₂ emissions from light-duty vehicles.
- Fang Ren K, Girasole T, Taylor A, Gouesbet G, Gréhan G (2003) Theoretical evaluation of a shadow Doppler velocimeter. *Optics Communications* 220 (4-6):269-280
- Fansler TD, Drake MC (2006) "Designer diagnostics" for developing direct-injection gasoline engines. *Journal of Physics: Conference Series* 45 (1):1
- Fincham A, Delerce G (2000) Advanced optimization of correlation imaging velocimetry algorithms. *Experiments in Fluids* 29 (0):S013-S022. doi:10.1007/s003480070003
- Fraidl G, Piock W, Wirth M (1996) Gasoline Direct Injection: Actual trends and future strategies for injection and combustion systems. SAE Technical Paper Series
- Gaydon M, Raffel M, Willert C, Rosengarten M, Kompenhans J (1997) Hybrid stereoscopic particle image velocimetry. *Experiments in Fluids* 23 (4):331-334
- Gharib M, Hernan MA, H. YA, Sarohia V (1985) Flow velocity measurement by image processing of optically activated tracers. *AIAA Journal*
- Giannadakis E, Papoulias D, Theodorakakos A, Gavaises M (2008) Simulation of cavitation in outward-opening piezo-type pintle injector nozzles. *Proceedings of the Institution of Mechanical Engineers, Part D: Journal of Automobile Engineering* 222 (10):1895-1910
- Glover AR, Skippon SM, Boyle RD (1995) Interferometric laser imaging for droplet sizing: A method for droplet-size measurement in sparse spray systems. *Applied Optics* 34 (36):8409-8421
- Gold M, Stokes J, Morgan R (2001) Air-Fuel Mixing in a Homogeneous Charge DI Gasoline Engine. SAE Technical Paper Series
- Goodman J (1968) *Introduction to Fourier Optics*. McGraw-Hill, New York
- Grant I (1994) *Selected papers on Particle Image Velocimetry*. (SPIE Milestone series). SPIE-International Society for Optical Engineering,

- Grant I (1997) Particle image velocimetry: a review. Proceedings of the Institution of Mechanical Engineers, Part C: Journal of Mechanical Engineering Science 211 (1):55-76
- Gui L, Lindken R, Merzkirch W (1997) Phase separated PIV measurements of the flow around systems of bubbles rising in water. Paper presented at the ASME Fluids Engineering Division Summer Meeting,
- Gui L, Merzkirch W (2000) A comparative study of the MQD method and several correlation-based PIV evaluation algorithms. Experiments in Fluids 28 (1):36-44. doi:10.1007/s003480050005
- Gui L, Wereley ST (2002) A correlation-based continuous window-shift technique to reduce the peak-locking effect in digital PIV image evaluation. Experiments in Fluids 32 (4):506-517
- Han D, Mungal MG (2001) Direct measurement of entrainment in reacting/nonreacting turbulent jets. Combustion and Flame 124 (3):370-386
- Hardalupas Y, Hishida K, Maeda M, Morikita H, Taylor AMKP, Whitelaw JH (1994) Shadow Doppler technique for sizing particles of arbitrary shape. Appl Opt 33 (36):8417-8426
- Hargrave G, Wigley G, Allen J, Bacon A (2000) Optical diagnostics and direct injection of liquid fuel sprays. Journal of Visualization 2 (3):293-300
- Hassan YA (1998) Multiphase measurements using particle image velocimetry. In: Hand Book of Fluid Dynamics. Johnson RW, West Palm Beach,
- Hassan YA, Blanchat TK, Seeley Jr CH, Canaan RE (1992) Simultaneous velocity measurements of both components of a two-phase flow using particle image velocimetry. International Journal of Multiphase Flow 18 (3):371-395
- Hentschel W (2000) Optical diagnostics for combustion process development of direct-injection gasoline engines. Proceedings of the Combustion Institute 28:1119-1135
- Hentschel W (2002) Optical Diagnostics in DI Gasoline Engines. In: Applied Combustion Diagnostics. Combustion: An International Series.
- Hentschel W, Homburg A, Ohmstede G, Muller T, Grunefeld G (1999) Investigation of spray formation of DI hollow-cone injectors inside a pressure chamber and a glass ring engine by multiple optical techniques. SAE Technical Paper Series
- Hess C Planar particle image analyzer. In: 9th International symposium on applications of laser techniques to fluid mechanics, Lisbon, Portugal, 1998.

- Hinsch KD (1995) Three-dimensional particle velocimetry. *Measurement Science and Technology* 6 (6):742
- Hinsch KD (2002) Holographic particle image velocimetry. *Measurement Science and Technology* 13 (7):R61
- Hinze J (1959) *Turbulence: An introduction to its Mechanism and Theory*. McGraw-Hill,
- Hitachi (2010) HV-F22F 3-CCD Colour Camera. http://www.hitachikokusai.com/Apps/hitachidenshi/content.jsp?page=progressive_scan/3_CCD_color_progressive/details/HV-F22F.html&level=2§ion=progressive_scan&parent=3_CCD_color_progressive&nav=left&path=jsp/hitachidenshi/products/industrial_video_systems/&nlid=iD. Accessed 19 August 2010
- Hoyer K, Holzner M, Lüthi B, Guala M, Liberzon A, Kinzelbach W (2005) 3D scanning particle tracking velocimetry. *Experiments in Fluids* 39 (5):923-934. doi:10.1007/s00348-005-0031-7
- Huang PS, Hu QY, Jin F, Chiang FP (1999) Color-encoded digital fringe projection technique for high-speed three-dimensional surface contouring. *Optical Engineering* 38 (6):1065-1071
- Hung DL, Harrington DL, Gandhi AH, Markle LE, Parrish SE, Shakal JS, Sayar H, Cummings SD, Kramer JL (2008) Gasoline Fuel Injector Spray Measurement and Characterization - A New SAE J2715 Recommended Practice. SAE Technical Paper Series
- Ido T, Murai Y (2006) A recursive interpolation algorithm for particle tracking velocimetry. *Flow Measurement and Instrumentation* 17 (5):267-275. doi:10.1016/j.flowmeasinst.2006.06.001
- Iwamoto Y, Noma K, Nakayama T, Yamauchi T, Ando H (2000) Development of Gasoline Direct Injection Engine. In: *Direct Fuel Injection for Gasoline Engines*. SAE, Warrendale, PA, USA,
- Jakobsen ML, Easson WJ, Greated CA, Glass DH (1996) Particle image velocimetry: Simultaneous two-phase flow measurements. *Measurement Science & Technology* 7 (9):1270-1280
- Keane RD, Adrian RJ (1990) Optimization of particle image velocimeters. I. Double pulsed systems. *Measurement Science and Technology* 1 (11):1202
- Keane RD, Adrian RJ (1992) Theory of cross-correlation analysis of PIV images. *Applied Scientific Research* 49 (3):191-215

- Khalitov DA, Longmire EK (2002) Simultaneous two-phase PIV by two-parameter phase discrimination. *Experiments in Fluids* 32 (2):252-268. doi:10.1007/s003480100356
- Kiger KT, Pan C (2000) PIV technique for the simultaneous measurement of dilute two-phase flows. *Journal of Fluids Engineering-Transactions of the Asme* 122 (4):811-818
- Kim M, Kihm K (2004) Microscopic PIV measurements for electro-osmotic flows in PDMS microchannels. *Journal of Visualization* 7 (2):111-118. doi:10.1007/bf03181583
- Kim S, et al. (2007) Effects of intake swirl and coolant temperature on spray structure of a high pressure multi-hole injector in a direct-injection gasoline engine. *Journal of Physics: Conference Series* 85 (1):012003
- Kim S, Nouri J, Yan Y, Arcoumanis C (2007) Effects of intake swirl and coolant temperature on spray structure of a high pressure multi-hole injector in a direct-injection gasoline engine. *Journal of Physics: Conference Series* 85 (1):012003
- Kleinstreuer C (2003) *Two-phase flow. Theory and Applications*. Taylor & Francis Books., New York
- Komine H (1990) System for measuring velocity field of fluid flow utilizing a laser-Doppler spectral image converter.
- Konrath R, Klein C, Schröder A, Kompenhans J (2008) Combined application of pressure sensitive paint and particle image velocimetry to the flow above a delta wing. *Experiments in Fluids* 44 (3):357-366
- Kosiwczuk W, Cessou A, Trinite M, Lecordier B (2005) Simultaneous velocity field measurements in two-phase flows for turbulent mixing of sprays by means of two-phase PIV. *Experiments in Fluids* 39 (5):895-908
- Kowalczyk M (1996) Laser speckle velocimetry. In: Pluta M, Jabczynski JK, Szyjer M (eds) *Optical Velocimetry*, vol 2729. Proceedings of the Society of Photo-Optical Instrumentation Engineers (Spie). Spie - Int Soc Optical Engineering, Bellingham, pp 139-145
- Kubo M, Sakakida A, Iiyama A (2003) Techniques for analyzing swirl nozzles of direct-injection gasoline engines and application to tapered tip nozzle analysis. *Jsme International Journal Series B-Fluids and Thermal Engineering* 46 (1):17-24
- Kume T, Iwamoto Y, Iida K, Murakami M, Akishino K, Ando H (1996) Combustion control technologies for direct injection SI engine. . In: *Direct Fuel Injection for Gasoline Engines*. SAE, Warrendale, PA, USA,

LaVision (2007) Flow Master, Product Manual.

LaVision (2010) FlowMaster Micro PIV. http://www.lavision.de/en/products/flowmaster/micro_piv.php. Accessed 11 August 2010

Lawson NJ, Wu J (1997) Three-dimensional particle image velocimetry: experimental error analysis of a digital angular stereoscopic system. *Measurement Science and Technology* 8 (12):1455

Le Gal P, Farrugia N, Greenhalgh DA (1999) Laser Sheet Dropsizing of dense sprays. *Optics & Laser Technology* 31 (1):75-83

Lee L, Nishida K (2003) Simultaneous flow field measurement of D.I. gasoline spray and entrained ambient air by LIF-PIV technique. SAE Technical Paper Series 2003-01-1115

Li Y, Zhao H, Peng Z, Ladommatos N (2002a) Particle image velocimetry measurement of in-cylinder flow in internal combustion engines - experiment and flow structure analysis. *Proceedings of the Institution of Mechanical Engineers Part D-Journal of Automobile Engineering* 216 (D1):65-81

Li Y, Zhao H, Peng Z, Ladommatos N (2002b) Tumbling flow analysis in a four-valve spark ignition engine using particle image velocimetry. *International Journal of Engine Research* 3 (3):139-155

Lindken, Lindken R, Merzkirch, Merzkirch W (2002) A novel PIV technique for measurements in multiphase flows and its application to two-phase bubbly flows. *Experiments in Fluids* 33 (6):814-825

Lindken R, Westerweel J, Wieneke B (2006) Stereoscopic micro particle image velocimetry. *Experiments in Fluids* 41 (2):161-171. doi:10.1007/s00348-006-0154-5

Liu B, Yu X, Liu H, Jiang H, Yuan H, Xu Y (2006) Application of SPIV in turbomachinery. *Experiments in Fluids* 40 (4):621-642

Maeda, Akasaka, Kawaguchi (2002) Improvements of the interferometric technique for simultaneous measurement of droplet size and velocity vector field and its application to a transient spray. *Experiments in Fluids* 33 (1):125-134. doi:10.1007/s00348-002-0453-4

Matsuura K, Komaki M, Ueyama K, Hironaga K (2004) Shadow Doppler velocimetry with double fiber-array sensors. *Experiments in Fluids* 36 (1):11-22. doi:10.1007/s00348-003-0601-5

- McGhee EJ, Towers CE, Chennaoui M, Jones AC, Towers DP Multi-constituent PIV using fluorescent particles and UV excitation. In: Sixth international symposium on particle image velocimetry, Pasadena, California , USA, 2005.
- McKeon B, Comte-Bellot G, Foss J, Westerweel J, Scarano F, Tropea C, Meyers J, Lee J, Cavone A, Schodl R, Koochesfahani M, Andreopoulos Y, Dahm W, Mullin J, Wallace J, Vukoslavčević P, Morris S, Pardyjak E, Cuerva A (2007) Velocity, Vorticity, and Mach Number. In: Springer Handbook of Experimental Fluid Mechanics. pp 215-471
- Meinhart CD, et al. (2000) Volume illumination for two-dimensional particle image velocimetry. *Measurement Science and Technology* 11 (6):809
- Meinhart CD, Wereley ST, Santiago JG (1999) PIV measurements of a microchannel flow. *Experiments in Fluids* 27 (5):414-419. doi:10.1007/s003480050366
- Melling A Seeding Gas Flows for Laser anemometry. In: AGARDograph Conference, Pennsylvania, USA, 1986. Advanced instrumentation for Aeroengine Components.
- Melling A (1997) Tracer particles and seeding for particle image velocimetry. *Measurement Science & Technology* 8 (12):1406-1416
- Merzkirch W (1987) *Flow Visualisation*. Academic Press,
- Meyers F (1991) *Generation of Particles and Seeding*. NASA Langley Technical Report Server,
- Meyers JF (1995) Development of Doppler global velocimetry as a flow diagnostics tool. *Measurement Science and Technology* 6 (6):769
- Meyers JF, Komine H (1991) Doppler Global Velocimetry, A New Way to Look at Velocity. Paper presented at the Fourth International Conference on Laser Anemometry, Cleveland, Ohio,
- Meynart R (1983) Instantaneous velocity field measurements in unsteady gas flow by speckle velocimetry. *Appl Opt* 22 (4):535-540
- Mitroglou J, Nouri J, Yan M, Gavaises M, Arcoumanis C (2007) Spray Structure Generated by Multi-Hole Injectors for Gasoline Directio Injection Engines. SAE Technical Paper Series
- Mitroglou N, Nouri J, Gavaises M, Arcoumanis C (2006) Spray Characteristics of a Multi-hole Injector for Direct-Injection Gasoline Engines. *International Journal of Engine Research* 7 (3):255-270

- Morrison GL, Jr CAG (2001) Uncertainty estimates in DGV systems due to pixel location and velocity gradients. *Measurement Science and Technology* 12 (4):369
- Muste M, Yu K, Fujita I, Ettema R (2009) Two-phase flow insights into open-channel flows with suspended particles of different densities. *Environmental Fluid Mechanics* 9 (2):161-186. doi:10.1007/s10652-008-9102-7
- Neilson JH, Gilchrist A (1969) An analytical and experimental investigation of the trajectories of particles entrained by the gas flow in nozzles. *Journal of Fluid Mechanics* 35 (03):549-559. doi:doi:10.1017/S0022112069001285
- Nishino K, Kasagi N, Hirata M (1989) Three-Dimensional Particle Tracking Velocimetry Based on Automated Digital Image Processing. *Journal of Fluids Engineering* 111 (4):384-391
- Nishino K, Kato H, Torii K (2000) Stereo imaging for simultaneous measurement of size and velocity of particles in dispersed two-phase flow. *Measurement Science and Technology* 11 (6):633
- Nobach H, Bodenschatz E (2009) Limitations of accuracy in PIV due to individual variations of particle image intensities. *Experiments in Fluids* 47 (1):27-38. doi:10.1007/s00348-009-0627-4
- Nobes DS, Ford HD, Tatam RP (2004) Instantaneous, three-component planar Doppler velocimetry using imaging fibre bundles. *Experiments in Fluids* 36 (1):3-10. doi:10.1007/s00348-003-0586-0
- Nogueira J, Lecuona A, Rodriguez P (1997) Data validation, false vectors correction and derived magnitudes calculation on PIV data. *Measurement Science and Technology* 8 (12):1493
- Olsen MG, Adrian RJ (2000) Out-of-focus effects on particle image visibility and correlation in microscopic particle image velocimetry. *Experiments in Fluids* 29 (0):S166-S174. doi:10.1007/s003480070018
- Olsen MG, Bourdon CJ (2007) Random error due to Brownian motion in microscopic particle image velocimetry. *Measurement Science and Technology* 18 (7):1963
- Ossen CW (1927) *Neuere Methoden und Ergebnisse in der Hydrodynamik*. Leipzig
- Pitcher G, Goodwin M, Wigley G Relationship between in-cylinder flows and GDI spray propagation. In: 12th International Symposium on Applications of Laser Techniques to Fluids Mechanics, Lisbon, 2004.
- Prasad AK (2000a) Particle Image Velocimetry. *Current Science* 79 (1)

- Prasad AK (2000b) Stereoscopic particle image velocimetry. *Experiments in Fluids* 29 (2):103-116. doi:10.1007/s003480000143
- Prasad AK, Adrian RJ (1993) Stereoscopic particle image velocimetry applied to liquid flows. *Experiments in Fluids* 15 (1):49-60
- Prasad AK, Jensen K (1995) Scheimpflug stereocamera for particle image velocimetry in liquid flows. *Appl Opt* 34 (30):7092-7099
- Prosperetti A, Tryggvason G (2009) *Computational Methods for Multiphase Flow*. Cambridge University Press,
- Raffel M, Westerweel J, Willert C, Gharib M, Kompenhans J (1996) Analytical and experimental investigations of dual-plane particle image velocimetry. *Optical Engineering* 35 (7):2067-2074
- Raffel M, Willert C, Kompenhans J (1998) *Particle Image Velocimetry. A practical guide*. *Experimental Fluid Mechanics*. Springer,
- Ragucci R, Cavaliere A, Massoli P (1990) Drop Sizing by Laser Light Scattering Exploiting Intensity Angular Oscillation in the mie regime. *Particle and Particle Systems Characterization* 7 (1-4):221-225
- Reeves M (1995) *Particle Image Velocimetry Applied to Internal Combustion Engine In-cylinder Flows*. Loughborough University of Technology, Loughborough
- Reeves M, Garner CP, Dent JC, Halliwell NA (1996) Particle image velocimetry analysis of IC engine in-cylinder flows. *Optics and Lasers in Engineering* 25 (6):415-432
- Reuss DL (1993) 2-DIMENSIONAL PARTICLE-IMAGE VELOCIMETRY WITH ELECTROOPTICAL IMAGE SHIFTING IN AN INTERNAL-COMBUSTION ENGINE. In: Cha SS, Trolinger JD (eds) *Optical Diagnostics in Fluid and Thermal Flow*, vol 2005. Proceedings of the Society of Photo-Optical Instrumentation Engineers (Spie). Spie - Int Soc Optical Engineering, Bellingham, pp 413-424
- Rottenkolber G, Gindele J, Raposo J, Dullenkopf K, Hentschel W, Wittig S, Spicher U, Merzkirch W (2002) Spray analysis of a gasoline direct injector by means of two-phase PIV. *Experiments in Fluids* 32 (6):710-721
- Samimy M, Wernet MP (2000) Review of planar multiple-component velocimetry in high-speed flows. *AIAA Journal* 38 (4):553-574

- Santiago JG, Wereley ST, Meinhart CD, Beebe DJ, Adrian RJ (1998) A particle image velocimetry system for microfluidics. *Experiments in Fluids* 25 (4):316-319. doi:10.1007/s003480050235
- Scarano F (2002) Iterative image deformation methods in PIV. *Measurement Science and Technology* 13 (1):R1
- Semidetnov N, Tropea C (2004) Conversion relationships for multidimensional particle sizing techniques. *Measurement Science & Technology* 15 (1):112-118
- Sepret V, Bazile R, Marchal M, Couteau G (2010) Effect of ambient density and orifice diameter on gas entrainment by a single-hole diesel spray. *Experiments in Fluids*:1-13. doi:10.1007/s00348-010-0869-1
- Shinohara K, et al. (2004) High-speed micro-PIV measurements of transient flow in microfluidic devices. *Measurement Science and Technology* 15 (10):1965
- Sick V, Drake MC, Fansler TD (2010) High-speed imaging for direct-injection gasoline engine research and development. *Experiments in Fluids* 49 (4):937-947. doi:10.1007/s00348-010-0891-3
- Sick V, Stojkovic B (2001) Attenuation Effects on Imaging Diagnostics of Hollow-Cone Sprays. *Appl Opt* 40 (15):2435-2442
- Solomon A, Anderson RW, Najt P, Zhao F (eds) (2000) *Direct Fuel Injection for Gasoline Engines*. Progress in Technology. SAE, Warrendale, PA, USA
- Spencer A, Hollis D (2005) Correcting for sub-grid filtering effects in particle image velocimetry data. *Measurement Science and Technology* 16 (11):2323
- Stansfield P, Wigley G, Justham T, Catto J, Pitcher G (2007) PIV analysis of in-cylinder flow structures over a range of realistic engine speeds. *Experiments in Fluids* 43 (1):135-146
- Sugii Y, et al. (2000) A highly accurate iterative PIV technique using a gradient method. *Measurement Science and Technology* 11 (12):1666
- Tchen CM (1947) Mean value and correlation problems connected with the motion of small particles suspended in a turbulent fluid. Delft University, Delft
- Tokuhiro A, Maekawa M, Iizuka K, Hishida K, Maeda M (1998) Turbulent flow past a bubble and an ellipsoid using shadow-image and PIV techniques. *International Journal of Multiphase Flow* 24 (8):1383-1406
- Tóth B, Anthoine J, Riethmuller M (2009) Two-phase PIV method using two excitation and two emission spectra. *Experiments in Fluids* 47 (3):475-487

- Towers DP, Towers CE (2004) Cyclic variability measurements of in-cylinder engine flows using high-speed particle image velocimetry. *Measurement Science and Technology* 15 (9):1917
- Towers DP, Towers CE (2008) High-Speed PIV: Applications in Engines and Future Prospects. In: Schroder A, Willert C (eds) *Particle Image Velocimetry New Developments and Recent Applications*. Springer, Heidelberg, Germany,
- Towers DP, Towers CE, Buckberry CH, Reeves M (1999) A colour ply system employing fluorescent particles for two-phase flow measurements. *Measurement Science & Technology* 10 (9):824-830
- Tropea C, Yarin A, Foss J (2007) Velocity, Vorticity and Mach number. In: Springer (ed) *Springer Handbook of Experimental Fluid Mechanics*.
- Turner J, Pearson R, Kenchington S (2005) Concepts for improved fuel economy from gasoline engines. *International Journal of Engine Research* 6 (2):137-157
- van Basshuysen R (2009) *Gasoline Engine with Direct Injection*. Vieweg and Teubner, Berlin
- van de Hulst HC (1957) *Light scattering by small particles*. Wiley, New York
- van Doorne C, Westerweel J (2007) Measurement of laminar, transitional and turbulent pipe flow using Stereoscopic-PIV. *Experiments in Fluids* 42 (2):259-279
- Voges M, Willert C, Monig R, Muller M, Schiffer H The challenge of stereo PIV measurements in the tip gap of a transonic compressor rotor with casing treatment. In: 15th International Symposium on Applications of Laser Techniques to Fluids Mechanics, Lisbon, 05-08 July 2010 2010.
- Voges M, Willert C, Schnell R, Müller MW, Zscherp C (2008) PIV Application for Investigation of the Rotor Blade Tip Interaction with a Casing Treatment in a Transonic Compressor Stage.
- Wagner V, Ipp W, Wensing M, Leipertz A (1999) Fuel distribution and mixture formation inside a direct-injection SI engine investigated by 2D Mie and LIEF techniques. *SAE Technical Paper Series*
- Wernet MP (2000) Application of DPIV to study both steady state and transient turbomachinery flows. *Optics & Laser Technology* 32 (7-8):497-525
- Westerweel J (1993) *Digital Particle Image Velocimetry-Theory and Application*. Delft University, Delft

- Westerweel J (1994) Efficient detection of spurious vectors in particle image velocimetry data. *Experiments in Fluids* 16 (3):236-247
- Westerweel J (1997) Fundamentals of digital particle image velocimetry. *Measurement Science & Technology* 8 (12):1379-1392
- Westerweel J (2008) On velocity gradients in PIV interrogation. *Experiments in Fluids* 44 (5):831-842
- Westerweel J, Dabiri D, Gharib M (1997) The effect of a discrete window offset on the accuracy of cross-correlation analysis of digital PIV recordings. *Experiments in Fluids* 23 (1):20-28
- Westerweel J, Scarano F (2005) Universal outlier detection for PIV data. *Experiments in Fluids* 39 (6):1096-1100. doi:10.1007/s00348-005-0016-6
- Wieneke B (2005) Stereo-PIV using self-calibration on particle images. *Experiments in Fluids* 39 (2):267-280
- Wigley G, Mehdi M, Williams M, Pitcher G, Helie J THE EFFECT OF FUEL PROPERTIES ON LIQUID BREAKUP AND ATOMISATION IN GDI SPRAYS. In: International Conference on Liquid Atomization and Spray Systems, Kyoto Japan, 2006.
- Willert CE, Gharib M (1991) Digital particle image velocimetry. *Experiments in Fluids* 10 (4):181-193. doi:10.1007/bf00190388
- Williams S, Park C, Wereley S (2010) Advances and applications on microfluidic velocimetry techniques. *Microfluidics and Nanofluidics* 8 (6):709-726. doi:10.1007/s10404-010-0588-1
- Yeh Y, Cummins HZ (1964) LOCALIZED FLUID FLOW MEASUREMENTS WITH AN HE-NE LASER SPECTROMETER1 (E). *Applied Physics Letters* 4 (10):176-&
- Yu X-J, Liu B-J (2007) Stereoscopic PIV measurement of unsteady flows in an axial compressor stage. *Experimental Thermal and Fluid Science* 31 (8):1049-1060
- Zhang W, Wang Y, Lee S (2008) Simultaneous PIV and PTV measurements of wind and sand particle velocities. *Experiments in Fluids* 45 (2):241-256
- Zhang ZH, Towers CE, Towers DP (2006) Time efficient color fringe projection system for 3D shape and color using optimum 3-frequency Selection. *Optics Express* 14 (14):6444-6455

- Zhao F (2009) *Advanced Direct Injection Combustion Engine Technologies and Development: Volume 1: Gasoline and Gas Engines*. Woodhead Publishing,
- Zhao F, Lai M, Harrington DL (1995) The spray characteristics of automotive port fuel injection. A critical review. SAE Technical Paper Series
- Zhao F, Lai M, Harrington DL (1999a) A Review of Mixture Preparation and Combustion Control Strategies for Spark-Ignited Direct Injection Gasoline Engines SAE Technical Paper Series
- Zhao F, Lai MC, Harrington DL (1999b) Automotive spark-ignited direct-injection gasoline engines. *Progress in Energy and Combustion Science* 25 (5):437-562